USC
UNIVERSIDADE
DE SANTIAGO
DE COMPOSTELA

ESCOLA DE DOUTORAMENTO
INTERNACIONAL

Ramón
Rial Silva

Tese de doutoramento

Developing physical properties of hierarchical nanostructures for biomedical applications

Santiago de Compostela, 2020

PD en Ciencia de Materiais


USC
UNIVERSIDADE
DE SANTIAGO
DE COMPOSTELA

TESE DE DOUTORAMENTO

DEVELOPING PHYSICAL PROPERTIES OF HIERARCHICAL NANOSTRUCTURES FOR BIOMEDICAL APPLICATIONS

Ramón Rial Silva

ESCOLA DE DOUTORAMENTO INTERNACIONAL DA UNIVERSIDADE
DE SANTIAGO DE COMPOSTELA
PROGRAMA DE DOUTORAMENTO EN CIENCIA DE MATERIAIS

SANTIAGO DE COMPOSTELA, 2020

USC
UNIVERSIDADE
DE SANTIAGO
DE COMPOSTELA

DECLARACIÓN DO AUTOR/A DA TESE

Developing physical properties of hierarchical nanostructures for biomedical applications.

D./Dna. Ramón Rial Silva

Presento a miña tese, seguindo o procedemento axeitado ao Regulamento, e declaro que:

1) A tese abarca os resultados da elaboración do meu traballo.
2) De selo caso, na tese faise referencia ás colaboracións que tivo este traballo.
3) A tese é a versión definitiva presentada para a súa defensa e coincide coa versión enviada en formato electrónico.
4) Confirmo que a tese non incorre en ningún tipo de plaxio doutros autores nin de traballos presentados por min para a obtención doutros títulos.

En Santiago de Compostela., …… de ………….. de 20…..

Asdo:

USC
UNIVERSIDADE
DE SANTIAGO
DE COMPOSTELA

AUTORIZACIÓN DO DIRECTOR/TITOR DA TESE

D./Dna. **Juan M. Ruso Veiras**

En condición de: **Titor/a e director/a**

Título da tese: **Developing physical properties of hierarchical nanostructures for biomedical applications.**

INFORMA:

Que a presente tese, correspóndese co traballo realizado por D/Dna Ramón Rial Silva, baixo a miña dirección/titorización, e autorizo a súa presentación, considerando que reúne os requisitos esixidos no Regulamento de Estudos de Doutoramento da USC, e que como director/titor desta non incorre nas causas de abstención establecidas na Lei 40/2015.

*En **Santiago de Compostela**, ... de .... de 20.............*

Sinatura:


USC
UNIVERSIDADE
DE SANTIAGO
DE COMPOSTELA

Ao meu Director.
Por abrirme os ollos e ensinarme que a ciencia é unha carreira de gran fondo. Por impulsarme na saída e guiarme sempre no camiño.

Aos colegas da *Universidad del Sur.*
Polas infinitas *pláticas*; amenas, valiosas, e instrutivas. Por conseguir transportarme á outra beira do planeta co seu carácter único, singular humor e co peculiar compañeirismo dos seus mates compartidos.

Aos colegas dos *3B's.*
Pola profesionalidade, entrega e constante axuda. Porque entre irmáns non existen as fronteiras.

Aos colegas do *Ångström Laboratory.*
Pola diversidade. Por integrarme con *fikas* no frío da terra onde a noite alumbra.

Aos do café e aos do cocido.
Pola indispensable compañía de mesa e sobremesas. Polos eternos debates de múltiple contido, fondo diverso e forma dispar. Por demostrar que se chega á fin do mundo cunha etapa en bicicleta.

Aos do Carril e aos da Capital. Aos da Serra e aos da Chaira. Aos das foliadas intensivas e rivalidades deportivas. Tamén aos que están fóra, pero que se levan ben dentro.

Á familia.
Por ser e sempre estar.

A Alba.
Por me acompañar.

Acknowledgements

Institutional

Fundación Ramón Areces, Spanish MINECO (MAT2015-71826-P), Xunta de Galicia (ED431B 2017/21), Programa Iacobus, financial support from “Fundação para a Ciência e Tecnologia" (grants SFRH/BPD/95446/2013 to R. R. C. and IF/00032/2013 to I. P.).

USC
UNIVERSIDADE DE SANTIAGO DE COMPOSTELA

Resumo

Comprender a base fisicoquímica e os diferentes modelos de nanosistemas é, actualmente, dunha importancia esencial nun gran número de áreas científicas e procesos industriais. Na presente disertación púxose un énfase específico nos nanosistemas creados por autoensamblaxe. A formación, organización e comportamento de unidades individuais a estas escalas presenta un enorme desafío no ámbito da investigación, tendo en conta as intrinsecamente pequenas dimensións implicadas, a susceptibilidade e vulnerabilidade ás mínimas flutuacións no sistema, e os problemas que aparecen ao intentar escalar estas estruturas para un uso extensivo e unha implantación xeral.

Os conceptos teóricos e o desenvolvemento de modelos computacionais para predicir diferentes propiedades dos procesos de autoagregación molecular son moi útiles para un mellor coñecemento do tema e para acadar enfoques máis eficientes. Neste senso, na primeira parte do presente documento (Capítulo 3), levouse a cabo unha combinación de estudos computacionais e experimentais para analizar a agregación, unión e interaccións de proteínas. Como modelos biomoleculares escolléronse a albúmina sérica bovina (BSA) e o fibrinóxeno (Fib), dúas proteínas cun uso moi estendido debido á súa ampla gama de funcións fisiolóxicas e biolóxicas.

O seu comportamento en presenza de surfactantes e drogas de diferente natureza avaliouse mediante simulacións de dinámica molecular (MD) e procedementos experimentais. Utilizouse a dispersión de raios X de pequeno ángulo (SAXS), calorimetría de titulación isotérmica (ITC), potencial zeta, UV-vis, fluorescencia, dicroísmo circular de radiación sincrotrón (SRCD), calorimetría de dixitalización diferencial (DSC) e espectroscopía Raman para corroborar, en maior profundidade, os mecanismos teóricos propostos, as interaccións implicadas e os cambios conformacionais suxeridos. Os resultados combinados poden ter unha importancia clave para achanzar o camiño cara unha mellor comprensión dos primeiros pasos de numerosas enfermidades neurodexenerativas, e abrirán novas vías cara á aplicación de información supra-molecular complexa no deseño racional de medicamentos.

En canto á evolución estrutural da albúmina sérica bovina coa adición de surfactantes, as simulacións de dinámicas moleculares revelaron que esta proteína, cando non hai ligandos, presenta unha forma expandida que permite a formación de dímeros. Os resultados de SAXS, en combinación cos de SRCD, demostraron que o

sistema en solución está composto por monómeros parcialmente despregados (75 %) e os seus respectivos dímeros (25 %) sen cambios na estrutura secundaria. Coa adición dos ligandos, as características máis importantes da interacción obtivéronse a partir da análise con ITC, mostrando que ámbolos surfactantes interactúan co monómero e o dímero en proporcións molares inferiores a 30: 1. Despois de alcanzar a saturación, os ligandos forman pequenos agregados distribuídos por toda a superficie do BSA. Os estudos de SAXS e de MD serven para inferir que o número de ligandos que forman os agregados mencionados é similar para ambos surfactantes, pero as súas estruturas sofren algúns cambios: estirados cunha forma moi similar e case superpostos no caso de SFPO e unha distribución máis ampla cunha notable superposición para SDS. Os datos de SRCD confirmaron que, ademais do proceso de agregación, a BSA tamén sofre alteracións na súa estrutura secundaria, pasando de α-helix a β-sheet.

No que se refire aos estudos relacionados co fibrinoxeno, avaliáronse os efectos estruturais e as propiedades de unión de dous betablocantes (acebutolol e propranolol) sobre o Fib desde o punto de vista teórico e experimental. Os resultados *in silico* previos mostraron que os valores de Enerxía Libre de Unión (FEB, polas súas siglas en inglés) para os complexos de acoplamento obtidos (acebutolol/fibrinóxeno e propanolol/fibrinóxeno) estan moi próximos. Ademais, os resultados teóricos obtidos mostran que o mecanismo de acoplamento para o propranolol e o acebutolol baséase principalmente en interaccións hidrofóbicas non covalentes, co sitio de unión na rexión E do fibrinóxeno. Do mesmo modo, demostrouse que o propranolol e o acebutolol son capaces de inducir cambios significativos na comunicación entre os residuos e nas propiedades de flexibilidade da rede de residuos da rexión E de fibrinóxeno, inducindo perturbacións locais en residuos alostéricos.

Avaliando as propiedades de unión e os efectos estruturais que os betablocadores (acebutolol e propranolol) teñen sobre o fibrinóxeno, os resultados do potencial zeta e do ITC demostraron que as interaccións son relativamente débiles para ambos os casos, sendo un pouco máis pronunciadas no caso do propranolol. Conxuntamente, os datos SAXS tamén dan algunha idea sobre o feito de que o acebutolol non é capaz de causar nin cambios conformacionais nin agregación no fibrinóxeno, de acordo cos resultados computacionais. Non obstante, os datos de SAXS sinalan que o propranolol ten un impacto significativo na estrutura do fibrinóxeno. Estes resultados poden ser moi importantes para comprender os primeiros pasos dos procesos de coagulación onde a unión da trombina no dominio E e posteriormente a polimerización do fibrinóxeno son aspectos esenciais.

Novamente, os resultados computacionais do modelado da interacción entre o Fib e o BTS mostraron que os valores de unión da enerxía libre de Gibbs para os complexos de acoplamento obtidos están moi próximos na maioría dos casos, e indican tamén que a súa formación está relacionado con procesos termodinámicos espontáneos. A través dos datos pode suxerirse que as diferenzas detectadas nos valores de FEB para as nove posturas de BTS poden explicarse en base ás diferentes composicións e propiedades de unión dos residuos en interacción presentes no ambiente biofísico do sitio de unión ao fibrinóxeno (rexión E). Ademais, o mecanismo de acoplamento parece deberse principalmente a interaccións hidrofóbicas non covalentes, como as Π - Π, e asociadas a pontes de hidróxeno, que xuntas contribúen á estabilidade dos complexos formados. Paralelamente, os datos experimentais do ITC confirmaron os resultados da enerxía libre de unión de Gibbs e as interaccións implicadas no proceso de unión do fibrinóxeno co BTS. Do mesmo xeito, demostrouse que todas as posturas de unión a BTS poden afectar directamente aos modos normais de flexibilidade ao diminuír o grao de colectividade no sitio de unión ao fibrinóxeno (residuos da rexión E). As medicións de UV-vis e fluorescencia apoiaron estas últimas conclusións. Estes resultados tamén foron confirmados por SAXS, técnica que non só corroborou a presenza de cambios conformacionais no fibrinóxeno, senón que tamén demostrou que dependen da concentración de fármacos.

Nun estudo similar avaliáronse tamén os mecanismos conformacionais de unión do fibrinóxeno baixo interacción con antibióticos β-lactam recoñecidos. Dun xeito semellante aos estudos anteriores, novamente os resultados computacionais apuntaron que, a pesar destas diferenzas conformacionais, ambos antibióticos presentan afinidade moi similar baseada nos valores de enerxía de unión libre obtidos. Ademais, a incorporación semisintética dun átomo de halóxeno (Cl) adicional na molécula de dicloxacilina respecto á molécula de cloxacilina e a súa orientación relativa á atracada na rexión E do fibrinóxeno poderían reducir significativamente a aparición de potenciais efectos secundarios fibrinolíticos que afectan á coagulación. proceso que normalmente está asociado a β-lactam administrado por vía parenteral. Ademais, os modos normais de baixa frecuencia colectiva e os mapas LPRS revelaron as sutís diferenzas na dinámica conformacional das cadeas de rexión E relevantes, en estado non ligado e en estado unido aos antibióticos β-lactam. Ademais, os resultados experimentais do fibrinóxeno ao contactar con antibióticos β-lactam, corroboraron excelentemente as predicións computacionais de: enerxías de unión, residuos diana e estequiometría. O enorme impacto que ten a estrutura molecular da penicilina no proceso de unión foi confirmado por datos calorimétricos cuantitativos sobre ITC. Pola súa banda, as medicións de DSC permitiron tamén cuantificar enerxeticamente o papel que xoga a elasticidade do fibrinóxeno. Finalmente, os resultados obtidos son de suma importancia durante o novo deseño racional de medicamentos derivados de antibióticos β-lactam para evitar potenciais efectos secundarios fibrinolíticos, aumentar a selectividade/especificidade obxectivo con taxas de beneficio/risco óptimas máis alá dos fenómenos de resistencia a antibióticos

β-lactam e favorecen a implementación de criterios rigorosos para unha terapia antibiótica máis personalizada.

Mentres que a bionanotecnoloxía orixinou un crecente interese no estudo das interaccións das nanoestruturas con entidades biolóxicas, en paralelo, importantes avances no campo da investigación biomédica demostraron a utilidade das nanopartículas como elemento central da liberación de fármacos/xenes, ou na enxeñaría de tecidos. As biocerámicas considéranse materiais axeitados para a reparación ósea debido á súa alta capacidade osteocondutora. Entre eles, a hidroxiapatita (HA) é a opción máis común para desenvolver substitutos sintéticos debido á súa composición química similar á fase mineral do óso. Trátase dun mineral ou biocerámica que poden producir os seres vivos de forma natural. *In vivo*, a nucleación de hidroxiapatita e o crecemento mineral ocorren dentro da matriz extracelular das células e ten a fórmula xeral $Ca_{10}(OH)_2(PO_4)_6$.

As partículas de escala nanométrica, ou nanopartículas, presentan múltiples aplicacións potenciais dentro da industria de dispositivos biomédicos. Non obstante, estas aplicacións requiren un control preciso dos seus tamaños, formas e morfoloxías, que xogan un papel principal na maioría das súas propiedades. A este respecto, estableceuse con éxito unha nova ruta para a síntese de nanopartículas de hidroxiapatita mediante un dispositivo microfluídico (Capítulo 4). O proceso lévase a cabo mediante un fluxo laminar continuo a través das canles dun microchip ou da combinación deles. As nanopartículas resultantes mostraron as mesmas propiedades de composición, lonxitude, orientación e rugosidade que as obtidas polos métodos convencionais. Ademais, este tipo de sistemas microfluídicos permiten afinar a estrutura mediante cambios razoadamente sinxelos e producir nanopartículas de diferente tamaño variando tan só as velocidades e relacións de fluxo. Demostrouse que a morfoloxía estrutural dos nanorods de hidroxiapatita sintetizada e relativamente homoxénea e uniforme cun patrón de rede desultorio composto por nanopartículas altamente aglomeradas, de tamaño similar. As distribucións resultantes non son isotrópicas, senón bimodais. Cun deseño axeitado e condicións apropiadas, este dispositivo é capaz de enxeñar nanopartículas de diferente tamaño, só variando os caudais. Estes resultados tamén poden iluminar o potencial dos dispositivos de microfluídicos como ferramenta para automatizar a síntese de nanopartículas de alta calidade debido ao seu gran rendemento, á flexibilidade e aos baixos custos que acarrexa.

As excelentes características que presentan estas nanopartículas biocerámicas permítenlles funcionar como material ideal para a enxeñaría de tecidos duros. Por outra banda, non se debe esquecer o feito de que o seu efecto biolóxico depende da capacidade de chegar aos órganos ou células obxectivo dentro do corpo. Conseguilo, implica vías de administración como a intravenosa, onde as nanopartículas interactúan cos compoñentes sanguíneos, proteínas plasmáticas, determinando así a súa compatibilidade sanguínea. Por iso, a avaliación de dita hemocompatibilidade require varios enfoques, incluíndo en particular, o estudo destas interaccións. Un dos conceptos que mellor define este tipo de relacións é a "coroa proteica", é dicir, a capa proteica absorbida na nanopartícula. Co fin de caracterizala, estudouse a interacción da BSA coas nanopartículas de hidroxiapatita empregando unha batería de técnicas: ITC, potencial zeta, UV-vis, fluorescencia e CD (Capítulo 5). Nesta liña, utilizouse un enfoque experimental múltiple para comprender e caracterizar a adsorción da albúmina sérica bovina sobre nanopartículas de hidroxiapatita. A análise microcalorimétrica revelou que a unión entre as nanopartículas de BSA e HA é exotérmica e diminúe gradualmente co aumento da concentración de HA. O modelo que mellor se axusta aos valores experimentais suxeriu que toda a proteína se adsorbe do mesmo xeito sobre a superficie das nanopartículas por enlaces non covalentes, tamén corroborada polo potencial zeta. Seguindo a teoría da transferencia de enerxía de resonancia Förster (FRET polas súas siglas en ingles), pódese inferir que o *quenching* é estático e o mecanismo implica unha formación complexa. Os estudos cinéticos tamén revelaron que a interacción entre a proteína e o composto inorgánico é bastante lenta, manténdose no tempo, xa que se obtén o valor máximo despois de 24 horas de interacción. Por último, os resultados espectrais de CD confirmaron que a excelente adaptación da BSA na superficie das nanopartículas é consecuencia da flexibilidade da súa estrutura 3D.

Unha vez definidos e caracterizados os procesos de autoagregación de sistemas moleculares mixtos e introducida a importancia da coroa proteica, o seguinte paso é deseñar e crear materiais híbridos complexos con atributos biolóxicos mellorados. Os seguintes capítulos da presente tese doutoral describen a síntese, caracterización fisicoquímica e biolóxica de diversos materiais co potencial uso na rexeneración ósea guiada (GBR), implantes ou dispositivos de fixación.

As estruturas sintetizadas preséntanse dende as mostras máis sutís e delicadas: membranas de bicapa (Capítulo 6); ás máis intrincadas e densas: hidroxeles complexos bioinspirados e micropartículas mixtas de hidroxel (Capítulos 9 e 10, respectivamente). Así mesmo, tamén se estudaron filmes ultra delgados (Capítulo 7) e estruturas biomiméticas (Capítulo 8) en termos da súa bioactividade, ou sexa, a capacidade de mineralización; e en termos da súa resposta celular, demostrando a súa biocompatibilidade e calidades osteocondutivas.

Fíxose un especial fincapé nas propiedades viscoelásticas, a rixidez mecánica e a resistencia. Ademais de permitir o crecemento natural do tecido óseo, as mostras deseñadas deben soportar adecuadamente os esforzos mecánicos, polo que co obxectivo de valorar estes parámetros, levouse a cabo unha análise reolóxica completa de diferentes hidroxeles (Capítulo 9). Os atributos inferidos a partir dos datos obtidos mostraron o notable impacto que ten a adición de nanorods biocerámicos á matriz branda no rendemento mecánico final das mostras, xunto coa esperable mellora das súas funcións biolóxicas.

Como xa foi mencionado, coa combinación dun precursor inorgánico e unha proteína adecuada, pódese crear un deseño composto único para obter unha interface biomaterial que imite as propiedades do óso natural ao combinar capas cerámicas con outras de materia branda. Como se explica en todo o documento, a forma alongada, en comparación coas formulacións esféricas, dos nanorods de HA resulta nun aumento da súa superficie. Esta peculiaridade mellora as interaccións electrostáticas cos policatos e permite a acumulación de LbL (Capítulo 7). Este tipo de materiais obtidos pola técnica LbL son axeitados para revestir dispositivos implantables xa que son osteocondutores e soportan a adhesión, a difusión e a viabilidade das células, abrindo un novo rango de posibilidades para crear interfaces biocompatibles.

Tendo en conta estas consideracións, pódense deseñar múltiples estruturas complexas e híbridas con fins biomédicos. A este respecto, creouse unha membrana de dúas caras (Capítulo 6) que reproduce a estrutura e a función do periostio. O alginato e diversas concentracións de nanohidroxiapatita combináronse para desenvolver membranas de bicapa cunha composición química, rugosidade e porosidade diferentes a cada lado. Demostrouse que se produciu unha interacción eficiente entre os nanorods de HA e as cadeas de ALG. Con maiores concentracións de HA, a lonxitude e ramificacións das redes de polímeros aumentaron e, á súa vez, diminueu a cantidade de auga na estrutura. Esta condición resultou nun aumento da viscosidade e, en consecuencia, na resistencia do hidroxel fresco, mentres que se reduciu a plasticidade. A membrana esta constituída por un lado fibroso moi poroso e un lado rico en minerais con maior rugosidade, confirmando a súa funcionalidade de bicapa. Observouse unha resposta celular favorable para todas as membranas probadas, específicamente no crecemento de osteoblastos no lado rico en minerais e fibroblastos no lado fibroso. Ademais, as membranas con maior cantidade de HA induciron notablemente a diferenciación de osteoblastos. As propiedades físico-químicas das membranas de bicapa poden axustarse facilmente, polo que proporcionan versatilidade para cumprir os complexos requirimentos da enxeñaría dos tecidos óseos.

Do mesmo xeito, tamén se crearon estruturas mecánicamente robustas, (Capítulo 8). Estes complexos biomateriais presentan unha estrutura de malla de fibra moi interconectada, debido á óptima distribución de nano-varillas de HA dentro da rede de xelatina-TA. As mostras presentaron un certo grao de rugosidade na superficie, unha propiedade que é esencial para acadar unha adecuada aceptación do tecido hóspede. Ademais, a distribución homoxénea de HA entre as cadeas de TA e proteínas resulta nun maior nivel de renaturación de GE en comparación co GE non ligado, o que leva a unha andamiaxe de resistencia mellorada. A presenza de partículas de nano-HA tamén induce unha mineralización mellorada dos andamiaxes, logrando un crecemento cristalino de forma, composición e orientación equivalente ao que presenta a fase mineral dos tecidos calcificados. Finalmente, corroboráronse as propiedades de degradación en diferentes condicións biolóxicas, e tamén a súa capacidade para inducir, baixo fluídos fisiolóxicos, un revestimento de hidroxiapatita bioxénica. Estas condicións son necesarias para a súa integración no tecido hóspede e cumpríronse satisfactoriamente.

Para analizar o comportamento reolóxico deste tipo de andamios de hidroxel, creáronse cinco xeles híbridos mecánicamente robustos coa combinación de xelatina, alxinato, fibrinóxeno, albúmina de soro bovino e hidroxiapatita. Todos eles presentan unha estrutura de malla altamente interconectada, confirmada por FT-IR. A microscopía confocal Raman revelou que tanto a BSA como o Fib se incorporan ás estadas mantendo a súa conformación nativa. Mentres que os xeles de fibrinóxeno manteñen as distribucións iniciais, a presenza de BSA homoxeneiza moito mellor todos os compoñentes. Este feito atribúese á maior flexibilidade do BSA que permite máis graos de liberdade ao andamio para minimizar a enerxía da formación de hidroxel. Ademais, o hidroxel Gel/Alg/BSA/HAp presentou mellores propiedades de degradación ao longo do tempo, debido en parte á mellor distribución da HA, que contribúe ao aumento da captación de auga. A análise reolóxica revela que o comportamento dos materiais corresponde a un material de vidro brando. A análise de fluencia demostrou que a inclusión de nanorods reforza a estrutura dos xeles, contribuíndo a fortalecelos e corroborou que a adición de BSA presenta un mellor comportamento reolóxico. Finalmente, tamén se demostrou que as propiedades morfolóxicas e mecánicas dos hidroxeles se poden axustar facilmente incluíndo varios compoñentes; proporcionando así mellores prestacións ás aplicacións de enxeñaría de tecidos brandos.

Xunto ca síntese, desenrolo e caracterización dos elementos constitutivos descritos, unha das singularidades da presente disertación é a aplicación de enfoques experimentais novedosos para substituír ós tradicionais, mediante a utilización de sistemas microfluídicos para fins que, ata o de agora, só se abordaran con procesos masivos. Alén da anteriormente mencionada síntese de HA, utilizaronse este tipo de técnicas para automatizar a creación de materiais híbridos complexos. Pola súa banda, as simulacións computacionais de fluxo demostraron ser unha ferramenta excepcional para predicir o comportamento das fases líquidas, modelar a formación das gotas nos dispositivos microfluidicos e para estudar a relación entre as propiedades físicas e as variacións dos diferentes caudais de entrada. Ditas liñas experimental e *in silico*, debido á súa importancia e actualidade, seguen sendo o centro de estudo de investigacións presentes e planificacións futuras.

Para concluír, cómpre destacar a importancia e a innovación deste traballo de doutoramento, que reside no estudo e optimización de sistemas de autoagregados, promovendo o desencadeamento de secuencias que conducen á deposición, nucleación e crecemento de cristais de hidroxiapatita coa xeometría e orientación adecuadas. Con este fin, desenvolvéronse de forma efectiva novas estratexias e novas rutas sintéticas, dando lugar a materiais economicamente viables que imitan a estrutura e a composición da matriz extracelular, facéndoos plenamente axeitados para numerosas aplicacións en rexeneración de tecidos e enxeñaría biomédica.

Summary

Understanding the physicochemical basis and the different models of nanosystems is, currently, of an essential importance on a significant number of scientific areas and industrial processes. In the present dissertation, specific focus has been put on nanosystems created by self-assembly. The formation, organization and behaviour of single units at these scales are a challenging topic in light of the inherently small dimensions involved, the susceptivity and vulnerability to minimal fluctuations, and the intrinsic problems that appear when trying to scale up these structures for extensive use and general implementation.

Theoretical concepts and the development of computational models to predict different properties of self-aggregation processes of mixed molecular systems, are remarkably convenient and useful for a better knowledge of this topic and for reaching more effective approaches. For that end, in the first part of this report (Chapter 3), a combination of computational and experimental studies was performed to analyse protein aggregation, binding and interactions. Bovine serum albumin (BSA) and fibrinogen (Fib), two widespread used proteins because of their wide range of physiological and biological functions, were chosen as the biomolecule models. Their behaviour in presence of surfactants and drugs of different nature was assessed by means of molecular dynamic simulations (MD) and experimental procedures. Small angle X-ray scattering (SAXS) was used to validate those models and isothermal titration calorimetry (ITC), zeta potential, UV-vis, fluorescence, synchrotron radiation circular dichroism (SRCD), differential scanning calorimetry (DSC) and Raman spectroscopy were applied to further corroborate the proposed theoretical mechanisms, the interactions involved and the conformational changes suggested. The combined results might be of a key importance to pave the way to better understand the early steps of numerous neurodegenerative diseases and shall open new avenues towards the application of complex supra-molecular information in rational drugs-design with biomedical applications.

While bionanotechnology led to an increasing interest in the study of the interactions of nanostructures with biological entities, in parallel, important investigations in the field of biomedical research have demonstrated the usefulness of nanoparticles as the centerpiece of drug/gene delivery, visualization, or tissue engineering. Bioceramics are considered suitable materials for bone repair because of

their high osteoconductive capacity. Among them, hydroxyapatite (HA) is the most common choice to develop synthetic substitutes due to its chemical composition that is similar to the mineral phase in the bone. It is thus a mineral or bioceramic that can be produced by the living beings. *In vivo*, hydroxyapatite nucleation and mineral growth occur within the extracellular matrix of cells and has the general formula $Ca_{10}(OH)_2(PO_4)_6$.

Particularly, nanoparticles have many potential applications within the biomedical device industry. However, these applications demand a precise control of their sizes, shapes and morphology which play a main role in most properties. In this regard, a new route for the synthesis of hydroxyapatite nanoparticles using a microfluidic device was successfully established (Chapter 4). The process is carried out by continuous laminar flow through the device. The obtained nanoparticles have shown same properties of composition, length, orientation and roughness than those produced by conventional methods. Besides, this type of microfluidic systems allows to fine tune the structure via simple engineering and produce nanoparticles of different size by only varying the flow velocities and ratios.

The excellent features that these bioceramic nanoparticles exhibit, enable them to function as ideal material for hard tissue engineering. On the other hand, it should not be overlooked the fact that their biological effect depends on the ability to reach the target organs or cells inside the body. Achieving these goals involves routes of administration such as intravenous, where the nanoparticles interact with blood components, namely plasma proteins, thus determining their hemocompatibility. Hence, the evaluation of hemocompatibility requires several approaches, including particularly, the study of these interactions. One of the concepts that best defines this type of relationships is the “protein corona”, that is, the protein layer absorbed on the nanoparticle. To characterize it, the biological interaction of bovine serum albumin and hydroxyapatite nanoparticles was presented by using a battery of techniques: ITC, zeta potential, UV-vis, fluorescence and CD (Chapter 5). Experimental data was analysed to determine important parameters such as rates, affinities, and stoichiometries of protein associated with the nanoparticles. Besides, the important role the protein flexibility plays on the mentioned biomedical purposes has been also evaluated.

Having defined and characterized the self-aggregation processes of mixed molecular systems, and having introduced the importance of the protein corona, the further step is to design and create complex hybrid materials with enhanced biological attributes. The following Chapters of the current doctoral thesis describe the synthesis, physicochemical and biological characterization of diverse materials with the potential use in guided bone regeneration (GBR) and implants or fixation devices as well.

Synthesized structures are presented from the more subtle and delicate samples: bilayer membranes (Chapter 6); to the more intricate and dense ones: bioinspired composite hydrogels and mixed hydrogel microparticles (Chapters 9 and 10, respectively). Likewise, ultrathin films (Chapter 7), and biomimetic scaffolds (Chapter 8) were also studied in terms of their bioactivity, i. e. mineralization capacities; and their cellular response, proving their biocompatibility and osteoconductive qualities. Special focus has been put on the viscoelastic properties, mechanical stiffness and strength. While allowing the natural growth of bone tissue, designed samples must also withstand properly the mechanical efforts, and therefore, a complete rheological analysis of different hydrogels has been carried out (Chapter 9). The attributes inferred from the data showed the notable impact the addition of bioceramic nanorods to the soft matrix has in the final mechanical performance alongside the predicted enhancement of the biological functions.

Equally important, it should also be highlighted the application of innovative experimental approaches to substitute traditional ones, by the utilization of microfluidics systems for purposes that, generally, were only addressed with bulk processes. In addition to the aforementioned HA synthesis, such techniques have been used to automate the creation of complex hybrid materials as well. For its part, computational flow simulations were probed to be an exceptional tool to predict comportment of the liquid phases, to model the droplet formation and to study the dependence on the physical properties and the rates of the respective flows. This subject, due to its relevance and topicality, remains the centre of study of present researches and future plans.

Conclusively, the importance and novelty of this proposal lies in the study and optimization of self-aggregate systems that promote the triggering of sequences leading to the deposition, nucleation and growth of hydroxyapatite crystals with the proper geometry and orientation. New strategies and novel synthetic routes were effectively developed, resulting in economically viable materials, that mimic the structure and composition of the extracellular matrix, making them eligible and suitable for numerous applications in tissue regeneration and biomedical engineering.

List of Publications

Some of the research leading to this thesis has appeared previously in the following publications.

Journal Articles

- Paula V. Messina, **Ramón Rial**, Juan M. Ruso, "Models for Self-assembly of nanoscale systems with biomedical applications". *Current pharmaceutical design*, vol. 22, no. 34, pp. 5211-5220, 2016.

  Journal Impact Factor (JIF): 2.611
  Average JIF Percentile: 54.669

- Paula V. Messina, Jose M. Besada-Porto, **Ramón Rial**, Humberto González-Díaz, Juan M. Ruso, "Computational modeling and experimental facts of mixed self-assembly systems". *Current pharmaceutical design*, vol. 22, no. 34, pp. 5249-5256, 2016.

  Journal Impact Factor (JIF): 2.611
  Average JIF Percentile: 54.669

- Javier Sartuqui, A. Noel Gravina, **Ramón Rial**, Luciano A. Benedini, Juan M. Ruso, Paula V. Messina, "Biomimetic fiber mesh scaffolds based on gelatin and hydroxyapatite nano-rods: Designing intrinsic skills to attain bone reparation abilities". *Colloids and Surfaces B: Biointerfaces*, vol. 145, pp. 382-391, 2016.

  Journal Impact Factor (JIF): 3.887
  Average JIF Percentile: 72.288

- **Ramón Rial**, Brandon Tichnell, Brendan Latimer, Zhen Liu, Paula V. Messina, Juan M. Ruso, "Structural and kinetic visualization of the protein corona on bioceramic nanoparticles". *Langmuir*, vol. 34, n. 7, pp. 2471-2480, 2016.

  Journal Impact Factor (JIF): 3.683
  Average JIF Percentile: 68.831

- **Ramón Rial**, J.F. Armando Soltero, Pedro V. Verdes, Zhen Liu, Juan M. Ruso, "Mechanical Properties of Composite Hydrogels for Tissue Engineering". *Current Topics in Medicinal Chemistry*, vol. 18, n. 14 pp. 1214-1223, 2018.

  Journal Impact Factor (JIF): 3.442
  Average JIF Percentile: 68.023

- **Ramón Rial**, Pablo G. Tahoces, Natalia Hassan, M.L. Cordero, Zhen Liu, Juan M. Ruso, “Noble microfluidic system for bioceramic nanoparticles engineering”. *Materials Science and Engineering: C*, vol. 102, pp. 221-227, 2016.

  Journal Impact Factor (JIF): 5.880
  Average JIF Percentile: 80.263

- Michael González-Durruthy, Gustavo Scanavachi, **Ramón Rial**, Zhen Liu, M. Natália D.S. Cordeiro, Rosangela Itri, Juan M. Ruso, “Structural and energetic evolution of fibrinogen toward to the betablocker interactions”. *International journal of biological macromolecules*, vol. 137, pp. 405-419, 2019.

  Journal Impact Factor (JIF): 5.162
  Average JIF Percentile: 86.689

- **Ramón Rial**, Rui R. Costa, Rui L. Reis, Zhen Liu, Iva Pashkuleva, Juan M. Ruso, “Mineralization of Layer-by-Layer Ultrathin Films Containing Microfluidic-Produced Hydroxyapatite Nanorods”. *Crystal Growth & Design*, vol. 19, n. 11, pp. 6351-6359, 2019.

  Journal Impact Factor (JIF): 4.089
  Average JIF Percentile: 74.819

- Noelia L. D’Elía, **Ramón Rial**, Javier Sartuqui, Daniel Ercoli, Juan M. Ruso, Paula V. Messina, Gemma Mestres, “Development and characterisation of bilayer periosteum-inspired composite membranes based on sodium alginate-hydroxyapatite nanoparticles”. *Journal of Colloid and Interface Science*, vol. 572, pp. 408-420, 2020.

  Journal Impact Factor (JIF): 7.489 (2019)
  Average JIF Percentile: 80.818 (2019)

- **Ramón Rial**, Zhen Liu, Juan M. Ruso, “Soft Actuated Hybrid Hydrogel with Bioinspired Complexity to Control Mechanical Flexure Behavior for Tissue Engineering”. *Nanomaterials*, vol. 10, n. 7, pp. 1302, 2020.

  Journal Impact Factor (JIF): 4.324 (2019)
  Average JIF Percentile: 65.762 (2019)

- Gustavo Scanavachi, Y.R. Espinosa, J.S. Yoneda, **Ramón Rial**, Juan M. Ruso, Rosangela Itri, “Aggregation features of partially unfolded bovine serum albumin modulated by hydrogenated and fluorinated surfactants: Molecular dynamics insights and experimental approaches”. *Journal of colloid and interface science*, vol. 572, pp. 9-21, 2020.

  Journal Impact Factor (JIF): 7.489 (2019)
  Average JIF Percentile: 80.818 (2019)

- Michael González-Durruthy, **Ramón Rial**, M. Natália D.S. Cordeiro, Zhen Liu, Juan M. Ruso, “Exploring the conformational binding mechanism of fibrinogen induced by interactions with penicillin β-lactam antibiotic drugs”. pp. 114667, 2020.

  Journal Impact Factor (JIF): 5.065 (2019)
  Average JIF Percentile: 81.277 (2019)

Conferences

- **Ramón Rial**, "Desenvolvemento de propiedades físicas de nanoestruturas xerárquicas para aplicacións biomédicas". *V Encontro Mocidade Investigadora*, Santiago de Compostela, 12-13 June, 2017.
- Noelia L. D'Elía, **Ramón Rial**, Javier Sartuqui, Daniel Ercoli, Juan M. Ruso, Paula V. Messina, Gemma Mestres, "Alginate-hydroxyapatite composites for guided bone regeneration: rheology and tensile strength". *SAP (Simposio Argentino de Polimeros)*, Buenos Aires, Argentina, 9-11 October, 2019.

Declaration of Authorship

Unless specified in the Experimental Section of each respective Chapter, all empirical procedures, experiments and measurements were performed by the Author.

Contents

List of Figures **xxix**

List of Tables **xxxv**

Glossary of Abbreviations, Acronyms and Therminology **xxxvii**

1 Introduction **1**

1.1 Nanoscale systems with biomedical applications 1
  1.1.1 Inorganic Nanostructures 2
  1.1.2 Organic Nanostructures 6
  1.1.3 Mixed Nanostructures 8
    1.1.3.1 Protein Corona 9
1.2 Elemental constitutive components. Tissue engineering 12
  1.2.1 Proteins. Properties, aggregation and interactions 12
    1.2.1.1 Protein folding 12
    1.2.1.2 Bovine Serum Albumin – Surfactants 13
    1.2.1.3 Fibrinogen – Betablockers 14
    1.2.1.4 Fibrinogen – Antibiotics 15
  1.2.2 Bioceramic materials 17
    1.2.2.1 Hydroxyapatite (HA) 17
  1.2.3 Complex implantable devices 19
    1.2.3.1 Composite membranes 20
    1.2.3.2 Hydrogels and fiber mesh scaffolds 20
    1.2.3.3 Hybrid Hydrogels 21
1.3 Computational tools and novel experimental approaches 22
  1.3.1 Computational modeling 22
    1.3.1.1 Molecular docking 22
    1.3.1.2 Computational studies of the physicochemical properties of binary systems 24
  1.3.2 Microfluidics 26
    1.3.2.1 Finite element method (FEM) 28

Bibliography **31**

2 Materials and methods 39
- 2.1 Materials . . . 40
  - 2.1.1 Inorganic reagents . . . 40
  - 2.1.2 Surfactants, buffer solutions and SBF . . . 40
  - 2.1.3 Polymers, proteins and organic compounds . . . 40
  - 2.1.4 Drugs . . . 41
  - 2.1.5 Cell culure . . . 41
- 2.2 Physicochemical characterization . . . 41
  - 2.2.1 HA nanorods . . . 41
    - 2.2.1.1 X-ray powder diffraction . . . 41
    - 2.2.1.2 Zeta-potential . . . 41
    - 2.2.1.3 Field emission scanning electron microscopy . . . 42
    - 2.2.1.4 Transmission electron microscopy . . . 42
    - 2.2.1.5 Digital images routine . . . 42
  - 2.2.2 Protein aggregation and complexation . . . 43
    - 2.2.2.1 Zeta potential . . . 43
    - 2.2.2.2 Scanning Electron Microscopy (SEM) . . . 43
    - 2.2.2.3 Isothermal Titration Calorimetry (ITC) . . . 44
    - 2.2.2.4 Differential scanning calorimetry . . . 44
    - 2.2.2.5 UV-vis absorption spectra . . . 44
    - 2.2.2.6 Fluorescence measurements . . . 45
    - 2.2.2.7 Raman spectroscopy . . . 45
    - 2.2.2.8 Synchrotron Radiation Circular Dichroism (SRCD) 45
    - 2.2.2.9 Small-angle X-ray scattering (SAXS) . . . 46
  - 2.2.3 Nanoparticle – protein interactions . . . 46
    - 2.2.3.1 Isothermal titration calorimetry . . . 46
    - 2.2.3.2 Fluorescence spectroscopy . . . 47
    - 2.2.3.3 UV-vis absorption spectra . . . 47
    - 2.2.3.4 Circular dichroism spectroscopy . . . 47
  - 2.2.4 Layer by Layer film assembly . . . 48
    - 2.2.4.1 Monitoring . . . 48
    - 2.2.4.2 Estimation of the film thickness and mass . . . 48
    - 2.2.4.3 Surface characterization of the LbL films . . . 48
    - 2.2.4.4 Mineralization studies . . . 49
  - 2.2.5 Bilayer Membranes . . . 49
    - 2.2.5.1 Fourier transform infrared spectrometry . . . 49
    - 2.2.5.2 In vitro degradation under physiological conditions 49
    - 2.2.5.3 Surface characterization . . . 50
  - 2.2.6 Biomimetic Scaffolds . . . 50

2.2.6.1 Field emission scanning electron microscopy 50
2.2.6.2 High resolution transmission electron microscopy . 50
2.2.6.3 FT-IR spectroscopy 51
2.2.6.4 Open porosity 51
2.2.6.5 Swelling kinetics and solvent absorption capacity . 51
2.2.6.6 Thermal characterization 52
2.2.6.7 In vitro hydrolytic and enzymatic degradation . . . 52
2.2.6.8 Incubation in simulated body fluid 53
2.2.7 Polymeric Hydrogels 53
2.2.7.1 FT-IR spectroscopy. 53
2.2.7.2 Raman microscopy. 53
2.2.7.3 Swelling behaviour. 54
2.3 Mechanical properties 54
2.3.1 Compressive strength 54
2.3.2 Tensile testing 55
2.3.3 Rheological characterization of the hydrogels 55
2.4 Biological studies 58
2.4.1 Ultrathin Films 58
2.4.1.1 In vitro cell culture 58
2.4.1.2 Characterization of adhered cells 58
2.4.2 Bilayer membranes 59
2.4.2.1 Osteoblasts and fibroblasts proliferation. 60
2.4.2.2 Osteoblasts differentiation. 61

Bibliography **63**

3 Protein aggregation and interactions **65**
3.1 Overview 65
3.2 Bovine Serum Albumin and surfactants 66
3.2.1 Effect of protein-surfactant interactions on the aggregation of Bovine Serum Albumin 66
3.2.2 BSA upon SDS and SPFO influence 70
3.3 Fibrinogen binding and complexation 71
3.3.1 Fibrinogen binding-interaction with betablocker agents . . . 71
3.3.2 Mechanisms of fibrinogen-BTS drug interactions 75
3.3.3 Binding mechanisms of fibrinogen-penicillin beta-lactam antibiotic drugs 81

Bibliography **87**

4 Bioceramic Precursor. Size-controllable HA synthesis 91
4.1 Overview 91
4.2 Experimental procedure 92
4.2.1 Microchip fabrication 92
4.2.1.1 Step 1: Substrate preparation 92
4.2.1.2 Step 2: Exposure 92
4.2.1.3 Step 3: Development 92
4.2.1.4 Step 4: Final assembly 92
4.2.2 Numerical solution applied to fluid flow 93
4.3 Discussion 93
4.3.1 Previously established synthesis method 93
4.3.1.1 Physical characterization 94
4.3.2 Microreactor-based synthesis method 95
4.3.2.1 Flow simulations 96
4.3.2.2 Physical characterization 97
4.3.2.3 Size control and distribution 101

Bibliography 103

5 Protein Corona on Bioceramic Nanoparticles 105
5.1 Overview 105
5.2 Experimental procedure 106
5.2.1 Preparation of BSA and HA samples 106
5.3 Discussion 106
5.3.1 Affinity, binding and thermodynamis of the interactions . . . 106
5.3.2 Kinetic properties of the adsorption 107
5.3.3 Structural and conformational changes 113

Bibliography 115

6 Bilayer composite membranes 117
6.1 Overview 117
6.2 Experimental procedure 118
6.2.1 Preparation of ALG-HA bilayer membranes 118
6.3 Discussion 118
6.3.1 Study of ALG-HA interaction 119
6.3.2 Mechanical performance under tensile strength 120
6.3.3 Degradation under in vitro physiological conditions 123
6.3.4 Surface characterization each side of the membrane 124
6.3.5 Cell culture 126

6.3.5.1 Osteoblast proliferation and differentiation on the MS of the membranes . . . 126
6.3.5.2 Fibroblast proliferation on the FS of the membranes 127

Bibliography 129

7 Ultrathin films containing HA nanoparticles 133
7.1 Overview . . . 133
7.2 Experimental procedure . . . 134
7.2.1 Layer by layer film assembly . . . 134
7.3 Discussion . . . 135
7.3.1 Layer by Layer Build-Up . . . 135
7.3.2 Mineralization . . . 136
7.3.3 Cell culture studies . . . 138

Bibliography 141

8 Biomimetic fiber mesh scaffolds 143
8.1 Overview . . . 143
8.2 Experimental procedure . . . 144
8.2.1 Preparation of nano-fibrous gelatin-HA scaffolds . . . 144
8.3 Discussion . . . 144
8.3.1 Mineralized cross-linked gelatin-HA scaffolds . . . 144
8.3.1.1 Physical characterization . . . 144
8.3.1.2 Thermal properties . . . 146
8.3.1.3 Bone-bonding potential and bio-degradability . . . 149

Bibliography 151

9 Mechanical properties of composite Hydrogels 153
9.1 Overview . . . 153
9.2 Experimental procedure . . . 154
9.2.1 Preparation of the multi-component crosslinked films . . . 154
9.3 Discussion . . . 155
9.3.1 Morphological and structural analysis . . . 155
9.3.2 Swelling and degradation behavior . . . 159
9.3.3 Viscoelastic properties . . . 160

Bibliography 167

10 Microfluidic-based synthesis of hydrogel microspheres 169
10.1 Overview 169
10.2 Experimental procedure 170
10.2.1 Monosized sodium alginate microdroplets 170
10.2.2 Ca-Alg microparticles and Chi-covered microspheres 170
10.2.3 Adsorption, kinetic and desorption. 171
10.2.3.1 Loading and release efficacy 172
10.3 Results and discussion 172
10.3.1 Flow simulations of the microdroplet generation 172
10.3.2 Formation of sodium alginate microdroplets 174
10.3.3 Gelation of Ca-Alg and Chi covered microparticles 176
10.3.4 Adsorption of Prop and Clox onto HA nanoparticles 177
10.3.5 Desorption/release profiles 178

Bibliography 181

11 Final conclusions 183

List of Figures

1.1 a) SEM image of a typical cauliflower like mineralized surface. b) Interactive tree-dimensional view of the surface. c) Different visualization with the respective surface parameters. 5
1.2 Scheme representing the protein corona formation in a ITC test. . . 10
1.3 a) Crystallographic structure of Bovine Serum Albumin protein (PDB 4F5S) and its three main domains. b) Representation of general crystallographic structure of fibrinogen protein (PDB 3GHG) 16
1.4 Representation of a human bone and its hierarchical structure at different scales. 18
1.5 a) Digital representation of a microfluidic device. b) Flux velocity simulation of a real assay. 27
1.6 a) Microfluidic device. b) Close up of the geometry and tridimensional mesh used in the microfluidics simulation. Each vertex represents a node, resulting in the discretization of the domain in finite elements. c) Bidimensional mesh. 28

2.1 a) Original image. b) Skeleton image. c) Straight-lines image. . . . 43
2.2 Burguer model comprising the Maxwell and Kelvin - Voigt models in series. 57
2.3 Scheme of the general protocol followed for cell seeding. 60

3.1 Experimental SAXS curves from BSA (1 mg/mL) 67
3.2 Variation of enthalpy as a function of surfactant:BSA molar ratio. . 70
3.3 Experimental SAXS data (open circles) from 0.5 mg/mL fibrinogen. 72
3.4 Experimental SAXS data from 0.5 mg/mL fibrinogen in the presence of acebutolol. 73
3.5 Experimental data from 0.5 mg/mL of fibrinogen in the presence of propanolol 75
3.6 a) Enthalpy as a function of molar ratio (BTS/fibrinogen). Experiments were performed by adding 1 mM BTS solutions into 0.033 mM of fibrinogen. b) Zeta potential of the complex BTS-fibrinogen as a function of drug-fibrinogen molar ratio. 76

3.7 a) Fluorescence emission spectra of Fibrinogen in the absence and presence of different concentrations of the BTS drug. b) Overlap of the normalized fluorescence spectrum of fibrinogen and the absorbance spectrum of the complex. 78
3.8 Pair distribution function calculated for the experimental SAXS curves for BTS solution in the absence of fibrinogen. 79
3.9 Experimental SAXS curves for the fibrinogen (0.5 mg/mL) in the presence of of BTS. 80
3.10 ITC profiles for the binding of cloxacillin (a) and dicloxacillin (b) to fibrinogen. 82
3.11 DSC thermograms of fibrinogen in the presence of different concentrations of cloxacillin (a) and dicloxacillin (b). 84
3.12 Raman spectra of fibrinogen in presence of different penicillin ratios, 100 and 400 for samples 1 and 2 respectively. 85

4.1 X-ray diffraction pattern of hydroxyapatite 94
4.2 a-c): SEM images of HA samples at different scales. d-e): TEM images of the same HA samples. 95
4.3 Diagram of the microfluidic system. 96
4.4 Schematic representation of the microfluidic system operation. . . . 97
4.5 Velocity countour planes for the whole device (a), first Y-junction (b) and second Y-junction (c). 98
4.6 X-ray diffraction pattern of HA nanorods obtained at different flow rates. 98
4.7 a) 3D surface plot from 1.5 flow rate sample x and y axes are in micrometers. b) Plots of the logarithm of the area of the framewoks against the logarithm of their side. 99
4.8 SEM microphotographs of samples obtained at different flow rates. . 101
4.9 Angle (a-c) and length (d-f) distributions obtained from different SEM images of the samples obtained at different flows: 3 ml/h (left), 2 ml/h (center) and 1.5 ml/h (right). 102

5.1 a) Heat of interaction for titration of HA nanoparticles into BSA solution. b) Zeta potential of HA nanoparticles as a function of BSA/HA ratio. 107
5.2 a) Fluorescence emission spectra of BSA in the absence and presence of different concentrations of HA nanoparticles: Pure BSA (i). Ratio [HA]/[BSA] = 1, 2, 4, 10, 20 (from ii to vi). b) Overlap of the fluorescence spectrum of BSA (II) and the absorbance spectrum of HA (I). Ratio [HA]/[BSA] = 1 109

5.3 a) Absorbance of BSA measured at $\lambda = 277\,\mathrm{nm}$. b) Linear pseudo-second-order kinetic curve for BSA after interaction with HA nanoparticles. 111
5.4 a) UV-visible absorption spectra of BSA in the presence of different concentrations of HA. (a–e): [BSA] = $5.00 \times 10^{-5}\,\mathrm{mol\,L^{-1}}$, [HA] = 0.00, 0.10, 0.20, 0.50, $1.00 \times 10^{-3}\,\mathrm{mol\,L^{-1}}$, and (f–g): [BSA] = 0, [HA] = 0.50, $1.00 \times 10^{-3}\,\mathrm{mol\,L^{-1}}$, some spectra are not shown to avoid confusion. b) Absorbance variation of BSA at 277 nm vs. [HA]. c) Standard Gibbs energy difference between protein folded and unfolded conformations as a function of HA concentration. d) Relationship between K_{BSA-HA} and ln [HA] at 298.15 K. 112
5.5 Circular Dichroism (CD) spectra of BSA under different molar ratios of HA:BSA as marked in the figure. 114

6.1 FTIR spectra of membranes M-0, M-0.11, M-0.55 and M-1.1, a) broad range 500-4000 $\mathrm{cm^{-1}}$, b) magnification between 1800 $\mathrm{cm^{-1}}$ and 600 $\mathrm{cm^{-1}}$ 119
6.2 Representative stress-strain curves of the membranes M-0, M-0.11, M-0.55 and M-1.1 showing the approximate location of elastic region, yield point and plastic region. 120
6.3 Tensile assay parameters of membranes M-0, M-0.11, M-0.55 and M-1.1. a) Elastic region: Young modulus and resilience. b) Yield point: yield stress and yield strain. c) Plastic region: maximum tensile strain and maximum tensile stress and, d) plasticity. 122
6.4 Degradation over time of the membranes M-0, M-0.11, M-0.55 and M-1.1 immersed in PBS at 37 °C. 123
6.5 Surface characteristics of M-1.1 membranes evaluated by SEM micrographs: a) FS surface and b) MS surface at a 200× magnification; c) FS surface showing the porosity and d) MS surface showing HA microaggregates, at a 1,000× magnification. Histograms displaying e) pore size distribution of the FS surface and f) HA microaggregates size present on the MS. 125
6.6 Roughness parameters of M-1.1 membrane for the a) MS and b) FS. R_a: arithmetic average surface roughness, R_{sk}: asymmetry coefficient, R_{ku}: kurtosis coefficient. 126
6.7 Osteoblasts cultured on the MS of the membranes M-0.11, M-0.55 and M-1.1: a) proliferation and b) differentiation. TCPS was used as control. Significant differences between HA-containing membranes and TCPS are indicated on the top of the column, while between the HA-containing membranes with brackets. Significance: * $p < 0.05$ and ** $p < 0.01$. 127

6.8 Fibroblasts proliferation on the FS of the membranes M-0.11, M-0.55 and M-1.1. TCPS was used as control. Significant differences between HA-containing membranes and TCPS are indicated on the top of the column, while between the 2 and 5 days with brackets. No differences were found between the HA-containing membranes. Significance: * $p < 0.05$ and ** $p < 0.01$. 128

7.1 Scheme representing the layer-by-layer assembly. 134
7.2 Representative normalized variations of frequency ($\Delta F_n/n$) and dissipation (ΔD_n) for the 5^{th} overtone during the assembly of $[PLL/HA]_3$ films. b) Thickness growth of the $[PLL/HA]_3$ films calculated from the Voigt-based viscoelastic model (black) and data fitting (blue) showing linear growth of the LbL construct. Three independent experiments are depicted. 135
7.3 Mineralization process. Quartz crystals were placed vertically on 15 mL Falcon tubes and put in contact with simulated body fluid. . 136
7.4 Mineralization assessment of $[PLL/HA]_3$ films. (a) QCM-D measurements of dissipation for the 5^{th} overtone. Data fitting depicts a logarithmic approximation (blue). (b) XRD spectra of the LbL constructs after 1, 4, 7 and 14 days of immersion in SBF. XRD spectra were treated to remove the strong diffraction signals produced by gold and quartz. 137
7.5 (a-g) Scanning electron microscopy of the assembled films after 0, 1, 4, 7 and 14 days in SBF. The lines in (a) and (b) are artifacts from defects on the gold surface. (f, g) High-resolution field emission scanning electron microscopy with different magnifications up to 14 days. 138
7.6 SaOs-2 osteoblast-like cells cultured on $(PLL/HA)_3$ and mineralized $(PLL/HA)_3$: (a) number of adherent cells and (b) their viability on $(PLL/HA)_3$ before and after 7 days of mineralization; (c, e) Representative fluorescence microscopy micrographs showing cytoskeletal organization of SaOs-2 cells. (d, f) SEM images of SaOs-2. 139

8.1 (a-b) Longitudinal and (c-d) transversal FE-SEM microphotographs of lyophilized GE-HA sample, 0.80 g/mL GE and 0.85 mg/mL HA. . 145
8.2 (a,b) Pore wall morphology of lyophilized GE-HA sample, 0.80 g/mL GE and 0.85 mg/mL HA. (c,d) 3D surface profiles of GE-HA scaffolds pore's walls. 146

8.3 FE-SEM microphotographs of GE-HA-TA cross-linked scaffolds. (a-d) 12.4 mg TA/g GE sample: (a) transversal and (b-d) longitudinal views. (e-h) 33.3 mg TA/g GE sample: (e) transversal and (f- h) longitudinal views. 147
8.4 DSC thermograms of GE-TA and GE-HA-TA scaffolds. 148
8.5 Biomimetic growth of HA crystals after (a-b) 7 days; (c-d) 14 days and (e-f) 21 days of immersion in SBF. (g) FT-IR of GE-HA-TA scaffold after immersion in SBF. (h) GE-HA-TA scaffold kinetic degradation process. 150

9.1 a) FTIR spectra of the different samples. b) FTIR of each of the elemental compounds. c) Close-up. 156
9.2 Optical images of the compound distributions using the integrates intensity of the Raman bands. 157
9.3 a) Degradation over time of the hydrogels. b) Close-up of the first 10 hours of degradation. a) Swelling behavior over time. b) Close-up of the first 10 hours of swelling. 159
9.4 Fitting results. a) Experimental and obtained data for the 5 studied samples. b) Close up. 161
9.5 a) Linear viscoelastic range. b) Oscillatory frequency sweep. c) Scheme representing the alignment of HA within the hydrogel along the streamline when shear rate increases. The ALG-Ca^{2+} and ALG-HA interactions are also represented. 163
9.6 a) Three interval thixotropy (3-ITT) test. b) Creep-recovery curves of the four studied samples. 163
9.7 a) Fitted curves for the creep phase. b) Fitted curves for the recovery phase. 165

10.1 a) Tridimensional representation of the microfluidic device. b) Schematic representation. Geometry, inlets, outlets and significant points. c) Computational simulations results. d) Optical images. The continuous formation of the droplets as well as the nanoparticle flow can be tracked in this point. 171
10.2 Droplet generation inside the microchannels depending on the Oil/Water phase flow rate. Optical images of the experimental assays from a) to d), and their respective counterparts using COMSOL Multiphysics simulation software from e) to h). 173
10.3 Scheme illustrating the dependence between the water-oil flow ratio and the droplet size and distribution. 175
10.4 Droplet size distribution at different Oil/Water ratios. 175

10.5 Schematic representation of the microfluidic system used in the obtention of the hydrogel microparticles. 177
10.6 a-b) Optical images of the crosslinked Ca-ALG microparticles. c-d) Chitosan-covered microparticles. 177
10.7 Kinetic adsorption studies for a) Prop and b) Clox. Avrami's model at 37 °C. 178
10.8 Desorption studies a) Propranolol and b) Cloaxacillin. All data fit to Korsmeyer-Peppas model. 179

List of Tables

3.1 Molecular Mass (MM) and radius of gyration (Rg) of native BSA state at pH 6.5 (PDB 4F5S). 68
3.2 Percentage of each crystal structure in solution obtained from the best fit to the experimental SAXS data from fibrinogen dispersed in buffer solutions containing different concentrations of acebutolol . . 74
3.3 Thermodynamic parameters: binding constant (k), enthalpy (ΔH), entropy ($T\Delta S$) and free energy (ΔG) of binding of cloxacillin and dicloxacillin with fibrinogen according to a single binding site. . . . 82
3.4 Thermodynamic parameters obtained from DSC thermograms in the presence of cloxacillin and dicloxacillin 85

4.1 Values of roughness, skewness and kurtosis of the differente surfaces obtianen from SEM images. 100
4.2 Mean values and standard deviation of lengths of HA nanoparticles obtained at different flows. 101

5.1 Percentage of the secondary structure of BSA at their interaction with different molar ratios of HA:BSA. 114

9.1 Flow Curve modeling 162
9.2 Values of the Burger model parameters. Results from the fits by Eq. (2.20) 164
9.3 Compliance of the Maxwell dashpot, Kevin-Voigt element and parameters obtained from the fitting by Eq. (2.21) 165
9.4 Maximum compliance and compliance of the Maxwell spring. 166
9.5 Percentage contribution of the Burger elements to the total recovery of the systems. 166

10.1 Size distribution. Mean and standard deviation. A minimum amount of 40 droplets were measured for each condition. 175
10.2 Kinetic adsorption parameters of Prop and Clox onto HA, obtained using Avrami equation at 37 °C 178
10.3 Desorption studies for Prop. Parameters of Korsmeyer – Peppas model for the three different samples. 179

10.4 Desorption studies for Clox. Parameters of Korsmeyer – Peppas model for the three different samples. 179
10.5 Cumulative in vitro release of Propranolol and Cloxacillin from HA nanoparticles, ALG micropartiles and CHI-ALG microspheres. . . . 180

Glossary of Abbreviations, Acronyms and Therminology

2-D, 3-D	Two- or three-dimensional, referring to spatial dimensions in an image.
3-IIT	Three interval thixotropy test.
Aceb	Acebutolol hydrochloride.
AcOH	Acetic acid.
ALG	Alginate.
ALP	Alkaline phosphatase activity.
ANM	Anisotropic network model.
BSA	Bovine serum albumin.
CD	Circular dichroism spectroscopy.
CFD	Computational fluid dynamics.
Chi	Chitosan.
Clo	Sodium cloxacillin.
cmc	Critical micelle concentration.
COC	Cyclic olefin copolymer.
CTAB	Hexadecyltrimethylammonium bromide.
Diclo	Sodium dicloxacillin.
DMEM	Dulbecco's Modified Eagle's medium.
DR	Degradation ratio.
DSC	Differential scanning calorimetry.
ECM	Extracellular matrix.
ED	Electron diffraction.
Fb, Fib	Fibrinogen.
FE-SEM	Field emission scanning electron microscopy.

FEM	Finite element method.
FRET	Förster resonance energy transfer.
FS	Fibrous side.
FT-IR	Fourier transform infrared spectrometry.
GBR	Guided bone regeneration.
Gel	Gelatin from bovine skin.
HA, HAn	Hydroxyapatite, Hydroxiapatite nanoparciles.
H-TEM	High resolution transmission electron microscopy.
ITC	Isothermal titration calorimetry.
LbL, L-b-L	Layer by layer.
LDH	Lactate dehydrogenase.
LFER	Linear free energy relationships.
LPRS	Local perturbation response scanning.
LSZ	Lysozyme.
LVR	Linear viscoelastic region.
MD	Molecular dynamics.
MM, MW	Molecular mass, molecular weight.
MS	Mineral side.
NPs	Nanoparticles.
NPT	Isothermal–isobaric ensemble. Substance (N), pressure (P) and temperature (T).
NVT	Canonical ensemble. Substance (N), volume (V) and temperature (T).
OFS	Oscillatory frequency sweep.
PBS	Phosphate buffer saline.
PDB	Protein data bank.
PDMS	Polydimethylsiloxane.
PGMEA	Propylene glycol monomethyl etheracetate.
PLL	Poly-L-lysine hydrobromide.
PPG	Polypropylene glycol.
Prop	Propranolol hydrochloride.

QCM	Quartz crystal microbalance.
R_a	Arithmetical average deviation.
Rg	Radius of gyration.
R_{ku}	Kurtosis.
RMSD	Root-mean-square deviation.
rpm	Revolutions per minute.
R_{sk}	Skewness.
RT	Room temperature.
SASA	Solvent accessible surface.
SAXS	Small-angle X-ray scattering.
SBF	Simulated body fluid.
SDS	Sodium dodecyl sulfate.
SEM	Scanning electron microscopy.
SPFO	Sodium perfluorooctanoate.
SR	Swelling ratio.
SRCD	Synchrotron radiation circular dichroism.
TA	Tannic acid.
TCPS	Tissue culture treated polystyrene.
TEM	Transmission electron microscopy.
TRP	Tryptophan.
UV	Ultraviolet.
XRD	X-ray powder diffraction patterns.

1

Introduction

Contents

1.1 Nanoscale systems with biomedical applications 1
  1.1.1 Inorganic Nanostructures 2
  1.1.2 Organic Nanostructures 6
  1.1.3 Mixed Nanostructures 8
1.2 Elemental constitutive components. Tissue engineering 12
  1.2.1 Proteins. Properties, aggregation and interactions . . . 12
  1.2.2 Bioceramic materials 17
  1.2.3 Complex implantable devices 19
1.3 Computational tools and novel experimental approaches 22
  1.3.1 Computational modeling 22
  1.3.2 Microfluidics 26

1.1 Nanoscale systems with biomedical applications

Nanoscale systems play an important role in different areas such as technology, energy, pharmacy, chemistry, food industries and biomedical circles as well. Researchers from all around the world are focusing their works on understanding and trying to control matter at the nanoscale, as it is widely believed it will lead to a scientific revolution which will profoundly benefit society [1]. For its part, nanomedicine, defined as the use of nanotechnologies in medicine, also underpins a strong research and emerging industrial healthcare sector.

Probably, there are different reasons to this new global revolution. One of them could be that it is a multidisciplinary area which requires knowledge from different fields such as physics, chemistry, biology, engineering and medicine. Another possible justification is the fast development of characterization techniques during the past years. New electronic microscopes, more precise, with better resolution, and easier to manipulate, have been developed to improve and simplify the characterization of novel nanoparticles. These nanomaterials are in the same size range scale as biomolecules, which facilitates their interaction, and consequently, allows to control and intervene in biological processes. The high specific surface that these nanoparticles have is another very important property, as it enables and tolerates the accommodation of a high concentration of drugs or required molecules [2].

In this line, nanostructures created by self-assembly are attracting a large interest, as they are the main route in bottom up strategies. They can be divided into three different categories: inorganic, organic and mixed nanostructures. To further understand them, it is essential to provide a comprehensive overview of the most important models for the synthesis, characterization and application of nanoscale systems. The emphasis should be put on covering a wide spectra of nanostructures, not only nanoparticles, and exploring their key physical properties.

1.1.1 Inorganic Nanostructures

The properties and characteristics of inorganic nanoparticles arise, basically, from their electromagnetic features, this is, the novel phenomena which appear when particles are reduced to the nanoscale. These phenomena appears because magnetic processes are characterized by specific length scales. When the physical size of a magnetic system is reduced to dimensions comparable (or smaller) than these characteristic lengths, novel behavior is observed: giant magnetoresistance, Coulomb blockade, perpendicular anisotropy, superparamagnetism and current induced switching. These mesoscopic characteristic length scales have various origins: domain size, domain wall width, exchange length, thin film perpendicular anisotropy threshold, spin diffusion length and spin precession length [3]. Although most properties of nanoparticles seem to be new, they can be explained by classical electrodynamics. Indeed, the scattering of electromagnetic waves by systems whose individual dimensions are small compared to a wavelength is a common and important occurrence. In such interactions it is convenient to think of the incident (radiation) fields as inducing electric and magnetic multipoles that oscillate in definite phase relationship with the incident wave and radiate energy in directions other than the direction of incidence. The exact form of the angular distribution of radiated energy is governed by the coherent superposition of multipoles induced by the incident fields and, in general, it depends on the state of polarization of the incident wave. If the wavelength of the radiation is long enough compared to the size of the scatterer, only the lowest multipoles, usually electric and magnetic dipoles, are relevant [4].

The basic situation is a plane monochromatic wave impacting on a scatterer. For simplicity, the surrounding medium is taken to have $\mu = \epsilon = 1$. If the incident direction is defined by the unit vector $\overrightarrow{n_0}$, and the incident polarization vector is $\overrightarrow{\epsilon_0}$, the incident fields are

$$\overrightarrow{E}_{inc} = \overrightarrow{\epsilon}_0 E_0 exp\{ik\overrightarrow{n}_0 x\} \tag{1.1}$$

$$\overrightarrow{H}_{inc} = \overrightarrow{n}_0 \times \overrightarrow{E}_{inc}/Z_0 \tag{1.2}$$

Where $k = \omega/c$ and Z_0 is the impedance of free space ($Z_0 = \sqrt{\mu_0/\varepsilon_0}$). These fields induce dipole moments $\overrightarrow{p}$ and $\overrightarrow{m}$ in the small scatterer and these dipoles radiate energy in all directions. Far away from the scatterer, the scattered (radiated) fields are found to be:

$$\overrightarrow{E}_{sc} = \frac{1}{4\pi\varepsilon_0} k^2 \frac{\exp\{ikr\}}{r} \left\{ (\overrightarrow{n} \times \overrightarrow{p}) \times \overrightarrow{n} - \overrightarrow{n} \times \frac{\overrightarrow{m}}{c} \right\} \tag{1.3}$$

$$\overrightarrow{H}_{sc} = \overrightarrow{n} \times \overrightarrow{E}_{sc}/Z_0 \tag{1.4}$$

where $\overrightarrow{n}$ is a unit vector in the direction of observation and r is the distance away from scatterer. The power radiated in the direction $\overrightarrow{n}$ with polarization $\overrightarrow{\epsilon}$ is a quantity with dimensions of area per unit solid angle. It is called the differential scattering cross section:

$$\frac{d\sigma}{d\Omega}(\overrightarrow{n}, \overrightarrow{\epsilon}; \overrightarrow{n}_0, \overrightarrow{\epsilon}_0) = \frac{k^4}{(4\pi\varepsilon_0 E_0)^2} \left| \overrightarrow{\epsilon}^* \cdot \overrightarrow{p} + \left(\overrightarrow{n} \times \overrightarrow{\epsilon}^*\right) \cdot \frac{\overrightarrow{m}}{c} \right|^2 \tag{1.5}$$

The dependence of the cross section on $\overrightarrow{n}_0$ and $\overrightarrow{\epsilon}_0$ is implicitly contained in the dipole moments $\overrightarrow{p}$ and $\overrightarrow{m}$. The variation of the differential (and total) scattering cross section with wave number as k^4 (or in wavelength as λ^{-4}) is an almost universal characteristic of the scattering of long-wavelength radiation by any finite system. This dependence on frequency is known as Rayleigh's law. Only if both static dipole moments vanish does the scattering fail to obey Rayleigh's law; the scattering is then via quadrupole or higher multipoles (or frequency-dependent dipole moments) and varies as ω^6 or higher.

In the case of the scattering by a small dielectric sphere of radius a with $\mu_r = 1$ and a uniform isotropic dielectric constant $\varepsilon_r(\omega)$. The electric dipole moment will be:

$$\overrightarrow{p} = 4\pi\varepsilon_0 \left(\frac{\varepsilon_r - 1}{\varepsilon_r + 2}\right) a^3 \overrightarrow{E}_{inc} \tag{1.6}$$

There is no magnetic dipole moment. The differential cross section will be:

$$\frac{\mathrm{d}\sigma}{\mathrm{d}\Omega} = k^4 a^6 \left|\frac{\varepsilon_r - 1}{\varepsilon_r + 2}\right|^2 \frac{1}{2}\left(1 + \cos^2\theta\right) \tag{1.7}$$

The polarization dependence is typical of purely electric dipole scattering. The scattered radiation is linearly polarized in the plane defined by the dipole moment direction, $\overrightarrow{\epsilon}_0$ and the unit vector $\overrightarrow{n}$.

Considering a conducting sphere of radius a; in a uniform electric field $\overrightarrow{E}_{inc}$, the induced surface-charge density will be:

$$\sigma = 3\varepsilon_0 E_0 \cos\theta \tag{1.8}$$

And the electric dipole moment:

$$\overrightarrow{p} = 4\pi\varepsilon_0 a^3 \overrightarrow{E}_{inc} \tag{1.9}$$

The sphere also possesses a magnetic dipole moment. For a perfectly conducting sphere the boundary condition on the magnetic field is that the normal component of $\overrightarrow{B}$ vanishes at $r = a$. Either by analogy with the dielectric sphere in a uniform electric field with $\epsilon = 0$, or by a simple direct calculation, it is found that the magnetic moment of the small sphere is:

$$\overrightarrow{m} = -2\pi a^3 \overrightarrow{H}_{inc} \tag{1.10}$$

For a linearly polarized incident wave the two dipoles are at right angles to each other and to the incident direction. The differential cross section is:

$$\frac{\mathrm{d}\sigma}{\mathrm{d}\Omega} = k^4 a^6 \left[\frac{5}{8}\left(1 - \cos^2\theta\right) - \cos\theta\right] \tag{1.11}$$

Dipole scattering with its ω^4 dependence on frequency can be viewed as the lowest order approximation in an expansion in k_d, where d is a length typical of the dimensions of the scatterer. In the domain $k_d \sim 1$, more than the lowest order multipoles must be considered. Then the discussion is best accomplished by use of a systematic expansion in spherical multipole fields. Resolving the equations with the appropriate frontier conditions solutions for specific system can be found. There are good reviews in the literature with interesting examples [5].

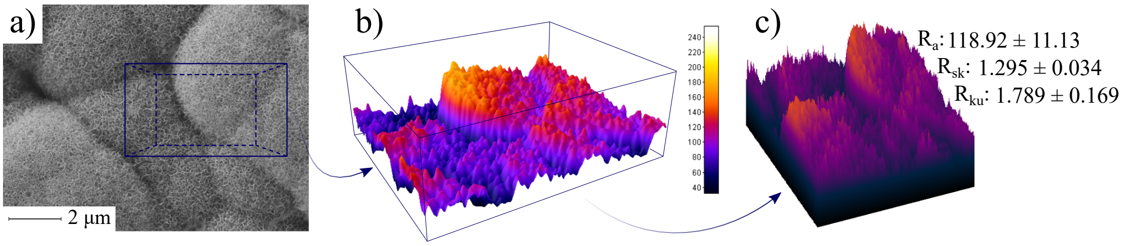

Figure 1.1: a) SEM image of a typical cauliflower like mineralized surface. b) Interactive tree-dimensional view of the surface. c) Different visualization with the respective surface parameters.

For its part, mesoporous materials are 3D-nanostructures with well-defined mesoscale (2–50 nm diameters) pores. They are of scientific and technological interest because of their ability to interact with atoms, ions and molecules, not only at their surfaces, but also throughout the bulk material. First, mesoporous materials were developed by researchers at Mobil Oil Corporation to be utilized as catalysis. After that, their use spread over different areas such as drug delivery, biosensor, pollutant removing, energy storage or medical imaging [6]. Self-assembled molecular aggregates or supramolecular assemblies employed as the structure–directing agents are one of the most used route in mesoporous synthesis. This idea was the trigger for a large number of studies where, both the composition of the template and the external factors, were combined to achieve optimal and economically efficient architectures [7].

Focussing on the biomedical perspective, it is essential to remember that the trabecular bone exhibits sponge like bicontinuity at the millimeter scale. Consequently, there is a growing and more than understandable interest in the synthesis of spongy-like sieves for the constructions of bio-active implantable materials. Different approaches have been proposed for this purpose. The synthesis of bicontinuous pore silica materials using different bile salts aqueous mixtures as templates is a good example. Depending on the type and amount of bile salts in the template mixture, the film can curve toward the a-polar or toward the polar side, leading to different final morphologies. Their structural properties are interrelated with their ability to induce a bone-like apatite layer in contact with simulated body fluid (SBF). As mentioned, the bioactive behavior is a function of the fraction of bile salts in the sample and although the thickness of the apatite-like coating reaches a saturated point after 10 days of soaking, the definite crystalline structure is achieved after soaking for 20 days in SBF [8].

Controlling the surface microrough properties is an efficient platform to manipulate the material bioactivity [9]. The topography of each material surface is characterized typically by a succession of peaks and valleys, which can be quantified using either 2D profiles or 3D roughness parameters: arithmetical average deviation (R_a); the root mean square roughness (R_q), maximum height of peaks (R_p), maximum deep of valleys, maximum height of the profile (R_t), Kurtosis (R_{ku}) and Skewness (R_{sk}):

$$R_a = \frac{1}{l}\int_0^l |y(x)|\,\mathrm{d}x \qquad\qquad R_q = \sqrt{\frac{1}{l}\int_0^l \{y(x)\}^2 \mathrm{d}x} \tag{1.12}$$

$$R_p = \max_i y_i \qquad\qquad R_v = \min_i y_i \qquad\qquad R_t = R_p - R_v \tag{1.13}$$

$$R_{sk} = \frac{1}{R_q^3}\int_{-\infty}^{\infty} y^3 p(y)\,\mathrm{d}y \qquad\qquad R_{ku} = \frac{1}{R_q^4}\int_{-\infty}^{\infty} y^4 p(y)\,\mathrm{d}y \tag{1.14}$$

where y_i is the height of the profile at point number i. Materials with $R_{sk} > 2.62$ favoured the formation on their surfaces of net-like phase with a high growth kinetic constant; while materials with $R_{sk} \leq 2.62$ induced the appearance of spherulitic-like structures and a growth rate 1.75 times inferior. The biocompatibility of the materials, confirmed by osteoblast viability and cellular adhesion tests, is a significant indicator of their potential abilities to induce the desired cellular response, favoring integration into the host tissue and stimulating self-healing processes.

1.1.2 Organic Nanostructures

As exposed above, and based on the enormous amount of publications, projects, patents and companies, it is quite obvious that nanotechnology has become a prevalent line of study in the research and academic fields. However, many scientists had been working on nano dimensions before the phenomenon would make so popular. More specifically, people involved in colloid science and molecular self-assembly. In this sense, surfactants, micelles, vesicles, proteins, copolymers or nucleic acids and all their possible combinations have been one of the most important foundations upon which nanotechnology was settled; and their impact, far from being diluted, increases exponentially, due to the development of the aforementioned bottom up strategies and biotechnology.

Self-assembly is a thermodynamic process in which single molecules spontaneously associate under defined conditions into supramolecular structures. This process depends on several physicochemical factors such as concentration, temperature, pH, ionic strength... The concentration above which aggregates form is usually known as critical micellar concentration (cmc). This phenomenon is the result of a complex balance among a diversity of forces, mainly the hydrophobic attraction and the electrostatic repulsion. The thermodynamic parameters of micellization can be determined directly, using the calorimetric technique, or indirectly, using the Van't Hoff method from critical micelle concentration, applying the mass action or pseudophase separation models.

A large number of drug molecules are amphiphilic and self-associate in aqueous environments to form aggregates [10, 11]. Usually, the pharmacological effects of amphiphilic drugs tend to appear at concentrations well below the cmc; however, it may occur that the accumulation of drug molecules in certain sites of the body cause localized high concentration, resulting in aggregation and consequent changes in biological activity due to decreased transport rates or decreased ability to pass through biological barriers. On the other hand, previous reports revealed that nanoparticles with different sizes and structures would bind to different tissues and organs [12]. Their thermal and mechanical stabilities are interesting issues that should be considered to increase their blood circulation time, thus contributing to reduce side effects. Molecular architecture is a key factor in the design of self-assembling systems for nanoparticle preparation. Structural information of the aggregates, like the packing parameter, directly related to the amphiphilic molecule structure and with its hydrophilic/hydrophobic balance, as well as thermodynamic properties as a function of temperature and of the concentration of the molecule itself or of any cosolute, represent the keystone of the proper analysis that should be done on new molecules with biomedical applications.

A new strategy involving self-assembled structures (spherical or worm-like micelles, vesicles or liquid crystals) has been recently defined. The resulting materials, known as "self-assembled drugs". They are formed uniquely by drugs that, combined, assemble in their structures. In these formations, all the individual compounds should display a therapeutic effect by themselves and the resulting self-assembled structure should display the role of support or vector at the same time. As it has been pointed out, many drugs exhibit amphiphilic properties, thus they can be combined with hydrotropic drugs to form different kind of self-assembled structures. The purpose of this idea is to prolong the release rate of the drug with the aim of increasing the bioavailability of the drug compound. The self-assembled drugs display advantages over the current methodologies based in the combination of drugs and vectors.

1.1.3 Mixed Nanostructures

The combinations of organic and inorganic matter at the nanoscopic scale in pursuit of creating a novel value-added entity are kwnon as mixed nanostructures (or hybrid nanostructures) [13]. In very general terms, the organic component typically has structural functions and may tune the mechanical features and processability of the final materials, whereas the inorganic component can introduce specific functionalities and/or reinforce the mechanical and thermal properties of the polymer. The final properties of the mixed nanostructures are very often not a simple addition of the properties of the independent component, but a unique result from synergetic effects [14]. The diversity of these mixed nanostructures is wide; organic entities comprise proteins, peptides, nuclei acids, lipids, fatty acid, etc., meanwhile inorganic ones include metallic composites, metal oxides, metallic salts, electric conductors, semiconductors, dielectrics or quantum dots. In the simplest format, the organic material overlies an inorganic core, or vice versa. In more complex formats, a huge diversity of structures can be formed, such as multilayers, porous or hollow metallic structures containing entrapped biomolecules, organic microparticles covering inorganic structures, small metallic nanoparticles attached along larger biomolecules...

One of the essential requirements when using this kind of materials as implants, is to try to understand the response of the body. For this purpose, it is insightful to first study the proteins interaction with solid surfaces. The creation of a proper implantable material requires a fundamental knowledge of the bio-response mechanism from the body and its ultimate effects at the interface of the material surface.

Consequently, the interaction of Si nanofibers with the third most abundant protein plasma in blood (Fibrinogen, Fb) was evaluated in a way to check the material hemocompatibility; thinking to the future use of such nano-fibers in three-dimensional scaffolds for the construction of implantable artificial devices [15]. By the exhaustive analysis of fibrinogen adsorption process under dynamic and static conditions it can be constructed a clear picture of how Si-nanofiber surface features critically influenced the amount, structure and distribution of the protein molecules attached to the material surface. The Fb adsorption process on the Si-nanofibers is complex and occurs in a stepwise fashion with an initial rapid adsorption controlled exclusively by diffusion mechanisms.

Due to the fibrinogen adsorption, the original SiO_2 fibrillar structure was wrecked. In some cases new fibrillar structures of higher dimensions ($d \approx 1\,\mu m$) were observed, and in others a bicontinuous structures appeared. Clearly, fibrinogen acts as an agglutinative of the Si nanofibrils. The interfacial ordering of protein residues seems to be the hallmark of a weak and labile electrostatic attraction between the substrate and the adsorbed macromolecule. Fibrinogen adsorption on 2D solid surfaces occurs basically in two different orientations: “side-on” (laying on the surface) and “end-on” (standing on the surface) [16]. The stochastic adsorption of the protein molecule leads to the formation of the two different structures: side-end adsorption favors both lateral and equilateral interactions generating large fibers and bicontinuous structures respectively, whereas the side-on adsorption promotes only equilateral interaction and therefore bicontinous structures.

Another example of application of these systems could be mimicking biological processes. Toward this goal, a protein-directed approach was proposed to template silica into 3D architectures through a hydrogel matrix formed from physically cross-linked fibrinogen. The hydrogel matrix has tunable physicochemical properties based on the thermal unfolding of the main domains of the protein. The network structures of the gels that are obtained are quite similar but differ in mean pore size and rheological properties.

The template assembly of silica nanostructures has been also checked with other hydrogels made up with different proteins (ovalbumin) and conditions (protenin concentration, pH and so on). The final silica architectures exhibit some common features with the hydrogel template: hierarchical roughness and high porosity. The fractal dimension of the silica structures followed the same pattern that the templates, when the concentration is increased the fractal dimension increases. Consequently, the bioscaffolding method helps the bottom-up assembly of silica precursors in nanostructures with defined three dimensional dimensions and provides a versatile route for the design of new architectures under green conditions [17].

1.1.3.1 Protein Corona

It should be not be overlooked the fact that the biological effect of the nanoparticles depends on their ability to reach the target organs or cells inside the body. Achieving these goals involves routes of administration such as intravenous, where the nanoparticles interact with blood components, namely plasma proteins, thus determining their hemocompatibility. Hence, the evaluation of hemocompatibility requires several approaches, including, in particular, the study of these interactions. One of the concepts that best characterizes and defines these types of relationships is the “protein corona”, that is, the protein layer absorbed on the nanoparticle. The importance of this fact is so huge that it has acquired its own identity and has become a key term in bionanotechnology. The adsorption is governed by protein–nanoparticle binding affinities as well as protein–protein interactions. Proteins that

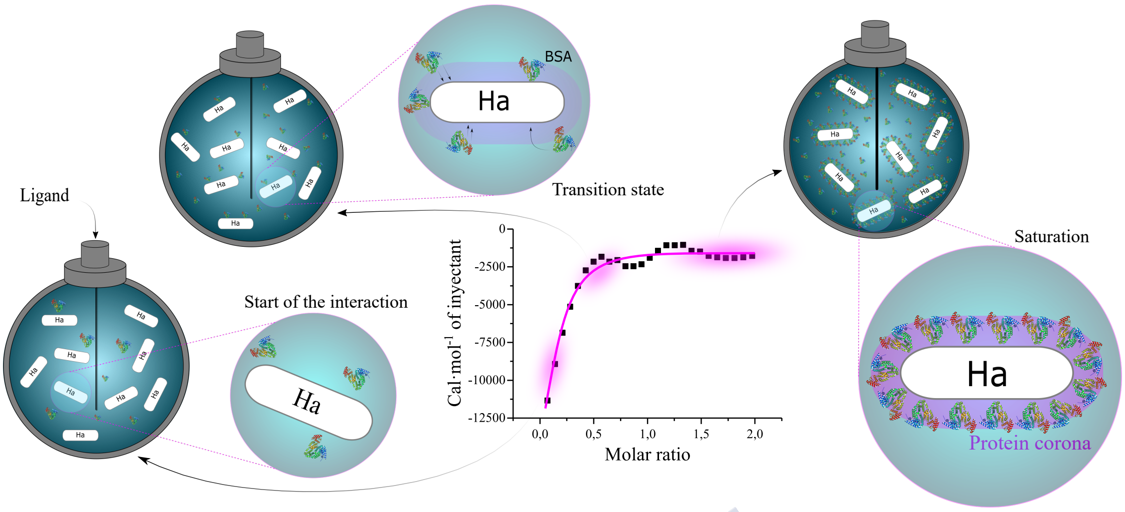

Figure 1.2: Scheme representing the protein corona formation in a ITC test.

adsorb with high affinity form what is known as the hard corona, consisting of tightly bound moleculess that do not readily desorb, and proteins that adsorb with low affinity form the soft corona, consisting of loosely bound ones [18].

The initial soft corona can be observed on short time scales that will subsequently evolve into a hard corona over higher periods of time [19]. However, the organization and composition of the protein corona depends on both the intrinsic properties of the nanoparticle and the proteins (size, charge, shape) as well as various extrinsic factors (time, concentration, velocity) [20]. The effect of nanoparticle size is a key factor, especially when nanoparticles are smaller than most proteins, with a consequent lack of information of their biological repercussions. It was recently demonstrated that the thickness and density of this protein coating depended strongly on particle size [21]. Variations of ionic strength or pH can alter nanoparticle collision rates, leading to modifications in their stability and promoting dissolution and changing the molecular-scale interaction with cells [22]. The effect of the surface charge has also been evaluated. It has been found that the adsorption of human serum albumin is independent of the sign of surface charge. In addition, both the adsorption model (slightly anti-cooperative) and the number of adsorbed protein molecules are similar for both positively and negatively charged nanoparticles [23]. The role of temperature on the formation of the corona has been approached much less frequently, despite its enormous relevance. Mahmoudi et al. [24] demonstrated that it is determinant in the degree of coverage and in the composition of the corona, magnifying its influence in the range of physiological temperatures. Computational approaches have also contributed to characterize the protein corona. Specifically, they have postulated that the surface adsorption energy is the primary driving force when nanoparticles are introduced into biological systems.

From the point of view of the proteins' spatial location, functional motifs and binding sites, among others, determine the adsorption process: stochastic, reversible, irreversible [25]. However, the nanoparticles can modify the function and tertiary structure of proteins, even through soft interactions, in a size dependent manner.Finally, it is clear that the combination of both entities offers many opportunities: BSA corona contribute to reduce the acute toxicity of gold nanorods by suppressing potentially destructive effects on the cell membrane [26]; functionalization of nanoparticles surfaces can modify steric hindrance, resulting in a significant inhibition of protein adsorption and less recognition by macrophages [27]...

Casals et al, studied the formation of the protein corona after exposure of gold nanoparticles (NPs), with sizes ranging from 4 to 40 nm, to cell culture media containing 10 % of fetal bovine serum. The results suggested that many proteins form transient complexes with gold nanoparticles with different sizes and surface states, and the outcome is determined by competitive binding toward the resulting protein corona, which constitutes a major element of the biological identity of the NP. In all cases, except for the small 4 nm NPs where the amino acid sequence could not be associated with any known protein, the corona was albumin rich, indicating that the biocompatibility of the material is improved when the surface favors albumin adsorption [28].

The subtle nature and delicate equilibrium of the protein corona have been demonstrate in other studies where, even though many of the major highly abundant proteins in the corona are independent of size and surface charge, a whole range of proteins form part of the corona. The nature of the proteins in the corona is determined by the local chemical property of the nanomaterial. However, even for a fixed material type, the size of the particles, and its surface modification are able to entirely change the nature of the biologically active proteins [29].

While protein corona onto metallic nanoparticles has been deeply studied, the formation onto nanobioceramics is still largely unexplored. Only a few papers have systematically focused on this topic [30, 31]. This fact draws much attention, especially considering that synthesis of nanobioceramics are cheaper than the metallic ones and without the use of harsh, toxic chemicals used in the latter.

1.2 Elemental constitutive components. Tissue engineering

1.2.1 Proteins. Properties, aggregation and interactions

In the last decade, a significant amount of different proteins have been applied to several nanotechnology applications as biomimetic materials, tissue engineering, printing of proteins, drug delivery, bioelectronics and nanoparticle patterning. As exposed, the understanding of molecular recognition in protein-protein and protein–ligand complexes is crucial to better comprehend the associated biological function and of practical importance in the discovery of new drugs, biosensors and biomaterials.

1.2.1.1 Protein folding

The energy landscape theory of protein folding provides a general framework on the many facets of a complex problem. Such theory proposes that in the early stages the energy funnel guides the polypeptide chain through many different sequences of traps toward the low-energy folded structure [32]. In fact, there is not a preferable pathway but a multiplicity of protein folding routes in a search for a specific structure where the key functional groups are brought into a close proximity. Once they are close enough, different interactions may occur, such as electrostatic, Hydrogen bonds, disulphide bonds, salt bridges and hydrophobic interactions, which will confer functional biological properties to the protein. Although each different unfolding route can have its own application and advantage in material processing and basic sciences, it is not surprising that the failure of proteins to fold correctly, or to remain correctly folded, is the origin of a wide variety of pathological conditions [33]. In addition, the ability to generate different protein patterns offers countless possibilities in biosensor technology, tissue engineering, or fundamental studies of cell biology [34].

Despite the huge diversity of protein misfolding, it is increasingly evident that there are some common features underlying the physicochemical and biochemical origins of various disorders. In fact, it was postulated that the ability to form amyloid fibrils is a generic property of proteins if appropriate conditions for unfolding can be found; although the conditions are protein-dependent, the generic ability is not [35]. The consensus is that fully or partially unfolded proteins are generally more susceptible to self-associate than their native states [36]. Fibrils can be associated with several degenerative diseases like Alzheimer, Parkinson, Huntington, bovine spongiform encephalopathy, dementia with Lewy bodies or spinocerebellar ataxia among others [37]. On the other hand, some fibrils also appear to be not harmful or even play a role in beneficial functions such as the formation of bacterial biofilm. This allows microbial organisms to adhere to cell surfaces, which facilitates host interactions [38].

Nowadays, the nucleated growth mechanism of fibril formation has received wide acceptance [39]: an initial lag time, where small metastable protein clusters of different shapes (spherical, beads, annular) are formed, followed by a rapid exponential growth where the clusters evolve to fibrils [40]. The full elucidation of this process requires the comprehension of the thermodynamics and kinetics of all the steps, especially those related to the small clusters formation, because it is believed that they could be the primary toxic agents involved in neurodegenerative disorders [40].

In spite of the fact that fibrillation is the focus of huge amount of research, a general rule has not yet been established which hinders protein aggregation. One of the plausible alternatives could be the use of small molecules or ligands which can inhibit the formation of fibrils [41]. In this sense, there are some examples in the literature referring to surfactants as fibril inhibitors [41] or fibril promoters [42]. It is well known that surfactants can interact with proteins via specific binding sites or cooperative processes. Hence, a good steric fit and a high degree of complementarity between the hydrophobic and polar parts of the surfactant and the macromolecule is ssential for high binding affinity [43].

1.2.1.2 Bovine Serum Albumin – Surfactants

Bovine Serum Albumin (BSA) is a water soluble model protein with a wide range of physiological functions [44]. It is composed by 585 amino acids residues generally grouped in three homologous domains (I, II and III, Figure 1.3a) resulting in a molecular mass around 66.4 kDa [45]. This protein is relatively stable due to 17 disulfide bridges and the isoelectric point is reported around pH 5.4 [46]. By lowering the pH below its isoelectric point, BSA partially expands up to pH 2.7 where it reaches its fully expanded conformation [44]. Despite its stability at pH 7.0, the thermal effect over 60 °C on BSA promoted the formation of protein aggregates observed by dynamic light scattering concomitantly with changes in its secondary structure from α-helix to β-sheet assigned by Th T and FTIR fluorescence in an elapsed time ranging from minutes to hours [47]. The BSA aggregates were also observed in the micrometric scale through electron microscopy measurements and X-ray diffraction analysis indicating a coexistence between amyloid-like fibers and amorphous aggregates [47]. BSA's aggregation can be modulated by the buffer pH, such that it happens faster at pH 3.0 than at pH 7, 9 or 10.5 for the BSA concentration ∼ 6 mg/ml (100 µM) at 65 °C [48]. These results suggest that the aggregation process increases in the low acid range because the protein is denatured [48]. The effect of the pH on the aggregation of BSA was also reported by studying the interaction of the anionic surfactant sodium dodecyl sulfate (SDS) with the protein at 25 °C [49]. At the molar ratio of 100:1 (SDS:BSA) and pH 3.65, the surfactant promoted the formation of large aggregates.

It must be remarked, however, that SDS does not promote aggregation of BSA at pH 5.65 (near the isoelectric point) and pH 7.65 (negative net charge of the protein) [49]. Such finding is in very good agreement with previous small angle X-ray scattering (SAXS) results that evidenced no BSA aggregation at pH 5.4 induced by SDS (10:1 up to 500:1 SDS:BSA molar ratio), but the formation of an unfolded BSA-surfactant complex towards a pearl-necklace model.

1.2.1.3 Fibrinogen – Betablockers

As explained above, proteins have to perform their functions in biological systems surrounded by high concentrations of different molecules or entities ranging in size from small ions to cells. This crowded environment remains stable by a delicate balance of countless interactions and reactions, mainly electrostatically and entropically driven [50].

Fibrinogen, a primary protein in the plasma associated with clotting process [51], has an important role to play in this regard. Not only is a protein engaging for bleeding problems, it is a high molecular protein containing highly diverse structures and multi-domain architecture [52]. Particularly, the N-terminal central nodule so-called "E-region" (∼ 35 kDa) is an essential part in the binding of the thrombin molecule and fibrine polymerization during the clotting process (see Figure 1.3. On the other hand, from the structural point of view, E-region presents a unique dimeric constitution formed by A_α and B_β chains with symmetric architecture forming a kind of hydrophobic cavity domain or funnel-shaped.

These characteristics offer to fibrinogen the necessary tools for high surface activity, such as structural flexibility, high charge density or hydrophobicity. It is precisely this heterogeneous and sensitive structure that gives fibrinogen the opportunity to modulate and optimize, in a cooperatively way, its interactions with different molecules and surfaces.

Although the topics discussed above are often addressed separately, there is an important point in common: fibrinogen-ligand interactions. The extensive bibliography on this topic indicates that the affinity between a ligand and a protein is determined by intermolecular hydrogen bonds and ionic interactions, as well as by the shape and charge complementarity of the contact surfaces of both partners [53]. The complete understanding of the structural basis of these systems depends to a large extent on the detailed three-dimensional information on the protein-ligand interactions. Given the nature of the current tasks, the main obstacles that need to be examined urgently are related to the great difficulties to understand the complex interaction mechanisms, at the molecular level, between fibrinogen and different molecules as well as translating those particular results to a macroscopic scale.

Acebutolol is one of the most prescribed beta-selective betablocker for treating hypertension. It has an aryloxipropranolamine chain as non-selective blocker but linked to an aromatic ring containing a polar-4 substituent. The molecule has the ability to self-assembly and the final result is determined by the rigidity and planarity of the aromatic ring and the hydrocarbon chain attached to it. The attraction of this molecule is that many of the β-adrenoceptor blocking agents have pharmacological effects independently of their β-blocking activity, such as the modification of the cell membrane. These effects are known as membrane stabilizing activities and include: non-specific cardiac depression, myocardial conduction velocity depression and local anesthetic activity. One of the routes of administration of acebutolol is intravenous, where it is immediately delivered to the bloodstream to interact with plasma proteins as fibrinogen [54]. Propranolol is a β-adrenergic blocking agent. It is an optically inactive compound, with only the 1-isomer having adrenergic blocking activity. It is the most commonly used drug for hypertension; it is also used for other disorders such as chronic stable angina. Like acebutolol, its pharmacological effects have its origin in the alteration of the properties of the cell membrane [55].

1.2.1.4 Fibrinogen – Antibiotics

Penicillin β-lactam antibiotics are recognized as one of the most common wide-spectrum antibiotics used for different infections. However, the therapy success with penicillin β-lactam antibiotics remains as unsolved problem since β-lactamase resistance due to the inappropriate use, is disseminating rapidly among pathogenic bacteria. Besides, considering the occurrence of potential hematotoxicity (off-target fibrinolytic interactions) as hemolytic anemia caused by intravascular hemolysis, and blood clotting disorders-mediated fibrinolysis (i.e., by interactions with the fibrinogen molecule) which are recognized as one of the most severe adverse reactions induced by the penicillin β-lactam antibiotics when are parenterally administered [56]. To overcome the potential hematotoxicity of the β-lactam antibiotics therapeutic strategies should consider the rational prescription, substitution and/or combination.

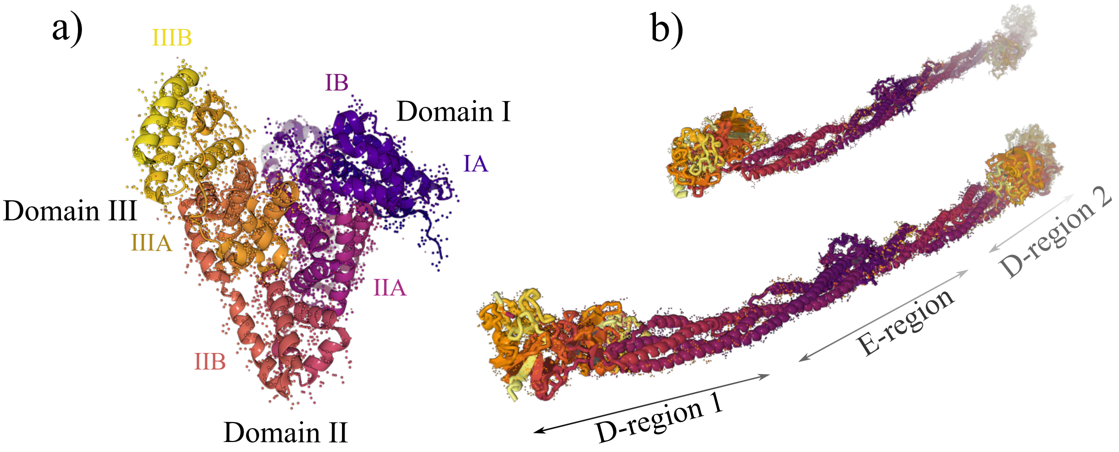

Figure 1.3: a) Crystallographic structure of Bovine Serum Albumin (PDB 4F5S). b) Representation of general crystallographic structure of fibrinogen protein (PDB 3GHG) by relevant regions formed by two quasi-symmetric C-terminal portions (D-regions 1 and 2) and the central part (E-region thrombin binding-domain).

In pursuing these aims, in the present work, the interactions and complexation of two penicillin β-lactam antibiotics, cloxacillin and dicloxacillin, with the fibrinogen serum protein were studied. The main focus has been put in correlate the effects of chemical substitution on molecular and thermodynamic properties of protein in the bulk with their effects on protein functional properties. The penicillin drugs selected for study form an interesting series of molecules in which the only variation in the molecular structure is the number and nature of the substituents on the aromatic ring: an additional chlorine atom on the phenyl ring of dicloxacillin. This selection provides an interesting opportunity to investigate the relationships of the molecular structure on the intermolecular interactions [57].

From the structural and functional point of view the human fibrinogen is a soluble glycoprotein composed by disulfide-linked dimer of three nonidentical polypeptide chains, Aα, Bβ, and γ. The NH2 terminal portions of the six chains are linked together to the central region (E) of the molecule by 11 disulfide bonds forming a small globular domain, the so-called disulfide knot, in the center. The C termini of each of the three chains end in globular domains, those of the Bβ, and γ chains are located at the ends of the molecule. The COOH$^-$ terminal portion of each fibrinogen Aα chain forms a compact αC-domain attached to the bulk of the molecule with a flexible αC-connector. In addition, fibrinogen shows a unique characteristic in its folding [54]. According to the current view, in fibrinogen, two αC-domains interact intramolecularly with each other and with the central region of the molecule, while in fibrin, they switch to an intermolecular interaction to form αC-polymers. The central region (E-region) is responsible for the fibrin polymerization during the clotting process [58]. Fibrinogen circulates in the plasma with a molecular weight of $\sim$ 340 kDa depending of Aα and Bβ chains and the γ-γ and α-α crosslinking chains content. It has a shape similar to a rod with dimensions of $9 \times 47.5 \times 6$ nm and presents a negative net charge with isoelectric pH = 5.8 in physiological conditions [59]. The normal concentration of fibrinogen is around 150 - 400 mg/dL in the blood plasma. Levels noticeably below or above this range are associated with pathological conditions like bleeding and/or thrombosis [60]. Crystallographic analysis of the molecule has been hindered for a long time by its complex and flexible structure. Finally, a planar sigmoidal structure was proposed: the axis of the α-helical coiled-coil rod adopts a sigmoidal shape that lies nearly in a plane, as the curvature is an intrinsic feature of fibrinogen's coiled coil [51].

1.2.2 Bioceramic materials

It is beyond expectation on what the bionanotechnology has accomplished and reached in just a matter of time. It has the potential to provide benefits to people and societies and improve health and environment. Bionanotechnology led to an increasing interest in the study of the interactions of nanostructures with biological entities. In parallel, important investigations in the field of biomedical research have demonstrated the usefulness of nanoparticles as the centerpiece of drug/gene delivery, visualization, or tissue engineering [61].

1.2.2.1 Hydroxyapatite (HA)

Bioceramics are considered suitable biomaterials for bone repair because of their high osteoconductive capacity. Among them, hydroxyapatite (HA) is the most common choice to develop synthetic substitutes due to its chemical composition that is similar to the mineral phase in the bone. It is thus a mineral or bioceramic that can be produced by the living beings. *In vivo*, hydroxyapatite nucleation and mineral growth occur within the extracellular matrix of cells and has the general formula $Ca_{10}(OH)_2(PO_4)_6$ [62].

Although natural raw hydroxyapatite can exhibit better levels of biocompatibility, it frequently presents impurities and/or inhomogeneities; while the synthetic ones, created under controlled and reproducible conditions, offer a better control over impurities. In addition, the possibility of varying the synthesis process and the quantities of precursors makes it possible to predict and design a final product with customized properties [63]. Due to all of these reasons, the synthesis of HA, ($Ca_{10}(PO_4)_6(OH)_2$), has been evolved as a central subject in chemistry and materials science.

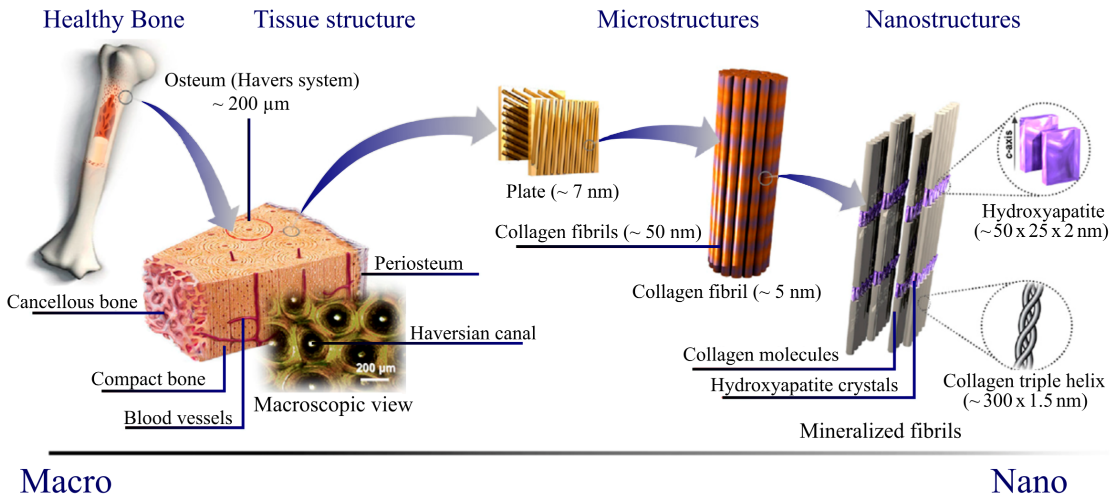

Figure 1.4: Representation of a human bone and its hierarchical structure at different scales.

Previously, the methodology to prepare HA nanoparticles was based on a method initially proposed by Liu et al. [64]. Basically the method consists in adding, one drop at a time, 1 mL of a solution of PPG (polypropylene glycol) to a dissolution of CTAB (hexadecyltrimethylammonium bromide) under mechanical stirring. Then it is added by order $NaNO_2$ and $CaCl_2$. Finally, $Na_3PO_4 \cdot 12H_2O$ is added, drop by drop for 1 h. The dissolution is stirred closed for 1 h and then inserted into an autoclave for a day. The obtained product is filtered, dried and calcined in a muffle. This process allows us to obtain cylindrical nanoparticles with a length between 25 and 50 nm and diameters in the order of 7–9 nm.

As mentioned, HA nanoparticles can be produced in different forms (e.g., spheres and needles) and in large amounts with controlled composition, size, and shape using relatively cheap synthetic approaches [65, 66]. Despite the fact that its chemical synthesis goes back several decades, the methodology has developed constantly over the years to satisfy the requirements of all of its applications. The most typical and widely used routes are: mechanochemistry synthesis, direct precipitation of aqueous solutions, electrochemical deposition, sol-gel procedures, hydrothermal synthesis and emulsification. However, both the microstructure and other properties (hardness, density. . .) of the resulting samples are extremely sensitive to internal and external variables. The pH value of the reaction system is crucial for the formation of HA, the temperature and the mixing procedure of the reagents are also of great importance for the final structure of the HA.

As a result, both current and future applications offer important challenges that need to be improved. One of them is the need to develop synthesis routes of HA that allow an exhaustive control of the final material, a large scale and an economically viable implementation. For achieving that, a novel microfluidic-based methodology of synthesis was developed and will be properly explained hereafter in this present document.

Calcium and phosphate concentrations between the implant and bone are augmented due to the dissolution of HA from the implanted material, leading to precipitation and formation of a crystalline layer. Thus, HA enhances the implant mineralization and induce the growth of a crystalline phase with shape, composition, and orientation that closely resemble the mineral phase of calcified tissues [67]. To reduce the problems of infection associated with polymeric catheters and percutaneous devices, it has been proposed to coat these systems with thin layers of HA, the proposal is achieving excellent results [68, 69]. These systems have shown their viability as vehicles for the well controlled drug delivery, where the presence of HA increases the loading drug capacity in a homogeneous way and also regulates its delivery by pH [70].

1.2.3 Complex implantable devices

Current clinical practices for bone repair are dominated by autologous and allogeneic bone graft, which ensure the preservation of fundamental properties such as osteoconduction, osteoinduction, and osteogenesis. The success of such procedures is nonetheless limited: autografts are challenging to obtain due to donor site morbidity and necessity to do a second surgery, whereas allografts limitations emerge from the shortage of donors, risk of disease transmission and rejection [71]. Moreover, there are no synthetic or heterologous bone substitutes available with the physical or biological properties as the original bone [72]. As a consequence, the majority of critical bone defects are still unrecoverable and neither efficiently nor adequately treated. The development of new biomaterials and processing routes of synthetic biomedical devices has been crucial to achieve enhanced bone repair. In this sense, the surface of an implant is the first contact established with the physiological environment: the events that take place at the surface of a new implant or a prosthetic device (e.g., proteins adsorption [73], osteoblast adhesion and proliferation [74]) are decisive to define whether there is osseointegration – the physical anchorage of the implant to the native bone – or device rejection by the host. It is thus essential that an implant surface exhibits good osteoinduction – the stimulation of progenitor cells into bone cells – as well as osteoconduction – the ability to promote mineralization and bone growth at the surface of the implant [75]. That is one of the major reason why the immobilization of a HA layer on the surface of implant/device that is in direct contact with body fluids and cells is of crucial importance for proper osseointegration.

Recently, tissue engineering has been developed to provide solutions to different demands that require medicine to restore damaged tissues or even complete organs [76]. This field combines biologically active scaffolds, cells and molecules in order to induce the regeneration and/or creation of tissue through the generation of a succession of events [77–79]. The fundamental function of the scaffold is to give three-dimensional support and to favour the microenvironment so that the cells and active elements can migrate and proliferate [80]. However, the biotechnology advancement of recent years has led to new demands. The scaffolding must be biodegradable to allow the natural growth of bone tissue and in turn the products of such disintegration are biocompatible. It must withstand the mechanical efforts that the affected area has suffered. Another fundamental premise is a porous structure with a high degree of connectivity between the pores. This condition ensures the mobility and transport of necessary nutrients, cells and fluids.

1.2.3.1 Composite membranes

The combination of HA and alginate (ALG) was developed for the first time in the late 1990's for tissue regeneration applications [81]. It was however not until mid-2000 when membranes were made with these materials [82]. Recently, colleagues from collaborative research groups have conceived a bioactive alginate (ALG) composite crosslinked by hydroxyapatite nanoparticles (HAn) [83]. A beneficial aspect of the aforementioned ALG-HAn hydrogels is their pH-dependent strength properties, as the hydrogel is firm right after implantation due to the acidic environment in healing wounds but degrades along with the tissue healing process. Its biodegradability is important for guided bone regeneration (GBR) membranes, since a second surgical extraction procedure is avoided. Regarding each compound, ALG is a widely used bioadhesive polymer with potential applications in biomedical science. On the other hand, HAn have been proven to stimulate mesenchymal stem cells adhesion [84], osteoblast differentiation [85] and blood clotting [86].

1.2.3.2 Hydrogels and fiber mesh scaffolds

Due to the notable improvements on the properties of the resultant material, research trends are currently interested on the addition of nanoparticles into the network scaffold. The interaction of these nanoparticles with the hydrogel internal structure results in the peculiar attributes. Nanoparticle addition may reinforce the structure and provide the scaffold with responsiveness to external stimuli, such as mechanical or thermal. For this purpose, the template must have the ability to promote the adequate spatial dispersion of nanoparticles. This ensures a proper balance between compatibilization and confinement [87].

In general, the separation of phases of a system is governed by the free energy of Gibbs, which is a function of the enthalpy and entropic contributions. These contributions are a function of the size of the components of the template and the Flory-Huggins interaction parameter. For these reasons, it is important to relate the morphology of the matrix with the geometry of the nanoparticles that you want to add to avoid steric hindrance [88]. Through the confinement of particles between the blocks of the template it is possible not only get an array with a desired nanostructure, but rather functional nanocomposite materials with different properties depending on the properties of confined nanoparticles. Finally, it is important to emphasize that to control the confinement of nanoparticles it could be necessary to perform a proper functionalization. In fact, functionalization is a very important factor for controlling the structuring of nanocomposites and knowledge of theoretical confinement of nanoparticles. It can be both chemical and physical, so that the organic part, the template, will be compatible with the inorganic portion.

In adittion, the physical and biological requests of an ideal synthetic bone substitute involve frameworks that closely mimic human tissue morphology, but also that are optimized to perform host tissue's specific functions. The human skeleton has an obvious mechanical function in supporting and protecting the body. Therefore, it becomes critically important to design scaffolds that must maintain their physical integrity during application subject to mechanical stresses, which might lead to bearing superior body loads [89].

1.2.3.3 Hybrid Hydrogels

Finding new materials with the suitable properties to be used as extracellular matrix (ECM) substitutes has always been one of the major goals of the tissue engineering. As already mentioned, in recent years, many works have focused on the study of polymeric hydrogels, since their properties of biocompatibility, biomimicry, receptivity, the possibility to adjust their mechanical properties and their intrinsic ability to contain great amounts of water make them excellent substitutes of the ECM for biomedical applications [90, 91]. Consequently, naturally derived polymeric hydrogels present themselves as flexible and adaptable scaffolds to mimic the natural features of native ECM such as the stimulation of tissue formation and maintain and conserve cellular functions. Another important point is the interaction between these scaffolds and proteins of the hosting tissue [92]. This process is crucial defining whether the treatment is going to be effective. In this regard, the mechanisms and the attributes that affect to the protein adsorption and interactions on the compounds are highly difficult to characterize [93]. Nevertheless, in order to design new materials or devices to be used in the regeneration of calcified tissues, it is of vital importance to understand the processes, that is the reason why this topic has been one of the major concerns in the field of regenerative medicine over the recent years. In this regard, polymeric scaffolds have been recently used to bioengineer 3D cell culture studies, as well as developing tissue formation ex vivo and cellular organization. However, the possibilities are not only limited to this field, excellent reviews have shown the great versatility of these compounds. Sanchez et al. [94], in addition to analyze the most popular synthesis routes, described some of the most surprising examples of applications, both commercial and prototype. The combination of the properties of organic (stabilization, softness) and inorganic compounds (strength, conductivity) is the key of hybrid materials for optics, bioimaging, plamonics, electronics, and storage [95]. The perfect synergy of the complementary properties of both components is also highlighted by Saveleva et al. [96], with an emphasis on the organization of the compounds (organic-in-inorganic and inorganic-in-organic). In order to produce hydrogels, the most typical and frequent materials used are biopolymers. Their properties and possibilities are so diverse that hydrogels have been used recently in a wide variety of possibilities, such as cell delivery, encapsulation systems, injectable materials, scaffolds and even as bioink for biofabrication [97]. However, pure or one-compound hydrogels are subject to significant limitations and their applications are restricted [98]. The combination of different biopolymers provides a useful and encouraging mixture of cell health promotion given by the proteins and the good mechanical properties provided by the polysaccharides.

1.3 Computational tools and novel experimental approaches

1.3.1 Computational modeling

1.3.1.1 Molecular docking

Molecular docking approaches has become an increasingly important and recognized tool in rational drug-design [99]. It is a *in silico* procedure based on molecular mechanics widely used to predict energies, binding modes, being able to generate a three-dimensional structures of ligands into a target protein in a variety of positions, conformations and orientations [100], allowing to efficiently elucidate key biochemical processes. One of the main limitations of the Docking it is the small area of the conformational space that can be explored. Therefore, it is necessary to look for a balance between the computational cost and the scanned search space. In practice, it means that different restrictions and approximations need to be applied in order to reduce the problem dimension. Despite the existence of great advances in computational pharmacology are still ignored how different binding-modes can modulate the pharmacological response. The molecular docking results generally suggest that the native binding-mode corresponds to a low free energy structure but not necessarily with the lowest values. In this sense, one of the main challenges, is to implement computational algorithms that allow to discriminate correctly the influence of a given conformational binding-modes of the ligand on the interaction energy (FEB values), which are usually, very close to each other [101]. Because, in most cases the different ligand-conformations obtained after the molecular docking simulations occupy the same biophysical environment in the protein binding-site. For this instance, the local perturbation response scanning maps (LPRS map images) could be considered as an efficient approach to identify differences-based penicillin-conformational binding-modes with fibrinogen protein [102, 103]. The LPRS maps allows the determination of the influence/sensitivity that each binding residue has on/to every other residue under ligand interaction, by performing a map-based matrix of interaction that works with an anisotropic network model (ANM), where the nodes refer to individual residues [104, 105].

The interaction between different types of amphiphilic molecules in solution has long received great interest from the experimental sciences. Recently, physical chemists have devoted particular attention to these systems in a phenomenological way to get accurate information on the forces responsible for molecular interactions; this is also expected to increase the efficiency and number of uses of these systems particularly when amphiphilic drugs are involved [106]. For example, due to the impediments that nucleic acids have to cross cell membranes, the efficiency of gene therapy depends greatly on the use of vectors which could deliver genetic material into a target cell with minimum toxicity. However, the current development of both molecular medicine and biotechnology has opened up endless possibilities.

From the biomedical perspective, the increase of resistant bacteria is a major public health concern. So, developing effective new antibacterials is an important social request. Cationic surfactants have been used as antimicrobials long time ago. Marafino et al. [107] present a very remarkable job for several reasons. Firstly, the authors design, synthesize (tris-cationic, tripled-headed, double-tailed amphiphiles) and characterize the compounds. Then, they study the physicochemical properties of both pure compounds and the mixtures (critical micellar concentration, thermodynamic parameters and minimum inhibitory concentration against six bacterial strains). Finally, they include combination studies, checkerboard technique, to determine if mixtures present synergism to kill E. coli or S. aureus, a first attempt to obtain structure–activity relationships. Both the designed compound and the method offer promise as future antibacterial agents in a wide variety of applications. Oliver et al. [108], also suggest that properties such as shape, dimension, and electric charge can be systematically and predictably tuned. Combinations of commonly used surfactants were studied by SAXS and ITC and the conclusions seem to be quite clear: the geometrical and physicochemical properties of the mixed aggregates can be expressed as a linear combination of the respective properties of the pure compounds.

1.3.1.2 Computational studies of the physicochemical properties of binary systems

The mixtures of a huge amount of surfactant types: nonionic-nonionic, anionic-nonionic, cationic-nonionic, anionic-anionic, cationic-cationic, cationic-anionic and anionic-biosurfactant; have been studied, and the theories of Clint [109], Motomura [110], Rubingh [106] and Blankschtein [111] have been used to analyze and compare the experimental results in order to understand the synergism and antagonism of the binary combinations. In addition to this, a theoretical approach of regular solution and molecular thermodynamic theory [112], (considering the contributions of the hydrophilic head and hydrophobic tail structures of the amphiphiles) has been applied on ternary mixtures of amphiphiles to predict the cmc and other micellar parameters on the basis of solution composition.

It is usually assumed that the first attempt to describe quantitatively the self-assembly of mixed system was performed by Blankschtein and co-workers [113, 114]. They used a molecular-thermodynamic framework to describe micellization, phase separation and thermodynamics. From an evaluation of the Gibbs free energy modeled as the sum of different contributions (the transfer of the surfactant hydrophobic tails from an aqueous to an oil-like environment, the formation of an interface, additional entropic constraints associated with anchoring one surfactant at the interface, the formation of the micelle interfacial region, steric interactions between the surfactant heads and counterions, electrostatic interactions at the micelle interface and entropy of mixing) they were able to predict qualitative trends of micellar and phase behavior as a function of surfactant molecular structure and the solution conditions. As a logic continuation of their work they have developed different user-friendly computer programs named PREDICT, MIX2, MIXn, SURF, and DYNAMIC.

Another example of combination of computational and experimental methods was proposed by Hassan et al. [115] They focused on catanionic systems (mixtures of oppositely charged surfactants). The experimental side made use of common techniques such as density and ultrosound velocities, electrical conductivities, transmission electron microscopy and dynamic light scattering. On the other hand, the computer simulation method used was molecular dynamics (MD). During the MD simulations, coordinates, velocities, and energies were stored every 10 ps for further analysis. Thus, they could observe that a variety of structures of different size coexist in solution with vesicles of ∼160 nm diameter. Interestingly, the nanostructures were observed to self-assemble in a time scale easily accessible by atomistic classical molecular dynamics simulations, allowing to provide a comprehensive structural and dynamic characterization of the surfactant molecules at atomic level in the different aggregates.

Jójárt et al. [116], combined experimental studies and Molecular Dynamics (MD) to study the system formed by sodium dodecyl sulphate and sodium cholate, two molecules with different architectures. The experimental part was cover with spectrofluorimetric, surface tension and electrical measurements. For the computational part, the Martini coarse-grained method was chosen. The use of coarse grained models simulation techniques has proven to be a valuable tool to probe the time and length scales of systems beyond what is feasible with traditional atomistic models. The equilibrium is reached after 0.60 µs. The size distribution shows a trimodal distribution. The greatest aggregate (around 41 molecules) is the dominant. It consists of 67% of SDS. The dynamics of the cluster formation was described as follows: initially SDS molecules create a stable cluster. Then sodium cholate molecules interact with the SDS cluster increasing the size of the aggregate and decreasing the number of SDS molecules.

The mixed polymer systems have also received attention. Prhashanna et al. [117], studied co-micellization behavior for binary mixtures of Poloxamers in dilute aqueous solution. The available techniques to predict properties of mixed systems of surfactants range from Monte Carlo, self-consistent field theory, dynamic density functional theory and so on. However, a problem with these techniques is that they all describe polymers confined to lattice conformations, and are not very well suited to describe branched polymers.

In addition, extra-thermodynamic approaches close related to Linear Free Energy Relationships (LFER) have been successfully used in Chemoinformatics [118, 119].

The designation as LFER equations comes from the use of parameters depending on the Gibbs free energy of the i^{th} process [120]. The changes on the values of this potential during a process obey a logarithmic statistical thermodynamic relationship with equilibrium constants K_i [121].

1.3.2 Microfluidics

Microfluidics consists of the handling of liquids in micrometric scale spaces. Such manipulation can be achieved, for instance, by making small channels through which the fluids are pumped. The best-known microfluidics products are “chips”, small tablets containing the microchannels through which the substances will perform mixing operations, separation, reaction, signaling, etc. Two main attributes are exploited in these systems: small size and laminar flow, allowing better control of processes [122]. These advantages coupled with a low consumption of reagents, high resolution and shorter analysis time explain the enormous development that this discipline has undergone. The first microchips were made of hard materials such as silicone and glass, taking advantage of the experience gained from electronic circuits. However, more recently, flexible materials such as polymers, elastomers and even paper are being used to make chips with certain advantages of manufacturing, fluid handling, economy and some organic compatibility for *in vivo* applications. There are several methods for the fabrication of the microchannels within the material depending on the nature of it. Some methods use chemicals to material removal, while others take advantage of UV rays for the same purpose. In the case of paper, channels are constructed when liquid wax is poured between them as part of a process simple and inexpensive. Microfluidic chipmaking is an area of study in permanent development.

Microfluidic devices are classified according to the operation they must perform. The Microchannels can be configured in different ways for a variety of functions. Goes from the most basic ones as “T”, “Y” or “H” junctions for mixing and observing the liquid-liquid interaction to tablets with hundreds of programmable functions on them. The equipment that usually is combined with these chips includes a pumping system, plastic hoses, fittings and in some cases, microscopes.

As it is such a recent field of study, microfluidics applications that were not previously contemplated are increasingly appearing. In this sense, microfluidics has an interdisciplinary character, from the point of view of both its study and its applications. Within the more interesting applications are those associated to biomedical sciences where microfluidics takes advantage of miniaturization to perform conventional medical tests using much less volume of reactants. The waiting

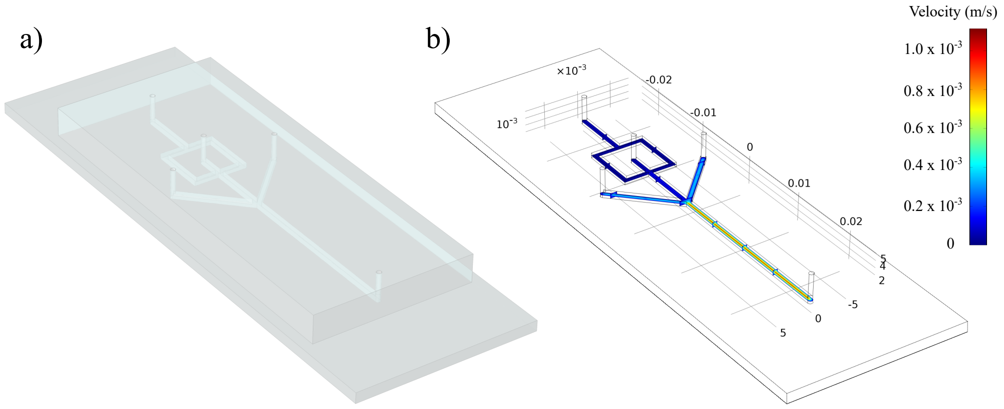

Figure 1.5: a) Digital representation of a microfluidic device. b) Flux velocity simulation of a real assay.

time for the diagnosis of a disease is considerably reduced with these devices due to the speed of reaction and diffusion that exists in such small spaces. The introduction of a certain drug into the body can be done on a scheduled basis and with the exact dose needed at that precise moment with the help of pump implants or microfluidic injection. The list of applications is extensive.

In particular, microfluidics systems have demonstrated a promising potential to modulate the critical stages in nanosynthesis, such as nucleation, growth and reaction conditions, so that the size, polydispersity, morphology and reproducibility of nanoparticles are optimized efficiently [123].

Specifically, in the present work microfluidic techniques were used for conventional HA nanoparticle synthesis and hydrogel microparticle generation. As explained, this novel method offers several advantages such as reproducibility, stability, and versatility. These devices enable a high precision in the liquid handling, resulting in precise control of properties like shape, size, and morphology simply by modifying inherent physical factors such as the residence time, the capillary length and the flow rate [124]. In addition, having continuous flow, unlike conventional production systems, enables online monitoring, which leads to superior control, and consequently, the costs can be notably reduced.

When injected at constant flow rates, fluid travels inside microchannels at controlled velocity, hence, within a microfluidic system, the stages of nucleation and growth in the synthesis of nanoparticles can be tracked as a function of the distance from the injections place.

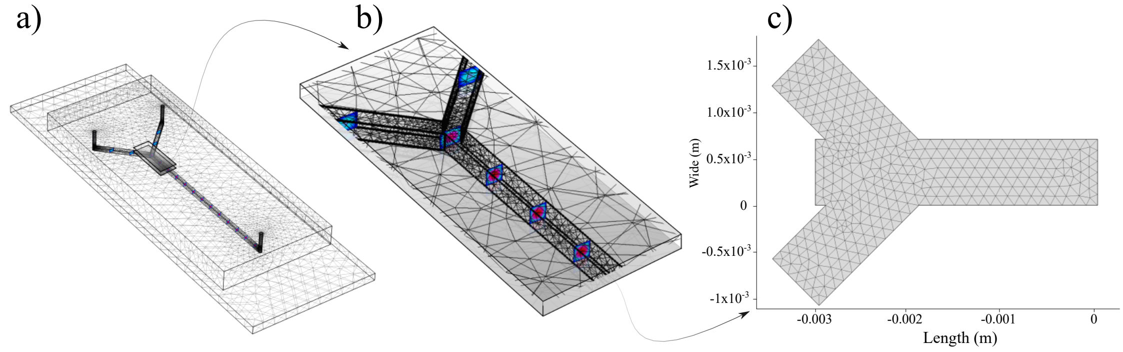

Figure 1.6: a) Microfluidic device. b) Close up of the geometry and tridimensional mesh used in the microfluidics simulation. Each vertex represents a node, resulting in the discretization of the domain in finite elements. c) Bidimensional mesh.

1.3.2.1 Finite element method (FEM)

For the theoretical study and prediction of the fluid behaviour inside the microfluidic microchannels, several computational simulations were performed. Often, the description of the laws of physics for space and time-dependent systems are defined by partial differential equations. In most cases, this expressions can not be solved analytically. In this regard, the finite element method (FEM) allows to obtain an approximate numerical solution on a body, structure or domain (when it is a continuous medium) on which certain differential equations are defined in weak or integral form that characterize the physical behavior of the problem, dividing it into a large number of non-intersecting subdomains called "finite elements". The set of finite elements forms a subdivision of the domain also called discretization.

Within each element, a series of representative points called "nodes" are distinguished. Two nodes are adjacent if they belong to the same finite element; furthermore, a node on the boundary of a finite element can belong to several elements. The set of nodes considering their adjacency relationships is called a "mesh".

The calculations are carried out on a mesh of points, which in turn serve as the basis for discretization of the domain in finite elements. The generation of the mesh is usually carried out with special programs called mesh generators, in a stage prior to the calculations that is called preprocessing. All the information of the model is transmitted between the different elements through the nodes. That is, if the nodes are not common or are not related in some way, even if they occupy the same position, there will be no information transfer. According to these adjacency or connectivity relationships, the value of a set of unknown variables defined at each node and called degrees of freedom is related. The set of relationships between the value of a certain variable between the nodes can be written in the form of a system of linear (or linearized) equations. The matrix of such a system of equations is called the stiffness matrix of the system. The number of equations in this system is proportional to the number of nodes and the number of degrees of freedom of each node.

In short, with this methodology, instead of obtaining the exact solution to a variable that meets a system of differential equations, the approximate value of said variable is obtained at certain points (nodes), subsequently estimating the rest of the associated variables.

Typically, in mechanical calculations, the analysis of the finite elements is computationally programmed to calculate the field of displacements and, later, through kinematic and constitutive relationships, the deformations and stresses respectively, when it is a problem of deformable solid mechanics or, more generally, a continuous media mechanics problem.

The finite element method is widely used due to its generality and the ease of introducing complex calculation domains (in two or three dimensions). In addition, the method is easily adaptable to problems of heat transmission, fluid mechanics to calculate fields of speeds and pressures or electromagnetic fields. Given the practical impossibility of finding the analytical solution to these problems, numerical methods and, in particular, finite elements, often become the only practical alternative for calculation in engineering practice.

Bibliography

[1] http://www.nano.gov/.

[2] J. M. de la Fuente and V. Grazu, *Nanobiotechnology. Inorganic Nanoparticles vs Organic Nanoparticles*. Great Britain: Elsevier, 2012.

[3] C. L. Dennis, R. P. Borges, L. D. Buda, U. Ebels, J. F. Gregg, M. Hehn, E. Jouguelet, K. Ounadjela, I. Petej, I. L. Prejbeanu, and M. J. Thornton, "The defining length scales of mesomagnetism: a review," *Journal of Physics: Condensed Matter*, vol. 14, no. 49, p. R1175, 2002.

[4] J. Jackson, *Classical Electrodynamics Third Edition.* Wiley, 1998.

[5] S. K. Ghosh and T. Pal, "Interparticle coupling effect on the surface plasmon resonance of gold nanoparticles: From theory to applications," *Chemical Reviews*, vol. 107, no. 11, pp. 4797–4862, 2007.

[6] M. Vallet Regí, F. Balas, and D. Arcos, "Mesoporous materials for drug delivery," *Angewandte Chemie International Edition*, vol. 46, no. 40, pp. 7548–7558, 2007.

[7] J. Y. Ying, C. P. Mehnert, and M. S. Wong, "Synthesis and applications of supramolecular-templated mesoporous materials," *Angewandte Chemie International Edition*, vol. 38, no. 1-2, pp. 56–77, 1999.

[8] M. Fernández-Leyes, V. Verdinelli, N. Hassan, J. M. Ruso, O. Pieroni, P. C. Schulz, and P. Messina, "Biomimetic formation of crystalline bone-like apatite layers on spongy materials templated by bile salts aggregates," *Journal of Materials Science*, vol. 47, no. 6, pp. 2837–2844, 2012.

[9] N. L. D'Elía, A. N. Gravina, J. M. Ruso, J. A. Laiuppa, G. E. Santillán, and P. V. Messina, "Manipulating the bioactivity of hydroxyapatite nano-rods structured networks: Effects on mineral coating morphology and growth kinetic," *Biochimica et Biophysica Acta (BBA) - General Subjects*, vol. 1830, no. 11, pp. 5014–5026, 2013.

[10] V. Mosquera, amp, x, ctor, J. M. Ruso, D. Attwood, M. N. Jones, G. Prieto, and F. Sarmiento, "Thermodynamics of micellization of surfactants of low aggregation number: The aggregation of propranolol hydrochloride," *Journal of Colloid and Interface Science*, vol. 210, no. 1, pp. 97–102, 1999.

[11] J. M. Ruso, D. Attwood, C. Rey, P. Taboada, V. Mosquera, and F. Sarmiento, "Light scattering and nmr studies of the self-association of the amphiphilic molecule propranolol hydrochloride in aqueous electrolyte solutions," *The Journal of Physical Chemistry B*, vol. 103, no. 34, pp. 7092–7096, 1999.

[12] P. V. Messina, J. M. Besada-Porto, and J. M. Ruso, "Self-assembly drugs: From micelles to nanomedicine," *Current Topics in Medicinal Chemistry*, vol. 14, no. 5, pp. 555–571, 2014.

[13] K. E. Sapsford, W. R. Algar, L. Berti, K. B. Gemmill, B. J. Casey, E. Oh, M. H. Stewart, and I. L. Medintz, "Functionalizing nanoparticles with biological molecules: Developing chemistries that facilitate nanotechnology," *Chemical Reviews*, vol. 113, no. 3, pp. 1904–2074, 2013.

[14] M. Hood, M. Mari, and R. Muñoz-Espí, "Synthetic strategies in the preparation of polymer/inorganic hybrid nanoparticles," *Materials*, vol. 7, no. 5, pp. 4057–4087, 2014.

[15] N. Hassan, V. Verdinelli, J. M. Ruso, and P. V. Messina, "Assessing structure and dynamics of fibrinogen films on silicon nanofibers: towards hemocompatibility devices," *Soft Matter*, vol. 8, no. 24, pp. 6582–6592, 2012.

[16] Z. Adamczyk, J. Barbasz, and M. Cieśla, "Mechanisms of fibrinogen adsorption at solid substrates," *Langmuir*, vol. 27, no. 11, pp. 6868–6878, 2011.

[17] P. V. Messina, N. Hassan, A. Soltero, and J. M. Ruso, "Identifying emerging trends of protein hydrogels for biological scaffolding," *RSC Advances*, vol. 3, no. 46, pp. 24256–24265, 2013.

[18] I. Lynch and K. A. Dawson, "Protein-nanoparticle interactions," *Nano today*, vol. 3, no. 1, pp. 40–47, 2008.

[19] L. Treuel, S. Brandholt, P. Maffre, S. Wiegele, L. Shang, and G. U. Nienhaus, "Impact of protein modification on the protein corona on nanoparticles and nanoparticle–cell interactions," *ACS Nano*, vol. 8, no. 1, pp. 503–513, 2014.

[20] R. Podila, R. Chen, P. C. Ke, J. M. Brown, and A. M. Rao, "Effects of surface functional groups on the formation of nanoparticle-protein corona," *Applied Physics Letters*, vol. 101, no. 26, p. 263701, 2012.

[21] J. Piella, N. G. Bastús, and V. Puntes, "Size-dependent protein–nanoparticle interactions in citrate-stabilized gold nanoparticles: The emergence of the protein corona," *Bioconjugate Chemistry*, vol. 28, no. 1, pp. 88–97, 2017.

[22] L. Treuel, K. A. Eslahian, D. Docter, T. Lang, R. Zellner, K. Nienhaus, G. U. Nienhaus, R. H. Stauber, and M. Maskos, "Physicochemical characterization of nanoparticles and their behavior in the biological environment," *Physical Chemistry Chemical Physics*, vol. 16, no. 29, pp. 15053–15067, 2014.

[23] D. Hühn, K. Kantner, C. Geidel, S. Brandholt, I. De Cock, S. J. H. Soenen, P. Rivera-Gil, J.-M. Montenegro, K. Braeckmans, K. Müllen, G. U. Nienhaus, M. Klapper, and W. J. Parak, "Polymer-coated nanoparticles interacting with proteins and cells: Focusing on the sign of the net charge," *ACS Nano*, vol. 7, no. 4, pp. 3253–3263, 2013.

[24] M. Mahmoudi, A. M. Abdelmonem, S. Behzadi, J. H. Clement, S. Dutz, M. R. Ejtehadi, R. Hartmann, K. Kantner, U. Linne, P. Maffre, S. Metzler, M. K. Moghadam, C. Pfeiffer, M. Rezaei, P. Ruiz-Lozano, V. Serpooshan, M. A. Shokrgozar, G. U. Nienhaus, and W. J. Parak, "Temperature: The "ignored" factor at the nanobio interface," *ACS Nano*, vol. 7, no. 8, pp. 6555–6562, 2013.

[25] P. M. Kelly, C. Åberg, E. Polo, A. O'Connell, J. Cookman, J. Fallon, KrpetićŽeljka, and K. A. Dawson, "Mapping protein binding sites on the biomolecular corona of nanoparticles," *Nat Nano*, vol. 10, no. 5, pp. 472–479, 2015.

[26] L. Wang, J. Li, J. Pan, X. Jiang, Y. Ji, Y. Li, Y. Qu, Y. Zhao, X. Wu, and C. Chen, "Revealing the binding structure of the protein corona on gold nanorods using synchrotron radiation-based techniques: Understanding the reduced damage in cell membranes," *Journal of the American Chemical Society*, vol. 135, no. 46, pp. 17359–17368, 2013.

[27] D. Pozzi, V. Colapicchioni, G. Caracciolo, S. Piovesana, A. L. Capriotti, S. Palchetti, S. De Grossi, A. Riccioli, H. Amenitsch, and A. Lagana, "Effect of polyethyleneglycol (peg) chain length on the bio-nano-interactions between pegylated lipid nanoparticles and biological fluids: from nanostructure to uptake in cancer cells," *Nanoscale*, vol. 6, no. 5, pp. 2782–2792, 2014.

[28] E. Casals, T. Pfaller, A. Duschl, G. J. Oostingh, and V. Puntes, "Time evolution of the nanoparticle protein corona," *ACS Nano*, vol. 4, no. 7, pp. 3623–3632, 2010.

[29] M. Lundqvist, J. Stigler, G. Elia, I. Lynch, T. Cedervall, and K. A. Dawson, "Nanoparticle size and surface properties determine the protein corona with possible implications for biological impacts," *Proceedings of the National Academy of Sciences*, vol. 105, no. 38, pp. 14265–14270, 2008.

[30] Y. Zhu, Q. Yang, M. Yang, X. Zhan, F. Lan, J. He, Z. Gu, and Y. Wu, "Protein corona of magnetic hydroxyapatite scaffold improves cell proliferation via activation of mitogen-activated protein kinase signaling pathway," *ACS Nano*, vol. 11, no. 4, pp. 3690–3704, 2017.

[31] N. L. D'Elia, N. Gravina, J. M. Ruso, J. L. Marco-Brown, J. M. Sieben, and P. V. Messina, "Albumin-mediated deposition of bone-like apatite onto nano-sized surfaces: Effect of surface reactivity and interfacial hydration," *Journal of colloid and interface science*, vol. 494, pp. 345–354, 2017.

[32] J. N. Onuchic, Z. L.-S. and, and P. G. Wolynes, "Theory of protein folding: The energy landscape perspective," *Annual Review of Physical Chemistry*, vol. 48, no. 1, pp. 545–600, 1997.

[33] M. R. Krebs, C. E. MacPhee, A. F. Miller, I. E. Dunlop, C. M. Dobson, and A. M. Donald, "The formation of spherulites by amyloid fibrils of bovine insulin," *Proceedings of the National Academy of Sciences of the United States of America*, vol. 101, no. 40, pp. 14420–14424, 2004.

[34] X. Cui, G. Gao, and Y. Qiu, "Accelerated myotube formation using bioprinting technology for biosensor applications," *Biotechnology Letters*, vol. 35, no. 3, pp. 315–321, 2013.

[35] A. M. Donald, "Aggregation in [small beta]-lactoglobulin," *Soft Matter*, vol. 4, no. 6, pp. 1147–1150, 2008.

[36] V. N. Uversky and A. L. Fink, “Conformational constraints for amyloid fibrillation: the importance of being unfolded,” *Biochim Biophys Acta*, vol. 1698, no. 2, pp. 131–53, 2004.

[37] D. Eisenberg and M. Jucker, “The amyloid state of proteins in human diseases,” *Cell*, vol. 148, no. 6, pp. 1188–1203, 2012.

[38] M. F. B. G. Gebbink, D. Claessen, B. Bouma, L. Dijkhuizen, and H. A. B. Wosten, “Amyloids - a functional coat for microorganisms,” *Nature Reviews Microbiology*, vol. 3, no. 4, pp. 333–341, 2005.

[39] J. Adamcik and R. Mezzenga, “Amyloid polymorphism in the protein folding and aggregation energy landscape,” *Angew Chem Int Ed Engl*, vol. 57, no. 28, pp. 8370–8382, 2018.

[40] M. G. Iadanza, M. P. Jackson, E. W. Hewitt, N. A. Ranson, and S. E. Radford, “A new era for understanding amyloid structures and disease,” *Nat Rev Mol Cell Biol*, vol. 19, no. 12, pp. 755–773, 2018.

[41] S. Feng, X. H. Song, and C. M. Zeng, “Inhibition of amyloid fibrillation of lysozyme by phenolic compounds involves quinoprotein formation,” *FEBS Lett*, vol. 586, no. 22, pp. 3951–5, 2012.

[42] S. S. Wang, K. N. Liu, and T. C. Han, “Amyloid fibrillation and cytotoxicity of insulin are inhibited by the amphiphilic surfactants,” *Biochim Biophys Acta*, vol. 1802, no. 6, pp. 519–30, 2010.

[43] R. Mannhold, H. Kubinyi, G. Folkers, H.-J. Böhm, and G. Schneider, *Protein-ligand interactions: from molecular recognition to drug design*, vol. 19. John Wiley & Sons, 2006.

[44] T. Peters Jr, *2 - The Albumin Molecule: Its Structure and Chemical Properties*, pp. 9–II. San Diego: Academic Press, 1995.

[45] L. R. S. Barbosa, M. G. Ortore, F. Spinozzi, P. Mariani, S. Bernstorff, and R. Itri, “The importance of protein-protein interactions on the ph-induced conformational changes of bovine serum albumin: A small-angle x-ray scattering study,” *Biophysical Journal*, vol. 98, no. 1, pp. 147–157, 2010.

[46] S. F. Santos, D. Zanette, H. Fischer, and R. Itri, “A systematic study of bovine serum albumin (bsa) and sodium dodecyl sulfate (sds) interactions by surface tension and small angle x-ray scattering,” *Journal of Colloid and Interface Science*, vol. 262, no. 2, pp. 400–408, 2003.

[47] N. K. Holm, S. K. Jespersen, L. V. Thomassen, T. Y. Wolff, P. Sehgal, L. A. Thomsen, G. Christiansen, C. B. Andersen, A. D. Knudsen, and D. E. Otzen, “Aggregation and fibrillation of bovine serum albumin,” *Biochimica et Biophysica Acta (BBA) - Proteins and Proteomics*, vol. 1774, no. 9, pp. 1128–1138, 2007.

[48] V. Vetri, M. D’Amico, V. Fodera, M. Leone, A. Ponzoni, G. Sberveglieri, and V. Militello, “Bovine serum albumin protofibril-like aggregates formation: Solo but not simple mechanism,” *Archives of Biochemistry and Biophysics*, vol. 508, no. 1, pp. 13–24, 2011.

[49] J. M. Khan, A. Qadeer, S. K. Chaturvedi, E. Ahmad, S. A. A. Rehman, S. Gourinath, and R. H. Khan, “Sds can be utilized as an amyloid inducer: A case study on diverse proteins,” *Plos One*, vol. 7, no. 1, 2012.

[50] R. Harada, N. Tochio, T. Kigawa, Y. Sugita, and M. Feig, “Reduced native state stability in crowded cellular environment due to protein–protein interactions,” *Journal of the American Chemical Society*, vol. 135, no. 9, pp. 3696–3701, 2013.

[51] A. Bratek-Skicki, P. Żeliszewska, and J. M. Ruso, “Fibrinogen: a journey into biotechnology,” *Soft Matter*, vol. 12, no. 42, pp. 8639–8653, 2016.

[52] N. Hassan, L. R. Barbosa, R. Itri, and J. M. Ruso, “Fibrinogen stability under surfactant interaction,” *Journal of Colloid and Interface Science*, vol. 362, no. 1, pp. 118–126, 2011.

[53] J. de Azevedo, F. Walter, R. A. Caceres, I. Pauli, L. F. S. Timmers, G. B. Barcellos, K. B. Rocha, and M. B. Soares, “Protein-drug interaction studies for development of drugs against plasmodium falciparum,” *Current drug targets*, vol. 10, no. 3, pp. 271–278, 2009.

[54] N. Hassan, J. M. Ruso, and P. Somasundaran, “Mechanisms of fibrinogen–acebutolol interactions: Insights from dsc, cd and ls,” *Colloids and Surfaces B: Biointerfaces*, vol. 82, no. 2, pp. 581–587, 2011.

[55] N. Hassan, J. Maldonado-Valderrama, A. P. Gunning, V. J. Morris, and J. M. Ruso, “Investigating the effect of an arterial hypertension drug on the structural properties of plasma protein,” *Colloids and Surfaces B: Biointerfaces*, vol. 87, no. 2, pp. 489–497, 2011.

[56] T. Nakano, A. Terawaki, and H. Arita, "Influence of β-lactam antibiotics on platelets. ii. in vitro effects of some β-lactam antibiotics on the biochemical responses of rat platelets," *Journal of pharmacobio-dynamics*, vol. 10, no. 8, pp. 408–420, 1987.

[57] P. Taboada, D. Attwood, J. M. Ruso, M. García, F. Sarmiento, and V. Mosquera, "Effect of electrolyte on the surface and thermodynamic properties of amphiphilic penicillins," *Journal of colloid and interface science*, vol. 220, no. 2, pp. 288–292, 1999.

[58] I. Pechik, S. Yakovlev, M. W. Mosesson, G. L. Gilliland, and L. Medved, "Structural basis for sequential cleavage of fibrinopeptides upon fibrin assembly," *Biochemistry*, vol. 45, no. 11, pp. 3588–3597, 2006.

[59] S. Kim, P. A. Thiessen, E. E. Bolton, J. Chen, G. Fu, A. Gindulyte, L. Han, J. He, S. He, and B. A. Shoemaker, "Pubchem substance and compound databases," *Nucleic acids research*, vol. 44, no. D1, pp. D1202–D1213, 2016.

[60] J. Madrazo, J. H. Brown, S. Litvinovich, R. Dominguez, S. Yakovlev, L. Medved, and C. Cohen, "Crystal structure of the central region of bovine fibrinogen (e5 fragment) at 1.4-Å resolution," *Proceedings of the National Academy of Sciences*, vol. 98, no. 21, pp. 11967–11972, 2001.

[61] C. Munoz-Menendez, D. Serantes, J. M. Ruso, and D. Baldomir, "Towards improved magnetic fluid hyperthermia: Major-loops to diminish variations in local heating," *Physical Chemistry Chemical Physics*, 2017.

[62] A. Fihri, C. Len, R. S. Varma, and A. Solhy, "Hydroxyapatite: A review of syntheses, structure and applications in heterogeneous catalysis," *Coordination Chemistry Reviews*, vol. 347, pp. 48–76, 2017.

[63] M. Šupová, "Substituted hydroxyapatites for biomedical applications: A review," *Ceramics International*, vol. 41, no. 8, pp. 9203–9231, 2015.

[64] Y. Liu, W. Wang, Y. Zhan, C. Zheng, and G. Wang, "A simple route to hydroxyapatite nanofibers," *Materials Letters*, vol. 56, no. 4, pp. 496–501, 2002.

[65] F. Lebre, R. Sridharan, M. J. Sawkins, D. J. Kelly, F. J. O'Brien, and E. C. Lavelle, "The shape and size of hydroxyapatite particles dictate inflammatory responses following implantation," *Scientific Reports*, vol. 7, no. 1, p. 2922, 2017.

[66] R. Rial, B. Tichnell, B. Latimer, Z. Liu, P. V. Messina, and J. M. Ruso, "Structural and kinetic visualization of the protein corona on bioceramic nanoparticles," *Langmuir*, vol. 34, no. 7, pp. 2471–2480, 2018.

[67] H. Zhou and J. Lee, "Nanoscale hydroxyapatite particles for bone tissue engineering," *Acta Biomaterialia*, vol. 7, no. 7, pp. 2769–2781, 2011.

[68] P. M. Zabetakis, C. M. Cotell, D. B. Chrisey, and R. C. Auyeung, "Pulsed laser deposition of thin film hydroxyapatite: Applications for flexible catheters," *ASAIO Journal*, vol. 40, no. 3, pp. M896–M899, 1994.

[69] N. C. Andrés, N. L. D'Elia, J. M. Ruso, A. E. Campelo, V. L. Massheimer, and P. V. Messina, "Manipulation of mg2+ – ca2+ switch on the development of bone mimetic hydroxyapatite," *ACS applied materials & interfaces*, vol. 9, no. 18, pp. 15698–15710, 2017.

[70] X. Hao, X. Hu, C. Zhang, S. Chen, Z. Li, X. Yang, H. Liu, G. Jia, D. Liu, and K. Ge, "Hybrid mesoporous silica-based drug carrier nanostructures with improved degradability by hydroxyapatite," *ACS nano*, vol. 9, no. 10, pp. 9614–9625, 2015.

[71] P. Baldwin, D. J. Li, D. A. Auston, H. S. Mir, R. S. Yoon, and K. J. Koval, "Autograft, allograft, and bone graft substitutes: Clinical evidence and indications for use in the setting of orthopaedic trauma surgery," *Journal of Orthopaedic Trauma*, vol. 33, no. 4, pp. 203–213, 2019.

[72] R. Agarwal and A. J. García, "Biomaterial strategies for engineering implants for enhanced osseointegration and bone repair," *Advanced Drug Delivery Reviews*, vol. 94, pp. 53–62, 2015.

[73] C. J. Wilson, R. E. Clegg, D. I. Leavesley, and M. J. Pearcy, "Mediation of biomaterial–cell interactions by adsorbed proteins: A review," *Tissue Engineering*, vol. 11, no. 1-2, pp. 1–18, 2005.

[74] P. Ducheyne and Q. Qiu, "Bioactive ceramics: the effect of surface reactivity on bone formation and bone cell function," *Biomaterials*, vol. 20, no. 23, pp. 2287–2303, 1999.

[75] F. E. Weber, "Reconsidering osteoconduction in the era of additive manufacturing," *Tissue Engineering Part B: Reviews*, pp. in press, DOI: 10.1089/ten.TEB.2019.0047, 2019.

[76] J. F. Alvarez-Barreto, S. M. Linehan, R. L. Shambaugh, and V. I. Sikavitsas, “Flow perfusion improves seeding of tissue engineering scaffolds with different architectures,” *Annals of biomedical engineering*, vol. 35, no. 3, pp. 429–442, 2007.

[77] H. Castaño-Izquierdo, J. Álvarez Barreto, J. v. d. Dolder, J. A. Jansen, A. G. Mikos, and V. I. Sikavitsas, “Pre-culture period of mesenchymal stem cells in osteogenic media influences their in vivo bone forming potential,” *Journal of biomedical materials research Part A*, vol. 82, no. 1, pp. 129–138, 2007.

[78] J. M. Ruso, N. Deo, and P. Somasundaran, “Complexation between dodecyl sulfate surfactant and zein protein in solution,” *Langmuir*, vol. 20, no. 21, pp. 8988–8991, 2004.

[79] H. Gonzalez-Diaz, S. Arrasate, A. Gomez-SanJuan, N. Sotomayor, E. Lete, L. Besada-Porto, and J. M. Ruso, “General theory for multiple input-output perturbations in complex molecular systems. 1. linear qspr electronegativity models in physical, organic, and medicinal chemistry,” *Curr Top Med Chem*, vol. 13, no. 14, pp. 1713–41, 2013.

[80] J. F. Alvarez-Barreto, M. C. Shreve, P. L. Deangelis, and V. I. Sikavitsas, “Preparation of a functionally flexible, three-dimensional, biomimetic poly (l-lactic acid) scaffold with improved cell adhesion,” *Tissue engineering*, vol. 13, no. 6, pp. 1205–1217, 2007.

[81] W. Paul and C. P. Sharma, “Infection resistant hydroxyapatite/alginate plastic composite,” *Journal of Materials Science Letters*, vol. 16, no. 24, pp. 2050–2051, 1997.

[82] M. Toda, K. Oshiro, H. Fujimori, and S. Yamamoto, “Fabrication of a novel bioceramic membrane for guided bone regeneration,” *Journal of the Ceramic Society of Japan*, vol. 114, no. 1334, pp. 799–801, 2006.

[83] L. Benedini, D. Placente, O. Pieroni, and P. Messina, “Assessment of synergistic interactions on self-assembled sodium alginate/nano-hydroxyapatite composites: to the conception of new bone tissue dressings,” *Colloid and Polymer Science*, vol. 295, no. 11, pp. 2109–2121, 2017.

[84] N. L. D’Elia, C. Mathieu, C. D. Hoemann, J. A. Laiuppa, G. E. Santillan, and P. V. Messina, “Bone-repair properties of biodegradable hydroxyapatite nano-rod superstructures,” *Nanoscale*, vol. 7, no. 44, pp. 18751–18762, 2015.

[85] N. L. D’Elía, A. N. Gravina, J. M. Ruso, J. A. Laiuppa, G. E. Santillán, and P. V. Messina, “Manipulating the bioactivity of hydroxyapatite nano-rods structured networks: Effects on mineral coating morphology and growth kinetic,” *Biochimica et Biophysica Acta (BBA) - General Subjects*, vol. 1830, no. 11, pp. 5014–5026, 2013.

[86] A. Contreras-García, N. L. D’Elía, M. Desgagné, C.-H. Lafantaisie-Favreau, G.-E. Rivard, J.-C. Ruiz, M. R. Wertheimer, P. Messina, and C. D. Hoemann, “Synthetic anionic surfaces can replace microparticles in stimulating burst coagulation of blood plasma,” *Colloids and Surfaces B: Biointerfaces*, vol. 175, pp. 596–605, 2019.

[87] P. Schexnailder and G. Schmidt, “Nanocomposite polymer hydrogels,” *Colloid and Polymer Science*, vol. 287, no. 1, pp. 1–11, 2009.

[88] C. Ocando, A. Tercjak, M. D. Martin, J. A. Ramos, M. Campo, and I. Mondragon, “Morphology development in thermosetting mixtures through the variation on chemical functionalization degree of poly (styrene-b-butadiene) diblock copolymer modifiers. thermomechanical properties,” *Macromolecules*, vol. 42, no. 16, pp. 6215–6224, 2009.

[89] A. R. Amini, C. T. Laurencin, and S. P. Nukavarapu, “Bone tissue engineering: Recent advances and challenges,” *Critical reviews in biomedical engineering*, vol. 40, no. 5, pp. 363–408, 2012.

[90] F. Brandl, F. Sommer, and A. Goepferich, “Rational design of hydrogels for tissue engineering: Impact of physical factors on cell behavior,” *Biomaterials*, vol. 28, no. 2, pp. 134–146, 2007.

[91] W. Zheng, L.-J. Chen, G. Yang, B. Sun, X. Wang, B. Jiang, G. Yin, L. Zhang, X. Li, M. Liu, G. Chen, and H.-B. Yang, “Construction of smart supramolecular polymeric hydrogels cross-linked by discrete organoplatinum(ii) metallacycles via post-assembly polymerization,” *Journal of the American Chemical Society*, vol. 138, 03 2016.

[92] J. Ruso and P. Messina, “Modelling and simulation of biological systems in medical applications,” 2017.

[93] P. V. Messina, G. Prieto, J. M. Ruso, and F. Sarmiento, “Conformational changes in human serum albumin induced by sodium perfluorooctanoate in aqueous solutions,” *Journal of Physical Chemistry B*, vol. 109, no. 32, pp. 15566–15573, 2005.

[94] C. Sanchez, B. Julián, P. Belleville, and M. Popall, "Applications of hybrid organic–inorganic nanocomposites," *Journal of Materials Chemistry*, vol. 15, no. 35-36, pp. 3559–3592, 2005.

[95] S. H. Mir, L. A. Nagahara, T. Thundat, P. Mokarian-Tabari, H. Furukawa, and A. Khosla, "Review—organic-inorganic hybrid functional materials: An integrated platform for applied technologies," *Journal of The Electrochemical Society*, vol. 165, no. 8, pp. B3137–B3156, 2018.

[96] M. S. Saveleva, K. Eftekhari, A. Abalymov, T. E. L. Douglas, D. Volodkin, B. V. Parakhonskiy, and A. G. Skirtach, "Hierarchy of hybrid materials-the place of inorganics-in-organics in it, their composition and applications," *Front Chem*, vol. 7, p. 179, 2019.

[97] Y. Xu and X. Wang, "Fluid and cell behaviors along a 3d printed alginate/gelatin/fibrin channel," *Biotechnology and Bioengineering*, vol. 112, no. 8, pp. 1683–1695, 2015.

[98] M. C. Catoira, L. Fusaro, D. D. Francesco, M. Ramella, and F. Boccafoschi, "Overview of natural hydrogels for regenerative medicine applications," *Journal of Materials Science. Materials in Medicine*, vol. 30, 2019.

[99] S. Hochreiter, G. Klambauer, and M. Rarey, "Machine learning in drug discovery," 2018.

[100] M. Feig, A. Onufriev, M. S. Lee, W. Im, D. A. Case, and C. L. Brooks III, "Performance comparison of generalized born and poisson methods in the calculation of electrostatic solvation energies for protein structures," *Journal of Computational Chemistry*, vol. 25, no. 2, pp. 265–284, 2004.

[101] S. Renner, S. Derksen, S. Radestock, and F. Mörchen, "Maximum common binding modes (mcbm): consensus docking scoring using multiple ligand information and interaction fingerprints," *Journal of chemical information and modeling*, vol. 48, no. 2, pp. 319–332, 2008.

[102] S. Mitternacht and I. N. Berezovsky, "Coherent conformational degrees of freedom as a structural basis for allosteric communication," *PLoS computational biology*, vol. 7, no. 12, p. e1002301, 2011.

[103] T. Oliwa and Y. Shen, "cnma: a framework of encounter complex-based normal mode analysis to model conformational changes in protein interactions," *Bioinformatics*, vol. 31, no. 12, pp. i151–i160, 2015.

[104] U. Emekli, D. Schneidman-Duhovny, H. J. Wolfson, R. Nussinov, and T. Haliloglu, "Hingeprot: automated prediction of hinges in protein structures," *Proteins: Structure, Function, and Bioinformatics*, vol. 70, no. 4, pp. 1219–1227, 2008.

[105] J. G. Greener and M. J. Sternberg, "Allopred: prediction of allosteric pockets on proteins using normal mode perturbation analysis," *BMC bioinformatics*, vol. 16, no. 1, p. 335, 2015.

[106] P. M. Holland and D. N. Rubingh, "Nonideal multicomponent mixed micelle model," *The Journal of Physical Chemistry*, vol. 87, no. 11, pp. 1984–1990, 1983.

[107] J. N. Marafino, T. M. Gallagher, J. Barragan, B. L. Volkers, J. E. LaDow, K. Bonifer, G. Fitzgerald, J. L. Floyd, K. McKenna, N. T. Minahan, B. Walsh, K. Seifert, and K. L. Caran, "Colloidal and antibacterial properties of novel triple-headed, double-tailed amphiphiles: exploring structure-activity relationships and synergistic mixtures," *Bioorg Med Chem*, vol. 23, no. 13, pp. 3566–73, 2015.

[108] R. C. Oliver, J. Lipfert, D. A. Fox, R. H. Lo, J. J. Kim, S. Doniach, and L. Columbus, "Tuning micelle dimensions and properties with binary surfactant mixtures," *Langmuir*, vol. 30, no. 44, pp. 13353–61, 2014.

[109] J. H. Clint, "Micellization of mixed nonionic surface active agents," *Journal of the Chemical Society, Faraday Transactions 1: Physical Chemistry in Condensed Phases*, vol. 71, no. 0, pp. 1327–1334, 1975.

[110] K. Motomura, M. Yamanaka, and M. Aratono, "Thermodynamic consideration of the mixed micelle of surfactants," *Colloid and Polymer Science*, vol. 262, no. 12, pp. 948–955, 1984.

[111] A. Shiloach and D. Blankschtein, "Predicting micellar solution properties of binary surfactant mixtures," *Langmuir*, vol. 14, no. 7, pp. 1618–1636, 1998.

[112] R. Crisantino, R. Lisi, and S. Milioto, "Energetics of sodium dodecylsulfate-dodecyldimethylamine oxide mixed micelle formation," *Journal of Solution Chemistry*, vol. 23, no. 6, pp. 639–662, 1994.

[113] S. Puvvada and D. Blankschtein, "Thermodynamic description of micellization, phase behavior, and phase separation of aqueous solutions of surfactant mixtures," *The Journal of Physical Chemistry*, vol. 96, no. 13, pp. 5567–5579, 1992.

[114] S. N. Moorkanikkara and D. Blankschtein, “New theoretical framework for designing nonionic surfactant mixtures that exhibit a desired adsorption kinetics behavior,” *Langmuir*, vol. 26, no. 24, pp. 18728–18733, 2010.

[115] N. Hassan, J. Ruso, and A. Piñeiro, “Hydrogenated/fluorinated catanionic surfactants as potential templates for nanostructure design,” *Langmuir : the ACS journal of surfaces and colloids*, vol. 27, pp. 9719–28, 2011.

[116] B. Jójárt, M. Poša, B. Fiser, M. Szőri, Z. Farkaš, and B. Viskolcz, “Mixed micelles of sodium cholate and sodium dodecylsulphate 1:1 binary mixture at different temperatures–experimental and theoretical investigations,” *PLoS One*, vol. 9, no. 7, p. e102114, 2014.

[117] A. Prhashanna, S. A. Khan, and S. B. Chen, “Co-micellization behavior in poloxamers: dissipative particle dynamics study,” *J Phys Chem B*, vol. 119, no. 2, pp. 572–82, 2015.

[118] K. Roy and J. T. Leonard, “Qsar analyses of 3-(4-benzylpiperidin-1-yl)-n-phenylpropylamine derivatives as potent ccr5 antagonists,” *J Chem Inf Model*, vol. 45, no. 5, pp. 1352–68, 2005.

[119] E. E. Anslyn and D. A. Dougherty, *Modern Physical Organic Chemistry.* University Science Books, 2006.

[120] J. Gibbs, *A Method of Geometrical Representation of the Thermodynamic Properties of Substances by Means of Surfaces.* The Academy, 1871.

[121] W. Greiner, D. Rischke, L. Neise, and H. Stöcker, *Thermodynamics and Statistical Mechanics.* Springer New York, 2000.

[122] G. M. Whitesides, “The origins and the future of microfluidics,” *Nature*, vol. 442, no. 7101, p. 368, 2006.

[123] J. Ma, S. M.-Y. Lee, C. Yi, and C.-W. Li, “Controllable synthesis of functional nanoparticles by microfluidic platforms for biomedical applications - a review,” *Lab on a Chip*, vol. 17, no. 2, pp. 209–226, 2017.

[124] D. Liu, S. Cito, Y. Zhang, C.-F. Wang, T. M. Sikanen, and H. A. Santos, “A versatile and robust microfluidic platform toward high throughput synthesis of homogeneous nanoparticles with tunable properties,” *Advanced Materials*, vol. 27, no. 14, pp. 2298–2304, 2015.

2

Materials and methods

Contents

2.1 Materials **40**
  2.1.1 Inorganic reagents 40
  2.1.2 Surfactants, buffer solutions and SBF 40
  2.1.3 Polymers, proteins and organic compounds 40
  2.1.4 Drugs 41
  2.1.5 Cell culure 41
2.2 Physicochemical characterization **41**
  2.2.1 HA nanorods 41
  2.2.2 Protein aggregation and complexation 43
  2.2.3 Nanoparticle – protein interactions 46
  2.2.4 Layer by Layer film assembly 48
  2.2.5 Bilayer Membranes 49
  2.2.6 Biomimetic Scaffolds 50
  2.2.7 Polymeric Hydrogels 53
2.3 Mechanical properties **54**
  2.3.1 Compressive strength 54
  2.3.2 Tensile testing 55
  2.3.3 Rheological characterization of the hydrogels 55
2.4 Biological studies **58**
  2.4.1 Ultrathin Films 58
  2.4.2 Bilayer membranes 59

2.1 Materials

2.1.1 Inorganic reagents

Sodium phosphate (Na_3PO_4, MW = $148\,\mathrm{g\,mol^{-1}}$, 96 % Sigma), calcium chloride ($CaCl_2$, MW = $91\,\mathrm{g\,mol^{-1}}$, 99 % Sigma) and sodium nitrite ($NaNO_2$, MW = $69\,\mathrm{g\,mol^{-1}}$, 97 % Sigma), were used without further purification. For solution preparation, only triple-distilled water was used.

2.1.2 Surfactants, buffer solutions and SBF

Hexadecyl-trimethyl ammonium bromide (CTAB, MW = $364.48\,\mathrm{g\,mol^{-1}}$, 99 % Sigma), SDS ($C_{12}H_{25}SO_4Na$) (purity > 99 % Lancaster and Alfa Aesar) and SPFO ($C_8F_{15}NaO_2$) (purity > 98 % Lancaster and Alfa Aesar) were used as surfactants. Acetic acid ($C_2H_4O_2$, MW = $60.05\,\mathrm{g\,mol^{-1}}$, 99 % Sigma-Aldrich), sodium acetate tri-hydrate ($C_2H_3NaO_2 \cdot 3H_2O$, MW = $136.03\,\mathrm{g\,mol^{-1}}$, 99 % Sigma-Aldrich), sodium hydroxide (NaOH, MW = $40\,\mathrm{g\,mol^{-1}}$, 90 % Sigma-Aldrich), tannic acid ($C_{76}H_{52}O_{46}$, MW = $1701.20\,\mathrm{g\,mol^{-1}}$, 99 % Sigma-Aldrich), tris (hydroxymethyl) aminomethane hydrochloride (Tris-HCl, 99 % Sigma-Aldrich), glycine (purity > 99 % Sigma) and phosphate buffer saline (PBS tablets, Sigma-Aldrich) were used to prepare the different buffer solutions. Sodium chloride (LaborSpirit), sodium bicarbonate (Sigma-Aldrich), potassium chloride (VWR), dipotassium hydrogen phosphate trihydrate (VWR), magnesium chloride hexahydrate (Sigma-Aldrich), calcium chloride (VWR), sodium sulphate (LaborSpirit), tris (hydroxymethyl) aminomethane (Sigma-Aldrich), and hydrochloric acid (VWR) were used for the preparation of the simulated body fluid (SBF).

2.1.3 Polymers, proteins and organic compounds

Poly (propylene glycol) (PPG, Sigma-Aldrich, MW = $425\,\mathrm{g\,mol^{-1}}$), Bovine plasma fibrinogen, fraction I, type IV, poly-L-lysine hydrobromide (15-30 kDa), collagen (type I solution from rat tail), heparin sodium salt of porcine intestinal mucosa (grade I-A, $\geq$180 USP units/mg), lysozyme from chicken egg (LSZ for molecular biology), commercial Alginic acid (Alg, from brown algae, ref. A7003, average MW = $120\,000 \sim 190\,000\,\mathrm{g\,mol^{-1}}$) and Gelatin from bovine skin (gel strength $\sim$ 225 g Bloom, Type B, average MW = $40\,000 \sim 50\,000\,\mathrm{g\,mol^{-1}}$) were purchased from Sigma-Aldrich and they were used for the synthesis of the samples directly without purification.

2.1.4 Drugs

Propranolol (1-[Isopropylamino]-3-[1-naphthyloxy]-2-propranol) hydrochloride (No. P-0884), acebutolol (N-[3-acetyl-4-(2-hydroxy-3-[isopropylamino] propoxy) phenyl] butanamide) hydrochloride (No. A-3669), Sodium cloxacillin [5-methyl-3- (*o*-chlorophenyl)- 4-isoxazolyl penicillin], sodium dicloxacillin [3-(2, 6-dichlorophenyl) -5-methyl-4-isoxazolyl penicillin], nafcillin sodium [6-(2-ethoxy-1-naphthamido) penicillin] and 3-(2-Benzothiazolylthio)-propanesulfonic acid (BTS) ($>97\,\%$ purity) were purchased from Sigma Chemical and used as received.

2.1.5 Cell culure

Human osteoblast-like Saos-2 cells (ATCC) and human dermal fibroblasts (hDF) (ECACC) were cultured in flasks in an incubator at 37 °C in a humidified air atmosphere of 5% CO_2. Dulbecco's Modified Eagle's medium (DMEM, Sigma-Aldrich), McCoy's 5A medium (Thermofisher Scientific, ref. n. 16600082), MEM/F12 medium (Fisher Scientific, ref. n. 11320082), MTS reagent (VWR), TrypLE Express (Alfagene), fetal bovine serum (FBS, Alfagene) DAPI (VWR), phalloidin (Sigma-Aldrich), Fibronectin (Gibco, ref. n. 33010-018) and sodium bicarbonate (Sigma-Aldrich) were purchased for the cell culture assays.

2.2 Physicochemical characterization

2.2.1 HA nanorods

2.2.1.1 X-ray powder diffraction

X-ray powder diffraction patterns (XRPD) of HA samples were obtained on a Philips type powder diffractometer fitted with Philips "PW1710" control unit, Vertical Philips "PW1820/00" goniometer, FR590 Enraf Nonius generator, a graphite diffracted beam monochromator and copper radiation source ($\lambda(K\alpha 1) = 1.5406$ Å), at 40 kV and 30 mA. XRPD were collected by measuring the scintillation response to Cu $K\alpha$ radiation versus the 2Θ value over a 2Θ range of 10-70. The step was 0.02° and the counting time 2 s per step.

2.2.1.2 Zeta-potential

The ζ-potential was determined by operating a Malvern Zeta Sizer Nano ZS90 (United Kingdom) with a He-Ne laser ($\lambda = 633$ nm). HA nanorods were dispersed in water by sonication for 30 min and then analyzed. The ζ-potential was calculated from electrophoretic mobility using the Henry equation (Eq. (2.1)) and the Malvern‘s ZetaSizer software (version 7.04):

$$U_E = \frac{2\varepsilon\zeta f(Ka)}{3\eta} \tag{2.1}$$

where ζ is the zeta potential, U_e is the electrophoretic mobility, ε is the dielectric constant, η is the viscosity of the sample and *f(Ka)* is the Henry’s function related to the size of the electric double layer.

2.2.1.3 Field emission scanning electron microscopy

Surface morphology was evaluated using a field emission scanning electron microscope (ZEISS FE-SEM ULTRA PLUS). To acquire all the SEM images a secondary electron detector was used. The accelerating voltage (EHT) applied was 3.00 kV with a resolution (WD) of 2.1 nm. The associated energy-dispersive spectrophotometer provided qualitative information about surface elemental composition.

2.2.1.4 Transmission electron microscopy

Particle shapes and size distributions were characterized by transmission electron microscopy (TEM) with a 200 kV ultrahigh resolution analytical electron microscope JEOL JEM-2010.

2.2.1.5 Digital images routine

An algorithm that has been specially designed for automatically extract some relevant information from images of HA was developed (Fig. 2.1a). More specifically, for the extraction of information related to the presence, distribution and orientation of molecular structures throughout an image. The algorithm has been described in detail elsewhere and consists of a cascade of filters that transform the original image to numbers that are related with the distribution of the molecules depicted on such image [1]. Briefly, the algorithm is composed of five main steps that are characterized by the application of specific filters on each step. Removal of noise (preserving the shape of the structures depicted in the image) is performed in the first place. Thereby, the random component of the pixel values of the image is partly eliminated, reducing in turn, the generation of artifacts in the following steps. Next, the borders of the main structures are enhanced by applying a gradient filter. Then, a threshold is applied to transform the multi-toned image to a binary map with only two values: “one” for border structures and “zero” for background. This threshold value is not a fixed number and is automatically adapted based on the particular

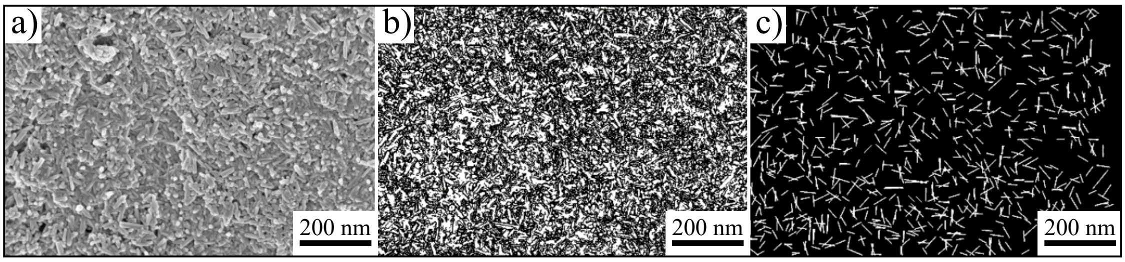

Figure 2.1: a) Original image. b) Skeleton image. c) Straight-lines image.

features of each image. An artifact removal filter is applied next. In this way, small artifacts that correspond with either isolated pixels or slightly connected (black pixels that have at least five neighboring black pixels) are removed. The resulting image is a schematic representation of the original image, where the structures that compound it, now are roughly depicted (Fig. 1.1b). Over this skeleton image a straight-line extraction filter is applied. In this way, hundreds of straight lines were virtually traced over each structure. Every straight line traced was then compared with the remain of the same structure. Straight lines with the shortest length were iteratively eliminated. Thereby, straight lines that overcome this iterative process, are supposed to be, the best representation of each structure generated, and its length and its slope are the length and slope of such structure (Fig. 2.1c).

2.2.2 Protein aggregation and complexation

2.2.2.1 Zeta potential

A Malvern Zeta Sizer Nano (ZS90) with a He-Ne laser ($\lambda = 633\,\mathrm{nm}$) was used. Malvern's software provided the zeta potential from electrophoretic mobilities using the Henry equation (Eq. (2.1)).

2.2.2.2 Scanning Electron Microscopy (SEM)

SEM measurements were performed at the Center of Electronic and Confocal Microscopy held in the University of Santiago de Compostela (Santiago de Compostela – Spain). A Zeiss FeSEM Ultra Plus equipped with Inca X-axt Penta FET Precision (Oxford Instruments) and STEM detectors were used, operated at 100 kV with magnification of 100.000x. Samples were diluted between 20 and 200-fold prior to deposition onto the grids. In the sequence, carbon-coated copper grids were prepared, blotted, washed, negatively stained with 2 % (w/v) of phosphotungstic acid, air dried, and then examined.

2.2.2.3 Isothermal Titration Calorimetry (ITC)

Experiments were carried out in a VP-ITC microcalorimeter (MicroCal Inc., Northampton, U.S. [2]. Samples were degassed in a ThermoVac system (MicroCal, USA) prior to use. In order to determine the binding isotherms, the surfactant, buffer or drug solutions were introduced into the syringe (296 µL), while the protein solutions (either BSA or Fib) were introduced into the sample cell (1.4166 mL). The stirring was kept constant at 416 rpm. Each titration experiment consisted of an initial 2 µL injection (neglected in the analysis) followed by subsequent 10 µL injections at 300 s intervals. To eliminate negative signals, a reference power of $25\,\mu J\,s^{-1}$ was applied. Thus, it is guaranteed that the signal is not altered by any overcompensation mechanism. Dilution experiments of pure surfactants and drugs were also conducted. The values obtained were systematically subtracted from those measured for the protein-surfactant, protein-drug systems. In this way, it is guaranteed that all the heat produced in the cell is due solely to the binding process. Following the described procedure, experiments were performed at a temperature of 298.15 K.

2.2.2.4 Differential scanning calorimetry

Differential scanning calorimetry (DSC) measurements were performed using a VP-DSC (MicroCal Inc., Northampton, MA) calorimeter with 0.542 ml twin cells for the reference and sample solutions. Prior to the DSC experiments, the samples and the references were degassed under vacuum while being stirred. Thermograms were recorded between 20 and 110 °C at a scan rate of 60 °C/h. To check the reproducibility, each experiment was repeated three times. The baseline reference, was subtracted from the thermograms of the samples. The heat capacity curves were evaluated using the MicroCal Origin 7.0 software to obtain ΔH and T_m values.

2.2.2.5 UV-vis absorption spectra

The UV-vis absorption measurements were recorded with a Cary 100 Bio UV-Vis Spectrophotometer. The investigated spectral range was 250-450 nm and the working temperature was maintained constant at 298.15 K

2.2.2.6 Fluorescence measurements

A Cary Eclipse spectrofluorimeter was used to perform the fluorescence measurements. The emission and excitation splits were 5 nm. The data interval was set to 1 nm and the averaging time at 0.5 seconds. The synchronous fluorescence spectra were obtained within a range of 290-450 nm upon excitation at 280 nm. The temperature was fixed at 298.15 K maintaining the Fibrinogen concentration constant at 1 µM, and increasing concentrations of drugs. In order to avoid unreliable results, the inner filter effects were corrected for the fluorescence quenching data as follows:

$$F_{cor} = F_{obs} \cdot e^{(A_{exc}+A_{em})} \tag{2.2}$$

where, $F_{corrected}$ and $F_{observed}$ are the corrected and observed fluorescence intensities and $A_{excitation}$ and $A_{emission}$ are the absorption of the systems at the excitation and the emission wavelength, respectively. UV-Vis-IR Spectral Software from FluorTools was used for data processing [3, 4].

2.2.2.7 Raman spectroscopy

The Raman scattering measurements were taken using a Raman microprobe instrument consisting of a Jobin–Yvon T64000 spectrometer equipped with a microscope, which allows a spatial resolution on the sample of about 1 µm. The Raman signal was detected by a multichannel CCD detector cooled with liquid nitrogen. Raman spectra over the whole optical frequency range were recorded using the subtractive configuration of the spectrometer, with a spectral resolution of about 2 cm^{-1}. To improve the resolution of closely spaced peaks, high-resolution scans of some frequency regions were recorded using the triple additive configuration, with a spectral resolution better than 1 cm^{-1}. The light was collected in backscattering geometry through an objective of numerical aperture 0.95. The 785 nm line of an Ar^+ laser was used as excitation, focused on a spot of $\approx$ 1 µm in diameter, with an incident power on the sample of $\approx$ 2 mW.

2.2.2.8 Synchrotron Radiation Circular Dichroism (SRCD)

The SRCD measurements were made at the Soleil (France) Synchrotron Beamline (DISCO). The SRCD spectra of samples were obtained over the wavelength range of 280-175 nm with 1 nm intervals and 1.2 s dwell time, collecting 3 individual scans at 25 °C, using a 0.005 or 0.010 or 0.020 cm pathlength quartz cuvette (Hellma Scientific). High Tension (HT) spectra were measured concomitantly, to demonstrate the level of light penetration into the samples, therefore indicating the wavelength cutoff of the spectra (190 nm for this case). All SRCD data were processed using CDTool software [5], which was employed to average the 3 individual scans, make the subtraction of the corresponding baseline spectra, which is an average of 3 scan of buffer Glycine 50 mM, pH 3.7. The spectra were zeroed between 263 and 270 nm,and smoothed with a Savitzky-Golay filter.

It was not possible to decompose the SRCD spectra to obtain the percentage of secondary structure for each sample mainly due to the small signal to noise ratio caused by the light scattering from the big aggregates. Then we performed an analysis taking in account the positive peak position between 192 nm and 198 nm, where they are the fingerprints of α-helix and β-sheet contents, respectively.

2.2.2.9 Small-angle X-ray scattering (SAXS)

SAXS experiments were carried out at SAXS beamline from the National Synchrotron Light Laboratory (LNLS) Campinas, Brazil. SAXS experiments from different concentrations of drugs and surfactants were taken in the absence and presence of proteins: 1 mg/mL of BSA and 0.5 mg/mL of fibrinogen-containing buffer solutions (50 mM glycine at pH 3.7 and 8.5, respectively). The scatterings from protein-free buffers containing the surfactants 0.012 Å^{-1} to 0.45 Å^{-1}, where q is the scattering vector ($q = (4\pi/\lambda) \cdot \sin\theta$ with 2θ the scattering angle). All measurements were performed at room temperature of 298 K.

2.2.3 Nanoparticle – protein interactions

2.2.3.1 Isothermal titration calorimetry

For the nanoparticle-protein calorimetric characterization, ITC experiments were conducted following a similar procedure to the one described in the previous section. Binding isotherms were obtained by filling the syringe (296 µL) with the Hydroxyapatite dispersions (0.2 mM and 0.5 mM) and the sample cell (1.4166 mL) with the BSA solutions (0.02 mM and 0.05 mM). To avoid HA precipitation the stirring was kept constant at 416 rpm. Initial equilibration time before starting each experiment was set to 1 h to ensure the stability of the power baseline. Injections of 10 µL at a constant rate of 0.5 $\mu\text{L}\,\text{s}^{-1}$ were performed every 300 s. Once again, care was taken to set the reference power of the ITC apparatus to a high enough value, typically of the order of 25 $\mu\text{J}\,\text{s}^{-1}$, to avoid negative signals. The experiments corresponding to the dilution of BSA were also performed; that is, the protein solution was placed in the cell, and the syringe was filled with pure water. In the dilution experiments, almost no calorimetric signal was detected. Therefore, the difference between the signals obtained with the HA-BSA samples and with pure water in the syringe afforded the signal specifically associated with the binding process. Following the described procedure, experiments were performed at a temperature of 298.15 K.

2.2.3.2 Fluorescence spectroscopy

Fluorescence measurements were performed on a Cary Eclipse spectrofluorimeter. The excitation and emission splits were 5 nm. The synchronous fluorescence spectra were obtained by setting the data interval at 1 nm and the averaging time at 0,5 seconds. The range used was 290 - 600 nm upon excitation at 280 nm. The fluorescence spectra of BSA-HA were recorded at 288.15, 298.15 and 309.15 K maintaining the BSA concentration constant at 0.05 mM, and increasing concentrations of HA from 0 mM to 1 mM. UV-Vis-IR Spectral Software from FluorTools was used for data processing [3, 4].

2.2.3.3 UV-vis absorption spectra

The UV-vis absorption measurements were recorded with a Cary 100 Bio UV-Vis Spectrophotometer. The investigated spectral range was 250 - 600 nm. Two different tests were performed: first a series of BSA solutions with increasing concentrations of HA, 0-0.5 mM, were studied; secondly two dynamic tests were carried out, in which the BSA concentration was maintained at 0.05 mM, and the HA concentrations were 0.05 and 0.5 mM, respectively. The absorption spectra were measured 1, 3, 6, and 24 hours after the samples preparation and they were constantly stirred at 250 rpm during the whole experiment.

2.2.3.4 Circular dichroism spectroscopy

Far-UV circular dichroism (CD) spectra were obtained using a JASCO-715 automatic recording spectropolarimeter (Japan) with a JASCO PTC-343 Peltier-type thermostated cell holder. Quartz cuvettes with 0.2 cm pathlength were used. CD spectra of pure BSA and nanoparticle-BSA dilute solutions were recorded from 190 to 270 nm. The following setting was used: resolution, 1 nm; bandwidth, 1 nm; sensitivity, 50 mdeg; response time, 8 s; accumulation, 3; and scan rate, 50 nm/min. Corresponding absorbance contributions from buffer solution were subtracted with the same instrumental parameters. Data was reported as molar ellipticity.

2.2.4 Layer by Layer film assembly

2.2.4.1 Monitoring

A QSense E4 quartz crystal microbalance (Sweden) with dissipation monitoring system was used to follow up the adsorption of PLL and HA nanorods at a fundamental oscillation frequency of 5 MHz and its overtones (3^{rd}, 5^{th}, 7^{th}, 9^{th}, 11^{th} and 13^{th}).

2.2.4.2 Estimation of the film thickness and mass

The thickness of the assembled films was estimated using the Voigt-based viscoelastic model [6], integrated into the Dfind software (version 1.1.2672.53037), based on Eqs.(2.3) and (2.4):

$$\Delta F \approx -\frac{1}{2\pi\rho_0 h_0}\left\{\frac{\eta_3}{\delta_3}+\sum_{j=k}\left[h_j\rho_j\omega-2h_j\left(\frac{\eta_3}{\delta_3}\right)^2\frac{\eta_j\omega^2}{\mu_j^2+\omega^2\eta_j^2}\right]\right\} \tag{2.3}$$

$$\Delta D \approx \frac{1}{2\pi f\rho_0 h_0}\left\{\frac{\eta_3}{\delta_3}+\sum_{j=k}\left[2h_j\left(\frac{\eta_3}{\delta_3}\right)^2\frac{\mu_j\omega}{\mu_j^2+\omega^2\eta_j^2}\right]\right\} \tag{2.4}$$

where k is the number of thin viscoelastic layers, ρ_0 and h_0 are the density and thickness of the quartz crystal, ρ_3 is the density of liquid, η_3 is the viscosity of the bulk liquid, δ_3 is the viscous penetration depth of the shear wave in the bulk liquid, μ is the elastic shear modulus of an overlayer, and ω is the angular frequency of the oscillation. The thickness was calculated from the 5^{th}, 7^{th} and 9^{th} overtones, setting the liquid density and HAp layer densities to default ($1000\,\mathrm{g\,L^{-1}}$), and PLL layer density to default hydrated protein ($1100\,\mathrm{g\,L^{-1}}$).

2.2.4.3 Surface characterization of the LbL films

Before any analysis, the samples were rinsed in ultrapure water three times and left drying overnight at room temperature. The elemental composition of $[\mathrm{PLL/HAp}]_3$ films and assessment of the growth of the mineral phase of the constructs prior and after incubation in SBF for different time-points was performed with a JEOL JSM-6010 LV SEM with energy-dispersive X-ray spectroscopy (SEM-EDS, Japan). Zeiss Auriga Compact high-resolution field emission SEM (HR-SEM, Germany) was used for visualization of the typical cauliflower morphology of mineralized hydroxyapatite with higher magnifications (up to 10000×) after 14 days of incubation in SBF.

2.2.4.4 Mineralization studies

$[PLL/HAp]_3$ films were prepared by dip coating on gold-coated quartz crystals keeping the deposition times obtained from the QCM-D measurements. The rinsing step was carried out in acetate buffer by a gentle agitation. After the assembly, each crystal with the deposited LbL was rinsed three times in ultrapure water and immersed in 15 ml of SBF at 37 °C [7]. Samples were retrieved after 1, 3, 7 and 14 days of immersion in SBF and analyzed as described below. Bare gold and $[PLL/HAp]_3$ as-produced films were immersed in PBS as a control for 14 days. All sample preparation and mineralization procedures were conducted in sterile conditions.

2.2.5 Bilayer Membranes

2.2.5.1 Fourier transform infrared spectrometry

Previously dried and ground membranes (M-0, M-0.11, M-0.55 and M-1.1) were homogenised with 1 % w/w KBr (FT-IR grade, Sigma-Aldrich, ref. n. 221864). The mixture was further dried at 40 °C for 48 h and placed on a microsample cup. The characterization was performed using a Fourier transform infrared spectrometry (FTIR, NICOLET Nexus 470) with an AVATAR Smart Diffuse Reflectance accessory. The measurements were done at 2 cm^{-1} resolution and 64 scans min^{-1}. The KBr spectrum was collected and subtracted from the samples' spectra.

2.2.5.2 In vitro degradation under physiological conditions

Degradation of the was evaluated through a gravimetric assay using an analytical balance (Radwag AS220/C/2) with a sensibility of 0.1 mg. The membranes were weighted (w_0) and placed in Petri dishes with 3 mL of phosphate buffer solution (PBS, pH 7.4, Sigma Aldrich, ref. n 806552) supplemented with 0.02 % w/v sodium azide as bactericidal agent. The membranes were immersed in PBS at 37 °C for 168 h, refreshing the solution every day to prevent saturation. At each time point, samples were carefully washed with distilled water to remove adsorbed ions and afterwards dried at 37 °C until constant weight (w_t). Experiments were conducted with n = 5 samples. The degradation of the membranes was directly related to the rate of weight loss (% w_L), which was calculated following Tampieri et al. [8] methodology (Equation (2.5)):

$$\%\, w_L = \frac{(W_0 - W_t)}{W_0} \times 100 \tag{2.5}$$

2.2.5.3 Surface characterization

The surface characterization of each side of the membranes was performed using a Field Emission Scanning Electron Microscope (FE-SEM, Zeiss Ultra Plus) coupled to an X-ray energy-dispersive (EDX) spectrometer. Images were acquired with a secondary electron detector (in lens) operated at an accelerating voltage (EHT) of 3.00 kV and at a working distance (WD) resolution of 2.1 nm. Local compensation of charge was achieved by injecting nitrogen gas.

The pore sizes of the surface and the size of the micro-aggregates of HAn were quantified from SEM microphotographs analysing between 50 to 110 measurements and an image visualization software (Image J 1.34 s, NIH Image, USA) [9]. Roughness parameters, specifically the arithmetic average (R_a), skewness (R_{sk}, asymmetry coefficient) and Kurtosis (R_{ku}, “tailedness” coefficient), were determined in the same visualization software using a surface area of 1000 µm^2.

2.2.6 Biomimetic Scaffolds

2.2.6.1 Field emission scanning electron microscopy

Surface morphology was evaluated using a field emission scanning electron microscope (ZEISS FE-SEM ULTRA PLUS). To acquire all the SEM images a secondary electron detector was used. The accelerating voltage (EHT) applied was 3.00 kV with a resolution (WD) of 2.1 nm. Local compensation of charge (by injecting nitrogen gas) was applied avoiding the sample staining. The associated energy-dispersive spectrophotometer provided qualitative information about surface elemental composition. The pore sizes of scaffolds were measured based on SEM images using image visualization software (Image J 1.34 s, NIH Image, USA)24. The average pore size was determined from about 100 measurements on a typical SEM image. The topography of samples was quantified from SEM microphotographs using image visualization software (Image J 1.34 s, NIH Image, USA) [10], with an uncertainty of 5 %.

2.2.6.2 High resolution transmission electron microscopy

H-TEM microphotographs were taken using a Libra 200 FE OMEGA transmission electron microscope operated at 200 kV with magnification of 1000000×. Observations were made in a bright field. Powdered samples were placed on carbon supports of 2000 mesh. The equipment is provided with electron diffraction (ED) system; d-spacing is computed based on the Bragg Law derived equation ($rd = L\lambda$), where “r” is the spot distance in the ED pattern, and $L\lambda = 1$ is the camera constant.

2.2.6.3 FT-IR spectroscopy

The experiments were done in a VARIAN FT-IR 670 Spectrophotometer. To avoid co-adsorbed water, the samples were dried under vacuum until constant weight was achieved and diluted with KBr powder before the FT-IR spectra were recorded.

2.2.6.4 Open porosity

The open porosity of the scaffolds was measured based on Archimedes's principle using a specific gravity bottle. This methodology was optimized by testing various immersion liquids as well as by establishing a standard test procedure following the Active Standard ASTM B962. Briefly, the open porosity of cubic shaped ($\approx$ 0.71 cm edge) scaffold's samples was determined as follows [11]:

$$Porosity\,(\%) = \frac{(W_2 - W_3 - W_s)/\rho_e}{(W_{1-}W_3)/\rho_e} \tag{2.6}$$

where, W_1 is the specific gravity bottle weight filled with ethanol, W_2 is the specific gravity bottle weight including ethanol and scaffold section, W_3 is the specific gravity bottle weight measured after taking out ethanol-saturated scaffold section from W_2, W_s is the ethanol-saturated scaffold section weight and ρ_e the density of ethanol; thus $(W_1\text{-}W_3)/\ \rho_e$ is the total volume of the scaffold including pores and $(W_2\text{-}W_3\text{-}W_s)/\ \rho_e$ is the pore volume in the scaffold.

2.2.6.5 Swelling kinetics and solvent absorption capacity

Swelling kinetics of the samples was carried out following a conventional gravimetric procedure [11]. Vacuum-dried cubic scaffolds samples (0.71 cm edge) were weighed before and after soaking in 0.1 M PBS kept in a thermostatic water bath at 37 °C. Samples were taken out after regular intervals of time and weighted. Weight of all gels was taken until the equilibrium was reached. Each experiment was repeated three times. The water uptake capacity ($\%W_u$) is given by:

$$\%W_u \ = \frac{(W_t - W_d)}{W_e} \times 100 \tag{2.7}$$

Where, W_t is the scaffold's weight at a time t, W_d is the dry scaffold's weight and W_e is the weight of the swollen scaffolds at the swelling equilibrium at a particular temperature. The weight-swelling ratio (W/S) was taken as a parameter to calculate solvent absorption capacity and it is computed as follows [11]:

$$W/S \ = \frac{(W_e - W_d)}{W_d} \tag{2.8}$$

2.2.6.6 Thermal characterization

The thermal properties of the cross-linked gelatin-HA scaffolds were measured using a Q20 Differential Scanning Calorimeter (TA Instruments). The temperature and enthalpy scales were calibrated using standard samples of indium (CAS No.7440-74-6/1, T_m = 156.6 °C, ΔH_m = 3.295 kJ/mol) and zinc (CAS No.7440-66-6/3, T_m = 419.53 °C, ΔH_m = 7.103 kJ/mol). The scaffold sample was completely dried by lyophilisation and sealed in a hermetic aluminum pan to prevent any loss of moisture during differential scanning calorimetric (DSC) measurement. The samples had been previously cooled to −20 °C during 1 min. Afterwards they were heated up to 200 °C at a rate 1 $°C\,min^{-1}$. Upon completing the first heating scan, the sample was quickly cooled at a rate of 10 $°C\,min^{-1}$ to −25 °C and a rerun of the cooled sample was conducted. Ultrapure nitrogen was used as purge gas at a rate of 20 $mL\,min^{-1}$ during the measurement. The baseline subtraction was made to correct any heat capacity difference between the sample and the reference furnace. All the experiments were done in triplicate. The specific heat C_p in $J\,g^{-1}\,K^{-1}$ of every sample was calculated from the DSC thermogram consisted of heat flow ($W\,g^{-1}$) by using Equation (2.9) [12]:

$$C_p = Q' \times 60/r \tag{2.9}$$

where r is the heating rate of the process in K/ min, Q' is heat flow in $W\,g^{-1}$. The resulting data were used to construct specific heat versus temperature curves.

2.2.6.7 In vitro hydrolytic and enzymatic degradation

Cross-linked gelatin-HA scaffolds were cut into a rectangular shape of about 0.71 cm edges for *in vitro* degradation studies. The specimens were weighted (W_0) and placed in glass test tubes containing 50 mL of PBS (pH 7.4, containing 0.05 % w/w of NaN_3). Then, these tubes were incubated in a water bath (37 ± 0.01 °C) for 3, 12, 16 and 25 days; PBS was renewed every week. At each time point, samples were collected in triplicate, rinsed thoroughly with distilled water, blotted with filter paper, and oven-dried until constant weight (W_t). Assuming that the local pH around the ruffled border of osteoclasts is from 4.0 to 5.0 during bone remodeling period [13], *in vitro* degradation under acidic conditions was evaluated by soaking scaffolds in an acetic acid/sodium acetate buffer solution (AcOH buffer) having a pH of 4.24 according to the method of Matsumoto et al. [14]. Enzymatic degradation was carried out similarly to the hydrolytic process, including lysozyme (LSZ) into PBS to form an enzymatic degradation medium with a concentration of 4 mg/mL.

This concentration was chosen reassembling to the normal LSZ concentrations in plasma that ranges from 4-13 mg/mL [15]. The PBS-containing lysozyme was also changed every week during enzyme degradation test. The degradability of cross-linked gelatin-HA scaffolds was estimated from the rate of weight loss (W_L) accordingly to Tampieri et al [8]:

$$\%W_L = \frac{(W_0 - W_t)}{W_0} \times 100 \tag{2.10}$$

2.2.6.8 Incubation in simulated body fluid

To evaluate the scaffolds bone-bonding potential, the materials were kept in contact with simulated body fluid (SBF) which has a composition and ionic concentration similar to that of human plasma, containing Na^+ (142.0 mM), K^+ (5.0 mM), Mg^{2+} (1.5 mM), Ca^{2+} (2.5 mM), Cl^- (148.8 mM), ${HCO_3}^-$ (4.2 mM), ${HPO_4}^{-2}$ (1.0 mM) and ${SO_4}^{-2}$ (0.5 mM). Following the standard procedure described by Kokubo *et al.* [16], the created materials were incubated in a water bath (37 ± 0.1 °C) in 1.5 SBF for periods of 7, 14, 21, 28 days; the specimens were removed from the fluid, rinsed with distilled water and oven-dried at 40 °C until constant weight.

2.2.7 Polymeric Hydrogels

2.2.7.1 FT-IR spectroscopy.

For the Fourier transform infrared spectroscopy (FT-IR), gels were dried and placed on a microsample cup. Data acquisition was performed using a FT-IR spectrometer (Varian FT-IR 670, Agilent, USA) coupled to a mapping microscope (Varian620-IR, Agilent, USA). Samples were studied in the interval 400 to 4000 cm^{-1} with a spectral resolution of 4 cm^{-1} and 64 scans min^{-1}.

2.2.7.2 Raman microscopy.

Spectroscopy data of the gels was obtained with a WITec Confocal Raman Microscopy model Alpha 300R+y. Dried samples were partially wet with triple distilled water to homogenize them and to avoid fluorescence. In a typical experiment, a frequency doubled laser at 532 nm of excitation wavelength with an output power of 38 mW was used. Spectra were recorded using a 50x Zeiss EC Epiplan-Neofluar Dic objective with a numeric aperture of 0.8. Signals were detected in the range of 1024 x 127 pixels. The number of accumulations was 30 and the integration time per pixel was 0.2 s. Data acquisition was driven by the WITec Control software.

2.2.7.3 Swelling behaviour.

The swelling and degradation characteristics of the polymeric hydrogels were performed in phosphate buffered saline (PBS) with pH 7.4 at 37 °C. For the swelling studies, samples were dried and weighed (W_d), then they were immersed in PBS and taken from the solution at selected time intervals of 0.5, 1, 3, 6, 8, 12, 24, 48 and 72 h, wiped with blotting paper, weighed (W_s) and placed again in PBS. For the degradation, hydrogels were synthesized, weighed (W_d) and also placed in PBS. In contact with the buffer, hydrogels suffer a modification in their structure, starting the release of material to the medium. At the specific timepoints, samples were removed from release medium and weighed after absorbing water on the surface with filter paper (W_r). The swelling ratio (SR) and degradation ratio (DR), in percentage, were calculated gravimetrically by the following equations:

$$Swelling\ Ratio\ (SR)\ (\%) = \frac{W_s - W_d}{W_d}\ x\ 100 \tag{2.11}$$

$$Degradation\ Ratio\ (DR)\ (\%) = \frac{W_d - W_r}{W_d}\ x\ 100 \tag{2.12}$$

2.3 Mechanical properties

2.3.1 Compressive strength

The compressive strength of cylindrical samples along the longitudinal and transverse direction was measured with a dynamical mechanical analyzer, MTS Insight electromechanical testing system, using a 1000 N load cell at a strain rate of 0.01 mm s^{-1}. A strain rate of 0.01 mm s^{-1} was selected because it is a regular strain rate at which bone is subjected [17] and is frequently used to test the implantable materials [18]. The compressive strength (σ) was calculated according to the following equation [19]:

$$\sigma = F/A \tag{2.13}$$

where F is the applied load (N), and A is the cross-sectional area of the gelatin scaffolds (m^2). Ultimate and yield strength, σ_{ult} and σ_Y, as well as compressive modulus, E, were obtained from the stress-strain plots [19].

2.3.2 Tensile testing

The membranes were cut into strips to a width of 10 mm. The Young modulus (E), maximum tensile stress (σ_{max}), maximum tensile strain (ϵ_{max}), yield stress (σ_y) and yield strain (ϵ_y) were measured along the longitudinal direction in an Instron Universal Testing Machine (Model 3369) using a 1 kN load cell at a strain rate of 0.01 mm s^{-1} and an initial gap separation of 5 cm. All experiments were conducted with n = 6 samples.

Maximum tensile stress was calculated by dividing the maximum load required to break the membrane by the cross-sectional area. Maximum tensile strain was calculated by dividing the membrane elongation at rupture by its initial length and multiplying by 100. Resilience modulus (Eq. (2.15)) [20] and plasticity (Eq. (2.16)) [21] were gauged based on the classic parameters:

$$\text{Resilience modulus } = \int_0^{\varepsilon y} \sigma \, \mathrm{d}\varepsilon \tag{2.14}$$

Assuming elastic region:

$$\text{Resilience modulus } = \sigma \mathrm{y}^2/2E \tag{2.15}$$

$$\text{Plasticity} = (\sigma_{max} - \sigma_y)/\sigma_{max} \tag{2.16}$$

2.3.3 Rheological characterization of the hydrogels

All the rheological measurements were carried out in a stress-controlled rheometer (Anton Paar MCR 302). A system of parallel plates of 25 mm diameter was chosen as the geometry to perform the tests. A humidity chamber and a Peltier cell were used to avoid undesired dehumidification and to control temperature, respectively. The gap was maintained constant through all the experiments at 0.5 mm. Finally, to minimize the differences in temperature and firmness, an equilibration time of 5 min was set before the start of the test.

Steady shear measurements. Tests were performed in rate-controlled mode. Samples were applied a linear ramp of shear rate, $\dot{\gamma}$ starting in 0.001 to 1000 Hz at 25 °C. The resulting curves were adjusted to some of the most used and reliable models, namely, Carreau, Cross, Ostwald-de Waele model and for a more detailed analysis of the dependence between shear rate and viscosity.

Cross model:

$$\eta = \eta_\infty + \frac{\eta_0 - \eta_\infty}{1 + K_1 \dot{\gamma}^d} \tag{2.17}$$

where η represents the shear viscosity $(\mathrm{Pa \cdot s})$, η_0 and η_∞ $(\mathrm{Pa \cdot s})$ are the no shear and the infinite viscosity $(\mathrm{Pa \cdot s})$, respectively, K_1 is constant that represents the characteristic relaxation time (s) and d is a dimensionless constant related to the mechanical nature of the measured material.

Ostwald-de Waele model:

$$\eta = K\ \dot{\gamma}^{n-1} \tag{2.18}$$

where η represents the shear viscosity $(\mathrm{Pa \cdot s})$, $\dot{\gamma}$ is shear rate $(\mathrm{s^{-1}})$, K is a constant, known as the viscosity index $(\mathrm{Pa \cdot s}^{n-1})$ and n is the flow index, which, depending on the value, gives important information about the type of material. For Newtonian fluids, $n = 1$; for pseudoplastic fluids, $n < 1$; and for dilatant fluids, $n > 1$.

Carreau model:

$$\frac{\eta - \eta_\infty}{\eta_0 - \eta_\infty} = \left[1 + (\lambda\dot{\gamma})^2\right]^{(n-1)/2} \tag{2.19}$$

where η represents the shear viscosity $(\mathrm{Pa \cdot s})$, η_0 and η_∞ represent the viscosity in the first Newtonian plateau $(\dot{\gamma} \to 0)$, and the second Newtonian plateau $(\dot{\gamma} \to \infty)$ $(\mathrm{Pa \cdot s})$, respectively; λ is the relaxation time (s) and n is the power index.

Dynamic measurements. Oscillatory frequency sweep measurements were performed over frequency range of ω oscillating in a range of 0.01 – 200 rad/s at 25 °C. A Peltier temperature controller and a humidity chamber were used to prevent solvent evaporation and to accurately regulate the temperature of the samples. Furthermore, in order to assure that all the tests were carried out in the linear viscoelastic region (LVR), dynamic amplitude sweeps were previously completed. According to ASTM D7175 and DIN 51810-2, the point where the storage modulus *G'* deviates by more than a 10 % from the initial plateau, indicates that the system is no longer working with a linear viscoelastic behaviour. In this case, the fixed strain chose for the frequency sweep test was 0,2 %, guarantying a linear viscoelastic regime.

Creep and recovery tests. To obtain the recover capability of the samples, creep tests were carried out. This type of tests can be divided in two main phases. In the first one, known as the load phase, the materials underwent a constant stress of 50 Pa during 173 s. After that, the shear was removed and the response of the materials was monitored for 340 s, corresponding to the recovery phase. Results were fitted to the Burger model, which is a combination of the Maxwell model, the Kevin-Voigt model and an empirical model, and could be expressed as follows:

$$J\left(t\right) = \frac{1}{G_0} + \frac{1}{G_1}\left(1 - e^{(-\mathrm{t}G_1/\eta_1)}\right) + \frac{1}{\eta_0} \tag{2.20}$$

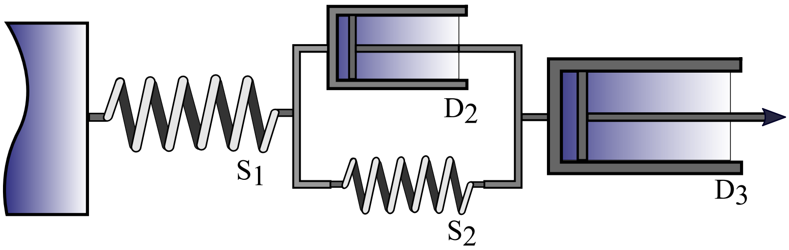

Figure 2.2: Burguer model comprising the Maxwell and Kelvin-Voigt models in series. S_1 and D_3 correspond to the Maxwell spring and dashpot, respectively, while S_2 and D_2 represent their Kelvin-Voigt counterparts.

J(t) represents the overall compliance at any time t. The springs correspond to Maxwell and Kelvin-Voigt (S_1 and S_2 in Figure 2.1) elastic sections with moduli G_0 and G_1, respectively. The dashpot of the Maxwell element (D_3) is associated with the residual viscosity, η_0, and the so-called internal viscosity, η_1, represents the dashpot of the Kelvin-Voigt element (D_2).

After the applied stress is stopped, the recovery of the systems follows a behavior that can be described with the following equation:

$$J\left(t\right) = J_{\infty} + J_{KV}e^{(-\propto t^{\beta})} \tag{2.21}$$

Where α and β are parameters related to the recovery speed of the samples. J_{∞} is the residual deformation, Maxwell dashpot (Figure 1.2, D_3) and J_{KV} represents the delayed compliance for the Kelvin-Voigt unit. The Maxwell spring contribution is represented by J_{SM} and can be calculated as follows:

$$J_{SM} = \ J_{MAX} - (J_{\infty} + J_{KV}) \tag{2.22}$$

Where J_{MAX} is the maximum deformation.

For a further characterization, the contribution of each of the elements can be determined as follows:

$$\%\ J = \left(\frac{J_{element}}{J_{MAX}}\right) \times\ 100 \tag{2.23}$$

Finally, the percentage of recovery of each sample after the removal of the shear can also be calculated following the equation:

$$\%\ R = \left(\frac{J_{MAX} - J_{\infty}}{J_{MAX}}\right)\ \times\ 100 \tag{2.24}$$

Thixotropic measurements. In order to test the thixotropic nature of the hydrogels, three interval thixotropy tests (3-ITT) were carried out. The assay involves measuring the material response to changes in the shear rate. In first place, a constant shear rate, $\dot{\gamma}$, of 0,25 Hz was applied for 10 s. After that, the shear rate, $\dot{\gamma}$, was deeply increased to 1000 Hz for 5 s. In the final step, the shear rate is set once more at 0,25 Hz and sustained for 50 s, until the end of the test. The differences in viscosity between steps give significant information about the time dependent structure breakdown and recovery of the samples, and consequently, about their thixotropic behaviour.

2.4 Biological studies

2.4.1 Ultrathin Films

2.4.1.1 In vitro cell culture

SaOs-2 cells were cultured in complete DMEM supplemented with 3.7 g L^{-1} sodium bicarbonate, 10 % FBS and 1 % penicillin-streptomycin. SaOs-2 cells were routinely grown in 75 cm^2 tissue culture flasks at 37 °C in a humidified air atmosphere of 5 % CO_2 exchanging the medium every three days until confluency was reached. Cells were detached from the flasks using TrypLE Express and resuspended in serum-free DMEM. A 100 µL cell suspension (2×10^4 cells/mL) was added on each studied surface (1.5 cm^2), namely bare gold, $[\text{PLL/HAp}]_3$ films, and films that were immersed in SBF for 7 days, placed in a 12-well plate. Additional 900 µL of serum-free medium was added 3 h after the seeding to each well and incubated in a humidified air atmosphere (5 % CO_2, 37 °C, 3 days).

2.4.1.2 Characterization of adhered cells

The samples were washed with PBS after culture for 3 days and then prepared for characterization. Cytoskeleton organization was visualized by fluorescence microscopy (AxioImager Z1M Zeiss, Germany). Cells were fixed with 10 % formalin at 4 °C for 30 min, rinsed with PBS, and a phalloidin solution in PBS (500 µL, 1:200) was added to each well to stain the actin filaments of the cells' cytoskeleton in red, left to react for 45 min at room temperature, followed by washing with PBS. The samples were then incubated in DAPI solution in PBS (500 µL, 1:1000) for 5 min to stain double-stranded DNA of the nuclei in blue, washed with PBS and imaged. Adhered cells were quantified by analyzing representative fluorescence pictures using ImageJ software (NIH, version 1.46r). MTS assay was used to assess cell viability. The samples were incubated in a 600 µL solution of MTS reagent in serum-free DMEM without phenol red (1:5) for 3 h at 37 °C. The absorbance was read at 490 nm in a BioTek Synergie HT microplate ELISA reader (USA) and was directly related to the number of live cells adhered to the films. HR-SEM was used to visualize the filopodia of the adherent cells on each substrate. The samples were dehydrated by a consecutive incubation in solutions with increasing ethanol:H_2O proportions (50:50, 70:30, 90:10 and 100:0). The dry samples were sputtered with gold and observed under HR-SEM with a magnification of 10000×.

2.4.2 Bilayer membranes

To test if the bilayer membrane would promote both bone regeneration and wound healing, osteoblast and fibroblasts cell assays were done on the mineral side (MS) and the fibrous side (FS), respectively. Human osteoblast-like Saos-2 cells (ATCC) and human dermal fibroblasts (hDF) (ECACC) were cultured in flasks in an incubator with a humidified atmosphere of 5 % CO_2 in air at 37 °C. Saos-2 were cultured in McCoy′s 5A medium (Thermofisher Scientific, ref. n. 16600082) supplemented with 15 % fetal bovine serum (FBS), whereas hDF cells with MEM/F12 medium (Fisher Scientific, ref. n. 11320082) supplemented with 10 % FBS. Both media were also supplemented with 1 % penicillin-streptomycin. The medium was changed every other day. Upon 80 % confluence, cells were detached with a minimum amount of TrypLE Express (Gibco), which was inactivated with complete medium after 5 min. The cells were then recultured or used for the experiments. All experiments were done with Saos-2 within passages 16-18 and hDF at passage 4.

The membranes were cut in circular shapes (8 mm diameter) using a biopsy punch (WPI, USA). Afterwards, they were sterilized by being exposed to a UVC lamp (254 nm) for 15 min on each side. The membranes were placed into the bottom of a 48-well plate with either the MS facing up when culturing osteoblasts Saos-2 cells, or with the FS facing up when culturing hDF cells. Since the membranes were very light, a support was needed to ensure that they would remain in place when seeding and culturing the cells [22, 23]. For this reason, ethanol-sterilized cyclic olefin copolymer (COC)-rings (6 mm inner diameter and 8 mm outer diameter) were placed on top of the membranes (Figure 2.3).

Before cell seeding, the membranes were preincubated with 50 µL of 5 $\mu g\,cm^{-2}$ fibronectin (Gibco, ref. n. 33010-018) for 2 h to promote initial cell attachment (Figure 2.3b). Afterwards, cells were seeded on the membranes using a low volume to minimize cell adhesion on the well plate. A drop of 50 µL of cell suspension $1.5x10^6$ cells/ml (expected 25,000 cells/cm^2 on each membrane) was added (Figure 2.3c). After 6 h of cell seeding, 300 µL complete medium was added into each well plate. The media was carefully refreshed every other day to ensure an adequate source of cell nutrients and waste removal (Figure 2.3d). Cells cultured in the

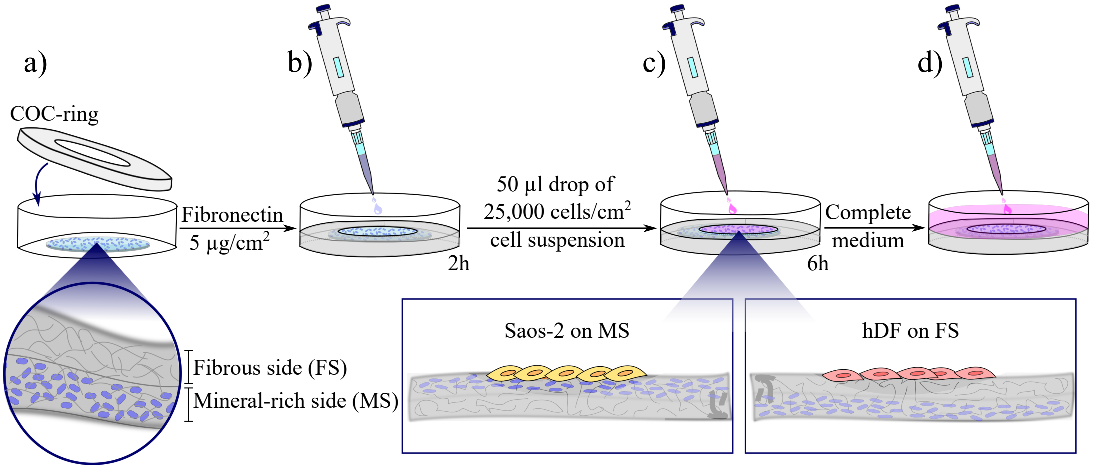

Figure 2.3: Scheme of the general protocol followed for cell seeding. a) First the membrane and then a COC-ring were placed into the well; b) fibronectin ($5\,\mu g\,cm^{-2}$) was added and placed into the incubator for 2 h, c) a drop of cells suspension in a high density ($25\,000\,cells/cm^2$) was seeded, either with the MS facing up for Saos-2 or the FS facing up for hDF. Cells were allowed to attach for 6 h. d) Finally, complete medium was added and the cells were analysed at the established time points.

same density on tissue culture treated polystyrene (TCPS) of well plates served as controls. Each sample was evaluated in triplicate and the entire experiment was performed twice with Saos-2 and once with hDF. Increasing cell densities were cultured on TCPS for 24 h and quantified to generate a standard curve, which allowed to transform the measured signals to cell numbers.

2.4.2.1 Osteoblasts and fibroblasts proliferation.

Saos-2 cells were cultured for 3, 7 and 14 days and hDF for 2 and 5 days. PrestoBlue assay (Invitrogen, ref. n. A13262), a resazurin-based solution, was used to monitor and quantify cell proliferation. Resazurin is a non-cytotoxic and redox-sensitive dye that is irreversibly reduced to fluorescent resorufin by aerobic respiration of metabolically active cells. PrestoBlue 10 % v/v was diluted in transparent medium (MEM alpha, Thermofisher, ref. n. 41061029) and was added into the well, which were previously washed with PBS. After 1h incubation, fluorescence was analysed on a microplate reader (Tecan Infinite M200®) using a fluorescence excitation wavelength of 560 nm and a fluorescence emission of 590 nm. One experiment was conducted for hDF and two full experiments were performed for Saos-2, using triplicates in each experiment.

2.4.2.2 Osteoblasts differentiation.

At days 7 and 14, cells were washed with PBS and then lysed with 0.1 % v/v triton X (Sigma-Aldrich, ref. n. X100) diluted in PBS. As per manufacturer's instructions, alkaline phosphatase activity (ALP) in the lysate was assessed using an alkaline phosphatase yellow p-nitrophenylphosphate (pNPP) liquid substrate system for ELISA (Sigma-Aldrich, ref. n. P7998). The yellow reaction product was read at 405 nm on a Tecan Infinite M200® microplate reader. ALP activity was normalized to the incubation time prior the measurement and the lactate dehydrogenase (LDH) protein absorbance (490 nm – 690 nm). Experiments were conducted twice with including triplicate samples.

Bibliography

[1] P. G. Tahoces, P. V. Messina, and J. M. Ruso, “Quantitative analysis of complex nanocomposites based on straight skeletonization,” *Colloids and Surfaces A: Physicochemical and Engineering Aspects*, vol. 562, pp. 71–78, 2019.

[2] T. Wiseman, S. Williston, J. F. Brandts, and L.-N. Lin, “Rapid measurement of binding constants and heats of binding using a new titration calorimeter,” *Analytical Biochemistry*, vol. 179, no. 1, pp. 131–137, 1989.

[3] S. Preus, K. Kilså, F.-A. Miannay, B. Albinsson, and L. M. Wilhelmsson, “Fretmatrix: a general methodology for the simulation and analysis of fret in nucleic acids,” *Nucleic acids research*, vol. 41, no. 1, pp. e18–e18, 2013.

[4] S. Preus, “Decayfit-fluorescence decay analysis software 1.3,” *http://www.fluortools.com*, 2014.

[5] J. G. Lees, B. R. Smith, F. Wien, A. J. Miles, and B. A. Wallace, “Cdtool - an integrated software package for circular dichroism spectroscopic data processing, analysis, and archiving,” *Analytical Biochemistry*, vol. 332, no. 2, pp. 285–289, 2004.

[6] M. V. Voinova, M. Rodahl, M. Jonson, and B. Kasemo, “Viscoelastic acoustic response of layered polymer films at fluid-solid interfaces: Continuum mechanics approach,” *Physica Scripta*, vol. 59, no. 5, p. 391, 1999.

[7] T. Kokubo and H. Takadama, “How useful is sbf in predicting in vivo bone bioactivity?,” *Biomaterials*, vol. 27, no. 15, pp. 2907–15, 2006.

[8] A. Tampieri, M. Iafisco, M. Sandri, S. Panseri, C. Cunha, S. Sprio, E. Savini, M. Uhlarz, and T. Herrmannsdörfer, “Magnetic bioinspired hybrid nanostructured collagen–hydroxyapatite scaffolds supporting cell proliferation and tuning regenerative process,” *ACS Applied Materials & Interfaces*, vol. 6, no. 18, pp. 15697–15707, 2014.

[9] E. Gadelmawla, M. Koura, T. Maksoud, I. Elewa, and H. Soliman, “Roughness parameters,” *Journal of Materials Processing Technology*, vol. 123, no. 1, pp. 133–145, 2002.

[10] C. A. Schneider, W. S. Rasband, and K. W. Eliceiri, “Nih image to imagej: 25 years of image analysis,” *Nat methods*, vol. 9, no. 7, pp. 671–675, 2012.

[11] N. Kathuria, A. Tripathi, K. K. Kar, and A. Kumar, “Synthesis and characterization of elastic and macroporous chitosan–gelatin cryogels for tissue engineering,” *Acta Biomaterialia*, vol. 5, no. 1, pp. 406–418, 2009.

[12] G. Kaletunç, *Calorimetry in food processing: analysis and design of food systems*, vol. 39. John Wiley & Sons, 2009.

[13] R. Baron, L. Neff, D. Louvard, and P. J. Courtoy, “Cell-mediated extracellular acidification and bone resorption: evidence for a low ph in resorbing lacunae and localization of a 100-kd lysosomal membrane protein at the osteoclast ruffled border,” *The Journal of Cell Biology*, vol. 101, no. 6, pp. 2210–2222, 1985.

[14] T. Matsumoto, M. Okazaki, M. Inoue, S. Yamaguchi, T. Kusunose, T. Toyonaga, Y. Hamada, and J. Takahashi, “Hydroxyapatite particles as a controlled release carrier of protein,” *Biomaterials*, vol. 25, no. 17, pp. 3807–3812, 2004.

[15] V. N. Uversky and A. Fink, *Protein Misfolding, Aggregation and Conformational Diseases: Part B: Molecular Mechanisms of Conformational Diseases*, vol. 6. Springer Science & Business Media, 2007.

[16] T. Kokubo, H. Kushitani, S. Sakka, T. Kisugi, and T. Yamamuro, “Solutions able to reproduce in vivo surface-structure changes in bioactive glass-ceramic a-w3,” *J. Biomed. Mat. Res.*, vol. 24, pp. 721–734, 1990.

[17] U. Hansen, P. Zioupos, R. Simpson, J. D. Currey, and D. Hynd, “The effect of strain rate on the mechanical properties of human cortical bone,” *Journal of Biomechanical Engineering*, vol. 130, no. 1, 2008.

[18] G. Ciardelli, P. Gentile, V. Chiono, M. Mattioli-Belmonte, G. Vozzi, N. Barbani, and P. Giusti, “Enzymatically crosslinked porous composite matrices for bone tissue regeneration,” *Journal of Biomedical Materials Research Part A*, vol. 92A, no. 1, pp. 137–151, 2010.

[19] T. M. Keaveny and W. C. Hayes, “Mechanical properties of cortical and trabecular bone,” *Bone*, vol. 7, pp. 285–344, 1993.

[20] M. E. Roy, L. A. Whiteside, J. Xu, and B. J. Katerberg, “Diamond-like carbon coatings enhance the hardness and resilience of bearing surfaces for use in joint arthroplasty,” *Acta Biomaterialia*, vol. 6, no. 4, pp. 1619–1624, 2010.

[21] J. Caeiro, P. González, and D. Guede, “Biomecánica y hueso (y ii): ensayos en los distintos niveles jerárquicos del hueso y técnicas alternativas para la determinación de la resistencia ósea,” *Revista de osteoporosis y metabolismo mineral*, vol. 5, no. 2, pp. 99–108, 2013.

[22] M.-C. Vincent-Vela, S. Álvarez, J. García, and E. Bergantiños, “Fouling dynamics modelling in the ultrafiltration of pegs,” *Desalination*, vol. 222, no. 1-3, pp. 451–456, 2008.

[23] W.-C. Chen, C.-H. Chen, H.-W. Tseng, Y.-W. Liu, Y.-P. Chen, C.-H. Lee, Y.-J. Kuo, C.-H. Hsu, and Y.-M. Sun, “Surface functionalized electrospun fibrous poly(3-hydroxybutyrate) membranes and sleeves: a novel approach for fixation in anterior cruciate ligament reconstruction,” *Journal of Materials Chemistry B*, vol. 5, no. 3, pp. 553–564, 2017.

3

Protein aggregation and interactions

Contents

3.1 Overview 65
3.2 Bovine Serum Albumin and surfactants 66
3.2.1 Effect of protein-surfactant interactions on the aggregation of Bovine Serum Albumin 66
3.2.2 BSA upon SDS and SPFO influence 70
3.3 Fibrinogen binding and complexation 71
3.3.1 Fibrinogen binding-interaction with betablocker agents . 71
3.3.2 Mechanisms of fibrinogen-BTS drug interactions 75
3.3.3 Binding mechanisms of fibrinogen-penicillin beta-lactam antibiotic drugs 81

3.1 Overview

Protein aggregation plays important roles in life science as, for instance, those associated to neurodegenerative diseases. Although extensive efforts have been done to elucidate all the possible variables related to the aggregation process, much has yet to be done to unveil the main pathways governing protein assembling. In the present chapter, bovine serum albumin (BSA) is used as a protein model and its association is studied by adding sodium dodecyl sulfate (SDS) and sodium perfluorooctanoate (SPFO) surfactants as promoters of protein aggregation. Correspondingly, binding-interactions between drugs of different nature and fibrinogen blood plasma protein (Fib) were also evaluated by an integrated computational-experimental study.

Findings of this research evidence that the ligand structural flexibility might be of a key importance in the pathway of protein aggregation and may pave the way to better understand the early steps of neurodegenerative disorders. Additionally, the obtained results open new perspectives for the "de novo rational drug-design" of new derivatives of β-adrenoreceptor blocking agents and β-lactam antibiotics with high pharmacodynamic selectivity/specificity to avoid side-effects toward achieving optimal benefit/risk rates, favoring the implementation of rigorous criteria for a more personalized therapy.

3.2 Bovine Serum Albumin and surfactants

3.2.1 Effect of protein-surfactant interactions on the aggregation of Bovine Serum Albumin

It is well known that BSA can alter its conformation upon changes in the pH environment [1]. At pH 6.5 the three primary domains of the protein are arranged in a heart-like shape with 17 disulfide bridges stabilizing the conformation. By lowering the pH below its isoelectric point BSA partially expands up to pH 2.7 where it reaches its fully expanded conformation. Molecular dynamic simulation was here performed to describe the protein conformation at pH 3.7 as a resource for SAXS data analysis. Further, a symmetric dimer as also obtained by using rigid body modeling through GLOBSSYM software [2].

As the protein partially unfolds it would be expected an increase of its surface area that is exposed to the solvent. Indeed, the MD analysis confirms the average increase of solvent accessible surface area (SASA) per residue and the root-mean-square deviation (RMSD) of atomic positions per residue of the partially unfolded monomer in respect to the folded one (PDB 4F5S) for each domain. For all the 3 domains there is an increase in SASA and the average residues positions are displaced in relation to the original positions (folded conformation). The average distance of the D1 and D3 domains are similar (15 Å/per residue) and almost two-fold greater than the D2 domain movement (6 Å/per residue). The opposite happens for the SASA increase, i.e. D2 SASA is almost two-fold greater than those found for D1 and D3 domains. These findings suggest that although the D1 and D3 domains moved away from the original position, they kept a folded conformation. On the other hand, the separation of D1 and D3 domains from the D2-domain caused an exposition of the residues that were buried between the domains leading to an increase in D2-domain SASA. Interestingly, Baler et al [3] also demonstrated that the D2 domain is the most exposed one upon pH lowering.

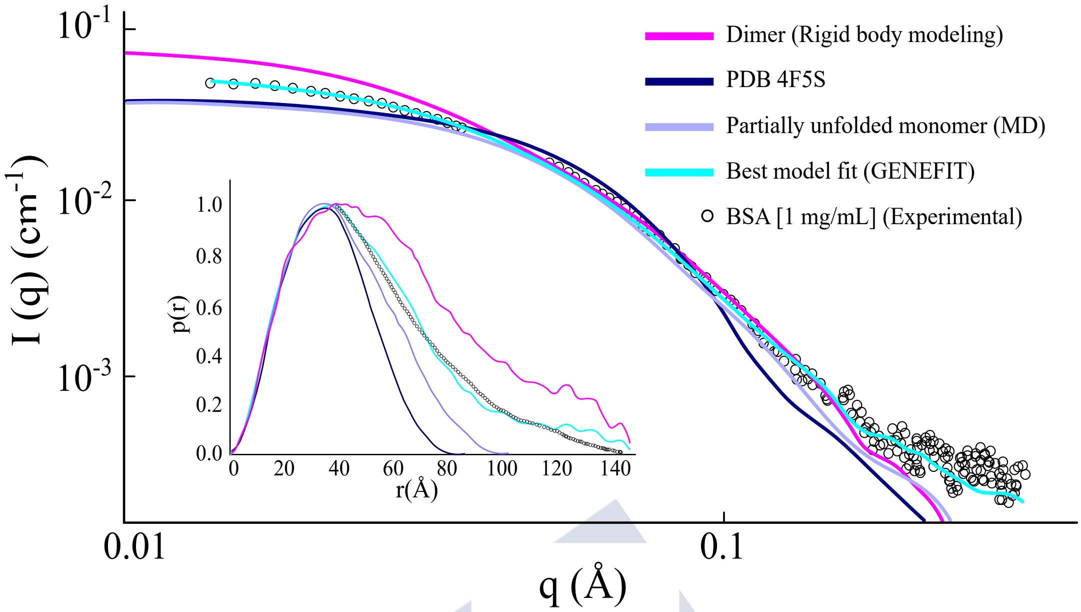

Figure 3.1: Experimental SAXS curves from BSA (1 mg/mL) at pH 3.7 (empty symbols) along with calculated SAXS curves for the following structures: PDB 4F5S (blue line), partially unfolded monomer (F-isoform) obtained by MD at pH 3.7 (light purple line), dimer obtained by rigid body modeling at pH 3.7 (pink line) and the best model fit (cyan) calculated by the software GENFIT as being composed of 75 % F-isoform and 25 % of respective dimer. Inset: corresponding pair distribution functions, *p(r)*, calculated by GIFT software, from folded monomer (PDB 4F5S), F-isoform and respective dimer represented by blue, light purple and pink lines, respectively; black and cyan lines correspond to *p(r)* obtained directly from the experimental curve (GIFT software) and from the best fitting through the GENFIT software.

Of note, a positive net charge of +99 was calculated, in good agreement to the value of +100 previously reported at pH 3.5 [3].

Furthermore, the partially unfolded conformation reported by Baler et al is more expanded than that found here. This probably happened because during the present simulations a constant pressure was imposed (NPT ensemble) which may restrict the movement of the atoms whereas Baler and co-workers imposed a NVT ensemble. This should allow atoms to reach longer distances from the original's positions.

Interestingly, MD results did not indicate any change in the α -helix secondary structure content by lowering the pH from 6.5 to 3.7. This is in very good agreement with theobtained SRCD data from BSA at pH 3.7 in 50 mM glycine buffer solution, which resulted in a 64 % α-helix at acidic environment (data not shown). Glycine is known for its ability to stabilize folded conformation [4].

Figure 3.1 shows the experimental SAXS data obtained from 1 mg/mL BSA (15 µM) dispersed in 50 mM glycine buffer solution at pH 3.7 along with the *P(q)* form factor (light purple line) calculated from the atomic coordinates assigned to

Table 3.1: Molecular Mass (MM) and radius of gyration (Rg) of native BSA state at pH 6.5 (PDB 4F5S); partially unfolded conformation at pH 3.7 here obtained by MD simulation; dimer determined by rigid body modeling using the GLOBSYMM software at pH 3.7; and same parameters obtained by Guinier's analysis $\left(\ln I\left(q \rightarrow 0\right) \propto \ln I\left(0\right) - \frac{Rg^2}{3}q^2\right)$ [6] from the experimental curve.

	PDB 4F5S	**Partially unfolded**	**Dimer**	**Guinier**
MM (kDa)	64.4	64.4	128.8	87 (2)
***Rg* (Å)**	26.9	32.0	49.2	39 (1)

the partially unfolded protein predicted by MD simulation (BSA-MD) and from the dimer (pink line) obtained by rigid body modeling. The *P(q)* form factor calculated from the native folded BSA state at pH 6.5 (PDB 4F5S) is also included in the figure for comparison purposes (blue line). As one can observe, none of form factors reproduces the experimental SAXS data. However, the partially unfolded conformation represents well the experimental data from 0.04 Å^{-1} to 0.35 Å^{-1} even though it fails to fit the data at short q values. The pair distribution *p(r)* functions obtained from *P(q)* form factors exhibit similar features: the maximum frequency of distances occurs around $r = 40$ Å with $D_{max} = 80$ Å, 100 Å and 150 Å for native, partially unfolded and dimer configurations, respectively (Figure 3.1 inset).

Furthermore, it is well known that *I(0)* is directly related to the protein molecular mass and, hence, its oligomeric state in solution [5]. So, the increase in intensity at short q values in respect to that predicted to monomeric BSA state (Fig. 3.1) reveals that partially unfolded BSA monomers at pH 3.7 must coexist with high-order aggregates in solution. Indeed, by analyzing the experimental SAXS data through Guinier's law at short q range [6], a molecular mass (MM) of 87(2) kDa was obtained. Such a value is 35 % higher than the MM expected for the monomer, suggesting that BSA is in equilibrium of partially extended monomers and aggregates.

Accordingly, the SAXS data analysis was proceeded by supposing that the experimental data has a contribution of the scattering of the partially unfolded monomer at pH 3.7 obtained by MD and the dimer modeled by rigid body modeling. By doing so, the cyan line on Fig. 3.1 represents the best fit to the experimental data, considering that circa of 75 % of partially unfolded BSA monomers at pH 3.7 coexist with $\sim$ 25 % of dimer species. Interestingly, Yeh et al. [7] also suggested a coexistence between monomer (82 %), dimer (16 %) and BSA oligomers (2 %) at similar pH as measured by high performance liquid chromatography. Further, the authors calculated a mean Rg of 38 Å which is very similar to the value here determined (Table 3.1).

Therefore, it is demonstrated by SAXS that the partially extended BSA isoform predicted by MD simulation at pH 3.7 may self-assemble as a dimer, even though it has a great net positive charge. This is intriguing. Nevertheless, one must have in mind that +99 is the total protein charge at pH 3.7, but a non-homogeneous charge distribution on protein surface may take place. As an example, it has been previously probed that native folded BSA, at pH ranging from 6.8 to 4.55, presents patches of positive and negative charges distributed on protein surface [8]. Here, the electrostatic surface potential for BSA at pH 3.7 (F-isoform predicted by MD) was calculated by means of the software APBS [9] embedded in VMD. The electrostatic surface potential is not homogeneous for the BSA F-isoform, including regions with almost null surface potential. Therefore, the exposition of such regions to the solution must permit that some proteins get close enough resulting in the formation of dimers (just 25 % of dimers according to the SAXS results).

BSA dimerization must depend on local transitions in the domains. Interestingly, it can be observed by MD an increase in the hydrophobic and hydrophilic surface area exposed to the solvent when lowering the pH to 3.7. This finding is in agreement with previous report on MD simulation of BSA at pH 3.5 [3] where the authors evidenced an increase of hydrophobic SASA for all three domains, thus exposing more hydrophobic aminoacids to the solvent. The exposition of hydrophobic surface may mediate the dimerization of BSA because the protein tends to bury those exposed aminoacids by binding to another monomer. Noteworthy, MD simulation evidenced that the greatest hydrophobic SASA occurred for the D3 domain for the partially unfolded conformation amounting to *circa* $3700\,\text{Å}^3$. In an interesting manner, D3 is the contact domain between the two monomers obtained by rigid body modeling used to analyze the SAXS experimental data. D1 and D2 domains of the partially unfolded conformation presented a hydrophobic SASA of about 2800 and $3000\,\text{Å}^3$, respectively.

In conclusion, the combined SAXS, SRCD and MD results demonstrate that individual BSA macromolecules are partially unfolded at pH 3.7 without changes in the α-helical content. The long range electrostatic repulsion between highly charged proteins (+99) must be overcome by an inhomogeneous charge distribution on protein surface. This may permit some protein approaching to short distances. Dimerization can eventually occurs coupled to an increase in the hydrophobic surface regions upon lowering the pH from 6.5 to 3.7.

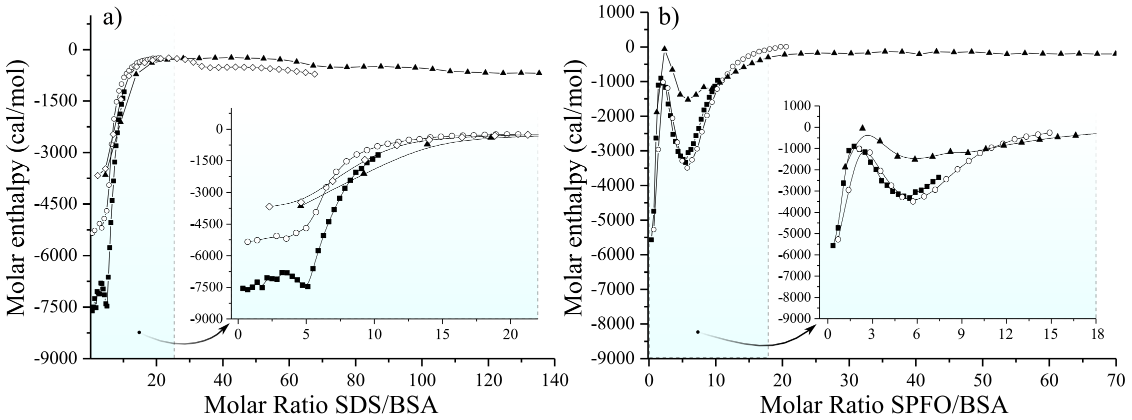

Figure 3.2: Variation of enthalpy as a function of surfactant:BSA molar ratio. a) SDS and b) SPFO. The titrations were carried out by adding SDS or SPFO: (■) 7 mM in BSA 0.15 mM.; (○) 15 mM in BSA 0.15 mM.; (▲) 50 mM in BSA 0.076 mM and (◇) 50 mM in BSA 0.15 mM.

3.2.2 BSA upon SDS and SPFO influence

Regarding the interaction of surfactants to the partially unfolded BSA, calorimetric (ITC) studies were carreid to determine enthalpy changes that may occur due to ligand-protein interaction and protein oligomerization. Figures 3.2a and 3.2b illustrate the resulting enthalpograms which present that all observable heat changes are exotermic (negative peaks) [10].

Observing both graphs, it is noteworthy that both systems reach a plateau for surfactant:BSA molar ratio around 20:1. This pattern is observed for all the initial concentration of surfactant and BSA (Figure 3.2). A plausible explanation is that initially surfactants interact energetically with the protein without promoting great changes in the conformational states and secondary structures. Over a given surfactant:molar ratio, intermolecular interactions between BSA:surfactant complexes take over the process, being manifested by drastic changes in size and spectroscopic properties. Previous studies indicated the structure of fibril-like morphologies are essentially identical with or without surfactants, which was explained by surfactants location almost exclusively found on the surface rather than inside the fibril due to differences in the intermolecular interactions [11]. Furthermore, in view of all plots in Figure 3.2, it is found that heat changes disappear from a molar ratio of 15:1 where no more heat flow was detected in the system. Knowing that, two facts can be concluded from the data. First, the aggregation process takes place as follow: initially the surfactants interact with the BSA forming a complex and then these complexes interact each other creating the supramolecular aggregates. Secondly, the absence of net heat flow over molar ratio of 15:1 reflects the balance between enthalpic (negative heat arising from van der Waals and hydrogen bonds interactions) and entropic (positive heat from conformational changes) interactions.

3.3 Fibrinogen binding and complexation

3.3.1 Fibrinogen binding-interaction with β-blocker agents

When analyzing the binding of fibrinogen with betablocker agents, resultant values from the ITC experiments show once again that all heat changes accompanying interactions are exothermic for both drugs. As explained, the binding reactions are typically exothermic (negative peaks) while conformational changes lead to endothermic (positive) peaks [10]. One aspect that draws attention is the small heat values that have been obtained for both systems. In order to ensure that the data is indeed a reflection of the interactions in the system, control measures using the same drugs and the model protein bovine serum albumin were also performed. In this case the heats are much higher, being so clear that the heats measured in these systems are not artifacts but the result of the interaction between the drug and fibrinogen. Analyzing data, it could be concluded that binding reaction is the driven force and some common patterns can be found in both systems. Initially, the interactions are intense and tend to decrease quickly to reach saturation. Saturation occurs at ratio values of 6 and 1.5 for acebutolol and propranolol, respectively. From the saturation points the graphs tend asymptotically to null interaction values. With regard to the kinetic evolution of the fibrinogen/drug complex, the equilibrium is reached after 20 and 90 minutes for propranolol and acebutolol respectively (obtained from calorimetric raw data). The best fit to the experimental data corresponds to the one-site binding model. In this sense, experimental results agree with the computational ones that also predicted one binding site. The obtained thermodynamic parameters accompanying the drug-fibrinogen interactions showed a negative enthalpy and entropy changes with values of $\Delta\mathrm{H} = -5.02\,\mathrm{cal/mol}$, $\Delta\mathrm{S} = -1.50\,\mathrm{cal/(mol\,^{\circ}C)}$ for propranolol and $\Delta\mathrm{H} = -4.48\,\mathrm{kcal/mol}$, $\Delta\mathrm{S} = -1.40\,\mathrm{cal/(mol\,^{\circ}C)}$ for acebutolol. Thus, the free energy of binding results $\Delta\mathrm{G} = -4.54\,\mathrm{kcal/mol}$ and $\Delta\mathrm{G} = -3.72\,\mathrm{kcal/mol}$ for propranolol and acebutolol, respectively. Although the results are in the same order of magnitude, there are some differences between the free energies obtained by both methods. However, it makes sense to think that the origin of such differences comes from the errors and limitations inherent in each method. ITC values are limited by the experimental procedure (number of injections, baseline uncertainty, environmental

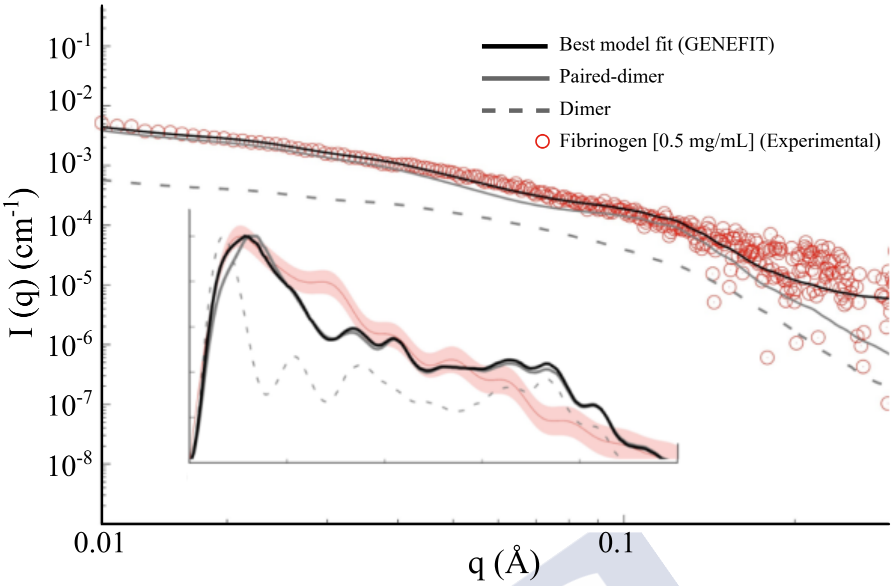

Figure 3.3: Experimental SAXS data (open circles) from 0.5 mg/mL fibrinogen dispersed in buffer solution at pH 8.5 at 23 °C. Solid black line represents the best fit to the experimental data revealing that the experimental curve can be well represented by the scattering of 63(2) % of the paired-dimer (solid grey line) and 37(2) % of the dimer (dashed grey line). The *p(r)* functions calculated by the GIFT software (model-free) for the paired dimer (solid grey line), dimer (dashed grey line) and experimental data for the fibrinogen solution (shaded red line) are in the inset. The maxima of the *p(r)* functions are normalized to 1 for comparison purposes. Furthermore, the *p(r)* function calculated by taking into account the percentage of each protein species is also showed.

perturbations, etc). In particular, in these systems, the low heat signals obtained were also a problem. Regarding the computational approach, there are also many challenges to solve: high quality of receptor structure (fibrinogen E-region), the protonation state of the ligand and binding-site residues, structures defined by crystallographic analysis, interactions not well-described by force fields [12]. Despite all this, the information is not contradictory and is complemented by offering a wide and clear vision of the binding process. Finally, the differences in free energy values of both beta-blockers are based on the overall structure of the aryl moiety. Aryloxypropranolamine beta-blockers differ in their liophilicity; highly lipophilicity (least polar functionality, propranolol) and intermediate lipophilicity (most polar functionality, acebutolol). Amide carbonyls are less reactive, susceptible to hydrolysis, because the nitrogen atom can provide greater resonance stabilisation to the carbonyl group through electron donation [13].

Again, SAXS patterns can be used to get information on the conformational and structural changes that drug adsorption might induce on fibrinogen. To characterize the conformation and the oligomeric state of the fibrinogen in solution, the SAXS

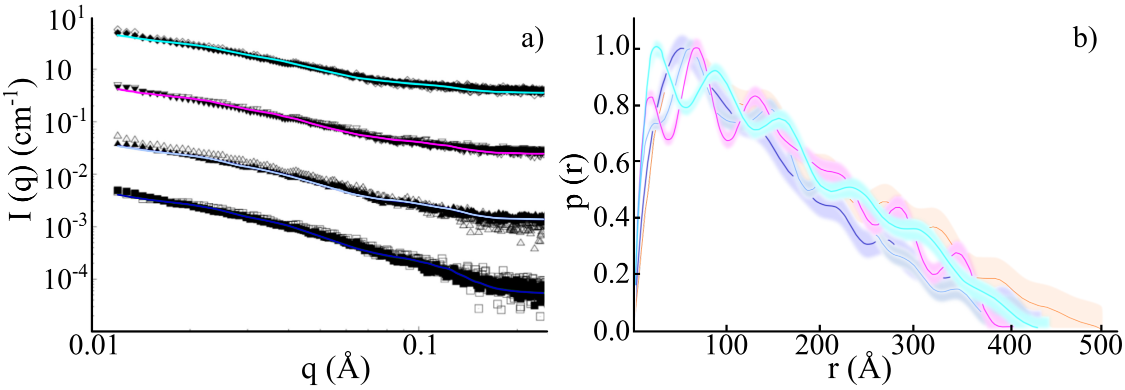

Figure 3.4: a) Experimental SAXS data from 0.5 mg/mL fibrinogen in the presence of acebutolol (solid symbols), and the expected data as a sum of scatterings from fibrinogen and acebutolol independently (empty symmbols), from bottom to top: 20 (squares), 30 (triangles), 68 (inverted triangles and 98 mM (diamonds) of acebutolol. The solid black line represents the best fit to the experimental curves. b) *p(r)* functions obtained from the scattering curves by the model-free analsis (GIFT software). Colors code: 0 mM (light red), 20 mM (dark blue), 30 mM (blue), 68 mM (magenta) and 98 mM (cyan) of acebutolol-containing fibrinogen solution.

curve from the protein at 0.5 mg/mL at room temperature (23 °C) displayed in Figure 3.3 was analyzed using the form factors, *P(q)*, of the crystalline structures of the paired-dimer and the fibrinogen dimer (PDB 3GHG).

The parameters obtained from the best fit to the drug-free fibrinogen scattering data pointed out the coexistence of 63(2)% of the paired-dimers and 37(2)% of the dimers in buffer solution at pH 8.5. Further, the *p(r)* function calculated by taking into account the percentage of each protein species (dashed line – Figure 3.3) is in a good agreement to the *p(r)* function obtained by the model-free analysis through GIFT software. Of note, it is possible to observe that *p(r)* is typical of long scatters (the longest dimension is quite larger than its cross-section dimension) and the maximum distances (D_{max} – where the *p(r)* goes to 0) for the the crystals structures are in good agreement to the maximum distances measured directly from the structures by using the Pymol Software [14], i.e. 490 and 460 Å, for the paired-dimer and fibrinogen dimer, respectively.

In the following, the impact of different concentrations of acebutolol and propranolol on the fibrinogen was also investigated by inspecting the coexistence of the two fibrinogen species found in betablockers-free solution.

Prior to the analysis of the experimental SAXS curves of the protein in the presence of each drug, the scattering data of both drugs dispersed in buffer solution was analyzed. In the case of acebutolol, a background-like scattering was detected up to 98 mM, even though this concentration is in the range of the cmc.

Table 3.2: Percentage of each crystal structure in solution obtained from the best fit to the experimental SAXS data from fibrinogen dispersed in buffer solutions containing different concentrations of acebutolol

Acebutolol (mM)	0	20	30	68	98
Paired-dimer (%)	63(2)	61(2)	65(2)	58(2)	61(2)
Dimer (%)	37(2)	39(2)	35(2)	42(2)	39(2)

Concerning the influence of the acebutolol on the fibrinogen structure, Figure 3.4 shows the SAXS curves from fibrinogen dispersed in buffer solution containing 20, 30, 68 or 98 mM acebutolol (solid symbols, from bottom to top). For comparison purposes, the expected data considering the scaterring from fibrinogen and the background produced by acebutolol can be considered as independent scatters and the sum is represented by the empty symbols. In other words, the expect data should be simply a sum from fibrinogen and acebutolol scatterings in due proportions.

As one can observe from Figure 3.4a, the experimental and the expected data as a sum of fibrinogen and acebutolol scattering for all drug concentrations are quite similar. Such finding suggests that the drug binding to the two fibrinogen paired-dimer and dimer species does not promote a conformational change or the changes induced by the acebutolol are subtle and cannot be detected by SAXS. Moreover, the corresponding *p(r)* functions displayed in the Figure 3.4b resemble that of drug-free fibrinogen solution (light red, Fig. 3.4b). Thus, the fitting of the experimental data allows retrieving the fibrinogen population coexisting in solution containing increasing acebutolol:fibrinogen molar ratio. Table 3.2 shows the results. Therefore, from SAXS results it is possible to infer that the acebutolol up to 98 mM (near cmc) does not lead to any alterations in the balance of the coexistence between the paired-dimers and the fibrinoger dimers in solution, without any indicative of protein conformational change.

Regarding to propranolol influence on fibringen structure, the scattering curves from the drug at different concentrations were measured and accounted for. The concentrations of 30, 60 and 100 mM of propranolol do not present a significant scattering pattern, suggesting the presence of monomers in solution. However, the SAXS curve from 130 mM of propranolol shows a different pattern that indicates the presence of micelles in solution as expected since the cmc is around 124 mM [15].

About the effect of the propranolol in the scattering curves of the fibrinogen, Figure 3.5 shows the SAXS curves of the fibrinogen in the presence of 30 (A), 60 (B), 100 (C) and 130 mM (D) of the drug (solid squares) in comparison to the expected data as a sum (empty squares) of fibrinogen scatters (empty red

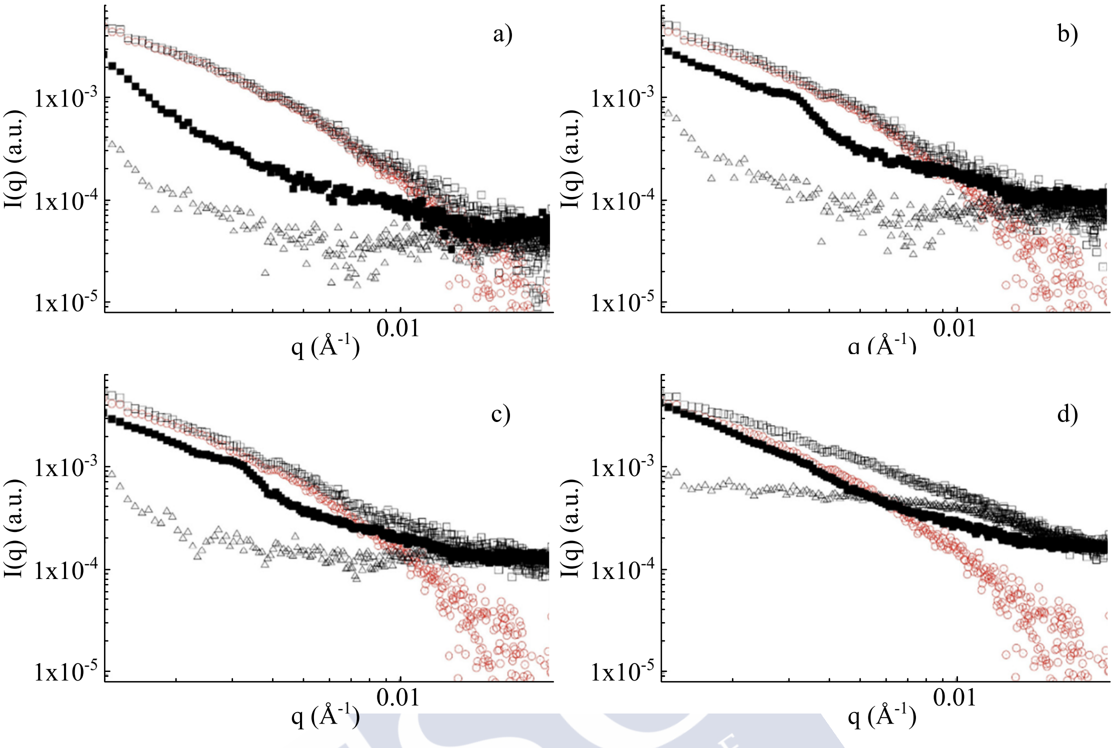

Figure 3.5: Experimental data from 0.5 mg/mL of fibrinogen in the presence of propanolol (solid squares), and the expected data as a sum of scatterings (empty squares) from fibrinogen (empty red circles) and propanolol (empty triangles) independently, for: 30 (A), 60 (B), 100 (C) and 130 mM (D) of propanolol.

circles) and propanolol scattering (empty triangles). Strinkingly, in these cases, the experimental curves present remarkable differences in respect to the expected ones considering independent scatters from fibrinogen and propranolol molecules.

Therefore, although acebutolol and propanolol have similar binding energies to fibrinogen as revealed by ITC, propanolol affects the protein in a more significative way than acebutolol as revealed by SAXS. This is an important fact because the modifications in fibrinogen energy-landscapes results in local population changes of protein conformation which can affect all surrounding interactions of fibrinogen with other targets. At this stage, it is very difficult to go into details of fibrinogen conformational changes under propanolol influence from SAXS data. In parallel, zeta potential data also point out that propanolol acts to a larger extent to fibrinogen structure than does acebutolol.

3.3.2 Mechanisms of fibrinogen-benzothiazole drug interactions

Characteristic microcalorimetric titration profile for the binding of BTS with fibrinogen is shown in Figure 3.6. Each point corresponds to the heat involved in a

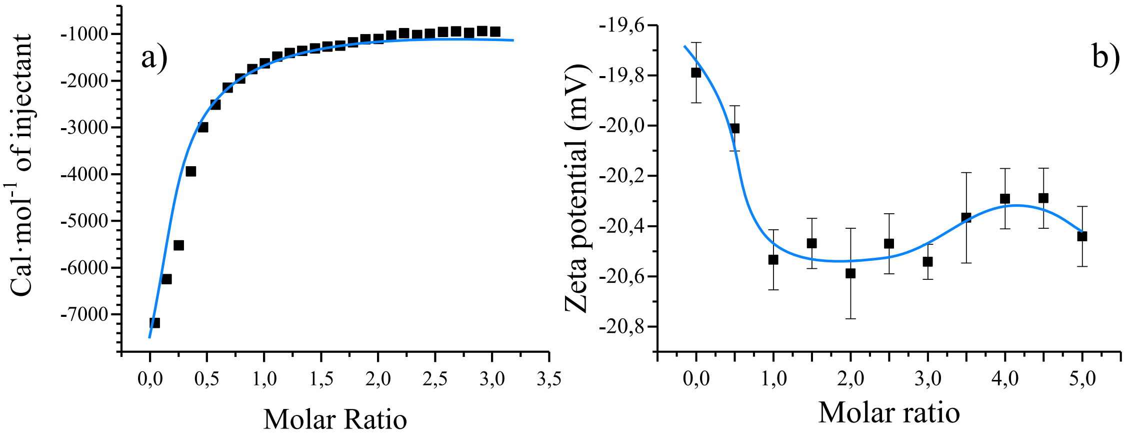

Figure 3.6: a) Enthalpy as a function of molar ratio (BTS/fibrinogen). Experiments were performed by adding 1 mM BTS solutions into 0.033 mM of fibrinogen. b) Zeta potential of the complex BTS-fibrinogen as a function of drug-fibrinogen molar ratio.

single injection of BTS (0.033 mM) into the fibrinogen solution (1 mM), corrected by subtracting the heats of mixing and dilutions. As represented, the aspect exposes an exothermic process with saturation occurring at BTS/fibrinogen molar ratio higher than 1. Regarding to the kinetic evolution of the fibrinogen/BTS complex, the equilibrium is reached after 150 minutes (obtained from calorimetric raw data). Experimental points were fitted according to the independent binding model, in order to obtain the relevant thermodynamic parameters of the binding process. Other binding models were also checked but large uncertainties were obtained for the associated binding parameters. Thus, the obtained values in this case were: 0.98, $6.27 \times 10^4\,\mathrm{M}^{-1}$, $-7.30\,\mathrm{kcal\,mol}^{-1}$ and $-2.55\,\mathrm{cal/(mol\,°C)}$ for stoichiometry, binding constant, enthalpy and entropy, respectively. The stoichiometry reveals that only one type of binding takes place. The binding constant suggests that BTS is a moderate binder. The obtained enthalpy and entropy values are negatives. Referring to enthalpy, this means that the binding is driven by the formation of non-covalent bonds (hydrogen bond, electrostatics, π-π interactions); in the case of negative entropy change, it reveals hydration and a loss of conformational freedom associated with the complex formation [16].

Figure 3.7a shows the influence of BTS on fluorescence emission spectra of fibrinogen. The absorption peak of the fibrinogen alone can be found at about 350 nm at the excitation wavelength of 280 nm. As the concentration of the drug was increased, the peaks suffered a gradual red shift to 353 nm. Simultaneously, the fluorescence emission intensity decreased regularly. From previous works, it is known that those changes in fluorescence are correlated with the number of cleaved disulfide bonds upon irradiation and the reduction of the disulfide bond makes the fluorescence intensity higher [17]. In this context, one may suggests that the interaction of the BTS with fibrinogen causes the raise in the polarity of its aromatic residues, being more hydrophilic with the increase of the drug in the solution which resulted in the decrease and red shift of the fluorescence [18]. Since the interaction has to occur in the pocket at E-domain, two residues, [Tyr]18:S and [Tyr]18:P were identified as the main responsible for this shift due to changes in their environment.

Considering that the binding sites were independent and non-interactive, the Stern-Volmer equation was used to study and analyze further the intrinsic quenching fluorescence [19].

$$\frac{F_0}{F} = 1 + K_{sv}\,[BTS] \tag{3.1}$$

F_0 and F are the fluorescence emission intensities with the presence or absence of BTS; [BTS] is the drug concentration and K_{sv} the Stern-Volmer quenching constant.

According to this equation, the linearity of F_0/F versus the drug concentration, [BTS], reveals the quenching type. In this system, linear correlations were probed at different temperatures with different values of R coefficient, meaning that all Trp(s) present in the macromolecule differ slightly in accessibility [20]. The slope of the straight line gives the K_{sv} value of $(6.56 \pm 0.30) \times 10^3\,\mathrm{L\,mol^{-1}}$ at 298.15 K. Since the fluorescence lifetime of the fibrinogen in water is $1 \times 10^{-8}\,\mathrm{s^{-1}}$, and considering that: $K_q = \frac{K_{sv}}{\tau_0}$, the K_q can be obtained and has a value of $6.56 \times 10^{11}\,\mathrm{L\,M^{-1}\,s^{-1}}$. The maximal dynamic quenching constant of the studied biopolymer is $2.0 \times 10^{10}\,\mathrm{L\,M^{-1}\,s^{-1}}$ [21]. So, in this case, it is safe to assure that the quenching of fibrinogen by BTS is not initiated by dynamic collision but from the formation of a complex [22].

Fluorescent measurements are also a great tool to get quantitative information about the static quenching process [23]. The binding constant (K_a) and the number of binding sites (n) can be obtained using the following equation:

$$\log\frac{(F_0 - F)}{F} = logK_a + n \cdot log\,[BTS] \tag{3.2}$$

Accordingly, the slope of the linear plot of log $[(F_0 - F)/F]$ as a function of $\log[BTS]$ gives the stoichiometry of binding [24], while the binding constant can be obtained from the intercept. In the present case, the values of n and K_a are 0.86 ± 0.05 and $(1.76 \pm 0.25) \times 10^3\,\mathrm{M^{-1}}$, respectively. That means that fibrinogen interacted with BTS in one independent class of binding sites, forming a 1:1 complex.

As shown in Figure 3.7b, the great overlap between the absorbance spectrum of the complex and the normalized fluorescence spectrum, it can be presumed that

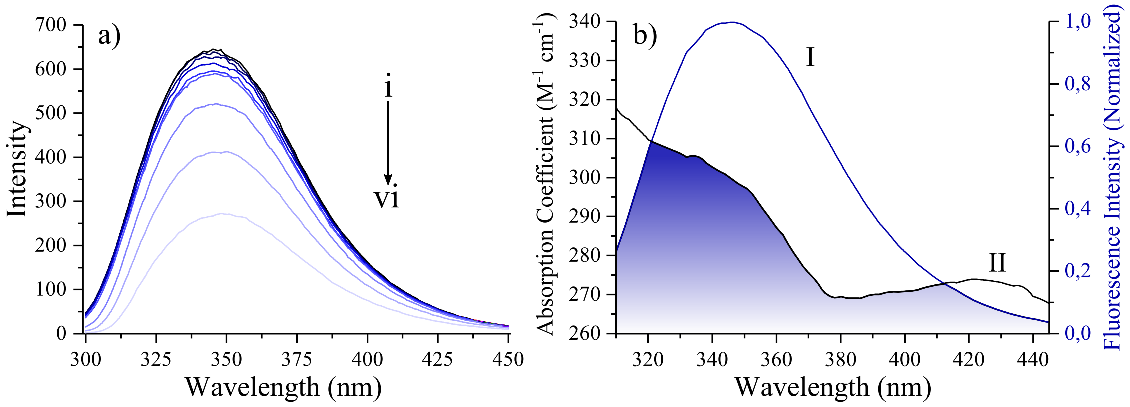

Figure 3.7: a) Fluorescence emission spectra of Fibrinogen in the absence and presence of different concentrations of the BTS drug. Fibrinogen concentration: (a-i) = 1 µM. BTS concentrations: (a-i) = (0, 1, 2, 4, 8, 10, 50, 100, 200 µM). b) Overlap of the normalized fluorescence spectrum of fibrinogen and the absorbance spectrum of the complex. [Fib]/[BTS] = 1.

the molecular details of the complex formed between the fibrinogen and the drug are obtained from non radiation energy transfer, as the fluorescence spectroscopy of the donor is not malformed. According to Förster theory of non-radiation energy transfer [25], the average spatial distance between the probed and excited transition dipoles can be estimated using the Förster-energy transfer rate equations [26]:

$$k_T\left(r\right) = \frac{Q_D \kappa^2}{\tau_D r^6}\left(\frac{9000 \ln 10}{128\ \pi^5 N n^4}\right)\int_0^{\infty} F_D\left(\lambda\right)\varepsilon_A\left(\lambda\right)\lambda^4 d\lambda \tag{3.3}$$

$$J\left(\lambda\right) = \frac{\int_0^{\infty} F_D\left(\lambda\right)\varepsilon_A\left(\lambda\right)\lambda^4 d\lambda}{\int_0^{\infty} F_D\left(\lambda\right) d\lambda} \tag{3.4}$$

$k_T\left(r\right)$ is the transfer rate for a donor and acceptor separated by a given distance, r [27]. Q_D is the quantum yield of the donor in the absence of acceptor; κ^2 is a factor that describes spatial orientation factor of the dipole, $J(\lambda)$ expresses the overlap integral between the fluorescence emission spectra of donor and the UV absorption spectra, $F(\lambda)$ is the fluorescence intensity of fluorescence donor when the wavelength is λ, $\varepsilon(\lambda)$ is the molar absorption coefficient of the acceptor at the wavelength of λ. (E) is the efficiency of energy transfer and is related to the fraction of photons absorbed by the donor and transmitted to the acceptor. Commonly, efficiency is obtained from the relative fluorescent intensity of the donor in the absence (F_D) and presence (F_{DA}) of the acceptor through the following equation:

$$E = 1 - \frac{F_{DA}}{F_D} = \frac{R_0^6}{R_0^6 + r^6} \tag{3.5}$$

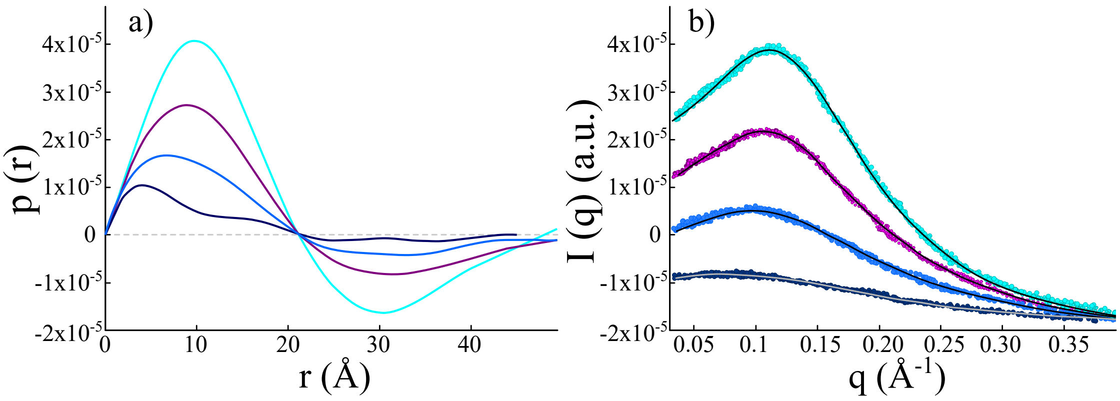

Figure 3.8: Pair distribution function calculated for the experimental SAXS curves for 70 (dark blue), 110 (blue), 150 (purple) and 180 mM (cyan) of BTS solution in the absence of fibrinogen. The experimental SAXS curves along with the corresponding *I(q)* from *p(r)* (solid lines) are presented in the inset. The *p(r)* functions were calculated by using GNOM software [30].

where R_0 is the critical distance when the transfer efficiency equals to 50 % $\left(R_0^6 = 8.79 \times 10^{-5}\,(\kappa^2 n^{-4} Q_D\ J\,(\lambda))\right)$. In the present work, n is given by the refractive index of water, 1.333; κ^2 is 2/3, and the Q_D is 0.15, consistent with the fluorescence quantum yield of tryptophan. Combining the above equations, the following values were determined: $J = 4.79 \times 10^{12}\,\mathrm{M^{-1}\,cm^{-1}\,nm^4}$, $E = 0.08$, $R_0 = 2.54\,\mathrm{nm}$, and $r = 2.29\,\mathrm{nm}$. As the distance between the donor and the acceptor is within 2-8 nm it is safe to assure that the energy transfer between fibrinogen and BTS is very probable and it demonstrates the presence of non radiation energy, meaning that the most excited elements could decay to the ground state [28, 29]. Once again, these results reinforce the hypotheses formulated in the computational section.

In order to evalute the impact of BTS in the fibrinogen conformation, the scattering of BTS-containing solution was first investigated at 70, 110, 150 and 180 mM. Figure 3.8 presents the pair distribution functions, *p(r)*, calculated for each experimental curve displayed in the inset.

As one can observe, the *p(r)* functions exhibit an oscilatory profile, typical of core-shell like aggregates with two regions of distinct electron densities in respect to that of the solution [31]. Such aggregates have maximum dimension around 50 Å. Of note, the core-shell like structure is not well formed at 70 mM BTS according to *p(r)* function, unlike the results obtained from BTS at concentrations greater than 110 mM. Therefore, it can be inferred that BTS molecules form pre-agregates at the lowest investigated concentration, evolving to core-shell like aggregates with drug concentration increase.

As previously suggested by NMR analysis of BTS aggregates between 50 mM and 290 mM, the shape and size of the small self-organized BTS are very similar

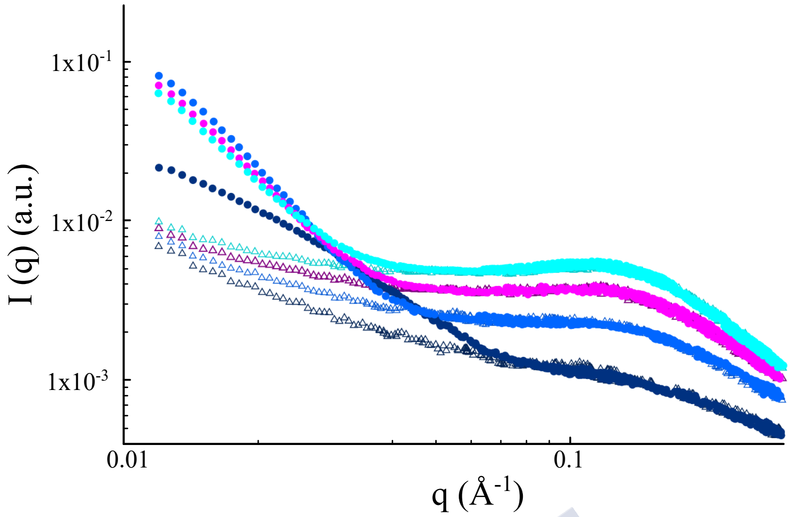

Figure 3.9: Experimental SAXS curves (solid symbols) for the fibrinogen (0.5 mg/mL) in the presence of 70 (dark blue), 110 (blue), 150 (purple) and 180 mM (cyan) of BTS. Expected SAXS curves (open triangles) by considering two independent scatters in solution: 0.5 mg/mL fibrinogen and BTS at 70 (dark blue), 110 (blue), 150 (purple) and 180 mM (cyan).

independently of the concentration [32] as observed here. Further, it was possible to suggest the presence of small BTS aggregates even at low concentrations (below cmc $\sim$ 170 mM).

Taken into account the SAXS curve for the drug-free fibrinogen solution at 0.5 mg/mL (data not shown), the result obtained is the same as already reported previously in this work: the protein coexists as 63 % of the paired-dimers and 37 % of the dimers.

After the evaluation of the BTS and fibrinogen pure solutions, the SAXS data obtained from fibrinogen mixed to BTS solutions at different concentrations is now presented. Figure 3.9 shows the SAXS results.

For the fibrinogen in the presence of 70 mM BTS, the experimental SAXS curve (dark blue circles) is consistent with the sum of the scattering of the protein and 70 mM BTS for q values higher than 0.07 Å^{-1}. A similar trend happens for the SAXS curves of fibrinogen in the presence of 110 (blue), 150 (purple) and 180 mM (cyan), in which the experimental curves are compatible with the sum of independent scatterings (triangles) for each case for q > 0.04 Å^{-1}. Such q range is related to the BTS self-assembled (Figure 3.8). Thus, it can be suggested the presence of BTS aggregates in the sample containing fibrinogen too. On the other hand, at low q range (related to the protein terciary and quaternary structure), the experimental curves are different from the ones obtained by the sum (open triangles) of protein and BTS in solution for all drug concentration. In particular, the experimental scattering intensities are higher than the hypothetical sum of individual scatterings. Such finding suggests the formation of fibrinogen oligomers complexed to BTS since I(0) is proportional to the molecular mass of the scattering complexes [33]. Of note, it was not possible to evaluate the complex molecular mass from *I(0)* value, as *I(0)* usually is determined as an extrapolation of Guinier's law for q $\rightarrow$ 0 [6]. However, the Guinier's q region restricted to $q_{max} \times Rg < 1.3$ (where Rg = radius of gyration) was not obeyed in these experiments (Figure 3.9).

It is also important to remark that a transition in the fibrinogen aggregation process must take place between 70 mM BTS and 110 mM BTS, due to the quite different scattering profiles at low q range exhibited from these two experiments. However, with the increase of drug concentration the SAXS curves are similar for $q < 0.03\,\text{Å}^{-1}$. This result suggests that similar protein–BTS complexes coexist with BTS aggregates in 110 mM to 180 mM BTS-containing solution.

3.3.3 Binding mechanisms of fibrinogen-penicillin β-lactam antibiotic drugs

Once again, to determine accurate thermodynamic parameters of Fib-cloxacillin and Fib-dicloxacillin interactions, ITC measurements were conducted. Representative calorimetric titration profiles of the binding of both systems are show in Figure 3.10. As before, similarly to the previous cases, the titration results in negative heat deflection indicating that the reactions are exothermic in nature, which shows that binding is the predominant reaction, while conformational changes of fibrinogen, if any, barely leave an energy footprint (endothermal peaks) in the graphs. In this case it is highly relevant to comment on the different patterns followed by both binding processes. While cloxacillin shows a more abrupt process characterized by sigmoid-type function, the interaction of dicloxacillin with fibrinogen has a smoother profile represented by a decreasing exponential function. That is, while dicloxacillin interacts immediately and constantly with fibrinogen, cloxacillin needs a threshold concentration, above which the interaction is more favorable, and the protein is saturated earlier. Previous molecular docking studies indicated that once adsorbed, both β-lactam antibiotics adopt a different crystallographic binding conformation (i.e., cloxacillin more extended and dicloxacillin more closed). This ability to adapt to the pocket makes the adsorption process of dicloxacillin easier and more gradual. While in the case of the cloxacillin, its greater rigidity makes the pocket needs to adapt previously, with a more abrupt interaction later.

Fits of a standard non-linear least-squares regression binding model to the ITC measurements revealed that both penicillin β-lactam antibiotics bind to fibrinogen

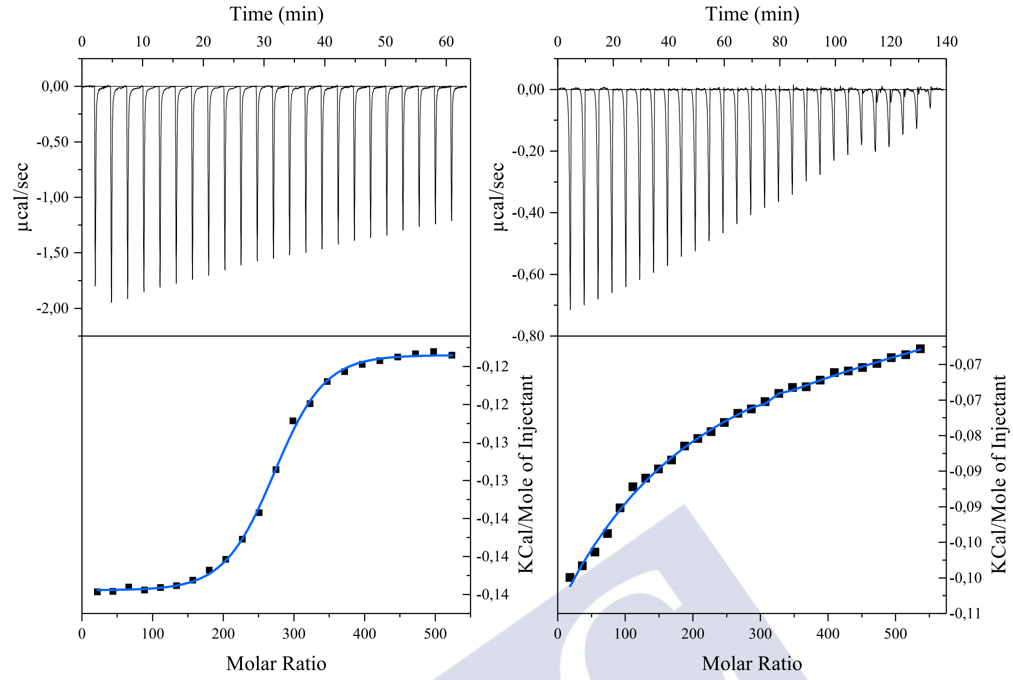

Figure 3.10: ITC profiles for the binding of cloxacillin (a) and dicloxacillin (b) to fibrinogen.

Table 3.3: Thermodynamic parameters: binding constant (k), enthalpy (ΔH), entropy ($T\Delta S$) and free energy (ΔG) of binding of cloxacillin and dicloxacillin with fibrinogen according to a single binding site.

	$\boldsymbol{K}$ (M^{-1})	$\boldsymbol{\Delta H}$ (kcal·mol^{-1})	$\boldsymbol{T\Delta S}$ (kcal·mol^{-1})	$\boldsymbol{\Delta G}$ (kcal·mol^{-1})
Cloxacillin	6.9×10^3	-13.1	-4.5	-8.6
Dicloxacillin	6.5×10^3	-11.4	-5.3	-6.1

binding site at a 1:1 molar ratio, corroborating the computational results that predicted a single adsorption in the E-region binding site (main pocket 1). The corresponding thermodynamic parameters are listed in Table 3.3. The values of the binding constants are on the order of 10^3, suggesting that both β-lactam antibiotics are moderate binders. As summarized in the Table 3.3, thermodynamic parameters show a common pattern for the two evaluated penicillins, although they differ in their numerical values. Hydrogen bond, hydrophobic force, and electrostatic interaction, mainly contributed to the interactions between proteins and ligands. The fraction of non-ionized molecules of cloxacillin and dicloxacillin at pH 8.5, is around 5.5 % [34]. This means that some of the molecules are neutral, which prevents their electrostatic interaction with fibrinogen, resulting in a decrease in the value of enthalpy. For this reason, within the interactions that have been pointed out as responsible for the bonding process, hydrogen bonds are the dominant. These experimental facts reinforce the theoretical results that underline the important role of Gauss 2 forces in these interactions. In the case of negative entropy change, it reveals hydration and a loss of conformational freedom associated to the complex formation. Bearing in mind the similarities between binding and β-lactam antibiotic self-aggregation process [35], it can be concluded that desolvation is not present in this binding process. So, changes in translational and rotational degrees of freedom, alterations of the conformational flexibility of the binding partners, and reorganization of solvation shells upon binding become the main contributions to entropy change. Comparison of values for cloxacillin and dicloxacillin shows that the former drug has more negative enthalpy values and higher affinity constant. These differences arise from the existence of a second Cl atom in a meta position to the first in dicloxacillin if compared to cloxacillin. Halogen bonding has been widely documented in supramolecular systems; specially for its possible role in the stabilization of small ligand–protein complexes. It is also shown that aromatic halogen substitutions affect the optimal geometries and σ-hole characteristics of the formed complexes; often, as the result of secondary interactions [36, 37]. Memic et al. [38] found that binding thermodynamic parameters are perturbed when the position and identity of halogen substituents are varied. In fact, they obtained an increase in entropy and a decrease in enthalpy when interactions take place in a single binding pocket. In view of the experimental results, associated to the effect of the second Cl atom, the conformational changes that cloxacillin undergoes must also be considered as the origin of the differences in thermodynamic magnitudes.

In order to complete the energy landscape of these binding processes, DSC measurements were also performed. The DSC thermograms from pure fibrinogen and in the penicillin β-lactam antibiotics containing solutions are shown in Figure 3.11. The three endothermic peaks at 52, 76 and 93 °C have been attributed to the denaturation of the D, C and E domains of the fibrinogen molecule. Due to the intensity and relevance of the two largest peaks, the focus will be put only on them, calling peak 1 and peak 3 respectively. The thermodynamic characteristics of the thermal denaturation, melting temperatures (T_m, temperatures at which a maximum occurred in the endothermic peaks), calorimetric enthalpy (ΔH), van't Hoff enthalpy (ΔH_v), and cooperativity (n, the ratio of calorimetric enthalpy to van't Hoff enthalpy) were obtained for all the systems studied and listed in Table 3.4.

As it can be seen in Figure 3.11, as the concentration of the β-lactam antibiotics increases, the area of the endothermic peaks decreases, and they move towards lower temperatures or disappear as in the case of the second peak with respect to

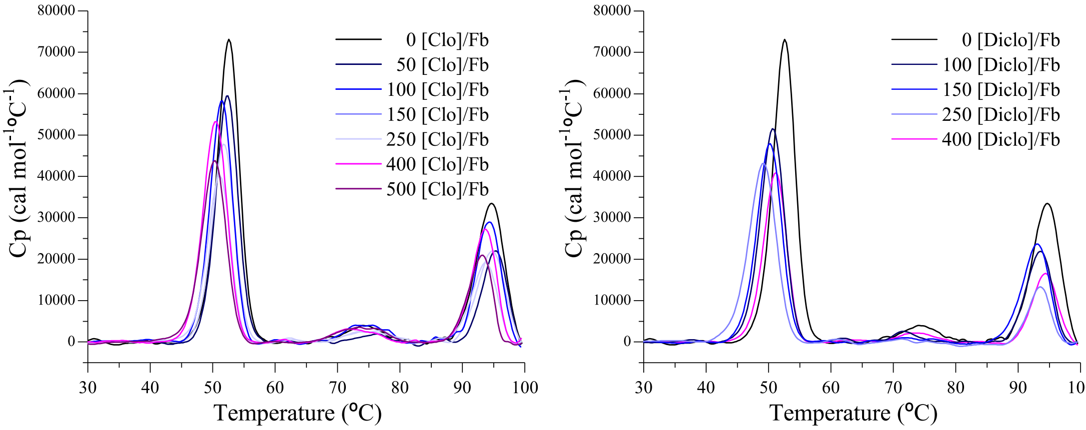

Figure 3.11: DSC thermograms of fibrinogen in the presence of different concentrations of cloxacillin (a) and dicloxacillin (b).

pure fibrinogen. Significant changes in peak characteristics are induced by higher penicillin concentrations. This first set of measurements points out a decrease in stability of fibrinogen with increase in the β-lactam antibiotic concentration. Such a fact has been previously observed in other systems [39]. Concerning cooperativity, n (the ratio between van't Hoff and calorimetric enthalpies) when $n > 1$, the unfolding is not a two-state process but involves unfolded intermediates states. In the case of $n < 1$, this implies that the overall protein is not correctly folded. For all studied systems, the values obtained are slightly higher than the unit. Theoretically, this implies that one or more intermediate states are populated in the temperature change [8], however, as it was demonstrated previously, in fibrinogen solutions coexists two species, the monomeric molecule (63 %) and a dimeric complex (37 %).

Data shown in the Table 3.4 can yield useful information about the effect of these drugs on fibrinogen stability. If the enthalpy values obtained for both peaks are extrapolated to null β-lactam antibiotic values, the values obtained are: 291 and 143 kcal mol^{-1} for cloxacillin and 273 and 149 kcal mol^{-1} for dicloxacillin (first and third peak, respectively). The total enthalpy of unfolding will be the sum of both peaks. These extrapolated values could be interpreted as the protein denaturation enthalpy in the absence of drug. However, their values are different. Even assuming the thermal unfolding of fibrinogen in the presence of the drugs in two stages: first, drugs are bound to the native protein (binding energy from ITC) and then, the complex is denatured (DSC). The sum of both enthalpies, binding and extrapolated, do not match the value of denaturation of pure fibrinogen. These energy differences, 92 and 201 kcal mol^{-1} for cloxacillin and dicloxacillin, serve to quantify the effect that β-lactam antibiotics have on the stability of the fibrinogen molecule. Thus,

Table 3.4: Thermodynamic parameters obtained from DSC thermograms in the presence of cloxacillin and dicloxacillin

Cloxacillin							
ratio	T_{m1} (ºC)	T_{m3} (ºC)	ΔH_1 (cal mol^{-1})	ΔH_3 (cal mol^{-1})	ΔH_{v1} (cal mol^{-1})	ΔH_{v3} (cal mol^{-1})	n
0	52.4	94.4	3.34×10^5	1.92×10^5	1.88×10^5	2.28×10^5	1.78
50	52.2	95.1	2.72×10^5	1.47×10^5	1.87×10^5	2.27×10^5	1.44
100	51.7	94.5	2.69×10^5	1.35×10^5	1.84×10^5	2.24×10^5	1.20
150	51.3	94.1	2.65×10^5	1.23×10^5	1.85×10^5	2.20×10^5	1.45
250	51.0	93.4	2.22×10^5	1.10×10^5	1.82×10^5	2.11×10^5	1.03
400	50.3	93.4	1.88×10^5	1.01×10^5	1.71×10^5	2.01×10^5	1.55
500	50.1	92.8	1.67×10^5	0.99×10^5	1.67×10^5	1.95×10^5	1.00

Dicloxacillin							
ratio	T_{m1} (ºC)	T_{m3} (ºC)	ΔH_1 (cal mol^{-1})	ΔH_3 (cal mol^{-1})	ΔH_{v1} (cal mol^{-1})	ΔH_{v3} (cal mol^{-1})	n
0	52.4	94.4	3.34×10^5	1.92×10^5	1.87×10^5	2.54×10^5	1.78
100	51.0	94.2	2.54×10^5	1.29×10^5	1.81×10^5	2.18×10^5	1.06
150	50.5	93.3	2.44×10^5	1.15×10^5	1.72×10^5	2.10×10^5	1.42
250	50.1	92.8	2.41×10^5	0.84×10^5	1.66×10^5	1.99×10^5	1.46
400	49.0	93.3	1.93×10^5	0.60×10^5	1.49×10^5	1.98×10^5	1.61

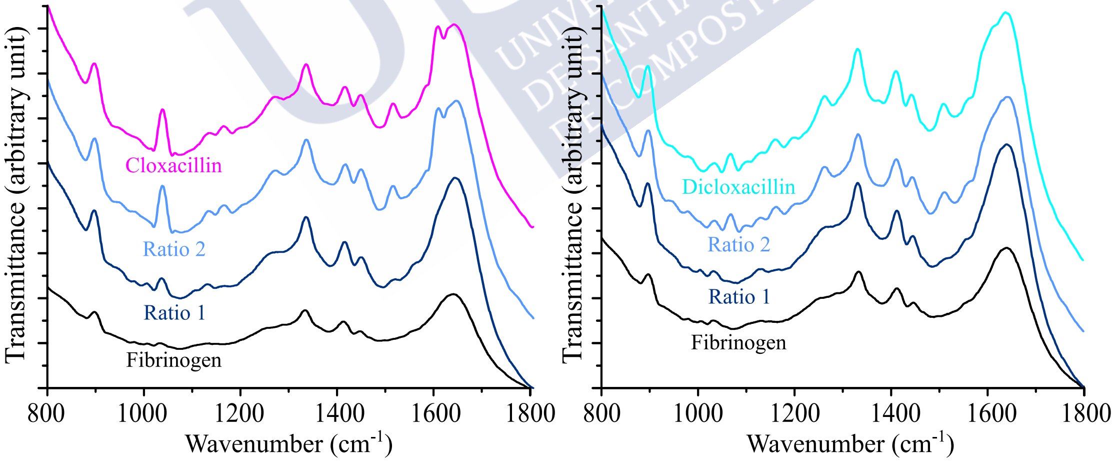

Figure 3.12: Raman spectra of fibrinogen in presence of different penicillin ratios, 100 and 400 for samples 1 and 2 respectively.

dicloxacillin has a much more destabilizing effect on the fibrinogen molecule. These quantitative measurements are perfectly consistent with LPRS maps that suggested that the process of penicillin β-lactam antibiotic adsorption involved allosteric signal perturbations in the fibrinogen molecule that were transmitted through the N and Q chains, these perturbations being greater for dicloxacillin.

Finally, In order to understand how drugs affect the secondary structure of the protein, Raman spectra for fibrinogen in the presence of both penicillins at two different ratios was analyzed (Figure 3.12). The amide I band, between 1600 $\mathrm{cm^{-1}}$ and 1700 $\mathrm{cm^{-1}}$ is stronger than the Amide III band and is composed by the contributions of α-helix at 1655 $\mathrm{cm^{-1}}$, β-sheet at 1670 $\mathrm{cm^{-1}}$ and random coil at 1680 $\mathrm{cm^{-1}}$. Other small peaks are attributed to: C_α-C stretch (895 $\mathrm{cm^{-1}}$), PHE and TRP (1035 $\mathrm{cm^{-1}}$), Amide II (1328 $\mathrm{cm^{-1}}$), N-H bend indole ring (1414 $\mathrm{cm^{-1}}$), C-H_2 and CH_3 deformation (1448 $\mathrm{cm^{-1}}$) and TRP (1554 $\mathrm{cm^{-1}}$) [40]. In the presence of penicillin, amide I band shifts to lower wavenumbers. These changes in the position (and intensity) of the amide I band indicate that under drug interactions, fibrinogen experiments changes in the secondary structure mainly in the α-helix content and with more intensity in the case of cloxacillin. Considering that the modifications in the spectrum occur mainly in this area, it can be postulated that the adsorption occurs in lateral chains of amino acids (N and Q chains, as suggested by the LPRS maps), altering the contents of secondary structure but with few changes in the general structure of the protein.

Bibliography

[1] T. Peters Jr, *2 - The Albumin Molecule: Its Structure and Chemical Properties*, pp. 9–II. San Diego: Academic Press, 1995.

[2] M. V. Petoukhov and D. I. Svergun, "Global rigid body modeling of macromolecular complexes against small-angle scattering data," *Biophys J*, vol. 89, no. 2, pp. 1237–50, 2005.

[3] K. Baler, O. A. Martin, M. A. Carignano, G. A. Ameer, J. A. Vila, and I. Szleifer, "Electrostatic unfolding and interactions of albumin driven by ph changes: a molecular dynamics study," *Journal of Physical Chemistry B*, vol. 118, no. 4, pp. 921–30, 2014.

[4] D. W. Bolen and I. V. Baskakov, "The osmophobic effect: natural selection of a thermodynamic force in protein folding," *Journal of Molecular Biology*, vol. 310, no. 5, pp. 955–63, 2001.

[5] L. R. S. Barbosa, F. Spinozzi, P. Mariani, and R. Itri, *Small-Angle X-Ray Scattering Applied to Proteins in Solution*, pp. 49–72. John Wiley & Sons, Inc., 2013.

[6] A. Guinier and G. Fourmet, *Small angle scattering of X-rays.* New York: Wiley, 1955.

[7] Y. Q. Yeh, K. F. Liao, O. Shih, Y. J. Shiu, W. R. Wu, C. J. Su, P. C. Lin, and U. S. Jeng, "Probing the acid-induced packing structure changes of the molten globule domains of a protein near equilibrium unfolding," *Journal of Physical Chemistry Letters*, vol. 8, no. 2, pp. 470–477, 2017.

[8] A. Cooper, M. A. Nutley, and A. Wadood, "Differential scanning microcalorimetry," *Protein-ligand interactions: Hydrodynamics and calorimetry*, pp. 287–318, 2000.

[9] N. Baker, D. Sept, S. Joseph, M. Holst, and J. McCammon, "Electrostatics of nanosystems: Application to microtubules and the ribosome," *Proceedings of the National Academy of Sciences*, vol. 98, pp. 10037–10041, 08 2001.

[10] D. E. Otzen, P. Sehgal, and P. Westh, "Alpha-lactalbumin is unfolded by all classes of surfactants but by different mechanisms," *J Colloid Interface Sci*, vol. 329, no. 2, pp. 273–83, 2009.

[11] R. Friedman and A. Caflisch, "Surfactant effects on amyloid aggregation kinetics," *Journal of Molecular Biology*, vol. 414, no. 2, pp. 303–312, 2011.

[12] D. L. Mobley and M. K. Gilson, "Predicting binding free energies: Frontiers and benchmarks," *Annual review of biophysics*, vol. 46, pp. 531–558, 2017.

[13] J. M. Ruso, N. Deo, and P. Somasundaran, "Complexation between dodecyl sulfate surfactant and zein protein in solution," *Langmuir*, vol. 20, no. 21, pp. 8988–8991, 2004.

[14] Schrödinger, LLC, "The PyMOL molecular graphics system, version 1.8." November 2015.

[15] J. M. Ruso, D. Attwood, C. Rey, P. Taboada, V. Mosquera, and F. Sarmiento, "Light scattering and nmr studies of the self-association of the amphiphilic molecule propranolol hydrochloride in aqueous electrolyte solutions," *The Journal of Physical Chemistry B*, vol. 103, no. 34, pp. 7092–7096, 1999.

[16] R. Huang and B. L. T. Lau, "Biomolecule–nanoparticle interactions: Elucidation of the thermodynamics by isothermal titration calorimetry," *Biochimica et Biophysica Acta (BBA) - General Subjects*, vol. 1860, no. 5, pp. 945–956, 2016.

[17] J. J. Ewbank and T. E. Creighton, “Structural characterization of the disulfide folding intermediates of bovine alpha-lactalbumin.,” *Biochemistry*, vol. 32 14, pp. 3694–707, 1993.

[18] G. Rabbani, M. H. Baig, E. J. Lee, W. Cho, J. Ma, and I. Choi, “Biophysical study on the interaction between eperisone hydrochloride and human serum albumin using spectroscopic, calorimetric, and molecular docking analyses,” *Molecular pharmaceutics*, vol. 14, 04 2017.

[19] G. Rabbani, M. H. Baig, A. T. Jan, E. J. Lee, M. Khan, M. Zaman, A.-E. Farouk, R. H. Khan, and I. Choi, “Binding of erucic acid with human serum albumin using a spectroscopic and molecular docking study,” *International Journal of Biological Macromolecules*, vol. 105, 04 2017.

[20] M. M. Lopez and D. Kosk-Kosicka, “Spectroscopic analysis of halothane binding to the plasma membrane ca 2+-atpase,” *Biophysical journal*, vol. 74, no. 2, pp. 974–980, 1998.

[21] G. Rabbani, E. Ahmad, N. Zaidi, and R. H. Khan, “ph-dependent conformational transitions in conalbumin (ovotransferrin), a metalloproteinase from hen egg white,” *Cell biochemistry and biophysics*, vol. 61, pp. 551–60, 07 2011.

[22] A. Sułkowska, “Interaction of drugs with bovine and human serum albumin,” *Journal of Molecular Structure*, vol. 614, no. 1–3, pp. 227–232, 2002.

[23] G. Rabbani, E. J. Lee, K. Ahmad, M. H. Baig, and I. Choi, “Binding of tolperisone hydrochloride with human serum albumin: Effects on the conformation, thermodynamics, and activity of hsa,” *Molecular Pharmaceutics*, vol. 15, 02 2018.

[24] G. Rabbani, M. Khan, A. Ahmad, M. Maskat, and R. H. Khan, “Effect of copper oxide nanoparticles on the conformation and activity of β-galactosidase,” *Colloids and surfaces. B, Biointerfaces*, vol. 123, 09 2014.

[25] B. Wieb van der Meer, D. M. van der Meer, and S. S. Vogel, *FRET - Förster Resonance Energy Transfer: From Theory to Applications*, pp. 63–104. 2013.

[26] S. Jang, M. D. Newton, and R. J. Silbey, “Multichromophoric forster resonance energy transfer,” *Phys Rev Lett*, vol. 92, no. 21, p. 218301, 2004.

[27] J. Lakowicz, *Principles of Fluorescence Spectroscopy.* Kluwer Academic / Plenum, 1999.

[28] Y.-Z. Zhang, N.-X. Zhang, A.-Q. Ren, J. Zhang, J. Dai, and Y. Liu, “Spectroscopic studies on the interaction of 2,4-dichlorophenol with bovine serum albumin,” *Journal of Solution Chemistry*, vol. 39, no. 4, pp. 495–510, 2010.

[29] J. Zhang, X.-F. Dai, and J.-Y. Huang, “Resveratrol binding to fibrinogen and its biological implication,” *Food Biophysics*, vol. 7, no. 1, pp. 35–42, 2012.

[30] D. Franke, M. V. Petoukhov, P. V. Konarev, A. Panjkovich, A. Tuukkanen, H. D. T. Mertens, A. G. Kikhney, N. R. Hajizadeh, J. M. Franklin, C. M. Jeffries, and D. I. Svergun, “Atsas 2.8: a comprehensive data analysis suite for small-angle scattering from macromolecular solutions,” *Journal of Applied Crystallography*, vol. 50, pp. 1212–1225, 2017.

[31] R. Itri and L. Q. Amaral, “Distance distribution function of sodium dodecyl-sulfate micelles by x-ray-scattering,” *Journal of Physical Chemistry*, vol. 95, no. 1, pp. 423–427, 1991.

[32] N. Hassan, M. P. Garate, T. Sandoval, L. Espinoza, A. Pineiro, and J. M. Ruso, “On the self-assembly of a highly selective benzothiazole-based tim inhibitor in aqueous solution,” *Langmuir*, vol. 26, no. 22, pp. 16681–9, 2010.

[33] G. Scanavachi, Y. R. Espinosa, J. S. Yoneda, R. Rial, J. M. Ruso, and R. Itri, “Aggregation features of partially unfolded bovine serum albumin modulated by hydrogenated and fluorinated surfactants: Molecular dynamics insights and experimental approaches,” *Journal of Colloid and Interface Science*, vol. 572, pp. 9–21, 2020.

[34] P. M. Keen, “The binding of penicillins to bovine serum albumin,” *Biochemical Pharmacology*, vol. 15, no. 4, pp. 447–463, 1966.

[35] P. Taboada, D. Attwood, J. M. Ruso, F. Sarmiento, and V. Mosquera, “Self-association of amphiphilic penicillins in aqueous electrolyte solution: a light-scattering and nmr study,” *Langmuir*, vol. 15, no. 6, pp. 2022–2028, 1999.

[36] K. E. Riley, J. S. Murray, J. Fanfrlík, J. Řezáč, R. J. Solá, M. C. Concha, F. M. Ramos, and P. Politzer, “Halogen bond tunability i: the effects of aromatic fluorine substitution on the strengths of halogen-bonding interactions involving chlorine, bromine, and iodine,” *Journal of Molecular Modeling*, vol. 17, no. 12, pp. 3309–3318, 2011.

[37] K. E. Riley and P. Hobza, “Strength and character of halogen bonds in protein–ligand complexes,” *Crystal Growth & Design*, vol. 11, no. 10, pp. 4272–4278, 2011.

[38] A. Memic and M. R. Spaller, “How do halogen substituents contribute to protein-binding interactions? a thermodynamic study of peptide ligands with diverse aryl halides,” *ChemBioChem*, vol. 9, no. 17, pp. 2793–2795, 2008.

[39] N. Hassan, L. R. Barbosa, R. Itri, and J. M. Ruso, “Fibrinogen stability under surfactant interaction,” *Journal of Colloid and Interface Science*, vol. 362, no. 1, pp. 118–126, 2011.

[40] J. Marx, G. Hudry-Clergeon, F. Capet-Antonini, and L. Bernard, “Laser raman spectroscopy study of bovine fibrinogen and fibrin,” *Biochim Biophys Acta*, vol. 578, no. 1, pp. 107–15, 1979.

4

Bioceramic Precursor. Size-controllable HA synthesis

Contents

4.1 Overview 91
4.2 Experimental procedure 92
    4.2.1 Microchip fabrication 92
    4.2.2 Numerical solution applied to fluid flow 93
4.3 Discussion 93
    4.3.1 Previously established synthesis method 93
    4.3.2 Microreactor-based synthesis method 95

4.1 Overview

In this chapter, the synthesis and characterization of HA nanorods are described. Additionally, a new route for the synthesis, using a microfluidic device, is reported. The process is carried out by continuous laminar flow through the system. The obtained nanoparticles have shown the same properties (composition, length, orientation, roughness) than those produced by conventional methods, however, this innovative device can afford to fine tune the structure via simple engineering, i.e., produce nanoparticles of different size only by varying the flow velocity. In addition to the efficiency and novelty of this system, the optimization of personnel costs makes it highly economical and profitable.

4.2 Experimental procedure

4.2.1 Microchip fabrication

The microfluidic device was created according to the soft lithograph technique, which is well characterized in the bibliography [1]. A detailed description of the process is outlined below:

4.2.1.1 Step 1: Substrate preparation

To obtain the mould, the substrate used was a 2 inch diameter silicon wafer that was exposed to oxygen plasma at 500 W for 8 min (Harrick Plasma) to clean and dehydrate the surface. An epoxy resin (GM1070 SU-8, Gersteltec Sarl) was spin coated onto the substrate at 500 rpm for 75 s which produced a final channel height of 136 µm. A pre-bake process was done in a hot plate with a temperature of 60 °C for 8 min and 90 °C for 15 min, to evaporate the solvent of the resin.

4.2.1.2 Step 2: Exposure

Once the Photoresist resin was solid onto the substrate, a previously fabricated transparency mask was aligned with the obtained substrate and they were exposed at 365 nm UV lamp for 4 min. In this step, it is critical to initiate the crosslinking of the resin. A postbake process (65 °C for 5 min and 95 °C for 10 min) was done to accelerate the crosslinking of the exposed areas, making them insoluble in the developer.

4.2.1.3 Step 3: Development

The obtained substrate was submerged in propylene glycol monomethyl ether acetate (PGMEA) for 10 min to remove the non-exposed resin of the substrate. After that, the reaction was stopped rinsing it with isopropanol. A final bake was done for 2 h at 135 °C to improve the robustness of the mould and eliminate small cracks on the surface of the resin.

4.2.1.4 Step 4: Final assembly

Microchannels were fabricated in polydimethylsiloxane (PDMS, Sylgard 184, Dow Corning). PDMS: curing agent (10 : 1) was used. PDMS was poured onto the obtained mould and it was left in an oven for 45 min at a constant temperature of 60 °C until completely cured. Microscope slides (to support the microchip) were covered with PDMS and cured as well. The microchip and the microscope slides were assembled after plasma cleaned (Harrick Plasma) for 1 min to activate their surfaces. Once in contact, the microchip and slide became irreversible bonded. The width and height of the channels are 513 µm and 136 µm, respectively. To increase the residence time of the reagents in the microchannel, the exit channel can be bent in several curves.

4.2.2 Description of the numerical solution applied to fluid flow

To characterize the profile of the velocity field inside the microfluidic device, a 3D model of the system was built. From this model, a mesh file was created, and finite volume method was applied to solve the associated differential equations that govern the fluid phase (see Chapter 1), in this case, the incompressible Navier-Stokes equations:

$$\nabla \cdot u = 0 \tag{4.1}$$

$$\rho u \cdot \nabla u = -\nabla P + \rho g + \nabla \cdot \left(\mu \left(\nabla u + \nabla u^T\right)\right) \tag{4.2}$$

being u, μ, P, ρ and g the velocity, viscosity, pressure, density and gravity, respectively. The Computational Fluid Dynamics (CFD) method was utilized to predict the velocity profiles of flow through the channels, contours of shear stress over the chorion surface and concentration of over time (SolidWorks 2011, Dassault Systemes SolidWorks Corp, Concord, MA, USA). Besides, the reagents were incompressible liquids, the mixture was suitable for simulating and the phases were treated as interpenetrating continua. Finally, the boundary condition for the inner walls of the channels was assumed as no-slip condition.

4.3 Discussion

4.3.1 Previously established synthesis method

Hydroxyapatite nanorods were synthesized following a previously developed protocol by D'Elia et al. [2] which, in turn, is based on a modification of the method proposed by Liu et al. [3]. First, 35 ml of a 3.13 mM CTAB aqueous solution were mixed with 2 mL of PPG and stirred at 500 rpm for 10 min. Second, 20 mL of 2 M sodium nitrite aqueous solution and 0.22 g calcium chloride were incorporated in sequence. Finally, 20 mL of 0.14 M of Na_3PO_4 aqueous solution was added to the above mixed solution drop by drop at room temperature under magnetic stirring at 500 rpm.

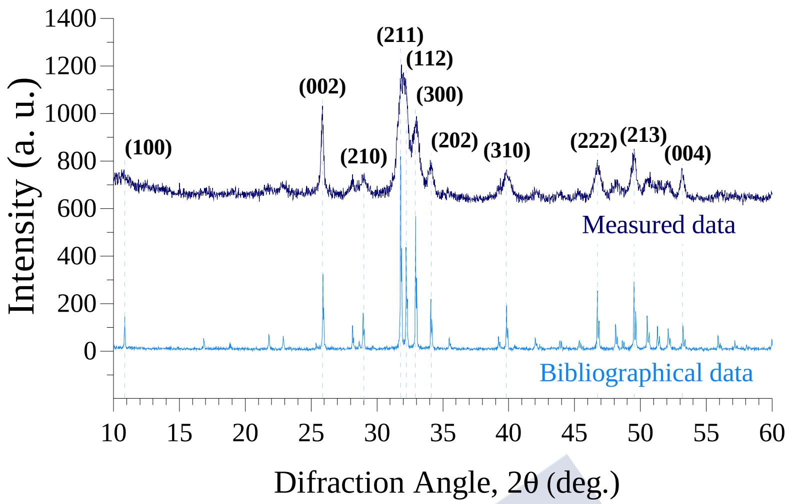

Figure 4.1: X-ray diffraction pattern of hydroxyapatite

After the integration of all reactants, the solution was magnetically stirred for 1 h and left for 24 h in an autoclave at 100 °C. The obtained materials were filtered, washed with triple-distilled water to remove impurities, and then dried at 50 °C for 24 h. Finally, the resulting material was ignited in the muffle furnace for 3 h at about 400 °C. As a result, bone-like HA nanorods were obtained.

4.3.1.1 Physical characterization

The XRD patterns of the obtained HA samples are shown in Figure 4.1. It can be observed that they are in good agreement with the bibliographical data; JCPDS file no. 9-432. All peaks were indexed as hexagonal $Ca_5(PO_4)_3(OH)$ and no characteristic peaks of impurities, such as $NaNO_2$ and Na_3PO_4, were found. The XRD peaks had markedly broadening effect. This fact suggests that HA structures were nanosized [3]. The fraction of crystalline phase was calculated by using the equation $X_c = 1 - \left(V_{112/300}/I_{300}\right)$ where I_{300} is the intensity of (300) diffraction peaks and $V_{112/300}$ is the intensity of the hollow between (112) and (300) diffraction peaks of HA. The value obtained was 0.76. This number indicates poor crystallinity, which is in very good agreement with biogenic hydroxyapatite. X_c is a very relevant magnitude, it has been demonstrated that as the crystallinity decreases the material is more resorbable and consequently more beneficial for early bone growth [4].

The general morphology of the samples was revealed by SEM images, top images of Figure 4.2. Samples have a uniform and homogeneous structure. At higher magnifications, it can be observed that the surface has a desultory network pattern composed by highly agglomerated nanoparticles. The clumped nanoparticles seem

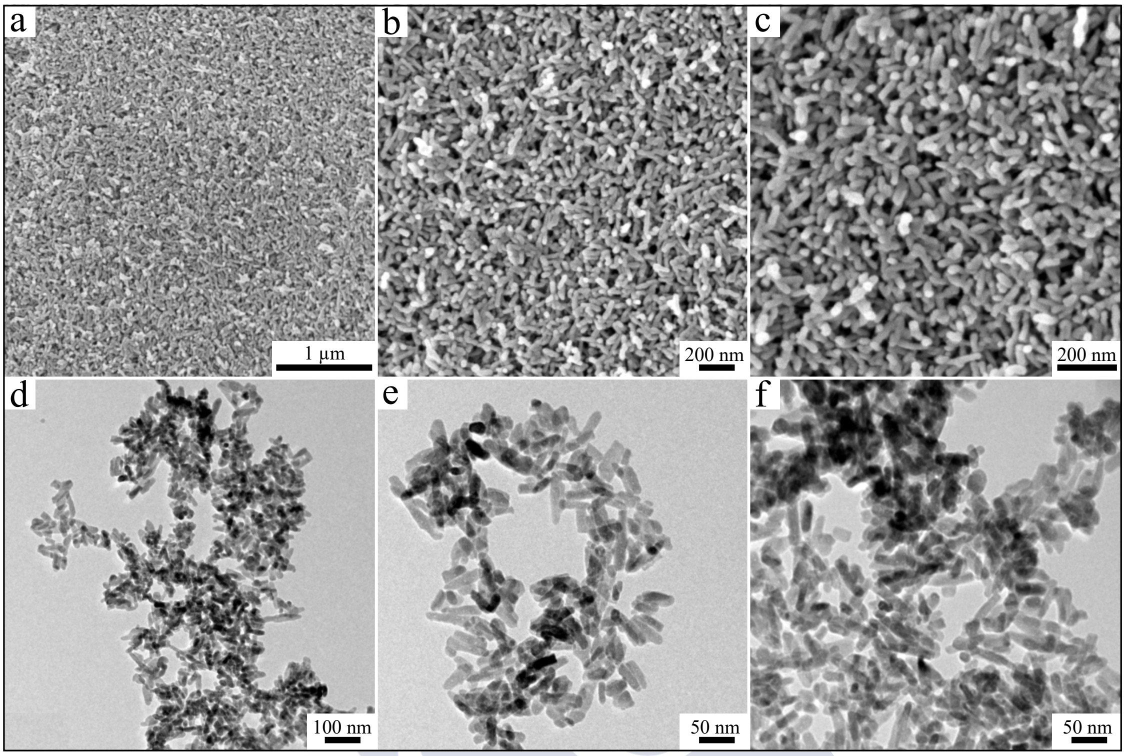

Figure 4.2: a-c): SEM images of HA samples at different scales. d-e): TEM images of the same HA samples.

to have a very similar size. This fact reveals that Ostwald ripening does not play an important role in this process and making this morphology thermodynamically stable. Quantitative examination of SEM images shown that the size distribution of the nanoparticles is unimodal with an average length of 96 nm, as it was expected from the bibliographical source, resulting in a very large aspect ratio [3].

For the complete characterization of the nanoparticles, these were diluted in butanol and sonicated. After that, samples obtained were observed by TEM (Figure 4.2 bottom). These images clearly show that the material is composed by uniform rod-like particles with similar aspect ratios (length/diameter). The size distribution histogram displays mean values of 9 ± 2 nm in diameter and 50 ± 7 nm in length.

4.3.2 Microreactor-based synthesis method

One of the key points in microfluidics is the choice of the geometry. In this case the option chosen was the one known as Y-junction structure. Microfluidic devices are very simple systems that can be associated in multiple ways, offering infinite possibilities. The main characteristics are the length, width and height of the channel. In most cases the width of the channel is greater than the height, with rates ranging from 1 to 1000 [5]. This condition, allows to operate with low Reynolds

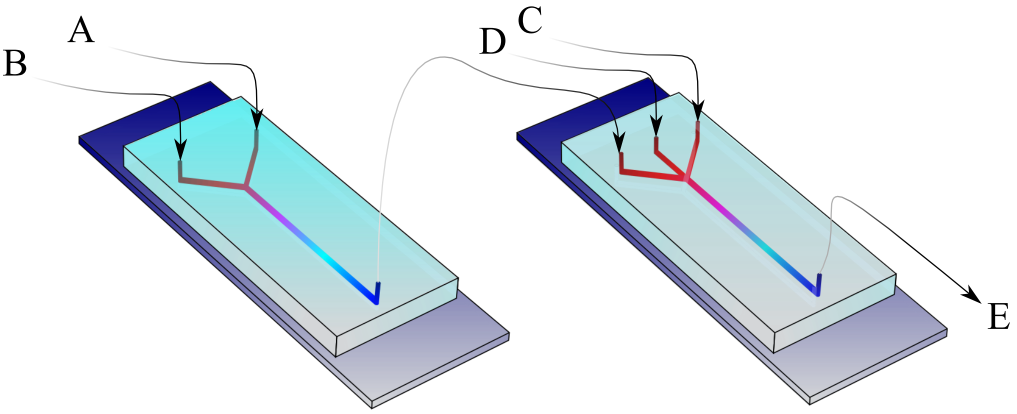

Figure 4.3: Diagram of the microfluidic system.

numbers. In this particular case, the microfluidic system consists of two Y-junction structures connected in series (Fig 4.3) with two and three inlets, respectively.

A solution of mixed micelles of CTAB/PPG was pumped into the microfluidic system to synthesize the material. The addition of the surfactant reduces the size of the nanoparticles as the CTAB and PPG form a micellar solution with a high degree of ionization. Above the critical micellar concentration, CTAB turns spherical micelles into rod-like shapes, constituting a template which gives HA its final elongated shape. CTAB interacts with the PO_4^{-3} groups [6] and then Ca^{2+} ions are attracted, thus initiating the nucleation of HA crystals at the interface of the micelles. Figure 4.4 shows a schematic representation of the complete microreactor-based system operation.

The inputs are connected to two syringe pumps (KDS 101 Legacy Syringe Pump) that allow to vary the speed of the injected flow. Specifically, the solutions needed for the reaction are loaded into the device as follows: B ($CaCl_2$), C ($NaNO_2$ + CTAB + PPG) and the micellar solution is pumped through inlet D (Na_3PO_4). The initial concentration in the syringe pumps were: 1.56 M $CaCl_2$, 1.56 M $NaNO_2$, 0.004 M CTAB, 0.18 PPG and 0.12 M Na_3PO_4. The A inlet is used to inject air, which produces a flow that drags the hydroxyapatite that can be formed through the channels, avoinding obstruction. In the second microreactor is where the mentioned ionic interactions and the final reaction take place.

4.3.2.1 Flow simulations

The pressure-driven speed profile ensures that the flow of the current lines is completely laminar and does not produce a convective mixture between them. The profile of this interface depends on a number of factors such as time, channel

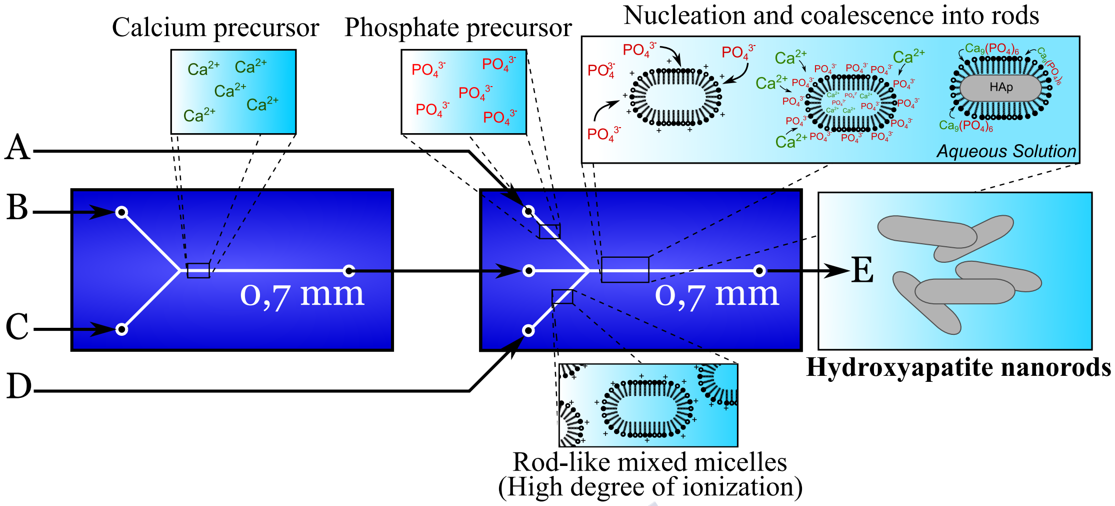

Figure 4.4: Schematic representation of the microfluidic system operation.

length, flow velocity, or the molecules diffusion coefficients. In order to ensure that effectively the flow is laminar throughout the device, computational fluid dynamics were performed as previously described. Considering the fluid model predictions, Figure 4.5a depicts the obtained velocity field gradients through the entire geometry for the highest input velocity in this study (3 ml/h). Figures 4.5b and 4.5c show the velocity cross-section for the first and second Y-junctions, respectively. Special emphasis was put on the most conflicting areas of this type of devices: pipe bends and junctions. For this reason, the turbulence field gradient into the channels was also obtained (not shown), from where it is possible to observe that, although they exist, do not disturb the velocity profile. Consequently, these results show that laminar flow is present through all the geometry and velocities, which is expected considering the Reynolds numbers. Thus, in this case, the only means by which molecules in different fluxes can be mixed is by molecular diffusion through the interface between the fluid streams.

4.3.2.2 Physical characterization

Once the device has been assembled and the microfluidic system prepared, different tests varying the flow rate of the pumps were performed: 3 ml/h, 2 ml/h and 1.5 ml/h. First of all, emphasis should be put on the fact that all the obtained materials by the different methods are effectively hydroxyapatite regardless of the flow rate. This result was probed by X-ray spectroscopy (Figure 4.6) by comparing the spectra with the reference patterns of the ICDD database, number JCPDS 9-432.

The topography of the surface of the materials is a very determinant factor since it influences processes of biological importance such as biomineralization,

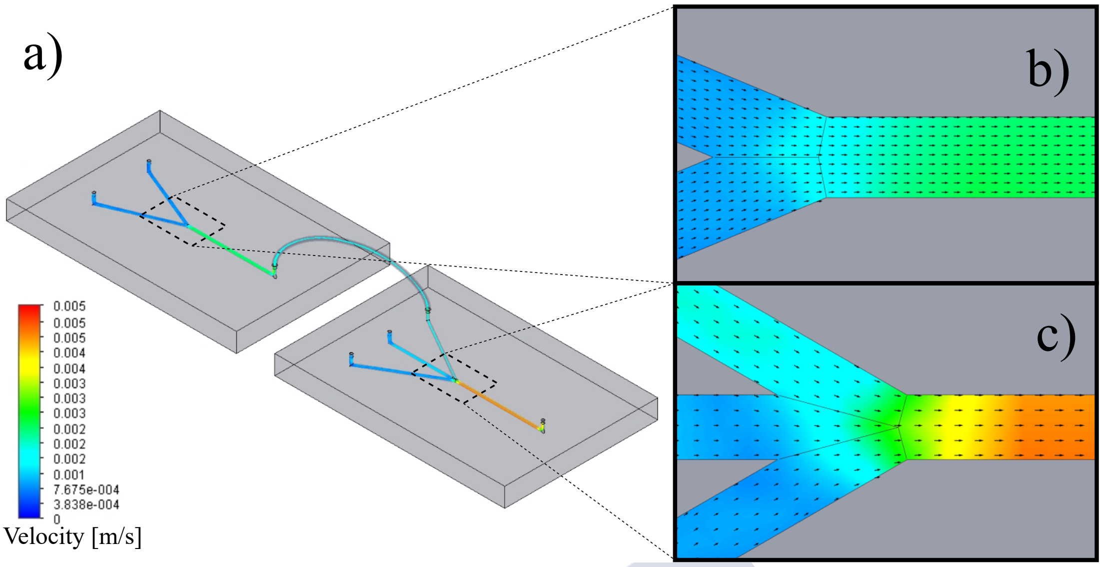

Figure 4.5: Velocity countour planes for the whole device (a), first Y-junction (b) and second Y-junction (c).

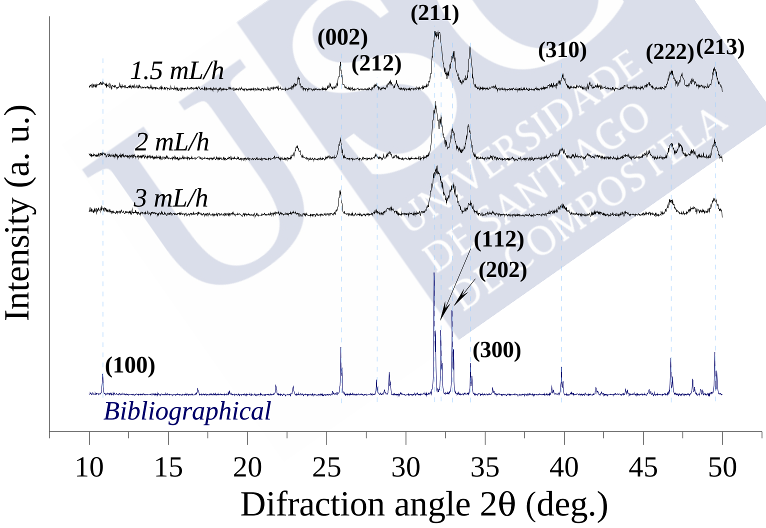

Figure 4.6: X-ray diffraction pattern of HA nanorods obtained at different flow rates.

cellular adhesion and protein adsorption. Morphological characterization of the samples was also performed by scanning electron microscopy (SEM). To compare the surface properties of the materials, their profiles should be analized. For this purpose, the surface topography of each material was obtained from the digital processing of SEM microphotographs (1 µm). Images are represented in 3D surface plots [7, 8], Figure 4.7a. A micron roughness pattern which is dominant throught the hole surface was found. This roughness arises from a grainlike structure with voids extended over the entire material in a fairly uniform distribution. The color

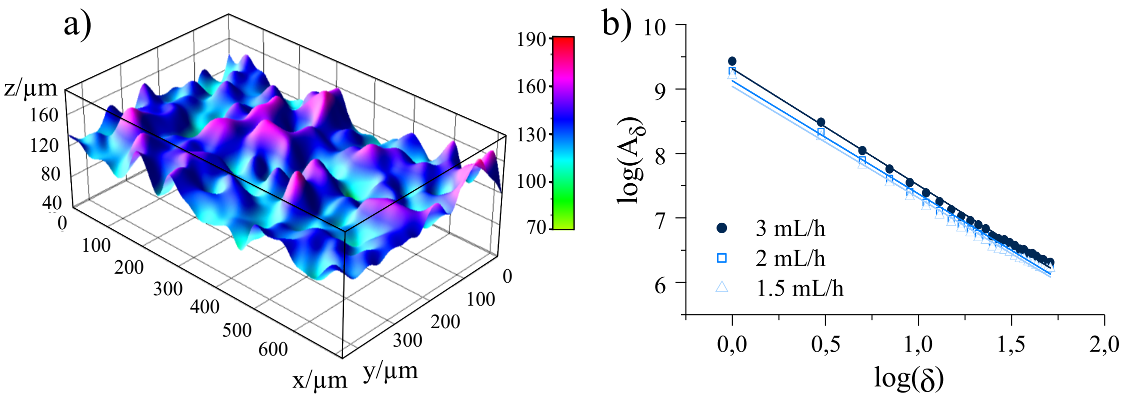

Figure 4.7: a) 3D surface plot from 1.5 flow rate sample x and y axes are in micrometers. b) Plots of the logarithm of the area of the framewoks against the logarithm of their side: 1.5 ml/h (△), 2 ml/h (□); 3 ml/h (●).

scale suggests a smooth surface without spiky ridges. Similar patterns were found for the rest of the samples created at different flows.

In addition to qualitative descriptions, mathematical formalisms have been developed that allow to characterize quantitatively the complexity of the surfaces in the microscale. Biological surfaces differs for the engineered ones, specially in their hierarchical character. Consequently, classical parameters could not be completely suitable. Basically, the topographic characterization of the surfaces are organized into two large groups: statistical descriptions and fractals. There is no unanimous agreement on which approximation is better [9]. Among these formalisms, basic ideas of fractal geometry methods have shown their usefulness in the analysis and description of surfaces that were formed as a results of deposition processes [10]. For example, the higher the fractal dimension, the lower the surface organization. Anselme et al. [11] demonstrated the role of the fractal dimension of surfaces on cell proliferation and cell adhesion. Such correlation arise from the contact area between the cell and the surface: the more the fractal dimension increased, the more the contact area between the cell and substrate decreased [11]. In this sense, Xie et al. [12] developed a method of fractal measurement, the projective covering method, to measure directly the fractal dimension of the surface. Here, the fractal dimension of the surface is calculated form the slope of the logaritm of the rough surfaces, A_δ, obtained at different scales, δ. Figure 4.7b shows the plots obtained for the three materials. Fractal dimensions were calculated from the slope of the linear fits. Final values were: 1.73, 1.75 and 1.80 for the surfaces obtained at 1.5, 2 and 3 ml/h, respectively. These results indicate, theoretically, that the surface geometry of these materials tends to be smoother when the flow is lower.

Table 4.1: Values of roughness, skewness and kurtosis of the differente surfaces obtianen from SEM images.

Sample	R_a	R_{sk}	R_{ku}
1.5 ml/h	111.36	1.31	1.92
2 ml/h	122.96	1.19	1.54
3 ml/h	128.00	1.19	1.54

To continue with the surface analysis, the focus should be put on the most known and used parameters; the statistical ones. The randomness of rough surfaces have already been emphasized. Therefore, these surfaces must be described with parameters which take into account different length scales. The arithmetic average surface roughness, R_a, is the average absolute deviation from the mean level. It is a quite simple measure, easy to obtain and define, for comparing different surfaces. Skewness (third moment of surface height about the mean), R_{sk}, is a measure of the symmetry of the surface about the mean value. Positive values indicate a surface with high peaks, while negative values indicate the presence of deep valleys. Kurtosis (fourth moment), R_{ku}, is related to the tailedness of the surfaces: surfaces with a great number of jagged peaks and narrow valley enhibit positive values; meanwhile, negative values are associated to wide valleys and eroded peaks [13]. It is often used interchangeably the term "excess kurtosis", which is defined as kurtosis minus 3. In this sense, the reference value is 3, so if $R_{ku} > 3$ the surface profile is rugged, while for $R_{ku} < 3$ the profile is considered smooth.

The microscale topography of the samples under study was measured quantitatively and the obtained data are presented in Table 4.1. Judging by the calculated values, low-flow surfaces are apparently smoother than high-flow surfaces. In particular, the average roughness of 1.5 ml/h sample and the other two differ appreciably. Data reveal that the surface obtained at the lowest flow can be distinguished in terms of the micro-roughness. It should be noted that R_{ku} of the 1.5 surfaces was notably different from that of the other surfaces, whereas minor differences were found for R_{sk} values among the three surfaces. The larger values of R_{ku} for the 1.5 surface is a signature of a more pronounced peakedness of the surface profile. Larger values of R_{sk} also suggest the occurrence of somewhat higher peaks for this surface. Consequently, the analysis presented here highlights the importance of a proper flow selection to achieve the desired surface profile. The surfaces obtained with low flow exhibited a rich picture of pronounced peaks at micro-scale with a more uniform peak pattern than in the case of higher flows.

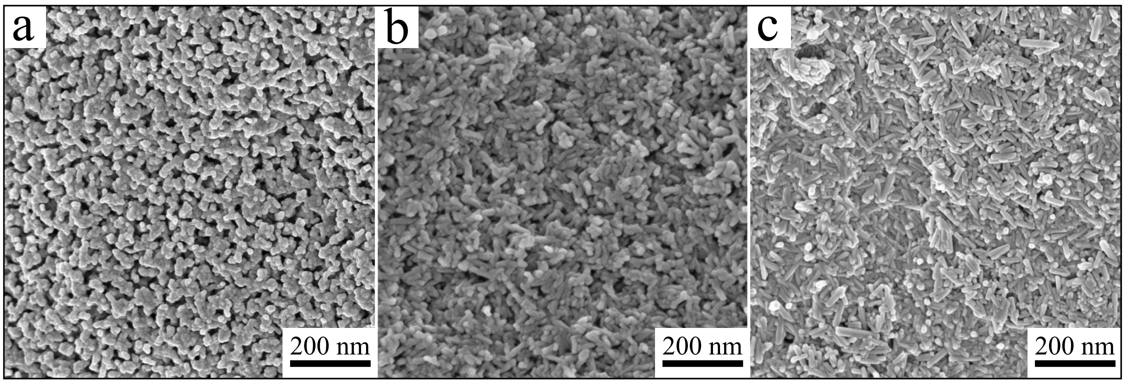

Figure 4.8: SEM microphotographs of samples obtained at different flow rates. a) 3 ml/h, b) 2 ml/h and c) 1.5 ml/h.

Table 4.2: Mean values and standard deviation of lengths of HA nanoparticles obtained at different flows.

Sample	**Length**
3 ml/h	99 ± 16
2 ml/h	113 ± 16
1.5 ml/h	221 ± 28

4.3.2.3 Size control and distribution

Figure 4.8 shows some representative images of the samples obtained for the three cases of study. In all the samples it can be clearly observed that the materials are composed by an agglomeration of nanoparticles disposed in a quite random way. This conformation is the typically found when these materials are synthesized with the traditional method. The images were analyzed to determine the distribution of sizes using the digital image routine described in Chapter 1. The histograms created for length and orientation values are shown in Figure 4.9. The three bottom pictures show that the length histograms actually present similar symmetrical curves corresponding to a normal distribution with equal mean and medium values. The average and standard deviation values can be consulted in Table 4.2. Regarding the orientation of the nanoparticles (top row), it is clear that the aggregation process is completely random without any privileged orientation. This fact can have its origin in a regular provision of ions through all the surface of the nanoparticles. It is safe to conclude then, that this process of synthesis, in addition to homogenize the shapes and sizes, also guarantees a homogeneous distribution of the electric charge.

Finally, in view of the results, it is now quite clear that the microfluidic system presented here not only allows to automate and save time in the process of the synthesis of hydroxyapatite nanoparticles, but also facilitates the production of

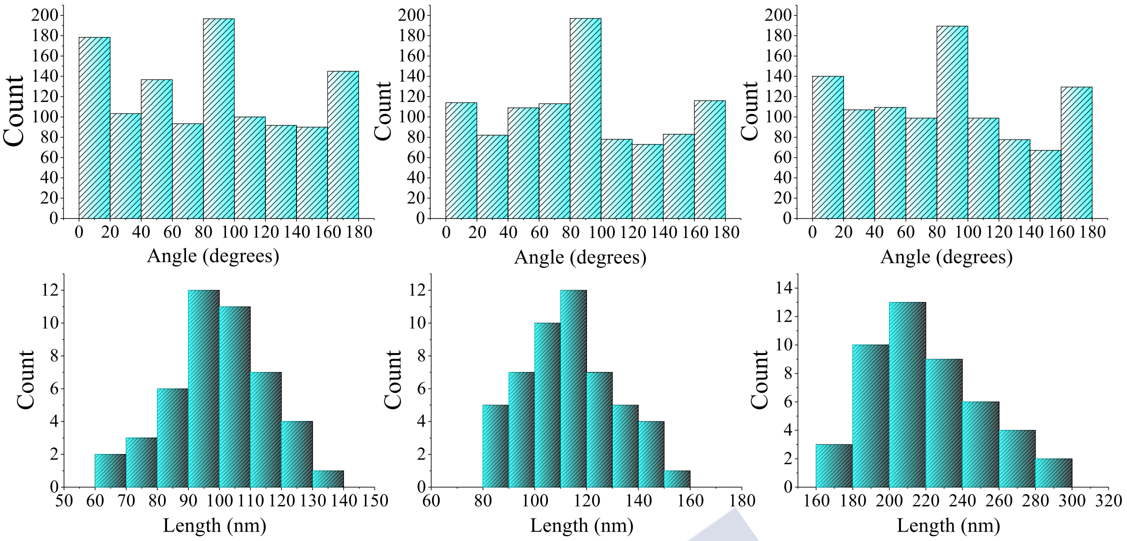

Figure 4.9: Angle (a-c) and length (d-f) distributions obtained from different SEM images of the samples obtained at different flows: 3 ml/h (left), 2 ml/h (center) and 1.5 ml/h (right).

particles with different sizes and consequential surface morphologies by using a single device, simply varying the rates and velocities of the inlet flows.

Bibliography

[1] J. C. McDonald and G. M. Whitesides, “Poly(dimethylsiloxane) as a material for fabricating microfluidic devices,” *Accounts of Chemical Research*, vol. 35, no. 7, pp. 491–499, 2002.

[2] N. L. D’Elía, A. N. Gravina, J. M. Ruso, J. A. Laiuppa, G. E. Santillán, and P. V. Messina, “Manipulating the bioactivity of hydroxyapatite nano-rods structured networks: Effects on mineral coating morphology and growth kinetic,” *Biochimica et Biophysica Acta (BBA) - General Subjects*, vol. 1830, no. 11, pp. 5014–5026, 2013.

[3] Y. Liu, W. Wang, Y. Zhan, C. Zheng, and G. Wang, “A simple route to hydroxyapatite nanofibers,” *Materials Letters*, vol. 56, no. 4, pp. 496–501, 2002.

[4] D. C. Carter and J. X. Ho, *Structure of Serum Albumin*, vol. Volume 45, pp. 153–203. Academic Press, 1994.

[5] N. C. Andrés, N. L. D’Elia, J. M. Ruso, A. E. Campelo, V. L. Massheimer, and P. V. Messina, “Manipulation of $mg2+ - ca2+$ switch on the development of bone mimetic hydroxyapatite,” *ACS applied materials & interfaces*, vol. 9, no. 18, pp. 15698–15710, 2017.

[6] N. L. D’Elía, A. N. Gravina, J. M. Ruso, J. A. Laiuppa, G. E. Santillán, and P. V. Messina, “Manipulating the bioactivity of hydroxyapatite nano-rods structured networks: Effects on mineral coating morphology and growth kinetic,” *Biochimica et Biophysica Acta (BBA) - General Subjects*, vol. 1830, no. 11, pp. 5014–5026, 2013.

[7] K. U. Barthel, “Entropy constrained fractal image coding,” *Fractals*, vol. 05, no. supp01, pp. 17–26, 1997.

[8] K. U. Barthel, H. L. Cycon, and D. Marpe, “Image denoising using fractal- and wavelet-based methods,” vol. 5266, p. 9, 2004.

[9] N. Michael and B. Bharat, “Biologically inspired surfaces: Broadening the scope of roughness**,” *Advanced Functional Materials*, vol. 18, no. 6, pp. 843–855, 2008.

[10] D. Rose, “Application of fractals to materials science,”

[11] A. K., B. M., N. B., D. E., J. D., I. A., and H. P., “Qualitative and quantitative study of human osteoblast adhesion on materials with various surface roughnesses,” *Journal of Biomedical Materials Research*, vol. 49, no. 2, pp. 155–166, 2000.

[12] H. Xie, J.-a. Wang, and E. Stein, “Direct fractal measurement and multifractal properties of fracture surfaces,” *Physics Letters A*, vol. 242, no. 1, pp. 41–50, 1998.

[13] T. R. Thomas, *Rough surfaces.* London: Imperial College Press, second ed., 1999.

5

Protein Corona on Bioceramic Nanoparticles

Contents

5.1 Overview **105**
5.2 Experimental procedure **106**
  5.2.1 Preparation of BSA and HA samples 106
5.3 Discussion **106**
  5.3.1 Affinity, binding and thermodynamis of the interactions 106
  5.3.2 Kinetic properties of the adsorption 107
  5.3.3 Structural and conformational changes 113

5.1 Overview

In this chapter, a multiple experimental approach was used to understand and characterize the adsorption of bovine serum albumin (BSA) onto hydroxyapatite (HA) nanoparticles. BSA was chosen because is a well-known model protein with a wide range of physiological functions and HA because of its excellent biocompatiblilty, bioactivity and osteoconductivity properties above exposed. The combination of these elements offers a promising avenue for applications in health and biomedical areas.

5.2 Experimental procedure

5.2.1 Preparation of BSA and HA samples

Protein solutions were freshly prepared by dissolving a known amount of the protein in buffer (PBS, pH 7.4) and used the day of each experiment. Therefore, a solution of $2.0 \times 10^{-4}\,\mathrm{mol\,L^{-1}}$ of BSA was prepared by dissolving 0.1992 g of solid BSA in vials with 0.015 L of buffer and stored at 273-277 K. Before the beginning of each experiment, BSA solutions were exposed to room temperature (RT) for a maximum of 1 h. To prepare the stock solutions of HA, 0.0301 g and 0.0030 g of HA powder, synthesized as explained in the previous (Chapter 4); were respectively added to vials with 0.015 L of distilled water. These solutions were vigorously sonicated for 10 minutes to obtain homogeneous dispersions.

5.3 Discussion

5.3.1 Affinity, binding and thermodynamis of the interactions

In order to explore the interaction of BSA with the nanoparticles, the isothermal titration calorimetry (ITC) technique was used. The BSA concentration in the calorimetric cell and the HA concentration in the syringe were 0.05 and 0.5 mM, respectively. Figure 5.1 shows the dependence between the amount of heat released per injection and the molar ratio of the HA to the BSA. Reported values were calculated after subtracting the blank from the experiments to neglect heats from protein and HA dilution. The results clearly show that the binding interaction between BSA and HA nanoparticles is exothermic and gradually decreased with increasing HA/BSA ratio. This result falls within the standard, most of the nanoparticle-protein interactions are monotonically exothermic, just some of them are endothermic [1].

The heat changes can be fitted into isothermal functions to quantify the corresponding thermodynamic parameters. After trying different models to determine which of them best fits the data, a single set of identical sites was selected in the binding analysis which means the protein adsorbed in the same way onto the nanoparticle surface. The binding constant (K), enthalpy change (ΔH), and binding stoichiometry (n) were determined from curve-fitting analyses. The entropy changes (ΔS) were calculated by using the standard thermodynamic equations.

The values obtained were: $n = 1.1 \pm 0.3$; $K = (4.87 \pm 1.23) \times 10^{-4}$ $\mathrm{M^{-1}}$; ΔH = -1093 ± 280 $\mathrm{kJ\,mol^{-1}}$ and ΔS = -9.23 ± 3.67 $\mathrm{kJ\,mol^{-1}}$. The negative value

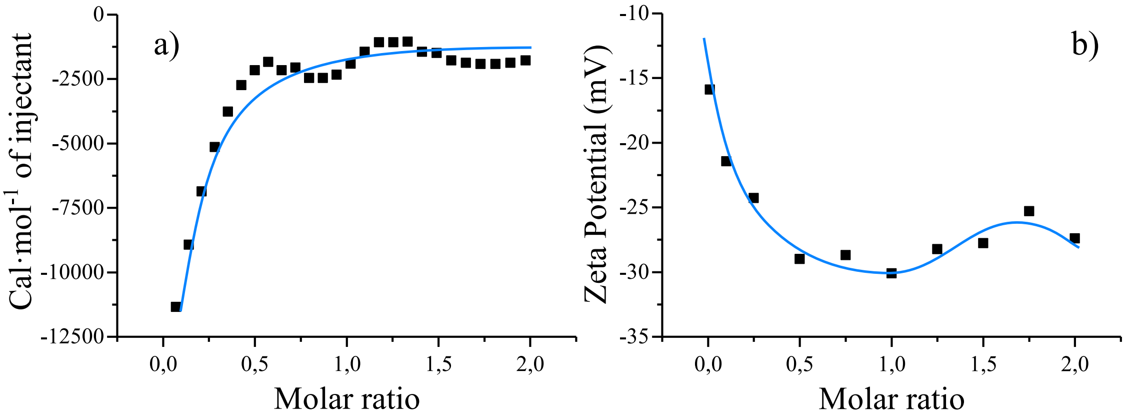

Figure 5.1: a) Heat of interaction for titration of HA nanoparticles into BSA solution at 298.15 K. Solid lines represent the fit using a one-site binding model. b) Zeta potential of HA nanoparticles as a function of BSA/HA ratio.

of enthalpy is directly related to the electrostatic and hydrophobic interactions, formation of hydrogen bonds and π-π interaction. On the other hand, hydration and conformational restriction of the amino acid residues on protein‘s surface following the adsorption contribute to unfavorable entropy loss. Thus, according to the obtained values, in the interaction of BSA with HA nanoparticles the enthalpy plays a key role in revealing that the main driving forces involved in the adsorption process were non-covalent bondings [2].

Concurrently, the ζ-potential measurements also showed an evolution of the protein corona. Figure 5.1 demonstrates the zeta potential measurements of the complex HA-BSA as a function of BSA/HA ratio. The initial negative value is very similar to those of pure HA nanoparticles (-16 mV). This value is consistent with previous understanding where it was found that the zeta potential of HA nanoparticles increases when their size decrease [3]. As the protein concentration increases an expeditious decrease in the zeta potential was found out, clearly suggesting the binding of BSA. After this minimum a slightly increase and a final plateau is observed. In this media, both the nanoparticles and the protein have negative charge, however, this is not surprising, it was previously reported that protein adsorption onto nanoparticles lead to a shift in zeta potential regardless of original surface charge [4]. Regarding the changes in zeta potential profile while considering the isotropic surface of the nanoparticles, intuitively the observed phenomena stemmed from the unique structural features of BSA.

5.3.2 Kinetic properties of the adsorption

The presence of chromophores in most proteins makes them viable for fluorescence spectroscopy analysis. BSA has two tryptophan residues located at positions 134 and 212 of the chain. Trp-212 is located within a hydrophobic binding pocket of the protein and Trp-134 is located on the surface of the molecule [4]. Figure 5.2 pictures the fluorescence emission spectra of BSA in the absence and presence of HA nanoparticles. During observation, BSA demonstrates a strong fluorescence emission band at 345 nm, while first being excited with a wavelength of 280 nm. The fluorescent emission intensity of BSA decreased in regularly when it is titrated with various concentrations of HA. The strong quenching of the BSA fluorescence suggests that the microenvironment around the Trp 134 residue was placed in an intensive hydrophobic environment after the addition of HA. In addition, no changes in shape or red/blue shifts have been observed in the peak. Considering independent and non-interactive binding sites, the fluorescence quenching data were analyzed by the well-known Stern-Volmer equation:

$$\frac{F_0}{F} = 1 + K_{sv}\,[Q] \tag{5.1}$$

F_0 and F are the steady-state fluorescence intensities in the absence and presence of quencher. K_{sv} the Stern-Volmer quenching constant. [Q] is the concentration of the quencher, in this case, hydroxyapatite.

The linearity of the F_0/F versus [Q], plots revealed the quenching type. These are either static or dynamic. The characteristic of the Stern–Volmer plot of quenching that fit both static and dynamic demonstrates an upward curvature [5]. In this case, linear correlations were observed between the intensities and the HA concentration (R^2 = 0.924, 0.973, 0.945) which suggests that all Trp(s) in the protein differ slightly in accessibility [6]. K_{sv}, obtained from the slopes, were $(8.90 \pm 0.01) \times 10^3$, $(8.69 \pm 0.01) \times 10^3$ and $(6.68 \pm 0.01) \times 10^3\,\mathrm{L\,mol^{-1}}$ at 288.15, 298.15 and 309.15 K. As the binding constant increases with a decrease in temperature, it can be safely inferred that a static quenching procedures is the probable quenching mechanism of fluorescence in BSA and HA. Applying static quenching procedure reveals the formation of a complex bounded by HA and BSA. This complex was confirmed from the values of quenching rate constant. This constant represents the maximum scatter collision quenching constant of various quenchers with the biopolymer, $K_q = K_{sv}/\tau_0$, where τ_0 is the average lifetime of the protein without the quencher. The value of τ_0 in the present case is $10^{-8}\,\mathrm{s^{-1}}$ [7], therefore, K_q has a value of: $8.69 \times 10^{10}\,\mathrm{L\,mol^{-1}\,s^{-1}}$. This value is greater than the maximum scatter collision quenching constant of various quenchers with the biopolymer which is $2 \times 10^{10}\,\mathrm{L\,mol^{-1}\,s^{-1}}$ [8]. K_q values of protein quenching procedure initiated by HA are greater than the K_q of the scattered procedure indicates that the probable quenching mechanism involves complex formation rather than dynamic collisions [9].

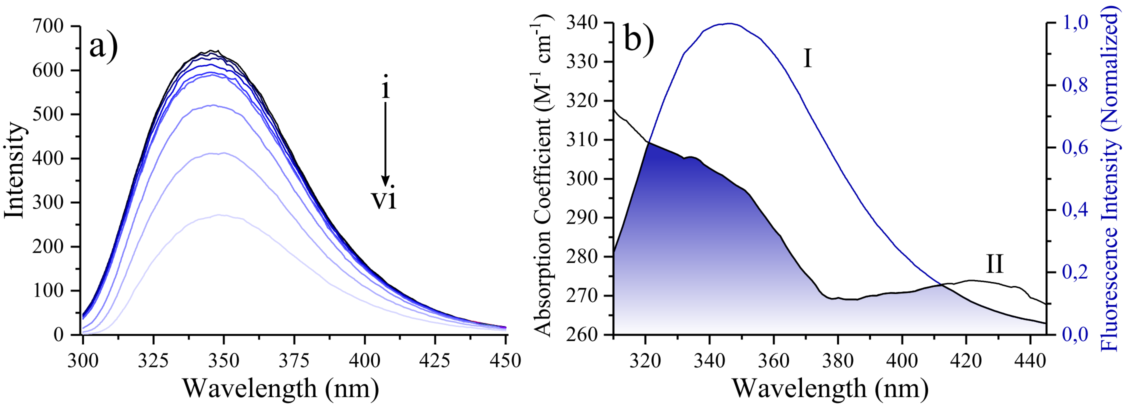

Figure 5.2: a) Fluorescence emission spectra of BSA in the absence and presence of different concentrations of HA nanoparticles: Pure BSA (i). Ratio [HA]/[BSA] = 1, 2, 4, 10, 20 (from ii to vi). b) Overlap of the fluorescence spectrum of BSA (II) and the absorbance spectrum of HA (I). Ratio [HA]/[BSA] = 1

Fluorescent measurements allow us to get quantitative information about the binding process. Assuming proteins are bound independently to a set of equivalents sites on nanoparticle surface, the following equation can be applied [10]:

$$\lg\frac{(F_0 - F)}{F} = \lg K_a + n \cdot \lg[Q] \tag{5.2}$$

K_a is the binding constant of HA with BSA and n the number of binding sites per BSA molecule. Linear fitting of experimental data indicates values of $(3.80 \pm 0.83) \times 10^3\,\mathrm{M}^{-1}$ and 1.24 ± 0.22 for K_a and n, respectively. It is safe to conclude then, that there is only one independent class of binding sites between HA and BSA, demonstrating astounding agreement with ITC measurements.

The distance between the protein and the bound HA could be determined using fluorescent resonance energy transfer (FRET). Energy transfer occurs when the fluorescent emission band of the donor overlaps with an excitation band of the acceptor molecule that is within 2-8 nm [11]. The overlap of the fluorescence emission spectra of BSA and the absorption spectra of HA at 298.15 K is pictured in Figure 5.2. The rate of transfer for a donor and acceptor separated by a distance r is given by [12]:

$$\mathrm{k_T}(r) = \frac{Q_D \kappa^2}{\tau_D r^6}\left(\frac{9000\ (\ln 10)}{128\ \pi^5 N n^4}\right)\int_0^\infty F_D(\lambda)\,\varepsilon_A(\lambda)\,\lambda^4 \mathrm{d}\lambda \tag{5.3}$$

Q_D is the quantum yield of the donor in the absence of acceptor; κ^2 is a factor describing the relative orientation in space of the transition dipoles of the donor and acceptor; n is the refractive index of the medium. N is Avogadro's number. r is the distance between the donor and acceptor, and τ_D is the lifetime of the donor in the absence of acceptor. $F_D(\lambda)$ is the corrected fluorescence intensity of the donor in the wavelength range λ to $\lambda + \Delta\lambda$ with the total intensity attained by taking the area under the curve, normalized to unity. $\varepsilon_A(\lambda)$ is the extinction coefficient of the acceptor at λ. The overlap integral ($J(\lambda)$) expresses the degree of spectral overlap between the donor emission and the acceptor absorption:

$$J(\lambda) = \frac{\int_0^\infty F_D(\lambda)\,\varepsilon_A(\lambda)\,\lambda^4 \mathrm{d}\lambda}{\int_0^\infty F_D(\lambda)\mathrm{d}\lambda} \tag{5.4}$$

The efficiency of energy transfer (E) is the fraction of photons absorbed by the donor and transferred to the acceptor. Efficiency is typically measured using the relative fluorescent intensity of the donor in the absence (F_D) and presence (F_{DA}) of the acceptor. This fraction is given by:

$$E = 1 - \frac{F_{DA}}{F_D} = \frac{R_0^6}{R_0^6 + r^6} \tag{5.5}$$

While considering the above equation, the Förster critical distance (R_0), at which 50 % of the excitation energy is transferred to the acceptor, can be calculated by the following expression:

$$R_0^6 = 8.79 \times 10^{-5}(\kappa^2 n^{-4} Q_D\, J(\lambda)) \tag{5.6}$$

In the present case, as the protein studied was BSA, the corresponding values of the parameters used were: $\kappa^2 = 2/3$, $Q_D = 0.15$, $n = 1.36$ [13]. Combining the experimental data with the equations: J, E, R_0 and r can be obtained with their respective values of: $J = 4.53 \times 10^{12}\,\mathrm{M^{-1}\,cm^{-1}\,nm^4}$, $E = 0.01$, $R_0 = 1.50\,\mathrm{nm}$, and $r = 3.24\,\mathrm{nm}$. The value of r is within 2-8 nm, which indicates that the energy transfer between HA and BSA is very probable. Furthermore comparing the values of r and R_0, it is right to conclude that there is a presence of static-type quenching mechanism, as HA-BSA distance, r, are larger than R_0 values observed in the present study [14].

Ultraviolet-visible (UV-vis) spectroscopy is another simple and effective method to explore the structural changes of protein and protein-complex formation. This technique is very sensitive and non-destructive that requires only small amount of material for analysis [15]. Prior to exploring the equilibrium binding behaviour of BSA to the HA nanoparticles, a brief kinetic investigation was performed to determine the estimated time required for the HA to saturate the BSA binding sites. Figure 5.3 shows the BSA-HA system spectra after 30 hours of interaction.

As seen above, the absorbance was increased over time and a slight blue shift was observed. Using a modified pseudo-second-order kinetic model, which assumes that the BSA concentration is present in excess, the adsorption kinetic curve of the BSA-HA was successfully fitted to extract a rate constant shown in Figure 5.3:

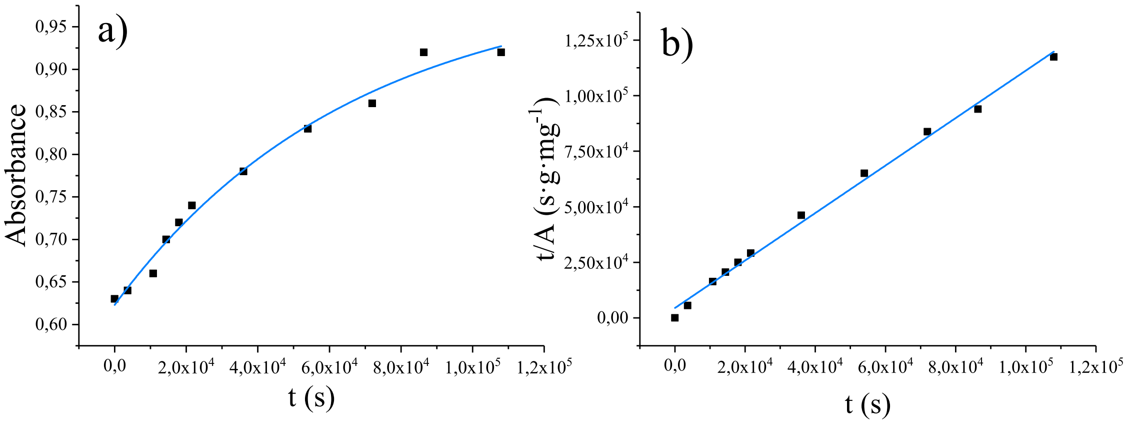

Figure 5.3: a) Absorbance of BSA measured at $\lambda = 277\,\mathrm{nm}$ over a time scale of $1.1 \times 10^5\,\mathrm{s}$ after immersion in HA solution ($5.00 \times 10^{-4}\,\mathrm{M}$) at 298 K. b) Linear pseudo-second-order kinetic curve for BSA after interaction with HA nanoparticles.

$$\frac{t}{A} = \frac{t}{A_e} + \frac{A_e^2}{k_2} \tag{5.7}$$

k_2 is the second-order rate constant, t the time. A and A_e are the absorbance of the maximum peak at time t and after equilibrium is reached [4]. By applying data, $k_2 = (2.15 \pm 0.65) \times 10^{-4}\,\mathrm{s}^{-1}$ suggesting that the interaction between the protein and the inorganic compound is slow, yielding the maximum value 24 hours after the preparation of the mixture.

The absorption spectra of BSA and BSA-HA mixed solutions after 24 hours of interaction are shown in Figure 5.4a. The pure BSA solution has strong absorption maximum, peaking at 277 nm. The BSA absorbance increases with the concentration of HA, which is mainly attributed to a BSA/HA interaction [16]. Furthermore, the absorption peak had a less obvious, but equally important shift towards lower wavelength regions which is a blue shift of about 1.1 nm. The changes in the peak position indicate that a structural change of BSA upon interaction with HA is occurring and supports the conclusion that the static quenching exists as a consequence of BSA-HA association [17].

Figure 5.4b, shows the absorbance difference at 277 nm of BSA ($\Delta \mathrm{A} = \mathrm{A} - \mathrm{A}^N$) as a function of HA concentration. A^N is the absorbance of BSA native folded state. There is an abrupt change in a narrow range of HA concentration, which suggests that, during the interaction with the nanoparticle surface, the native (N) conformation of the protein was disrupted. This fact has a significant biological impact and should be analyzed further. The obtained results were fitted to the Boltzmann sigmoidal model and the midpoint of the transition, that is,

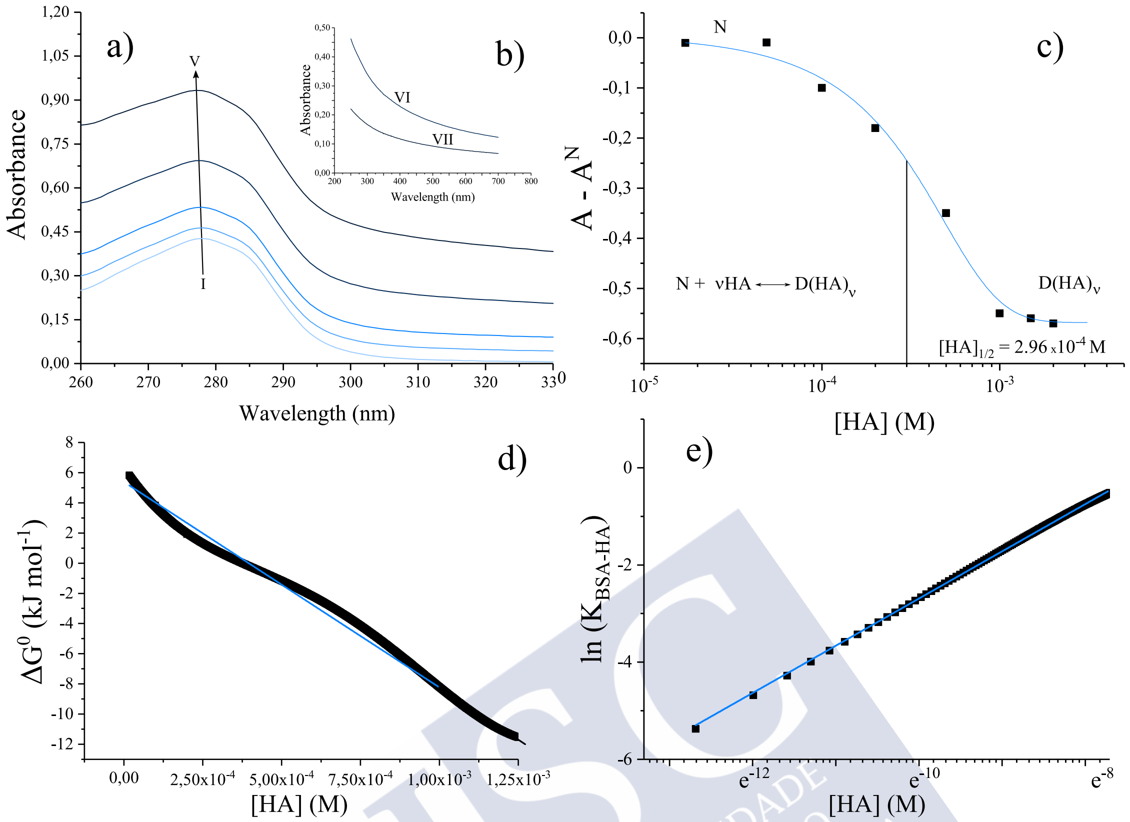

Figure 5.4: a) UV-visible absorption spectra of BSA in the presence of different concentrations of HA. (a–e): [BSA] = $5.00 \times 10^{-5}\,\mathrm{mol\,L^{-1}}$, [HA] = 0.00, 0.10, 0.20, 0.50, $1.00 \times 10^{-3}\,\mathrm{mol\,L^{-1}}$, and (f–g): [BSA] = 0, [HA] = 0.50, $1.00 \times 10^{-3}\,\mathrm{mol\,L^{-1}}$, some spectra are not shown to avoid confusion. b) Absorbance variation of BSA at 277 nm vs. [HA]. c) Standard Gibbs energy difference between protein folded and unfolded conformations as a function of HA concentration. d) Relationship between K_{BSA-HA} and ln [HA] at 298.15 K.

the concentration of protein free in the solution at half-coverage in equilibrium, is given at $[\mathrm{HA}]_{1/2} = (2.96 \pm 0.69) \times 10^{-4}\,\mathrm{M}$.

The induction of conformational changes due to the interaction between native BSA and hydroxyapatite nanoparticles (HA) may be expressed as an equilibria accordingly to the following equation [18]:

$$N + \nu HA \leftrightarrows D(HA)_{\nu} \tag{5.8}$$

D is the denaturalized form of BSA, and ν is the average number of HA nanoparticles bound to the complex D(HA). The equilibrium constant (K) for the above mentioned reaction can thus be written as:

$$K = [D(\mathrm{HA})_{\nu}]/[N]\,[\mathrm{HA}]^{\nu} = K_{BSA-HA}/[\mathrm{HA}]^{\nu} \tag{5.9}$$

taking logarithms,

$$\ln K = \ln K_{BSA-HA} - \ln [\text{HA}] \tag{5.10}$$

K_{BSA-HA} is the molar ratio of BSA-HA complex and native protein molecules. [HA] is the equilibrium concentration of free HA nanoparticles. The small initial protein concentration BSA $= 5.0 \times 10^{-5}$ M and its low affinity for HA nanoparticles [19] dictates that HA is negligibly different from the total nanoparticle concentration. The values of K_{BSA-HA} as a function of HA were computed from the extent of denaturation degree (α), accordingly to the method described by Pace [20] and shown in Figure 5.4d:

$$\alpha = \left(A - A^N\right) / \left(A^D - A^N\right) K_{BSA-HA} = \alpha/(1-\alpha) \tag{5.11}$$

A^D is the absorbance for the BSA denaturated conformation. The linearity of $ln\ K_{BSA-HA}$ as a function of [HA] is consistent with the following equations:

$$\ln K_{BSA-HA} = \ln K_{BSA-HA,w} - (m/RT)\,[\text{HA}]\,\Delta G^0 = \Delta G^0_w - m\,[\text{HA}] \tag{5.12}$$

ΔG^0 is the difference in the standard Gibbs energy between the folded and unfolded conformations, ΔG^0_w is the value of ΔG^0 for the transition in the absence of the HA nanoparticles. m is a measure of the dependence of $\Delta \mathrm{G}^0$ on the nanoparticles concentrations. Although curvature is displayed in Figures 5.4c and 5.4d, it is not a consistent feature. The analysis based on linearity was considered more appropriate than higher-order regression. The BSA-HA equilibrium constant $K = (1.123 \pm 0.001) \times 10^3$, obtained from Figure 5.4d is of the same order than the found by fluorescent quenching measurements. The average number of HA nanoparticles bound to form the BSA/HA complex is closer to one ($\nu = 0.971 \pm 0.002$), suggesting that the BSA/HA binding is faintly anti-cooperative [21].

5.3.3 Structural and conformational changes

The next step is to determine if adsorption of BSA onto HA induce any structural change. In these experiments, CD spectra were taken in the wavelength range of 200 to 290 nm, resulting as mean residue ellipticity in millidegrees. Figure 5.5 shows typical CD spectra of BSA in the absence of HA and at different molar ratios. The CD result shows that free BSA has a high α-helix content of 63 % and β-sheet of 2.8 % in Table 5.1, consistent with the literature report [22]. The ellipticity values in the CD spectra slightly decrease in the presence of HA nanopaticles. BSA is mainly

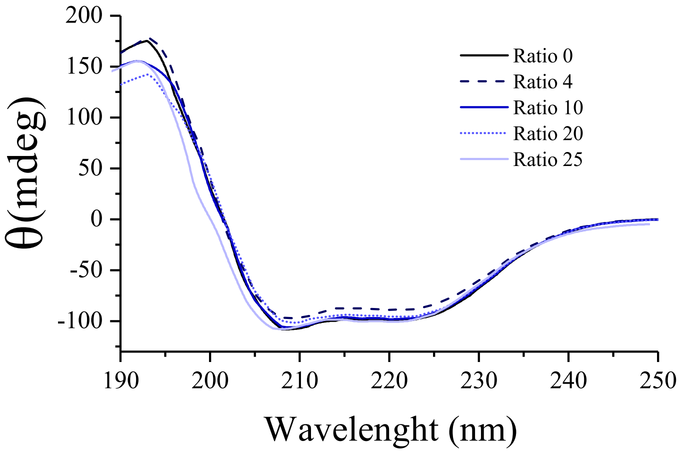

Figure 5.5: Circular Dichroism (CD) spectra of BSA under different molar ratios of HA:BSA as marked in the figure.

Table 5.1: Percentage of the secondary structure of BSA at their interaction with different molar ratios of HA:BSA.

Sample	**Alpha helix** (%)	**Beta turn** (%)
BSA (5μM)	63.4	2.8
Ratio 4	60.4	3.6
Ratio 10	60.2	3.5
Ratio 20	59.8	3.9
Ratio 25	57.9	4.8

α-helical in secondary structure. The increases in the negative peaks at 209 and 222 nm in the spectrum indicate a loss of BSA α-helical structure and an increase in the β-turn in the presence of the nanoparticles. This behavior has already been observed in similar systems, attributing it to the aromatic amino acid residues of the main chain which are bound to the nanoparticle surface destroying the hydrogen bonding networks of the native structure of the protein [23]. The minor changes indicate that the conformational changes are limited and occur locally. The protein secondary structure is slightly disturbed by the nanoparticles [24]. This result agrees with the fact that the structure of BSA is relatively flexible because of the large α-helix content. The flexibility provided facilitates the adsorption of BSA onto the nanoparticle surface while preserving the 3D structure [25]. Significant changes in the secondary structure of BSA already appear at low nanoparticle concentration. When the concentration of nanoparticles is increased, changes in the secondary structure are significantly reduced. It is evident that HA nanoparticles have very minute effects on the BSA conformation, which demonstrate excellent biocompatibility.

Bibliography

[1] D. C. Carter and J. X. Ho, *Structure of Serum Albumin*, vol. Volume 45, pp. 153–203. Academic Press, 1994.

[2] R. Huang and B. L. T. Lau, “Biomolecule–nanoparticle interactions: Elucidation of the thermodynamics by isothermal titration calorimetry,” *Biochimica et Biophysica Acta (BBA) - General Subjects*, vol. 1860, no. 5, pp. 945–956, 2016.

[3] Y. Cai, Y. Liu, W. Yan, Q. Hu, J. Tao, M. Zhang, Z. Shi, and R. Tang, “Role of hydroxyapatite nanoparticle size in bone cell proliferation,” *Journal of Materials Chemistry*, vol. 17, no. 36, pp. 3780–3787, 2007.

[4] D. H. Jo, J. H. Kim, T. G. Lee, and J. H. Kim, “Size, surface charge, and shape determine therapeutic effects of nanoparticles on brain and retinal diseases,” *Nanomedicine: Nanotechnology, Biology and Medicine*, vol. 11, no. 7, pp. 1603–1611, 2015.

[5] P. B. Kandagal, S. Ashoka, J. Seetharamappa, S. M. T. Shaikh, Y. Jadegoud, and O. B. Ijare, “Study of the interaction of an anticancer drug with human and bovine serum albumin: Spectroscopic approach,” *Journal of Pharmaceutical and Biomedical Analysis*, vol. 41, no. 2, pp. 393–399, 2006.

[6] M. M. Lopez and D. Kosk-Kosicka, “Spectroscopic analysis of halothane binding to the plasma membrane ca 2+-atpase,” *Biophysical journal*, vol. 74, no. 2, pp. 974–980, 1998.

[7] M. D. Meti, S. T. Nandibewoor, S. D. Joshi, U. A. More, and S. A. Chimatadar, “Multi-spectroscopic investigation of the binding interaction of fosfomycin with bovine serum albumin,” *Journal of Pharmaceutical Analysis*, vol. 5, no. 4, pp. 249–255, 2015.

[8] P. N. Naik, S. A. Chimatadar, and S. T. Nandibewoor, “Study on the interaction between antibacterial drug and bovine serum albumin: A spectroscopic approach,” *Spectrochimica Acta Part A: Molecular and Biomolecular Spectroscopy*, vol. 73, no. 5, pp. 841–845, 2009.

[9] A. Sułkowska, “Interaction of drugs with bovine and human serum albumin,” *Journal of Molecular Structure*, vol. 614, no. 1–3, pp. 227–232, 2002.

[10] T. Yang, H. Zhang, H. Fu, Y. She, C. Huang, Y. Hu, and L. Wang, “Comparative studies on the interaction of cochinchinenin a and loureirin b with bovine serum albumin,” *Journal of Spectroscopy*, vol. 2013, p. 9, 2013.

[11] N. Wang, L. Ye, B. Zhao, and J. Yu, “Spectroscopic studies on the interaction of efonidipine with bovine serum albumin,” *Brazilian Journal of Medical and Biological Research*, vol. 41, pp. 589–595, 2008.

[12] J. Lakowicz, *Principles of Fluorescence Spectroscopy*. Kluwer Academic / Plenum, 1999.

[13] J. Li, J. Li, Y. Jiao, and C. Dong, “Spectroscopic analysis and molecular modeling on the interaction of jatrorrhizine with human serum albumin (hsa),” *Spectrochimica Acta Part A: Molecular and Biomolecular Spectroscopy*, vol. 118, pp. 48–54, 2014.

[14] Y.-Z. Zhang, N.-X. Zhang, A.-Q. Ren, J. Zhang, J. Dai, and Y. Liu, “Spectroscopic studies on the interaction of 2,4-dichlorophenol with bovine serum albumin,” *Journal of Solution Chemistry*, vol. 39, no. 4, pp. 495–510, 2010.

[15] F.-X. Schmid, “Biological macromolecules: Uv-visible spectrophotometry,” in *eLS*, John Wiley & Sons, Ltd, 2001.

[16] C. N. Pace, F. Vajdos, L. Fee, G. Grimsley, and T. Gray, “How to measure and predict the molar absorption coefficient of a protein,” *Protein Sci*, vol. 4, no. 11, pp. 2411–23, 1995.

[17] X. Peng, J. Yu, Q. Yu, H. Bian, F. Huang, and H. Liang, “Binding of engeletin with bovine serum albumin: Insights from spectroscopic investigations,” *Journal of Fluorescence*, vol. 22, no. 1, pp. 511–519, 2012.

[18] I. Lynch and K. A. Dawson, “Protein-nanoparticle interactions,” *Nano today*, vol. 3, no. 1, pp. 40–47, 2008.

[19] N. L. D’Elia, N. Gravina, J. M. Ruso, J. L. Marco-Brown, J. M. Sieben, and P. V. Messina, “Albumin-mediated deposition of bone-like apatite onto nano-sized surfaces: Effect of surface reactivity and interfacial hydration,” *Journal of colloid and interface science*, vol. 494, pp. 345–354, 2017.

[20] C. N. Pace and D. V. Laurents, “A new method for determining the heat capacity change for protein folding,” *Biochemistry*, vol. 28, no. 6, pp. 2520–2525, 1989.

[21] P. Maffre, S. Brandholt, K. Nienhaus, L. Shang, W. J. Parak, and G. U. Nienhaus, “Effects of surface functionalization on the adsorption of human serum albumin onto nanoparticles – a fluorescence correlation spectroscopy study,” *Beilstein Journal of Nanotechnology*, vol. 5, pp. 2036–2047, 2014.

[22] B. E. Givens, N. D. Diklich, J. Fiegel, and V. H. Grassian, “Adsorption of bovine serum albumin on silicon dioxide nanoparticles: Impact of ph on nanoparticle-protein interactions,” 2017.

[23] F. Ahmad, Y. Zhou, Z. Ling, Q. Xiang, and X. Zhou, “Systematic elucidation of interactive unfolding and corona formation of bovine serum albumin with cobalt ferrite nanoparticles,” *RSC Advances*, vol. 6, no. 42, pp. 35719–35730, 2016.

[24] S. H. D. P. Lacerda, J. J. Park, C. Meuse, D. Pristinski, M. L. Becker, A. Karim, and J. F. Douglas, “Interaction of gold nanoparticles with common human blood proteins,” *ACS Nano*, vol. 4, no. 1, pp. 365–379, 2010.

[25] L. Wang, J. Li, J. Pan, X. Jiang, Y. Ji, Y. Li, Y. Qu, Y. Zhao, X. Wu, and C. Chen, “Revealing the binding structure of the protein corona on gold nanorods using synchrotron radiation-based techniques: Understanding the reduced damage in cell membranes,” *Journal of the American Chemical Society*, vol. 135, no. 46, pp. 17359–17368, 2013.

6

Bilayer composite membranes

Contents

6.1 Overview **117**
6.2 Experimental procedure **118**
    6.2.1 Preparation of ALG-HA bilayer membranes 118
6.3 Discussion **118**
    6.3.1 Study of ALG-HA interaction 119
    6.3.2 Mechanical performance under tensile strength 120
    6.3.3 Degradation under in vitro physiological conditions . . . 123
    6.3.4 Surface characterization each side of the membrane . . . 124
    6.3.5 Cell culture 126

6.1 Overview

In this chapter, the synthesis, characterization and properties of periosteum-inspired biodegradable bilayer ALG-HA membranes are described. This material, rather than merely acting as a passive barrier, guide bone regeneration on the side facing the bone defect due to its osteoconductive and osteoinductive properties, and promote wound healing on the other side. For this application, these composites should have appropriate mechanical properties and enhanced biological behaviour. The interaction between ALG and HA was evaluated by Fourier transform infrared spectroscopy. Mechanical performance, surface properties and degradation of the final membranes were studied. Finally, osteoblast proliferation and differentiation were tested on the mineral-rich side while fibroblast proliferation on the fibrous side.

6.2 Experimental procedure

6.2.1 Preparation of ALG-HA bilayer membranes

Crystalline hydroxyapatite-nanoparticles (HA), measuring 8 ± 1 nm diameter and 28 ± 3 nm length, were obtained as previously described in Chapter 4.

ALG-HA bilayer membranes were synthesized using a modified version of Benedini et al. synthesis [1]. A 2 % w/v solution of alginic acid in water was kept under stirring at 350 rpm for 3 h at 40 °C. Afterwards, 4.5 mL aliquots of the ALG solution were added to 35 mm diameter Petri dishes and left drying at 40 °C for 24 h. Meanwhile, three different fresh crosslinking solutions containing a constant concentration of $CaCl_2$ (110 mM) and increasing concentrations of HA (0.11, 0.55 and 1.1 % w/v in water were prepared. The crosslinking solutions were sonicated for 1 h and added into empty 35 mm Petri dishes. Subsequently, ALG films were carefully placed on top of the solution to avoid wrinkles and bubbles formation. Finally, hydrogels were stirred on an orbital shaker at 150 rpm, at room temperature for 3 h, to ensure a complete crosslinking and drying. The three membranes synthesized were named in accordance with the content of HA, herein M-0.11, M-0.55 and M-1.1, respectively. Membranes without HA served as controls and were named M-0.

In this Chapter, the preparation of the samples, Fourier-transform infrared spectroscopy (FTIR), mechanical characterization measurements and cell culture studies were performed by collaborators from *Universidad del Sur*, Argentina.

6.3 Discussion

Guided bone regeneration membranes must fulfill a series of properties to be successful, including good mechanical performance, steady biodegradation and promotion of tissue regeneration. In this work, through the combination of two well-known biocompatible materials such as ALG and HA, novel bilayer membranes were developed. The influence of different amounts of HA in the mineral-rich side of the membranes was analysed through several physico-chemical properties. Moreover, the ability of each membrane side to influence cells behaviour was determined in an attempt to predict their tissue-specific regeneration capability.

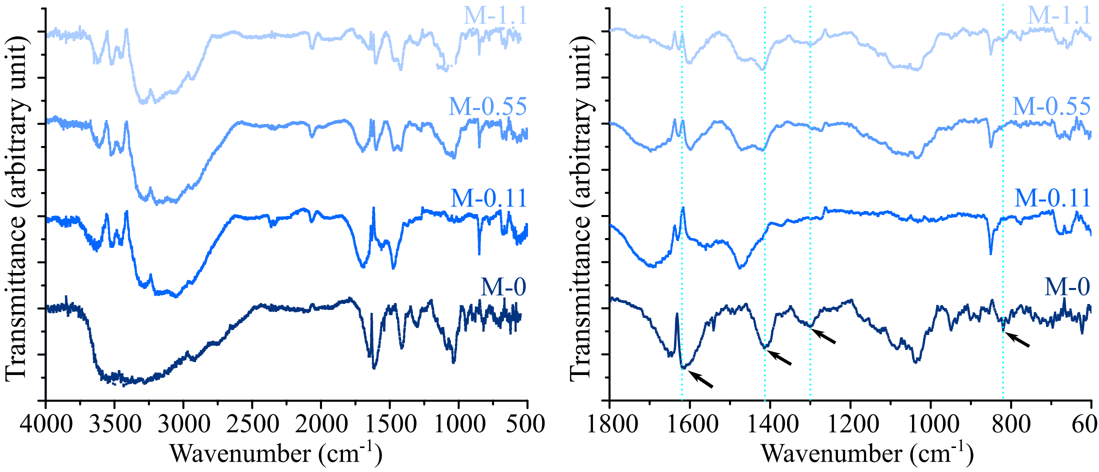

Figure 6.1: FTIR spectra of membranes M-0, M-0.11, M-0.55 and M-1.1, a) broad range 500-4000 cm^{-1}, b) magnification between 1800 cm^{-1} and 600 cm^{-1} is displayed. The arrows indicate characteristic ALG bands attributed to carboxylic groups (COO^-) in the wavenumbers 1616 and 1413 cm^{-1}, and hydroxyls (OH^-) from the carboxylic groups in 1303 and 818 cm^{-1}.

6.3.1 Study of ALG-HA interaction

The membranes were studied by Fourier-transform infrared spectroscopy (FTIR), an essential technique for assessing the chemical interaction between ALG and HA. The spectra obtained for the HA-free membrane (M-0) and the HA-containing membranes (M-0.11, M-0.55 and M-1.1) are showed in Figure 6.1a. Alginate membranes without HA (M-0) displayed bands at 1616 and 1413 cm^{-1} that can be attributed to asymmetric and symmetric stretching vibrations, respectively, of ionized carboxylic group (COO^-) on the polymeric backbone characteristic of ALG. The bending of the OH^{--} group of the carboxyl is depicted at 1303 and 818 cm^{-1} [2]. Interestingly, consistent differences were observed on the bands of the spectrum corresponding to M-0 (only ALG) in comparison with the membranes containing HA (Figure 6.1b). Specifically, the two ALG bands at 1616 and 1413 cm^{-1} were shifted and their intensity decreased in M-0.55 and M-1.1 spectra, whereas it was difficult to identify them in M-0.11. On the other hand, the bands at 1303 and 818 cm^{-1} disappeared in all the HA-containing membranes. This effect was previously observed in ALG-HA composites [3, 4] and could be attributed to Ca^{2+} active sites, present in the HA surface, that form bonds with the oxygen sites of COO^- groups of ALG [5]. These results support the fact that the incorporation of HA contributed in the hydrogels strength as shown in the rheology analysis.

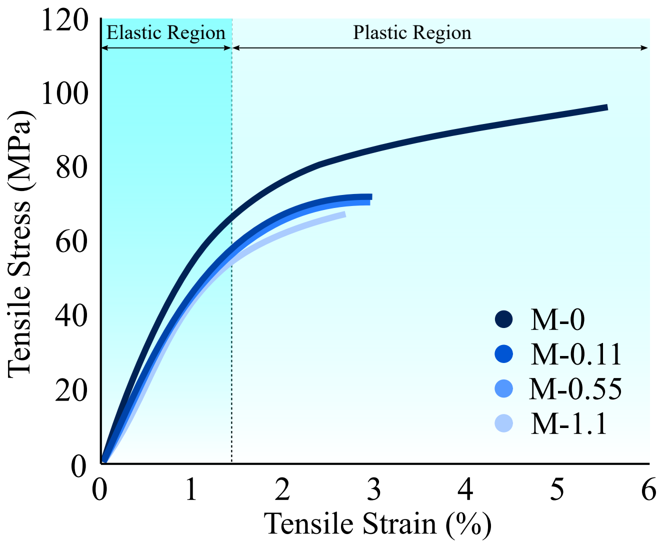

Figure 6.2: Representative stress-strain curves of the membranes M-0, M-0.11, M-0.55 and M-1.1 showing the approximate location of elastic region, yield point and plastic region.

6.3.2 Mechanical performance under tensile strength

Adequate mechanical properties are essential for membranes aimed for guided bone regeneration (GBR) applications, since these properties determine their clinical handling during implantation as well as its performance once in place. Strain-stress curves, obtained by the tensile test of the membranes, were evaluated regarding their parameters in the elastic region, yield point and plastic region (Figure 6.2).

An important parameter of the elastic region is the Young modulus *(E)*, a mechanical property that measures the stiffness of a solid material. It indicates the relationship between shear stress and shear strain in the elastic region, where the deformation is still reversible. This parameter was slightly influenced by the presence of HA, and a statistically significant difference was only found between M-0.11 and M-1.1 ($p = 0.003$) (Figure 6.2a). The maximum E values were reached with M-0.11 and M-0.55, suggesting that 0.11 and 0.55 % HA led to the highest crosslinking interactions for the selected ALG concentration (2 % w/v). Interestingly, these E values ($\sim$ 5 - 6 GPa) were higher than other membranes aimed to similar applications [6, 7], and were comparable with E of cranial bone ($E \sim 5$ - 18 GPa) [8]. This fact is notably important since it is well known that E of a biomaterial should closely match with the E of the host tissues to avoid mechanically compromising the site. In fact, it was proved that a significant difference between the E of a biomaterial and that of the surrounding tissue could lead to mechanical stress resulting in encapsulation, inflammation and the final failure of tissue regeneration [9].

Continuing with the elastic region of the stress-strain curves, the resilience modulus, which represents the energy required to stress the material from the zero stress to the yield stress point, showed no significant differences among the three HA-containing membranes values between 0.17 MPa and 0.20 MPa (Figure 6.3a). These results indicated that the resilient nature of the membranes was not affected by the amount of HA added. This is worth to consider because resilience, which was also acknowledged by the membranes' capability to recover their original structure after handling, is needed in order to facilitate membrane placement during surgical procedures. Nevertheless, as expected, due to the crystal nature of HA [10], the resilience modulus of M-0 was significantly higher than those found in the HA-containing membranes. It is important to consider that these results showed that all the HA-containing membranes tested have a similar behaviour in the elastic region of the stress-strain curves despite of the immersed HA crystals.

Increasing the stress above the threshold that begins to cause permanent damage to the membranes structural integrity allowed to obtain information about the yield point (Figure 6.3b). The yield stress (σ_y) values of all the membranes, which were between 33.8 MPa and 63.0 MPa, exceed to those obtained for human trabecular bone (1.7 MPa) under tensile load [11]. In contrast, the yield strain (ϵ_y) values of all membranes (between 1.0 % and 1.4 %), were comparable with the trabecular (0.8 %) [11] and cortical bone (0.6 % - 0.9 %) [12].

In the plastic region, the maximum tensile strain (ϵ_{max}) and the maximum tensile stress (σ_{max}) were evaluated. These two intimately related parameters that can be interpreted as the deformation percentage of the membranes at the breaking point (ϵ_{max}) and the highest load supported (σ_{max}), respectively, showed an indirect correlation between maximum load and HA concentration. In the case of ϵ_{max}, the obtained value of M-0 was $\sim$5.5 % when a σ_{max} $\sim$98 MPa was applied. In contrast, HA-free membrane (M-0) had a statistically higher ϵ_{max} than the three HA-containing membranes, while among σ_{max} values only M-0.11 was statistically significantly higher than M-1.1 (Figure 6.3c). The ϵ_{max} of M-0.11 and M-0.55 was $\sim$3 % when a σ_{max} of $\sim$75 MPa was applied, and for the membranes with the highest HA content (M-1.1) both the tensile strain and the tensile stress were reduced even further ($\sim$2.6 % when $\sim$63 MPa was applied). In spite of this fact, the ϵ_{max} were comparable or lower than other membranes applied to GBR [7, 13]. Interestingly, all the σ_{max} parameters determined were higher than those found in the trabecular bone of human mandible, which have been ranged between 0.2 and 10.4 MPa [14]. Plasticity, which refers to the permanent deformations made to the

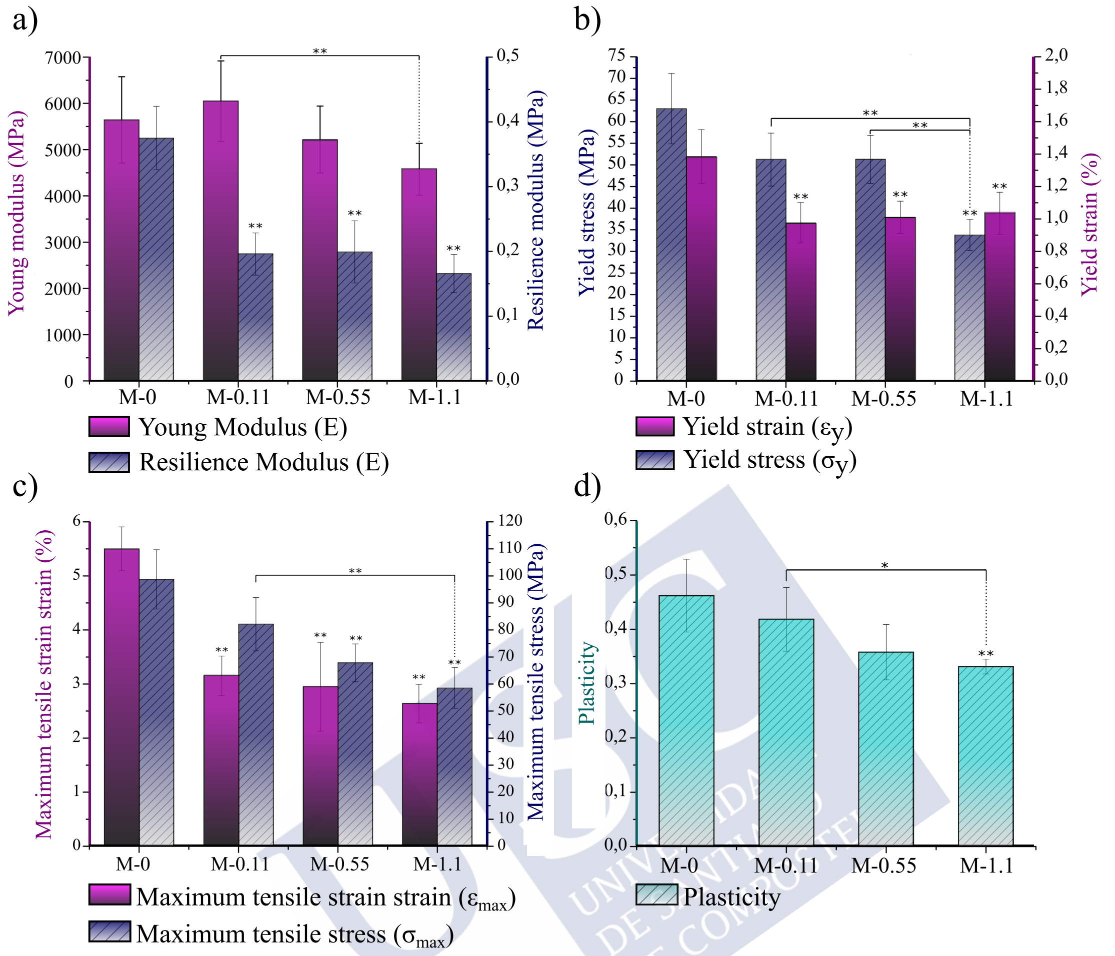

Figure 6.3: Tensile assay parameters of membranes M-0, M-0.11, M-0.55 and M-1.1. a) Elastic region: Young modulus and resilience. b) Yield point: yield stress and yield strain. c) Plastic region: maximum tensile strain and maximum tensile stress and, d) plasticity. Significant differences between HA-containing membranes and M-0 are indicated on the top of the column, while between the HA-containing membranes with brackets. Significance: * $p < 0.05$ and ** $p < 0.01$.

materials, is another parameter of the plastic region. In this particular case, M-0 and M-0.11 had a statistically significant higher plasticity than M-1.1 (Figure 6.3d).

In summary, the presence of HA affected the tensile strength of the membranes, without major differences among HA-containing membranes. This performance may be due to the presence of the nanoparticles, which are highly ordered structures and once introduced in an amorphous conformation such as ALG could generate failure points. In addition, as previously described in the rheological studies of the hydrogels, the presence of HA particles reduced the capacity of hydrogels to absorb water, making them less flexible. As water acts as a plasticizer of polymers [15], its decrease in the membranes together with the presence of HA could synergically

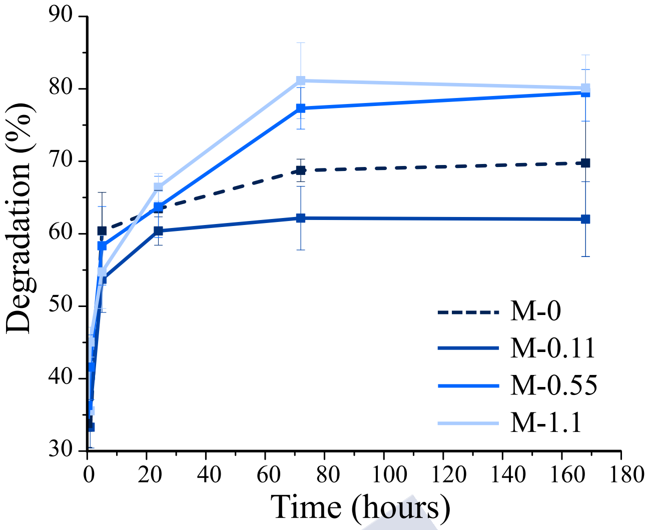

Figure 6.4: Degradation over time of the membranes M-0, M-0.11, M-0.55 and M-1.1 immersed in PBS at 37 °C.

make the membranes more rigid. Similarly, the increment in stiffness generated by the presence of HA nanoparticles was previously reported for chitosan-HA [16, 17], chitosan-glass nanoparticles [18] and polycaprolactone-glass microparticles [19].

6.3.3 Degradation under in vitro physiological conditions

The degradation behaviour of the membranes immersed in PBS is shown in Figure 6.4. During the first 24 h, all membranes had a similar degradation rate, with a quick degradation of ∼60-66 %. Between 24 h and 72 h, a steady degradation was observed for M-0.55 and M-1.1 (degradation ∼77-81 %), whereas M-0 and M-0.11 slowed down their degradation (degradation ∼62-69 %). None of the membranes seem to degrade any further between 72 h and 168 h. At the last time-point of immersion, 168 h, the degradation of M-0.11 was ∼62 %, significantly lower than both M-0.55 and M-1.1 in PBS ($p = 0.004$ and 0.01, respectively). However, there were no differences between the two membranes with the highest amount of HA (M-0.55 and M-1.1). At the last time-point, the degradation for M-0 (69 ± 13 %) was in-between the two groups of HA-containing membranes (∼62 - 80 %).

The degradation decreased in the membranes with the lowest amount of HA (0.11 % w/v), since the chemical interaction between ALG and HA was enhanced. In contrast, higher concentrations (0.55 and 1.1 % w/v) promoted degradation, which could be attributed to the instability generated in the structure by the crystalline phase. Moreover, as the HA amount increased, a higher number of HA aggregates were also formed. These aggregates create instability in the ALG-HA structure and contribute to the degradation process. This correlates well with the results of the tensile assays, where HA aggregates compromised the mechanical performance of the membranes in the plastic region, as they increased the rigidity of the membranes and in turn generated failure points. The steady degradation over time observed for all the samples increase the potential of these membranes for GBR applications. This would, on one hand, provide space for the newly formed bone tissue and, on the other hand, avoid a second surgical procedure for extracting the membrane.

6.3.4 Surface characterization each side of the membrane

It is well known that surface characteristics of biomaterials deeply affect cell behavior, influencing adhesion, proliferation and differentiation [20]. Micrographs displaying both FS and MS surface of M-1.1 (the membrane with maximized chemical differences between both sides) are shown in Figure 6.5a-d. The FS showed a highly porous structure, with pore sizes varying from 19 µm to 150 µm with a mean value of $65.9 \pm 28.0\,\mu\text{m}$ (Figure 6.5e). On one hand, pores $\sim 100\,\mu\text{m}$ are usually considered advantageous to achieve an adequate vascularization of the tissue being repaired [21]. On the other hand, pores smaller than $\sim 40\,\mu\text{m}$ can prevent infiltration of unwanted cells [22]. Therefore, the porosity of the FS surface could be expected to allow transport of oxygen and nutrients, irrigation and blood vessels formation, while migration would probably be hindered since no specific methodology was used to promote pores interconnectivity throughout the membrane.

The MS surface exhibited lower pore density than the FS one (Figure 6.5a,b). A similar result was previously shown on chitosan-HA membranes [23], where the addition of HA reduced the biomaterial porosity. The lower pore density observed in the MS surface could be attributed to the effective crosslinking interactions between HA and ALG chains, reinforcing the membrane structure. The bonding between ALG molecules and HA had an immediate effect not only on the microstructures of the membranes, but also in the chemical interaction of the hydrogels [24]. Therefore, it can be hypothesized the ALG chains were successfully grafted on HA surface, making the biomaterials ordered at the nanoscale range.

In addition, HA microaggregates measuring $2.51 \pm 0.65\,\mu\text{m}$ dispersed all over the MS surface were observed (Figures 6.5b, 6.5d). These aggregates are expected to promote the bioactivity of the membranes due to their capability to nucleate and grow calcium phosphate crystals in contact with physiological fluids. As it is well known, this could further stimulate bone regeneration [25]. Moreover, the HA microaggregates would increase the surface area on the MS, enhancing its bioactivity as well as increasing chances for protein entrapment, essential processes

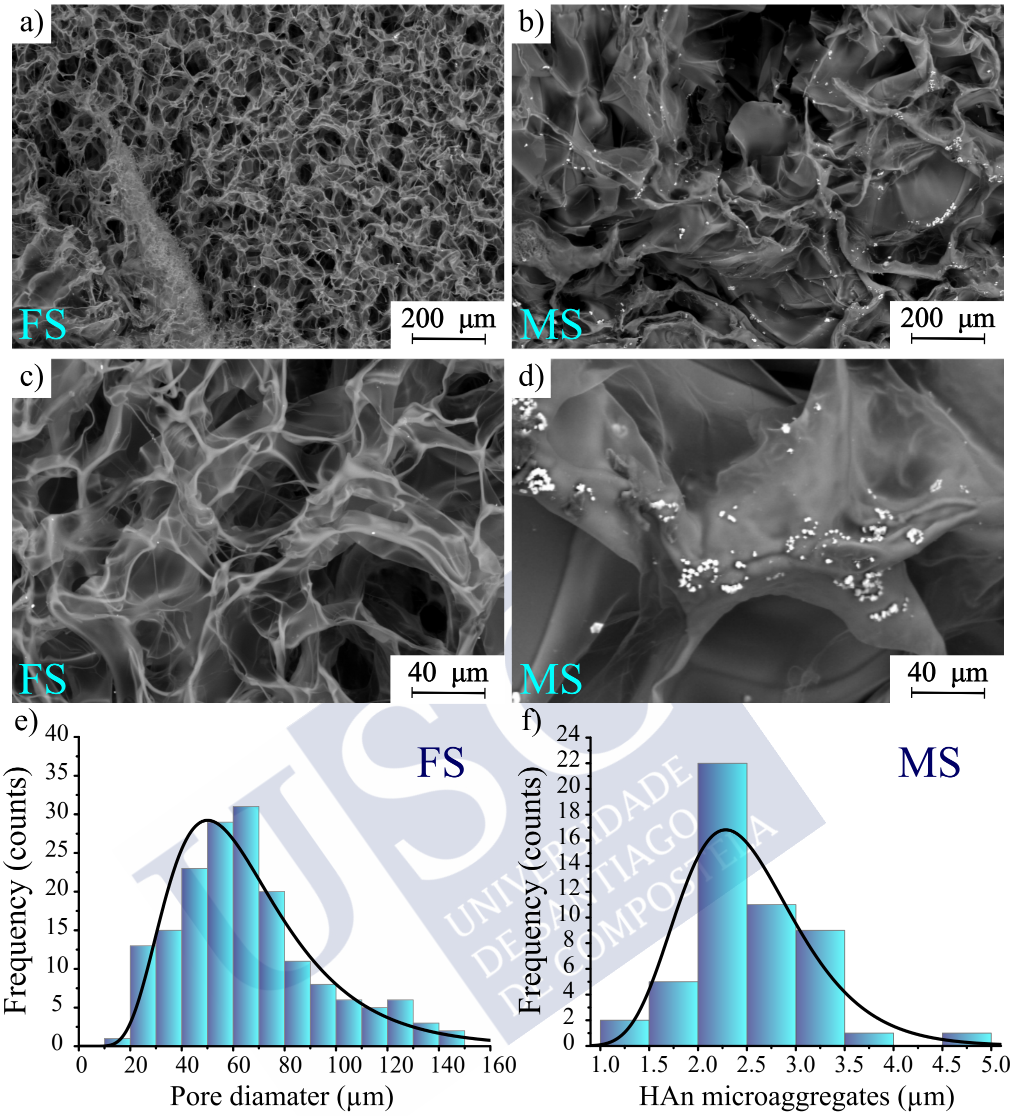

Figure 6.5: Surface characteristics of M-1.1 membranes evaluated by SEM micrographs: a) FS surface and b) MS surface at a 200× magnification; c) FS surface showing the porosity and d) MS surface showing HA microaggregates, at a 1,000× magnification. Histograms displaying e) pore size distribution of the FS surface and f) HA microaggregates size present on the MS.

for the osteoblasts adhesion [26]. Consequently, the HA microaggregates randomly distributed could be expected to enhance discontinuous bone ingrowth. This effect has been correlated with an enhanced osteogenesis since bone would form not only from the margins, but also throughout the whole area [27, 28].

The roughness analysis performed with SEM micrographs was in accordance with the microstructure imaged. The porous FS surface resulted in statistically lower values for both R_a and R_{sk} ($p \leq 0.01$) than the MS surface, which had a lower pore density (Figure 6.6). An appropriate surface roughness can produce beneficial

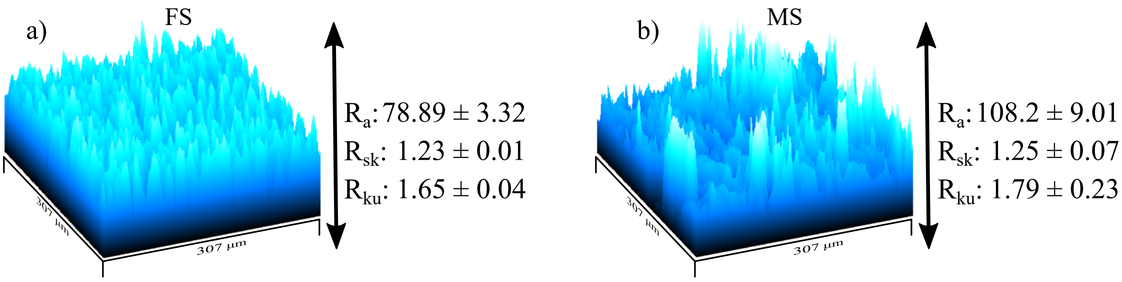

Figure 6.6: Roughness parameters of M-1.1 membrane for the a) MS and b) FS. R_a: arithmetic average surface roughness, R_{sk}: asymmetry coefficient, R_{ku}: kurtosis coefficient.

interlocking of the cells at the initial adhesion stage and improve cell adhesion. The asymmetry coefficient (R_{sk}) used to study the symmetry of the roughness profile over the midline, was positive for both FS and MS, indicating profiles with a high shear resistance, where peaks predominate over valleys [29]. The kurtosis coefficient (R_{ku}) was used for the detection of sharp peaks and isolated deep valleys, since it describes the sharpness of the probability density of the profile [30]. This parameter was lower than 3 for both in MS and FS, meaning a platykurtic distribution of the profile curve, characteristic of profiles with few sharp peaks [30]. Previous studies have proved that the presence of a large number of sharp peaks ($R_{ku} > 3$) on the surface of biomaterials generates an increase in the concentration of stresses in the tissue-biomaterial interface [31], which could even lead to the failure of the biomaterial. Therefore, better responses are in general expected on surfaces with $R_{ku} < 3$, such as the ones found in both surfaces.

6.3.5 Cell culture

6.3.5.1 Osteoblast proliferation and differentiation on the MS of the membranes

Osteoblasts were cultured on the MS of the membranes and their proliferation over time was evaluated using PrestoBlue, an indicator of metabolic active cells (Figure 6.7a). At 3 days, no differences were found among membranes. The number of cells was significantly lower on membranes M-0.11 ($p = 0.016$) and M-0.55 ($p = 0.041$) compared to the TCPS (control), while there were no differences between M-1.1 and TCPS. At 7 days, there were no differences between any of the samples. At day 14, a statistically significant higher number of cells was observed on M-1.1 compared with M-0.55 and M-0.11 ($p = 0.018$ and 0.022, respectively), although no difference was shown between M-0.55 and M-0.11. Interestingly, M-0.55 and M-1.1 had a statistically higher number of cells than TCPS at day 14 ($p = 0.003$). The results showed that all membranes allowed osteoblasts proliferation and this effect

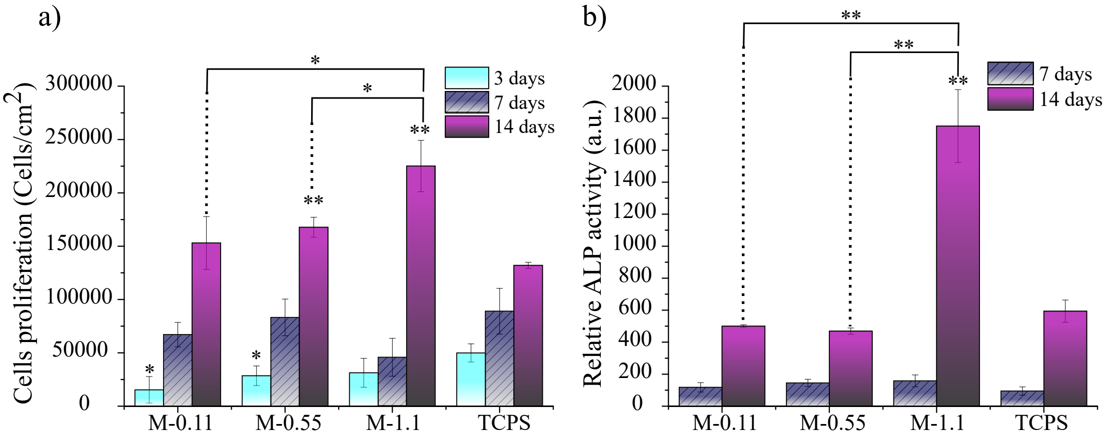

Figure 6.7: Osteoblasts cultured on the MS of the membranes M-0.11, M-0.55 and M-1.1: a) proliferation and b) differentiation. TCPS was used as control. Significant differences between HA-containing membranes and TCPS are indicated on the top of the column, while between the HA-containing membranes with brackets. Significance: * $p <$ 0.05 and ** $p < 0.01$.

seemed to be directly dependent on the amount of HA present on the membranes. HA-0 was not added as a control since good viability of osteoblast on alginate has already been proved before [32].

The capacity of each membrane to stimulate the differentiation of osteoblast-like cells on MS was determined by ALP activity, an early marker of osteoblast differentiation that is expressed just before matrix mineralization begins. Results at 7 days manifested that there were no differences between the tested membranes and TCPS. However, at 14 days, cells showed a statistically superior ALP activity when cultured on M-1.1 compared to the other two membranes ($p = 0.005$ for both, M-0.11 and M-0.55) and TCPS ($p = 0.007$). At the same time point, cells cultured on M-0.11 and M-0.55 did not show any differences compared to TCPS (Figure 6.7b). These results confirm the osteogenic potential of HA [33, 34]. Specifically, a previous study found that a HA coating induced the expression of specific markers involved in stem cell osteogenic differentiation [34].

6.3.5.2 Fibroblast proliferation on the FS of the membranes

Fibroblasts (hDF cells) were cultured on the FS of the membranes to evaluate their growth over time. No differences were found between membranes at any time point. An increase in cell number along time was observed for all materials as well as for TCPS ($p = 0.003$, 0.048, 0.007 and 0.005 for, M-0.11, M-0.55, M-1.1 and TCPS, respectively). Compared with the TCPS, a statistically significant lower number of

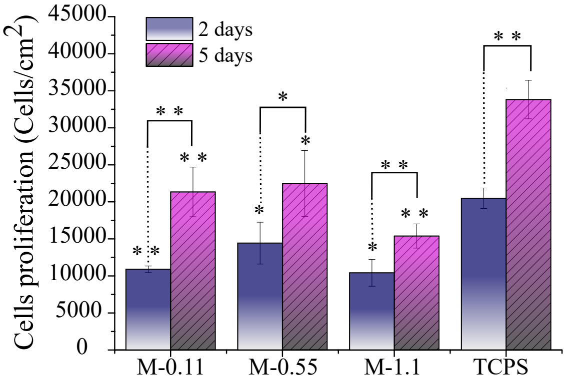

Figure 6.8: Fibroblasts proliferation on the FS of the membranes M-0.11, M-0.55 and M-1.1. TCPS was used as control. Significant differences between HA-containing membranes and TCPS are indicated on the top of the column, while between the 2 and 5 days with brackets. No differences were found between the HA-containing membranes. Significance: * $p < 0.05$ and ** $p < 0.01$.

fibroblasts was determined for all the membranes at day 2 ($p = 0.0003$, 0.03 and 0.015 for M-0.11, M-0.55 and M-1.1, respectively) and at day 5 day ($p = 0.002$, 0.048 and 0.002 for M-0.11, M-0.55 and M-1.1, respectively) (Figure 6.8). However, the control substrate used in this work, TCPS, was mainly used to determine an adequate cell growth rather than evaluating a fair comparison with membranes due to its different chemical and physical properties. Consistently, these results suggest that the fibroblast behaved similarly in all membranes regardless the HA amount used during the crosslinking in the MS. The good viability of fibroblasts on alginate samples was already shown before [32].

Bibliography

[1] L. Benedini, D. Placente, O. Pieroni, and P. Messina, “Assessment of synergistic interactions on self-assembled sodium alginate/nano-hydroxyapatite composites: to the conception of new bone tissue dressings,” *Colloid and Polymer Science*, vol. 295, no. 11, pp. 2109–2121, 2017.

[2] L. F. Sukhodub, L. B. Sukhodub, O. Litsis, and Y. Prylutskyy, “Synthesis and characterization of hydroxyapatite-alginate nanostructured composites for the controlled drug release,” *Materials Chemistry and Physics*, vol. 217, pp. 228–234, 2018.

[3] J. Barros, M. P. Ferraz, J. Azeredo, M. H. Fernandes, P. S. Gomes, and F. J. Monteiro, “Alginate-nanohydroxyapatite hydrogel system: Optimizing the formulation for enhanced bone regeneration,” *Materials Science and Engineering: C*, vol. 105, p. 109985, 2019.

[4] C. Sharma, A. K. Dinda, P. D. Potdar, C.-F. Chou, and N. C. Mishra, “Fabrication and characterization of novel nano-biocomposite scaffold of chitosan–gelatin–alginate–hydroxyapatite for bone tissue engineering,” *Materials Science and Engineering: C*, vol. 64, pp. 416–427, 2016.

[5] Y. Guesmi, H. Agougui, R. Lafi, M. Jabli, and A. Hafiane, “Synthesis of hydroxyapatite-sodium alginate via a co-precipitation technique for efficient adsorption of methylene blue dye,” *Journal of Molecular Liquids*, vol. 249, pp. 912–920, 2018.

[6] R. Mishra, B. Basu, and A. Kumar, “Physical and cytocompatibility properties of bioactive glass–polyvinyl alcohol–sodium alginate biocomposite foams prepared via sol–gel processing for trabecular bone regeneration,” *Journal of Materials Science: Materials in Medicine*, vol. 20, no. 12, p. 2493, 2009.

[7] S. Datta, A. P. Rameshbabu, K. Bankoti, P. P. Maity, D. Das, S. Pal, S. Roy, R. Sen, and S. Dhara, “Oleoyl-chitosan-based nanofiber mats impregnated with amniotic membrane derived stem cells for accelerated full-thickness excisional wound healing,” *ACS Biomaterials Science & Engineering*, vol. 3, no. 8, pp. 1738–1749, 2017.

[8] J. A. Motherway, P. Verschueren, G. Van der Perre, J. Vander Sloten, and M. D. Gilchrist, “The mechanical properties of cranial bone: The effect of loading rate and cranial sampling position,” *Journal of Biomechanics*, vol. 42, no. 13, pp. 2129–2135, 2009.

[9] J. Hilborn and L. M. Bjursten, “A new and evolving paradigm for biocompatibility,” *Journal of Tissue Engineering and Regenerative Medicine*, vol. 1, no. 2, pp. 110–119, 2007.

[10] N. L. D’Elía, A. N. Gravina, J. M. Ruso, J. A. Laiuppa, G. E. Santillán, and P. V. Messina, “Manipulating the bioactivity of hydroxyapatite nano-rods structured networks: Effects on mineral coating morphology and growth kinetic,” *Biochimica et Biophysica Acta (BBA) - General Subjects*, vol. 1830, no. 11, pp. 5014–5026, 2013.

[11] D. L. Kopperdahl and T. M. Keaveny, “Yield strain behavior of trabecular bone,” *Journal of Biomechanics*, vol. 31, no. 7, pp. 601–608, 1998.

[12] H. H. Bayraktar, E. F. Morgan, G. L. Niebur, G. E. Morris, E. K. Wong, and T. M. Keaveny, “Comparison of the elastic and yield properties of human femoral trabecular and cortical bone tissue,” *Journal of Biomechanics*, vol. 37, no. 1, pp. 27–35, 2004.

[13] D. Huang, L. Niu, J. Li, J. Du, Y. Wei, Y. Hu, X. Lian, W. Chen, and K. Wang, "Reinforced chitosan membranes by microspheres for guided bone regeneration," *Journal of the Mechanical Behavior of Biomedical Materials*, vol. 81, pp. 195–201, 2018.

[14] C. E. Misch, Z. Qu, and M. W. Bidez, "Mechanical properties of trabecular bone in the human mandible: Implications for dental implant treatment planning and surgical placement," *Journal of Oral and Maxillofacial Surgery*, vol. 57, no. 6, pp. 700–706, 1999.

[15] S. Mali, L. S. Sakanaka, F. Yamashita, and M. V. E. Grossmann, "Water sorption and mechanical properties of cassava starch films and their relation to plasticizing effect," *Carbohydrate Polymers*, vol. 60, no. 3, pp. 283–289, 2005.

[16] C. Xianmiao, L. Yubao, Z. Yi, Z. Li, L. Jidong, and W. Huanan, "Properties and in vitro biological evaluation of nano-hydroxyapatite/chitosan membranes for bone guided regeneration," *Materials Science and Engineering: C*, vol. 29, no. 1, pp. 29–35, 2009.

[17] S.-H. Teng, E.-J. Lee, B.-H. Yoon, D.-S. Shin, H.-E. Kim, and J.-S. Oh, "Chitosan / nanohydroxyapatite composite membranes via dynamic filtration for guided bone regeneration," *Journal of Biomedical Materials Research Part A*, vol. 88A, no. 3, pp. 569–580, 2009.

[18] J. Mota, N. Yu, S. G. Caridade, G. M. Luz, M. E. Gomes, R. L. Reis, J. A. Jansen, X. F. Walboomers, and J. F. Mano, "Chitosan/bioactive glass nanoparticle composite membranes for periodontal regeneration," *Acta Biomaterialia*, vol. 8, no. 11, pp. 4173–4180, 2012.

[19] M. Dziadek, B. Zagrajczuk, E. Menaszek, and K. Cholewa-Kowalska, "A new insight into in vitro behaviour of poly(ε-caprolactone)/bioactive glass composites in biologically related fluids," *Journal of Materials Science*, vol. 53, no. 6, pp. 3939–3958, 2018.

[20] D. O. Costa, P. D. H. Prowse, T. Chrones, S. M. Sims, D. W. Hamilton, A. S. Rizkalla, and S. J. Dixon, "The differential regulation of osteoblast and osteoclast activity by surface topography of hydroxyapatite coatings," *Biomaterials*, vol. 34, no. 30, pp. 7215–7226, 2013.

[21] Q. L. Loh and C. Choong, "Three-dimensional scaffolds for tissue engineering applications: Role of porosity and pore size," *Tissue Engineering Part B: Reviews*, vol. 19, no. 6, pp. 485–502, 2013.

[22] M. Masoudi Rad, S. Nouri Khorasani, L. Ghasemi-Mobarakeh, M. P. Prabhakaran, M. R. Foroughi, M. Kharaziha, N. Saadatkish, and S. Ramakrishna, "Fabrication and characterization of two-layered nanofibrous membrane for guided bone and tissue regeneration application," *Materials Science and Engineering: C*, vol. 80, pp. 75–87, 2017.

[23] S. B. Qasim, R. M. Delaine-Smith, T. Fey, A. Rawlinson, and I. U. Rehman, "Freeze gelated porous membranes for periodontal tissue regeneration," *Acta Biomaterialia*, vol. 23, pp. 317–328, 2015.

[24] Q. Wang, R. Hou, Y. Cheng, and J. Fu, "Super-tough double-network hydrogels reinforced by covalently compositing with silica-nanoparticles," *Soft Matter*, vol. 8, no. 22, pp. 6048–6056, 2012.

[25] T. Kokubo and H. Takadama, "How useful is sbf in predicting in vivo bone bioactivity?," *Biomaterials*, vol. 27, no. 15, pp. 2907–2915, 2006.

[26] M. S. Laranjeira, M. H. Fernandes, and F. J. Monteiro, "Innovative macroporous granules of nanostructured-hydroxyapatite agglomerates: Bioactivity and osteoblast-like cell behaviour," *Journal of Biomedical Materials Research Part A*, vol. 95A, no. 3, pp. 891–900, 2010.

[27] J. L. Simon, T. D. Roy, J. R. Parsons, E. D. Rekow, V. P. Thompson, J. Kemnitzer, and J. L. Ricci, "Engineered cellular response to scaffold architecture in a rabbit trephine defect," *Journal of Biomedical Materials Research Part A*, vol. 66A, no. 2, pp. 275–282, 2003.

[28] V. Karageorgiou and D. Kaplan, "Porosity of 3d biomaterial scaffolds and osteogenesis," *Biomaterials*, vol. 26, no. 27, pp. 5474–5491, 2005.

[29] K. N. Hansson and S. Hansson, “Skewness and kurtosis: important parameters in the characterization of dental implant surface roughness—a computer simulation,” *ISRN Materials Science*, vol. 2011, 2011.

[30] N. Tayebi and A. A. Polycarpou, “Modeling the effect of skewness and kurtosis on the static friction coefficient of rough surfaces,” *Tribology International*, vol. 37, no. 6, pp. 491–505, 2004.

[31] S. Hansson, “Surface roughness parameters as predictors of anchorage strength in bone: a critical analysis,” *Journal of Biomechanics*, vol. 33, no. 10, pp. 1297–1303, 2000.

[32] A. C. Hernández-González, L. Téllez-Jurado, and L. M. Rodríguez-Lorenzo, “Alginate hydrogels for bone tissue engineering, from injectables to bioprinting: A review,” *Carbohydrate Polymers*, vol. 229, p. 115514, 2020.

[33] N. L. D’Elia, C. Mathieu, C. D. Hoemann, J. A. Laiuppa, G. E. Santillan, and P. V. Messina, “Bone-repair properties of biodegradable hydroxyapatite nano-rod superstructures,” *Nanoscale*, vol. 7, no. 44, pp. 18751–18762, 2015.

[34] J. Sartuqui, C. Gardin, L. Ferroni, B. Zavan, and P. V. Messina, “Nanostructured hydroxyapatite networks: Synergy of physical and chemical cues to induce an osteogenic fate in an additive-free medium,” *Materials Today Communications*, vol. 16, pp. 152–163, 2018.

7

Ultrathin films containing HA nanoparticles

Contents

7.1 Overview 133
7.2 Experimental procedure 134
  7.2.1 Layer by layer film assembly 134
7.3 Discussion 135
  7.3.1 Layer by Layer Build-Up 135
  7.3.2 Mineralization 136
  7.3.3 Cell culture studies 138

7.1 Overview

In this chapter, layer-by-layer (LbL) were used to coat surfaces with HA nanomaterials. LbL is a straightforward and versatile bottom-up surface modification technique that can be applied to coat substrates with different geometries, from simple planar membranes to complex three-dimensional shapes [1–3]. It consists of the consecutive deposition of different materials that are held together by supramolecular forces, such as electrostatic interactions, hydrogen bonding, and van der Walls forces [4]. Its main advantage is the possibility for the incorporation of several classes of materials, including biomolecules and inorganic particles. The surfaces modified by LbL thus exhibit properties that are transferred from the incorporated building blocks. LbL versatility, together with the possibility to use aqueous solutions,

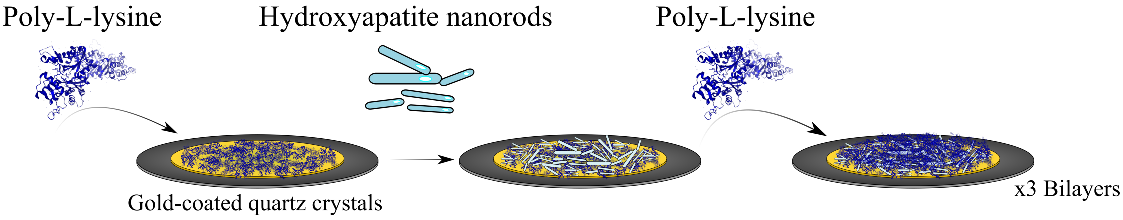

Figure 7.1: Scheme representing the layer-by-layer assembly.

makes this approach a mild and sustainable choice for bioactive surface buildup [5]. LbL films were prepared by combining the polycation poly-L-lysine (PLL) and negatively charged HA nanorods. The electrostatic interactions between PLL and the bioactive HA nanorods result in a sequential hybrid nanocoating consisting of alternate layers of a biomacromolecule and a bioceramic. The starting hypothesis was that the incorporated nanorods resemble not only structurally the inorganic phase of the bone but also biofunctionally, i.e. they will promote osteoinduction and osteoconduction [6, 7].

7.2 Experimental procedure

7.2.1 Layer by layer film assembly

LbL was assembled on gold-coated quartz crystals pre-cleaned by a consecutive immersion in acetone, ethanol, and isopropanol (ultrasound bath, 40 °C, 5 min each). Afterward, the crystals were washed with distilled water, dried under an N_2 flow and plasma treated with UV and O_3. Clean crystals were placed in the QCM-D flow chambers. A dispersion of HA nanorods (0.5 mg/mL) and a solution of PLL (0.1 mg/mL) were prepared separately using acetate buffer (0.1 M, pH = 4.00). A constant flow rate of $50\,\mu\mathrm{L\,min^{-1}}$ at 25 °C was used for the deposition of each layer. The build-up started with PLL injected into the flow chambers for 10 min aided by a peristaltic pump, followed by the HA deposition until frequency (F) and dissipation (D) stabilized. All deposition steps were followed by a rinsing step with acetate buffer (10 min) to remove loosely bound material. LbL constructs with three bilayers were obtained and abbreviated as $[\mathrm{PLL/HA}]_3$.

Cell culture studies presented in this Chapter were conducted by collaborators from the *3B's Research Group*, Portugal.

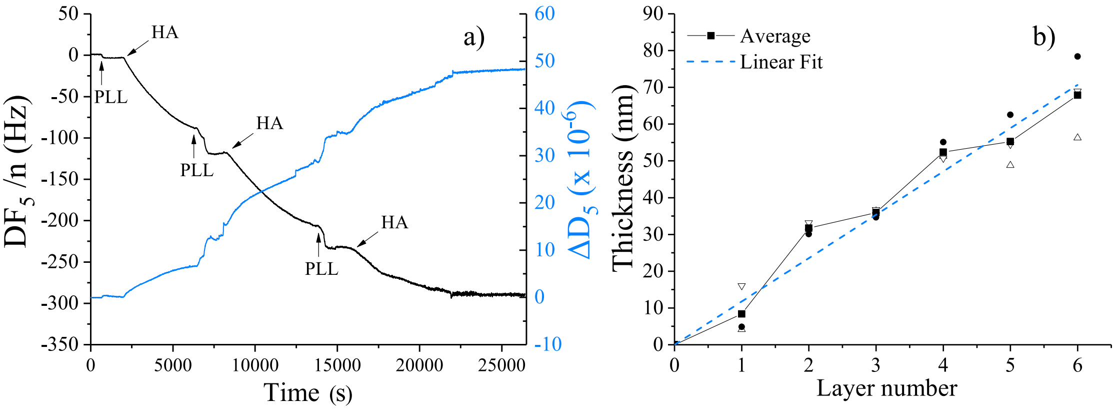

Figure 7.2: Representative normalized variations of frequency ($\Delta F_n/n$) and dissipation (ΔD_n) for the 5th overtone during the assembly of [PLL/HA]$_3$ films. b) Thickness growth of the [PLL/HA]$_3$ films calculated from the Voigt-based viscoelastic model (black) and data fitting (blue) showing linear growth of the LbL construct. Three independent experiments are depicted.

7.3 Discussion

7.3.1 Layer by Layer Build-Up

HA exhibits Ca^{2+} and $PO_4{}^{3-}$ on its surface, which can act as adsorption sites for electrostatic proteins [8]. HA nanorods dispersed in water have ζ-potential of -14 mV and is consistent with previous studies [9]. This negative ζ-potential suggested that HA nanorods can interact with cationic polypeptides via electrostatic interactions. Real time by QCM-D (Figure 7.2) was used to confirm this hypothesis. This equipment allows detection of adsorption of small amounts of material (in the order of nanograms per square centimeter) to a gold-coated quartz sensor [10–12]. In QCM-D, the quartz crystals are exposed to acoustic excitation and oscillate as a result. The oscillation frequency is related to the quantity of adsorbed materials and quantification of frequency changes upon contact with a solute are used to determine whether deposition occurs.

The continuous decrease in $\Delta F_5/5$ with each incremental deposition step confirms successful LbL buildup (Figure 7.2a). Changes in dissipation are related with variations of the viscoelastic properties of the formed construct: high dissipation indicates viscous behavior and damping, associated with the assembly of “soft” films. Likewise, a decrease in ΔD_5 is typical of structural transformation from a dissipative nonrigid surface to a stiffer one. Herein, ΔD_5 increases with each incremental layer, including during the adsorption of the HA nanorods. One would expect that the adsorption of a ceramic material would increase the stiffness of the films, but the results suggest presence of interfacial hydration layers on the

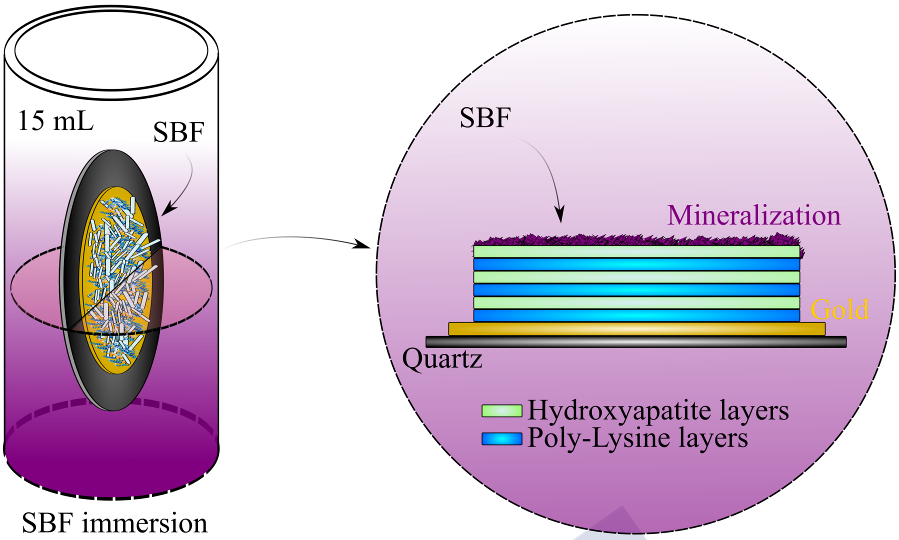

Figure 7.3: Mineralization process. Quartz crystals were placed vertically on 15 mL Falcon tubes and put in contact with simulated body fluid.

surface of HA [13]. Such a layer appears mainly constituted by H_2O molecules coordinated to superficial Ca^{2+} ions approximately in a 1:1 ratio [14]. The film thickness (Figure 7.2b) increased linearly during the buildup. After the adsorption of 3 bilayers, a thickness of 67 nm was obtained, which corresponds to a total area density of $7.8\,\mu g\,cm^{-2}$. Of note, the film growth was higher during the adsorption of HA nanorods (Figure 7.2a). This is due to the contribution of the above mentioned interfacial hydration layers, which translates into more film mass per surface area than their more flexible polycationic macromolecular counterparts. It is also noteworthy how HA nanorods were easily intercalated with the macromolecular compound. Previous experiments with Bioglass® nanospheres required the use of additional polyanion layers to form stable LbLs as the charge of the inorganic material was not sufficient to build a stable construct [6, 7].

7.3.2 Mineralization

The osteoconductive potential of HA-embedded LbL films was evaluated by immersion of the constructs in SBF (Figure 7.3).

The ΔD_n of the films increased as time progressed. Significant increases were produced up to the seventh day, after which the variation was less pronounced (Figure 7.4). The rise in dissipation is consistent with the formation of interfacial hydration layers which are coupled to the nucleation and growth of a mineral hydroxyapatite phase over time [15]. Apatite crystallization is associated with a decrease in the Gibbs free energy as a result of the electrostatic interactions that

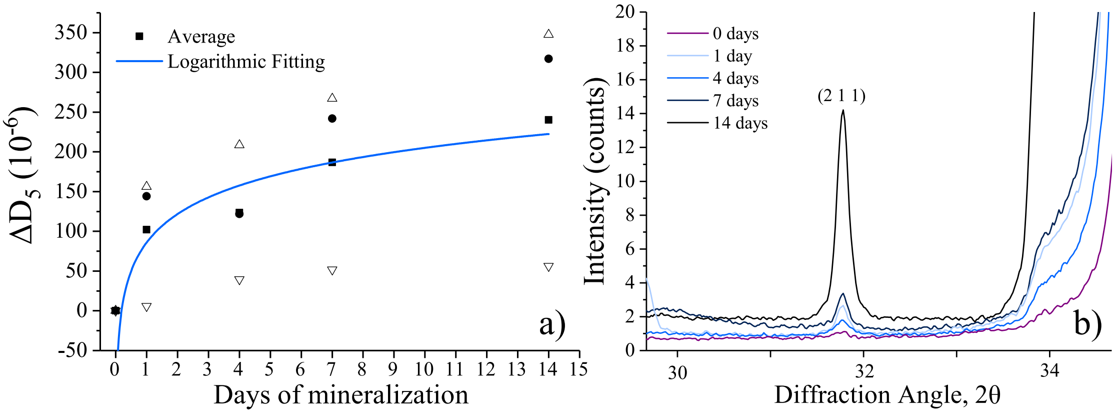

Figure 7.4: Mineralization assessment of $[\text{PLL/HA}]_3$ films. (a) QCM-D measurements of dissipation for the 5^{th} overtone. Data fitting depicts a logarithmic approximation (blue). (b) XRD spectra of the LbL constructs after 1, 4, 7 and 14 days of immersion in SBF. XRD spectra were treated to remove the strong diffraction signals produced by gold and quartz.

induce calcium and phosphate nucleation [16]. Mineralization starts with a complex process of initial nuclei formation and growth. There are different theories explaining this phenomenon. Works from Rodríguez Clemente et al [17]. and López Macipe et al [18]. have described the crystallization route of hydroxyapatite at 37 °C as the result of the coexistence of the amorphous calcium phosphate and octacalcium phosphate precursors in the mineralization solutions. Furthermore, Takadama et al [19]. have reported that an amorphous calcium phosphate initially forms during the nucleation stage and then mutates to a crystalline apatite. X-ray diffraction was used to analyze the crystallinity of the mineralized phase (Figure 7.4b). Information about the development of the mineralization progress was obtained by the reflection specific to the apatite phase ((211) [$2\Theta = 31.8$ degrees]). The intensity of this peak increased over time, getting to the highest value after 14 days of mineralization. This increase showcases the formation of crystalline hydroxyapatite similar to the ones found in natural bone. Furthermore, as it can be inferred from the SEM images (Figure 7.5c–i), the mineralization of $[\text{PLL/HA}]_3$ films started to manifest notoriously after the fourth day of immersion in SBF. After 14 days, the surface was entirely covered by a mineral layer with the typical cauliflower-like morphology of apatite layers. Thus, the *in vitro* formation of HA layer by SBF demonstrated that $[\text{PLL/HA}]_3$ films are osteoconductive.

The QCM-D, XRD and SEM results are in good agreement with the EDS analysis (not shown). On the one hand and as expected, the Ca and P presence in the samples increased gradually as the mineralization progressed. On the other hand, surfaces mineralized for 14 days exhibited a Ca/P ratio of 1.91. As mentioned above,

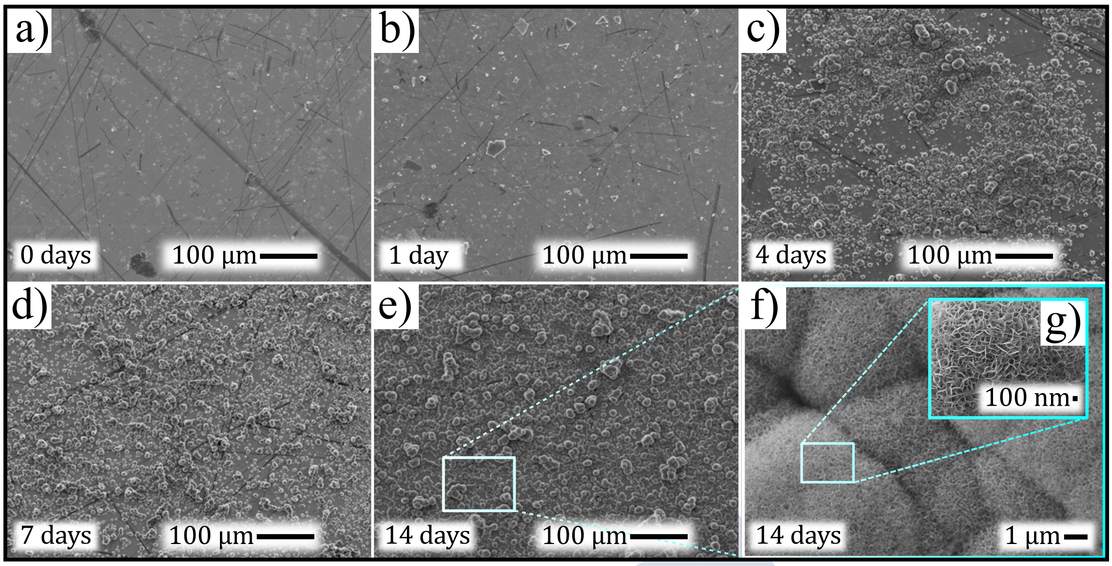

Figure 7.5: (a-g) Scanning electron microscopy of the assembled films after 0, 1, 4, 7 and 14 days in SBF. The lines in (a) and (b) are artifacts from defects on the gold surface. (f, g) High-resolution field emission scanning electron microscopy with different magnifications up to 14 days.

ACP is a precursor phase that precedes the formation of crystalline hydroxyapatite in a supersaturated calcium phosphate solution. ACP particles consist of a random assembly of ion clusters, with a Ca/P molar ratio of about 1.2 compared to the ratio of 1.67 found in stoichiometric hydroxyapatite [20]. The ratio of 1.91 determined for the studied LbL is higher than either of these values, suggesting that, in addition to calcium phosphate, calcium oxide (CaO) is forming as well. Previous studies have demonstrated that higher Ca/P ratios induce increased osteoblast adhesion [21], but can also lower osteoblast viability [22]. Cells response towards the substrate is paramount to develop bone/biomaterial interfaces, as the adhesion of cells to biomedical devices and their viability is an essential factor in defining biological compliance.

7.3.3 Cell culture studies

SaOs-2 osteoblast-like cells were used to evaluate the cytotoxicity of $[PLL/HA]_3$ envisaging the application of these films as mineralizing coatings for implantable devices that will interface with bone. Cells were cultured in contact with $[PLL/HA]_3$ films and $[PLL/HA]_3$ films incubated for 7 days in SBF. This period of mineralization was chosen based on the hydroxyapatite layer growth (Figure 7.6).

After 3 days of culture, the number of osteoblasts adhered to the substrates and their viability was assessed (Figure 7.6). The number of adherent cells (Figure 7.6a)

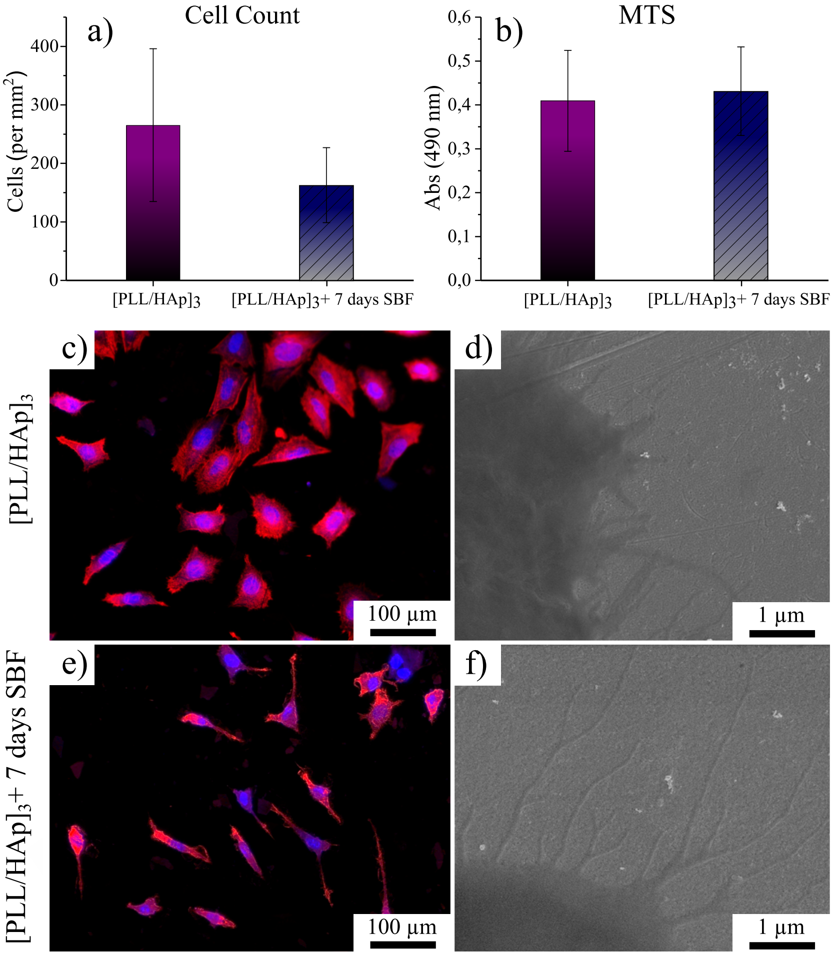

Figure 7.6: SaOs-2 osteoblast-like cells cultured on [PLL/HA]$_3$ and mineralized [PLL/HA]$_3$: (a) number of adherent cells and (b) their viability on [PLL/HA]$_3$ before and after 7 days of mineralization; Data are means ± standard deviation ($p > 0.05$). (c, e) Representative fluorescence microscopy micrographs showing cytoskeletal organization of SaOs-2 cells after 3 days of culture in contact with the studied substrates (nuclei stained in blue with DAPI and actin filaments in the cytoskeleton in red with phalloidin). (d, f) SEM images of SaOs-2 showing formation of filopodia with different lengths in response to the underlaying substrate.

and cell viability (Figure 7.6b) was similar for both substrates. However, microscopy observation evidenced clear morphological differences (Figures 7.6c–f). Staining the cytoskeleton with phalloidin showed that the cells adhered to mineralized substrates were more elongated than cells on [PLL/HA]$_3$ films. HR-SEM images confirmed the formation of filopodia extensions from osteoblasts adherent on both substrates, though these cytoplasmic projections were more numerous, longer, and branched in the SaOs-2 cells cultured on mineralized surfaces as compared with the pristine ones. The abundance of long filopodia with lateral protrusions is in agreement with the response of osteoblastic cells to surfaces engineered to promote high spreading and strength of adhesion [23, 24]. With more developed filopodia from SaOs-2 cells on our mineralized films, we confirm that their resemblance with the crystalline hydroxyapatite promote a more intimate contact of osteoblasts than on non-mineralized $[PLL/HA]_3$ films.

Bibliography

[1] R. R. Costa and J. F. Mano, “Polyelectrolyte multilayered assemblies in biomedical technologies,” *Chemical Society Reviews*, vol. 43, no. 10, pp. 3453–3479, 2014.

[2] P. T. Hammond, “Engineering materials layer-by-layer: Challenges and opportunities in multilayer assembly,” *AIChE Journal*, vol. 57, no. 11, pp. 2928–2940, 2011.

[3] X. Q. Liu and C. Picart, “Layer-by-layer assemblies for cancer treatment and diagnosis,” *Advanced Materials*, vol. 28, no. 6, pp. 1295–1301, 2016.

[4] J. a. Borges and J. a. F. Mano, “Molecular interactions driving the layer-by-layer assembly of multilayers,” *Chemical Reviews*, vol. 114, no. 18, pp. 8883–8942, 2014.

[5] J. J. Richardson, M. Björnmalm, and F. Caruso, “Technology-driven layer-by-layer assembly of nanofilms,” *Science*, vol. 348, no. 6233, p. aaa2491, 2015.

[6] S. J. Rego, A. C. Vale, G. M. Luz, J. F. Mano, and N. M. Alves, “Adhesive bioactive coatings inspired by sea life,” *Langmuir*, vol. 32, no. 2, pp. 560–568, 2016.

[7] J. R. Rodrigues, N. M. Alves, and J. F. Mano, “Biomimetic polysaccharide/bioactive glass nanoparticles multilayer membranes for guided tissue regeneration,” *RSC Advances*, vol. 6, no. 79, pp. 75988–75999, 2016.

[8] L. J. Cummings, M. A. Snyder, and K. Brisack, “Protein chromatography on hydroxyapatite columns,” *Methods in Enzymology*, vol. 463, pp. 387–404, 2009.

[9] Y. Cai, Y. Liu, W. Yan, Q. Hu, J. Tao, M. Zhang, Z. Shi, and R. Tang, “Role of hydroxyapatite nanoparticle size in bone cell proliferation,” *Journal of Materials Chemistry*, vol. 17, no. 36, pp. 3780–3787, 2007.

[10] K. A. Marx, “Quartz crystal microbalance: A useful tool for studying thin polymer films and complex biomolecular systems at the solution-surface interface,” *Biomacromolecules*, vol. 4, no. 5, pp. 1099–1120, 2003.

[11] P. Roach, D. Farrar, and C. C. Perry, “Interpretation of protein adsorption: Surface-induced conformational changes,” *Journal of the American Chemical Society*, vol. 127, no. 22, pp. 8168–8173, 2005.

[12] C. Tamerler, E. E. Oren, M. Duman, E. Venkatasubramanian, and M. Sarikaya, “Adsorption kinetics of an engineered gold binding peptide by surface plasmon resonance spectroscopy and a quartz crystal microbalance,” *Langmuir*, vol. 22, no. 18, pp. 7712–7718, 2006.

[13] D. Zahn and O. Hochrein, “Computational study of interfaces between hydroxyapatite and water,” *Physical Chemistry Chemical Physics*, vol. 5, no. 18, pp. 4004–4007, 2003.

[14] L. Bertinetti, A. Tampieri, E. Landi, C. Ducati, P. A. Midgley, S. Coluccia, and G. Martra, “Surface structure, hydration, and cationic sites of nanohydroxyapatite: Uhr-tem, ir, and microgravimetric studies,” *The Journal of Physical Chemistry C*, vol. 111, no. 10, pp. 4027–4035, 2007.

[15] J. Zhan, Y.-H. Tseng, J. Chan, and C.-Y. Mou, “Biomimetic formation of hydroxyapatite nanorods by a single-crystal-to-single-crystal transformation,” *Advanced Functional Materials*, vol. 15, no. 12, pp. 2005–2010, 2005.

[16] Y. Xie, X. Liu, P. K. Chu, and C. Ding, “Nucleation and growth of calcium–phosphate on ca-implanted titanium surface,” *Surface Science*, vol. 600, no. 3, pp. 651–656, 2006.

[17] R. Rodríguez-Clemente, A. López-Macipe, J. Gómez-Morales, J. Torrent-Burgués, and V. M. Castaño, “Hydroxyapatite precipitation: A case of nucleation-aggregation-agglomeration-growth mechanism,” *Journal of the European Ceramic Society*, vol. 18, no. 9, pp. 1351–1356, 1998.

[18] M. M. Lopez and D. Kosk-Kosicka, “Spectroscopic analysis of halothane binding to the plasma membrane ca 2+-atpase,” *Biophysical journal*, vol. 74, no. 2, pp. 974–980, 1998.

[19] H. Takadama, H.-M. Kim, F. Miyaji, T. Kokubo, and T. Nakamura, *Mechanism of Apatite Formation Induced by Silanol Groups—TEM Observation*, vol. 108. 2000.

[20] J. Yun, B. Holmes, A. Fok, and Y. Wang, “A kinetic model for hydroxyapatite precipitation in mineralizing solutions,” *Crystal Growth & Design*, vol. 18, no. 5, pp. 2717–2725, 2018.

[21] C. Ergun, H. Liu, T. J. Webster, E. Olcay, c. Yilmaz, and F. C. Sahin, “Increased osteoblast adhesion on nanoparticulate calcium phosphates with higher ca/p ratios,” *Journal of Biomedical Materials Research Part A*, vol. 85A, no. 1, pp. 236–241, 2008.

[22] H. Liu, H. Yazici, C. Ergun, T. J. Webster, and H. Bermek, “An in vitro evaluation of the ca/p ratio for the cytocompatibility of nano-to-micron particulate calcium phosphates for bone regeneration,” *Acta Biomaterialia*, vol. 4, no. 5, pp. 1472–1479, 2008.

[23] D. Guadarrama Bello, A. Fouillen, A. Badia, and A. Nanci, “A nanoporous titanium surface promotes the maturation of focal adhesions and formation of filopodia with distinctive nanoscale protrusions by osteogenic cells,” *Acta Biomaterialia*, vol. 60, pp. 339–349, 2017.

[24] M. Salido, J. I. Vilches, J. L. Gutierrez, and J. Vilches, “Actin cytoskeletal organization in human osteoblasts grown on different dental titanium implant surfaces,” *Histology and Histopathology*, vol. 22, no. 12, pp. 1355–64, 2007.

8

Biomimetic fiber mesh scaffolds

Contents

8.1 Overview 143
8.2 Experimental procedure 144
8.2.1 Preparation of nano-fibrous gelatin-HA scaffolds 144
8.3 Discussion 144
8.3.1 Mineralized cross-linked gelatin-HA scaffolds 144

8.1 Overview

In this chapter, the preparation of collagenous derived fiber mesh frameworks was manipulated in order to display a specific composition, morphology, open macroporosity, surface roughness and permeability characteristics. Next, the effect of the induced physicochemical attributes on the scaffold's mechanical behavior, bone bonding potential and biodegradability were evaluated. It was found that the scaffold microstructure, their inherent surface roughness, and the compression strength of the gelatin scaffolds can be modulated by the effect of the cross-linking agent and, essentially, by mimicking the nano-scale size of hydroxyapatite in natural bone. A clear effect of bioactive hydroxyapatite nano-rods on the scaffolds skills can be appreciated and it is greater than the effect of the cross-linking agent, offering a huge perspective for the upcoming progress of bone implant technology.

8.2 Experimental procedure

8.2.1 Preparation of nano-fibrous gelatin-HA scaffolds

Bone-like HA nanoparticles of 8 ± 1 nm diameter and 28 ± 3 nm length were prepared by the methodology described in Chapter 4. To obtain the cross-linked gelatin-HA scaffolds, a 0.80 g/mL gelatin (GE) solution was prepared by dissolution of the proper amount of commercial GE in 35 mL of sodium acetate buffer ($\mathrm{pH} = 4.5$). First, GE was left to hydrate for 30 minutes at RT, and then dissolved at 58 °C under stirring at 500 rpm during 30 minutes; finally it was allowed to rest in a thermostatic bath for 24 h in order to reach equilibrium. Afterward 0.85 mg/mL of HA nanoparticles were added to the previouly described GE solution under vigorous sonication. After the homogeneous dispersion of HA into GE solution was obtained, cross-linking modified scaffolds were prepared using tannic acid (TA) as cross-linking agent. First, GE-HA solution's pH was adjusted to $\mathrm{pH} = 11$ by addition of $NaHCO_3$. Second, TA powder (12.4 and 33.3 mg/g GE) was added to the solution slowly under stirring at 500 rpm. Finally, after the integration of all reagents, the solution was magnetically stirred for 20 minutes to achieve the crosslinking process. The obtained gels were cooled under -50 °C during 24 h and lyophilized in a Rificor L-A-B4 lyophilizer. The selected amounts of GE, TA and HA used in this work are the suitable to guarantee an effective cross-linking effect on gelatin matrix avoiding the grafting and branching reactions between gelatin and TA in conjunction with the hydrogen bonding between gelatin and TA molecules [1]; and for the attainment of uniaxial orientation porouss framework [2]. Scaffolds mineralization process was performed following the layer by layer deposition method described by Taguchi et al. [3].

In the present Chapter, the preparation of the samples, thermal characterization and mineralization studies were performed by collaborators from *Universidad del Sur*, Argentina.

8.3 Discussion

8.3.1 Mineralized cross-linked gelatin-HA scaffolds

8.3.1.1 Physical characterization

The success of a scaffold material requires the activation of the appropriate and beneficial responses from the cells with which it is seeded or from the tissue where it is implanted [4]. A critical configuration of pore degree, interconnection, geometry, orientation and sizes is necessary to maintain the proper cell–cell interactions, the

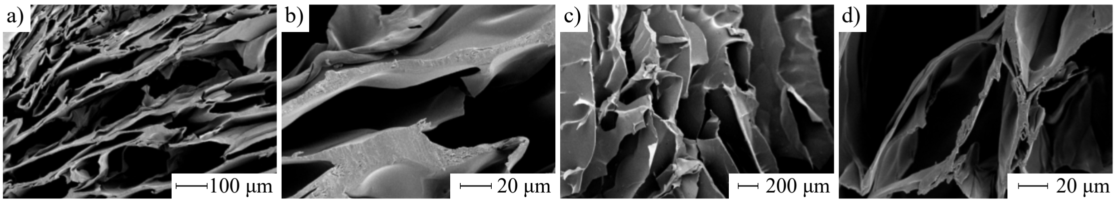

Figure 8.1: (a-b) Longitudinal and (c-d) transversal FE-SEM microphotographs of lyophilized GE-HA sample, 0.80 g/mL GE and 0.85 mg/mL HA.

cellular density and to provide the correct mass transfer of oxygen, nutrients and waste products [4]. In order to examine if those characteristics can be attained by the GE-HA nano-rods interaction under the selected experimental conditions, transverse and longitudinal sections of the GE-HA lyophilized solutions were taken and analyzed using FE-SEM; results are shown in Figure 8.1. Cross and vertical sections of the samples exhibited a nearly analogous highly interconnected macroporous structure, denoting homogeneity between HA nanoparticles and the organic polymer intermingling; Figure 8.1a-d. Nano-sized HA particles were uniformly distributed within the pore walls and no aggregates appeared in pores, their presence was confirmed by X-ray diffraction patterns. The width of the open interconnected macropores typically ranges between 35 and 288 µm with a mean pore size of 102 ± 25 µm in their smallest dimension, and from 90 - 1300 µm with a mean pore size of 300 ± 32.5 µm in the largest one. Their dimensions are comparable to those given in literature [4, 5] for materials that resulted in an acceptable cell response, suggesting that it might be suitable for osseous regeneration. The pore wall surface of GE-HA material was not smooth and emerged as an assembly of aligned fibers with more than ten microns in length, Figures 8.2a and b. Stress points will arise in the bone adjacent to the implant roughness peaks as a result of the elasticity modulus of the graft material that is substantially higher than that of native tissue [6]. In order to evaluate the pore wall surface roughness and to characterize their asymmetry, surface profiles were performed and the kurtosis (R_{ku}) and skewness (R_{sw}) coefficients were computed by means of digitalized scanning electron microscopy (SEM) images, Figure 8.2b. The scaffolds' pore walls present positive values of skewness coefficient ($R_{sk} = 1.592$) showing the presence of a surface profile composed of filled valleys and/or high peaks. The obtained value was of $R_{ku} = 2.165$; since a $R_{ku} < 3$ the distribution curve is said to be platykurtoic and denotes the presence of relatively few high peaks and low valleys, Figure 8.2c and d.

The sharper the asperities of the implant surface roughness, the higher the stress peaks in the bone interface [7] and, excessive bone stresses will result in bone resorption [8]. Taking into consideration that this material exhibits a certain

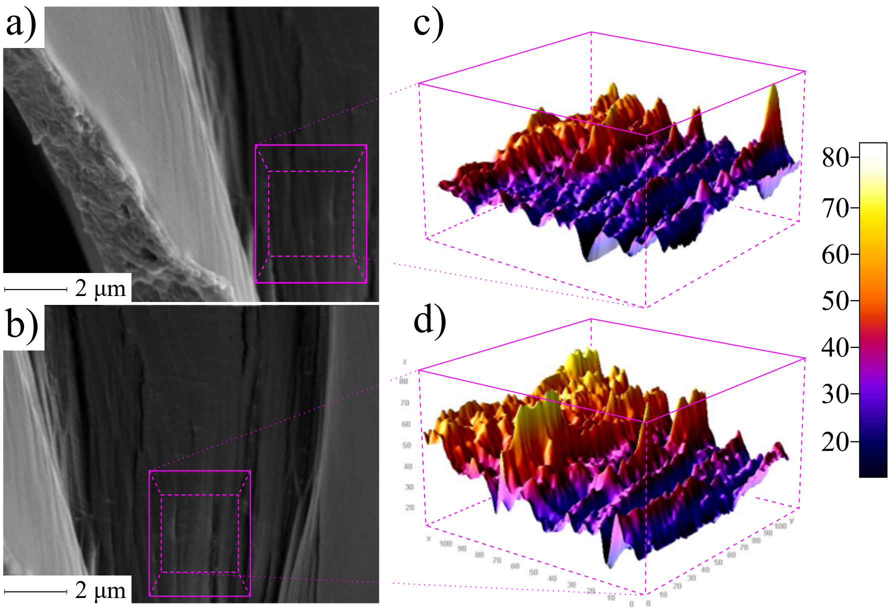

Figure 8.2: (a,b) Pore wall morphology of lyophilized GE-HA sample, 0.80 g/mL GE and 0.85 mg/mL HA. (c,d) 3D surface profiles of GE-HA scaffolds pore's walls.

degree of roughness in the pore wall surfaces, but not an excess of high peaks, it is safe to suggest that it might lead to less stress and better acceptance by the host tissue. Figure 8.3 shows the cross-linked GE-HA scaffolds prepared using two different concentrations of the cross-linked agent (TA), no differences can be appreciated among transversal and longitudinal views. Scaffolds retain their macroporous structure and roughness ($R_{ku} = 2.261$ and $R_{sk} = 1.425$) with a reduction of the mean pore diameter to 72.5 ± 8.9 µm, an increased interconnection and valley landscapes on its topography profile. The fiber structure is clearly visible forming a random mesh network; no significant differences can be appreciated on scaffolds' morphology and roughness among the selected TA concentrations.

8.3.1.2 Thermal properties

It is important to carry out studies on the thermal properties of the scaffolds; the changes in thermal stability are good indicators of structuration and the cross-linking. Although gelatin is the denatured form of collagen [9]; under the proper conditions, i.e., a scaffolding process activated by a cross-linking agent, the chains are able to undergo into a conformational disorder-order transition and to recover a percentage of the triple-helix structure by a partial renaturation process [9]. The differential scanning calorimetric (DSC) thermograms of the GE-TA and GE-HA-TA scaffolds, shown in Figure 8.4, displayed two transitions due to heating. The temperature of the first transition was determined as a point of a sudden increase

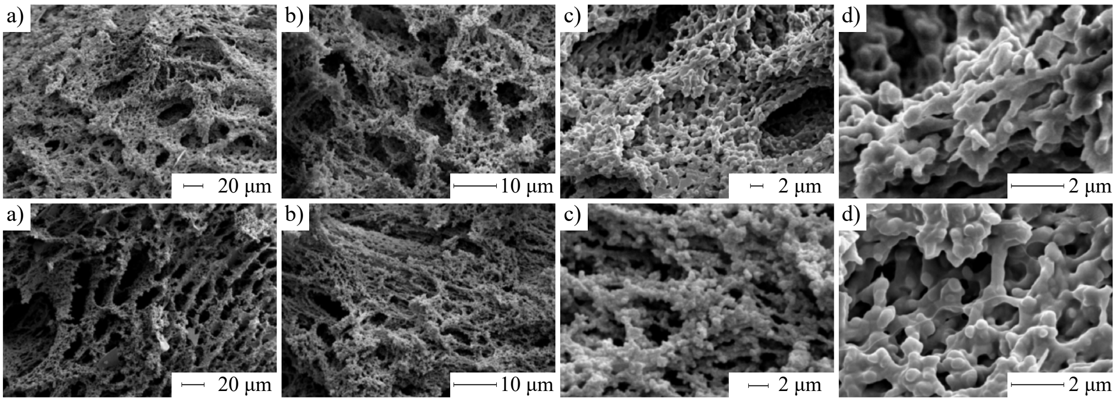

Figure 8.3: FE-SEM microphotographs of GE-HA-TA cross-linked scaffolds. (a-d) 12.4 mg TA/g GE sample: (a) transversal and (b-d) longitudinal views. (e-h) 33.3 mg TA/g GE sample: (e) transversal and (f- h) longitudinal views.

in the thermogram base line (line *i-ii*), whereas the temperature of the second one was evaluated as the maximum of its endothermic peak (peak *iii*). These temperatures represent the glass (T_g) and the melting (T_m) transition, respectively. Glass transition seemed to overlap with an enthalpy relaxation phenomena. Several sub-T_g relaxations can be detected in biopolymers [10], as observed in collagenous materials, they could correspond to the intermolecular mobility of tropocollagen molecules (α relaxation mode) and to the intermolecular mobility of polar sequences (β relaxation modes) [11]. These chains' movements are highly sensitive to hydration and the formation of H-bonds; an increment of cross-linking agent concentration or the presence of HA nano-rods provokes the resolution of the intermolecular bonds and to the rearrangements of gelatin's chains segments linked by these hydrogen bonds. Analyzing the obtained T_g values, a higher glass transition temperature respect to uncross-linked gelatin sample can be distinguished with the increase of TA concentration and with the incorporation of HA nano-rods; indicating an improved thermal stability as a consequence of the increased degree of cross-linking. For the scaffolds prepared with high content of TA and HA nano-rods, DSC thermograms exhibited an endothermic overshoot in the temperature range of the glass to liquid transition. This overshoots are the main signature of enthalpy relaxation during physical aging [12]. They systematically shift to lower temperatures and intensify in magnitude with the presence of HA nano-rods. For the uncross-linked gelatin sample, T_m is referred to as the helix-coil transition [13]. The area underneath the endotherm melting peak divided by the total sample weight (ΔH, J/g) indicates the percentage of structural order in the scaffold. The stability of the helix is primarily dependent on the special features of three polypeptide strands that were held together in a helical conformation by hydrogen bonds, supplemented by inter-chain

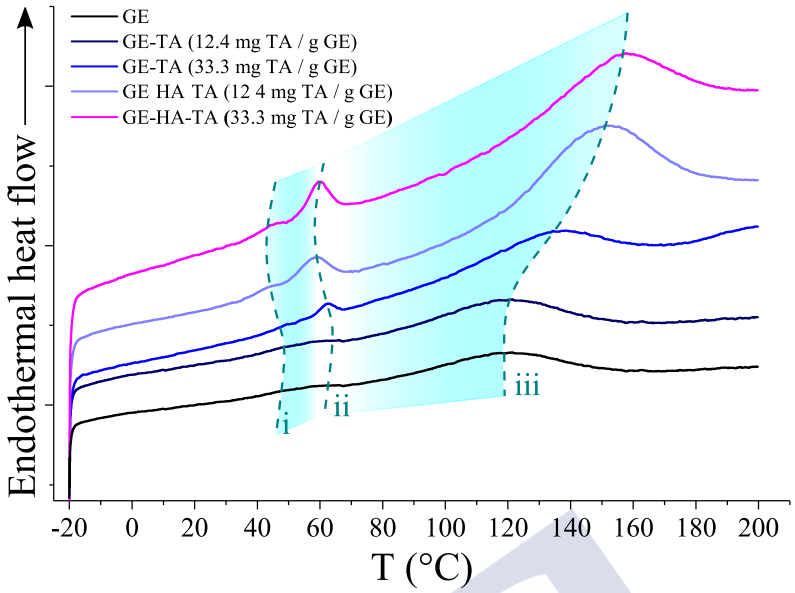

Figure 8.4: DSC thermograms of GE-TA and GE-HA-TA scaffolds.

hydrogen bonds at the positions occupied by glycine [14]. It should be noticed that all the samples used in the DSC analysis were lyophilized exhibiting a negligible water content, which would exclude their potential influence on the denaturation temperature and the enthalpy of helix–coil transition, and hence, the differences in their respective thermal behaviors were a consequence of processing and cross-linking. In all cases cross-linking increases the melting temperature, cross-linked agent plus the presence of HA nano-rods cause a rising of thermal stability in comparison with uncross-linked gelatin sample. The intensification of the transition enthalpy associated with this peak is related to the relative amount of triple helical structure in the samples, and it is significantly greater for the scaffolds containing higher amounts of TA and HA nano-rods. In addition, the higher enthalpy value for the scaffolds prepared from gelatin with nano-rods HA indicates that it had superior renaturation level than their counterparts, which would result to an improved percentage of elongation valueas and mechanical strength [15].

The activation energy (E_a) values for denaturation of scaffolds are higher than the obtained for uncross-linked gelatin sample. This fact clearly shows that more energy is required to denature the scaffolds systems when compared to native gelatin. For its part, analyzing the heat capacity change due to cross-links, which is much less pronounced than the effect over T_m and the subsequent enthalpy contribution, the results for GE-TA-HA scaffolds with the highest cross-linking agent show a slight ΔC_p increase as compared with the sample before cross-linking. However, the changes are too small to establish if the cross-links affect the configurational and vibrational contributions of protein stability. Heat capacity can be expressed as the covariance in enthalpy-entropy fluctuations, $C_p = \delta H \delta S/kT$, that is an estimation of the entropy-enthalpy compensation [16]. From values of ΔH and ΔC_p, it can be inferred that entropy changes are important.

8.3.1.3 Bone-bonding potential and bio-degradability

On basis of the previous results, the mineralized GE-HA-TA (12.4 mg TA/ g GE) scaffold was selected as the specimen with the best mechanical properties, thermal stability, porosity volume fraction and structural permeability to indirectly evaluate their potential use in bone tissue reparation. *In vivo*, degradability can be attained by simply dissolution in biological fluids or cell mediated interactions [17, 18]. The scaffolds degradability was analyzed in three different situations: (i) dissolution under pH = 7.4 conditions concerning to physiological fluids; (ii) dissolution under pH = 4.2 conditions regarding to resorption process in charge of osteoclast and (iii) dissolution by enzymatic catalyzed decomposition. The results, Figure 8.5h, clearly show that the initial degradation rate as well as the scaffold maximum degradation was attained after enzymatic catalyzed conditions, followed by the degradation under resorption conditions (pH = 4.2). The scaffold also experiment a partial degradation (15 %) under physiological fluids conditions and that affect the deposition of biogenic HA crystals, Figure 8.5a-f, an essential processes to ensure osseo-integration [19].

Bioactivity is defined as the property of materials to develop a direct, adherent and strong bonding with bone tissue. A simpler method to estimate the bone-bonding potential of materials consists of the immersions of this material in simulated body fluid (SBF). According to Kokubo et al. [19], an essential requirement is the formation of a calcium phosphate layer on the material surface, usually called bone-like apatite. This bone-like apatite seems to activate signaling proteins and cells to start the cascade of events that results in bone formation [20]. In others words, as previously explained in this work, a way to evaluate the *in vivo* behavior is from the bioactivity test by immersion of the synthetic material into SBF solution [21]. Figures 8.5a-e show the SEM microphotographs of apatite coatings deposited on the studied materials after 7, 14 and 21 days incubation in 1.5 SBF. After the first 7 days of immersion, a continuous layer of mineral coating, exhibiting a spherulitic micro-morphology, grew on scaffold surfaces, Figures 8.5a and b. The nuclei were spherical-like globules with 2 µm in diameter composed by agglomerates of plate-like nano-morphology crystals of ∼150 nm length. After 14 days of immersion in 1.5 SBF, the HA crystal coatings exhibited the same basic micro-morphology but with a reduction of resolution; the perfect spherulitic agglomerates of HA

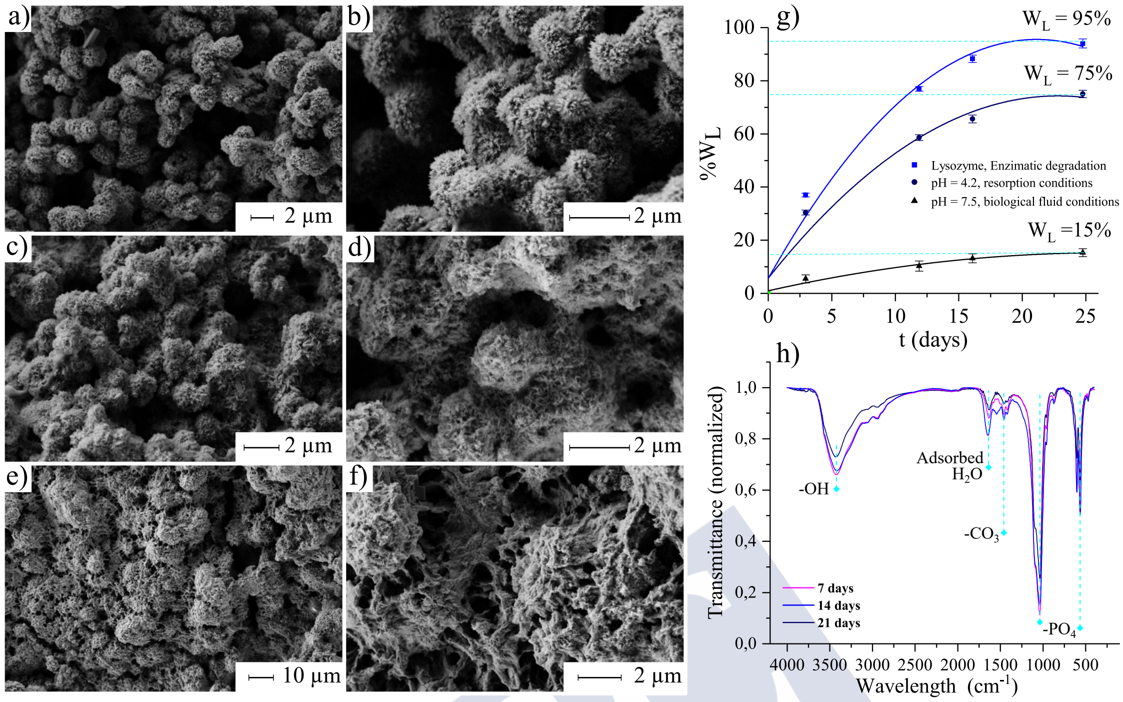

Figure 8.5: Biomimetic growth of HA crystals after (a-b) 7 days; (c-d) 14 days and (e-f) 21 days of immersion in SBF. (g) FT-IR of GE-HA-TA scaffold after immersion in SBF. (h) GE-HA-TA scaffold kinetic degradation process.

crystals that were visible after 7 days, looked elongated and eroded, Figures 8.5c and d. Subsequently, completed the 21 days of immersion it can be appreciated gaps between the spherulitic structures, Figures 8.5e and f. It can be safely assumed that it is due to a partial degradation of the scaffold and thereby to a partial destruction of the structure that supports the deposited HA layer. As seen in the FT-IR spectra, there is a reduction of the peaks relating to hydroxyapatite with the rise of immersion, Figure 8.5g. For its part, EDX microanalysis showed that after the bioactivity assay the material with spherulitic-like coating showed a Ca/P = 1.64 that would be ascribed to HA crystals. A reduction of Ca/P ratio can be appreciated with the increment of immersion time, in agreement with the scaffold degradation time evolution. However at all times the Ca-P globules covering the scaffold surface exhibited a Ca/P ratio close to that exists in the trabecular and cortical bone, and their morphology is similar to that considered essential for the development of events involving osteoblasts to attain osseo-integration [19, 20].

Bibliography

[1] X. Zhang, M. D. Do, P. Casey, A. Sulistio, G. G. Qiao, L. Lundin, P. Lillford, and S. Kosaraju, "Chemical modification of gelatin by a natural phenolic cross-linker, tannic acid," *Journal of agricultural and food chemistry*, vol. 58, no. 11, pp. 6809–6815, 2010.

[2] J. Sartuqui, N. D'Elía, A. N. Gravina, and P. V. Messina, "Analyzing the hydrodynamic and crowding evolution of aqueous hydroxyapatite-gelatin networks: Digging deeper into bone scaffold design variables," *Biopolymers*, vol. 103, no. 7, pp. 393–405, 2015.

[3] T. Taguchi, A. Kishida, and M. Akashi, "Apatite formation on/in hydrogel matrices using an alternate soaking process: Ii. effect of swelling ratios of poly (vinyl alcohol) hydrogel matrices on apatite formation," *Journal of Biomaterials Science, Polymer Edition*, vol. 10, no. 3, pp. 331–339, 1999.

[4] J. Velema and D. Kaplan, *Biopolymer-based biomaterials as scaffolds for tissue engineering*, pp. 187–238. Springer, 2006.

[5] P. Sepulveda, A. H. Bressiani, J. C. Bressiani, L. Meseguer, and B. König, "In vivo evaluation of hydroxyapatite foams," *Journal of Biomedical Materials Research*, vol. 62, no. 4, pp. 587–592, 2002.

[6] S. Timoshenko, "Jn goodier theory of elasticity," *New York, McGraw-Hill*, vol. 5, p. 50o, 1951.

[7] K. N. Hansson and S. Hansson, "Skewness and kurtosis: important parameters in the characterization of dental implant surface roughness—a computer simulation," *ISRN Materials Science*, vol. 2011, 2011.

[8] F. Isidor, "Loss of osseointegration caused by occlusal load of oral implants. a clinical and radiographic study in monkeys," *Clinical oral implants research*, vol. 7, no. 2, pp. 143–152, 1996.

[9] Y. Zhang, J. Venugopal, Z.-M. Huang, C. Lim, and S. Ramakrishna, "Crosslinking of the electrospun gelatin nanofibers," *Polymer*, vol. 47, no. 8, pp. 2911–2917, 2006.

[10] Y. Liu, B. Bhandari, and W. Zhou, "Glass transition and enthalpy relaxation of amorphous food saccharides: a review," *Journal of agricultural and food chemistry*, vol. 54, no. 16, pp. 5701–5717, 2006.

[11] B. Nasser, "Rehydration mechanisms in collagen as seen by thermally stimulated current," *European Scientific Journal*, vol. 9, no. 9, 2013.

[12] V. M. Boucher, D. Cangialosi, A. Alegría, and J. Colmenero, "Enthalpy recovery of glassy polymers: Dramatic deviations from the extrapolated liquidlike behavior," *Macromolecules*, vol. 44, no. 20, pp. 8333–8342, 2011.

[13] P. Sobral and A. Habitante, "Phase transitions of pigskin gelatin," *Food hydrocolloids*, vol. 15, no. 4, pp. 377–382, 2001.

[14] M. D. Shoulders and R. T. Raines, "Collagen structure and stability," *Annual review of biochemistry*, vol. 78, p. 929, 2009.

[15] M. Jridi, N. Souissi, A. Mbarek, G. Chadeyron, M. Kammoun, and M. Nasri, "Comparative study of physico-mechanical and antioxidant properties of edible gelatin films from the skin of cuttlefish," *International journal of biological macromolecules*, vol. 61, pp. 17–25, 2013.

[16] N. V. Prabhu and K. A. Sharp, "Heat capacity in proteins," *Annu. Rev. Phys. Chem.*, vol. 56, pp. 521–548, 2005.

[17] R. Baron, L. Neff, D. Louvard, and P. J. Courtoy, "Cell-mediated extracellular acidification and bone resorption: evidence for a low ph in resorbing lacunae and localization of a 100-kd lysosomal membrane protein at the osteoclast ruffled border," *The Journal of Cell Biology*, vol. 101, no. 6, pp. 2210–2222, 1985.

[18] X. Zhou, Q. Cai, N. Yan, X. Deng, and X. Yang, "In vitro hydrolytic and enzymatic degradation of nestlike-patterned electrospun poly (d, l-lactide-co-glycolide) scaffolds," *Journal of Biomedical Materials Research Part A*, vol. 95, no. 3, pp. 755–765, 2010.

[19] T. Kokubo, H. Kushitani, S. Sakka, T. Kisugi, and T. Yamamuro, "Solutions able to reproduce in vivo surface-structure changes in bioactive glass-ceramic a-w3," *J. Biomed. Mat. Res.*, vol. 24, pp. 721–734, 1990.

[20] P. S. Vanzillotta, M. S. Sader, I. N. Bastos, and G. de Almeida Soares, "Improvement of in vitro titanium bioactivity by three different surface treatments," *Dental Materials*, vol. 22, no. 3, pp. 275–282, 2006.

[21] N. L. D'Elía, A. N. Gravina, J. M. Ruso, J. A. Laiuppa, G. E. Santillán, and P. V. Messina, "Manipulating the bioactivity of hydroxyapatite nano-rods structured networks: Effects on mineral coating morphology and growth kinetic," *Biochimica et Biophysica Acta (BBA) - General Subjects*, vol. 1830, no. 11, pp. 5014–5026, 2013.

9

Mechanical properties of composite Hydrogels

Contents

9.1 Overview **153**
9.2 Experimental procedure **154**
  9.2.1 Preparation of the multi-component crosslinked films . . 154
9.3 Discussion **155**
  9.3.1 Morphological and structural analysis 155
  9.3.2 Swelling and degradation behavior 159
  9.3.3 Viscoelastic properties 160

9.1 Overview

As exposed previously, hydrogels exhibit excellent properties that enable them as nanostructured scaffolds for soft tissue engineering. However, single-component hydrogels have significant limitations due to the low versatility of the single component. To achieve this goal, in this chapter, the design and characterization of different multi-component hydrogels composed of gelatin, alginate, hydroxyapatite and a protein (BSA and fibrinogen) is described. First, the surface morphology of the samples and the main characteristics of the physiological interplay are analyzed by using FT-IR and Confocal Raman microscopy. Then, their degradation and swelling were studied and mechanical properties were determined by rheology measurements. Experimental data were carefully collected and quantitatively analyzed by developing specific approaches and different theoretical models to determine the most notable parameters. Finally, it was also determined how the nanoscale of the system influences its macroscopic properties and to which extent each component maintains its own functionality; demonstrating that, with the optimal components in the right proportion, multifunctional hydrogels can be developed.

9.2 Experimental procedure

9.2.1 Preparation of the multi-component crosslinked films

Step 1. *Preparation of the protein solutions.* To synthesize the hydrogels, each one of the protein solutions was prepared separately. First, a known amount of the alginic acid sodium salt powder was dissolved in PBS to obtain a 5 % (w/v) solution. The mixture was then kept under gentle agitation at 250 rpm during 3 h at 37 °C. Next, and similarly, a 2 % (w/v) gelatin solution was prepared by dissolving the gelatin powder in PBS. The solution was magnetically stirred at 300 rpm and 58 °C.

Meanwhile, both Fibrinogen and Bovine Serum Albumin 0,5 % (w/v) solutions were prepared by dissolving the proper amount of each one of the materials in the buffer and agitated until complete dissolution.

Step 2. *Obtention of the protein mixtures.* When all the solutions were ready, alginate was combined with fibrinogen or bovine serum albumin, respectively, at a 1:1 ratio, to obtain the initial Alg/Fib and Alg/BSA mixtures. Then, the gelatin was added to both mixtures at a volume ratio of 2:1:1 (Gelatin : Alginate : Fib/BSA) and stirred gently until getting the homogeneous viscous solutions Gel/Alg/Fib and Gel/Alg/BSA.

Step 3. *Formation and drying of the films.* Once the final protein mixtures were obtained, aliquots of 4.5 mL were added to 35 mm. diameter Petri dishes and left drying during 24 h at 45 °C. When the protein mixtures were appropriately dried, as a consequence of the great loss of liquid they suffer in the oven, they become fragile films that lay in the bottom of the Petri dishes (Gel/Alg/Fib and Gel/Alg/BSA films).

Step 4. *Preparation of the crosslinking solutions.* Meanwhile, two different fresh crosslinking solutions (C1 and C2) were prepared in Falcon tubes. The first crosslinking solution C1 was composed of 3.48 mL of a 110 mM aqueous solution of $CaCl_2$, 7.08 mL of 1 mM HA solution and 7.44 mL of water. Crosslinking solution C2 was prepared similarly, but without the presence of HA: 3.48 mL of 110 mM of $CaCl_2$ and 14.52 mL of water. The addition of $CaCl_2$ assured the alginic acid polimerization and the crosslinking by calcium diffusion through the gels.

Step 5. *Crosslinking process and obtention of the final hydrogels.* At this point, Falcon tubes containing the crosslinking solutions were sonicated for 10 min. and vortexed. Finally, 1,5 mL of the crosslinking solutions C1 and C2 were added into empty Petri dishes. Dryed protein films were subsequently placed on top of the solutions using tweezers, carefully enough to avoid wrinkles and bubbles in the membranes. Next, films were left on an orbital shaker at 150 rpm at RT for 3 hours, to ensure a complete crosslinking. Following this procedure, each of the films crosslinked with the C1 solution contained a final amount of HA of 6.525 mg.

Hydrogels resulting from the crosslinking with the C1 solution were named Gel/Alg/Fib/HAp and Gel/Alg/BSA/HAp and the ones crosslinked with the solution C2, Gel/Alg/Fib and Gel/Alg/BSA. Furthermore, in order to explore the influence of fibrinogen and bovine serum albumin on the properties of the hydrogels, a blank sample Gel/Alg/HAp was also prepared following the explained methodology and crosslinked with the solution C1.

9.3 Discussion

9.3.1 Morphological and structural analysis

FTIR analysis was performed to characterize and determine the interactions and structural changes of the different components of the matrix. In order to be able to determine the effects of these components, in Figure 9.1 it is shown the spectra that have been obtained for samples with different composition. The characteristic peaks of alginate can be observed in the four samples: 3270 $\mathrm{cm^{-1}}$ (O-H stretching), 2930 $\mathrm{cm^{-1}}$ (C-H stretching), 1626 (C=O stretching) and 1026 (pyranosyl ring stretching). On the other hand, most of the characteristics peak of gelatin are also present: 3069 $\mathrm{cm^{-1}}$ (C-H stretching), 2934 $\mathrm{cm^{-1}}$ (C-H stretching), 1626 $\mathrm{cm^{-1}}$ (C=O stretching) and 1540 $\mathrm{cm^{-1}}$ (N-H stretching of secondary amide). At the same time, it is important to note that some of the peaks exhibit shifts, broadening and changes, with regard to the pure compounds, which reveals information about the changes in structure. For example, the very broad signal on all spectra observed in the region 3000-3600 $\mathrm{cm^{-1}}$ correspond to a range of wavenumbers for the different O-H bonds that are uncovering the great number of hydrogen bonds present in the samples, confirming the formation of the hydrogel. Because of this broad signal, some typical peaks, for example 3321 $\mathrm{cm^{-1}}$ (N-H stretching) in gelatin, cannot be clearly identified. Another characteristic peaks of gelatin at 1553 $\mathrm{cm^{-1}}$ have been shifted to 1540 $\mathrm{cm^{-1}}$ because of the effect of double bonds C=N and C=O. The hydrogel formation has been attributed to the reaction between aldehyde

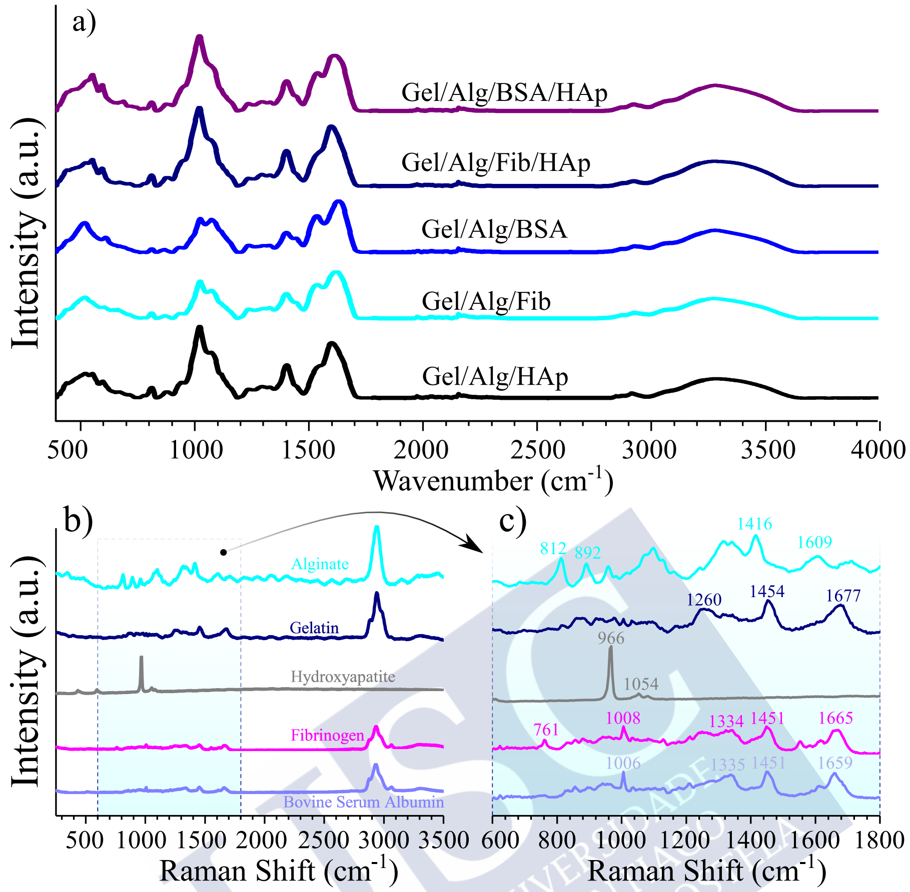

Figure 9.1: a) FTIR spectra of the different samples. b) FTIR of each of the elemental compounds. c) Close-up.

groups of alginate and amino groups of gelatin. The carbon-carbon bonds of the cis-diol groups in the molecular chain of the alginate can be cleaved to generate reactive aldehyde functions by periodate oxidation, which can develop chemical crosslinking with amino functions via Schiff's linkage. This fact is the cause of the enlargement of the 1626 cm^{-1} because of overlapping with the band at 1630 cm^{-1} of amide I of uncrosslinked gelatin [1]. On the other hand, the strong weakening of pure gelatin absorption peak in C–C stretching in between 1200 and 1350 cm^{-1} confirms the formation of hydrogel.

As shown in the Figure 9.1, the introduction of other components into the basic matrix of gelatin and alginate has a mild effect on the spectra. Despite this fact, the footprint of the components can be recognized. Regarding the hydroxyapatite, the peak placed at 603 cm^{-1} is attributed to the vibration of hydroxyl ions in the nanoparticles, the characteristics bands showing phosphate bending vibration in HA can be observed at 557 cm^{-1}, peak corresponding to the phosphate stretching is placed at 883 cm^{-1}, being indicative of the carbonate ion substitution. Finally,

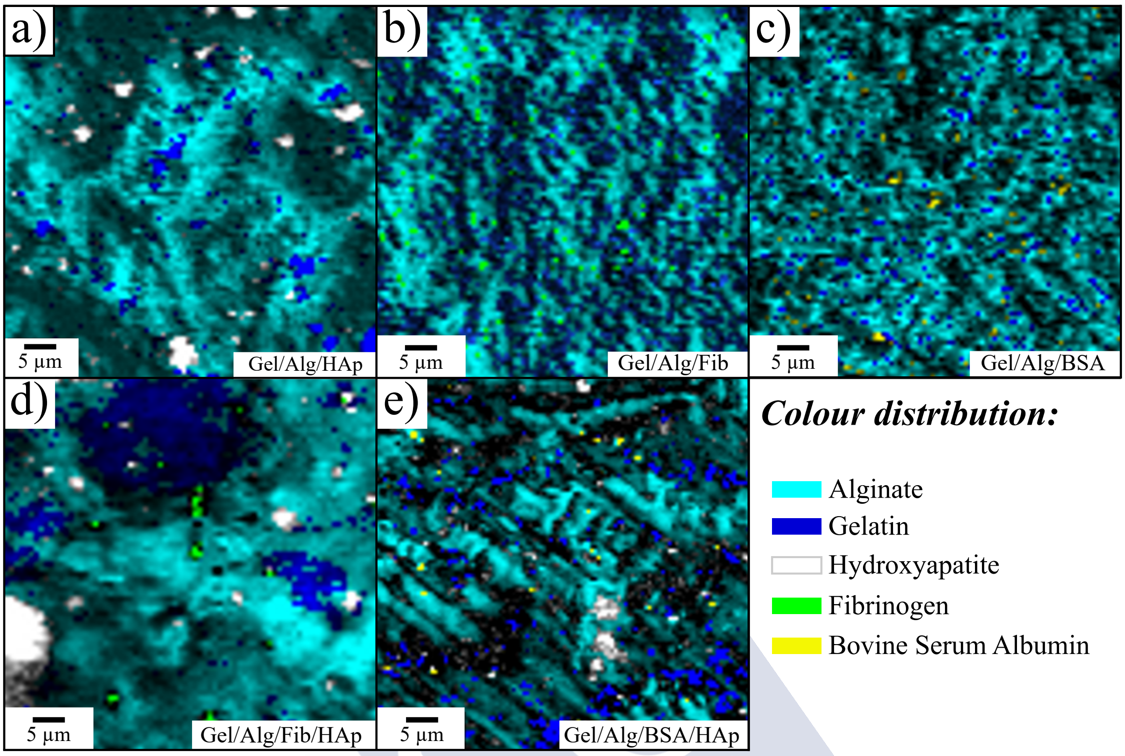

Figure 9.2: Optical images of the compound distributions of the five studied samples (wet) obtained using the integrates intensity of the Raman bands: gelatin (navy blue), alginate (dark turquoise), hydroxyapatite (white), fibrinogen (green) and BSA (yellow).

the absence of the characteristic 1170 cm^{-1} peak suggests the presence of ionic interactions between the negative charges of HA and positive residues of gelatin, mainly arginine and lysine. The addition of the proteins BSA and fibrinogen also results in small changes in the spectra. However, conformational changes can be inferred. The changes of the protein secondary structure can be deduced from changes in main band in the Amide I region, at about 1655, 1672 and 1636 cm^{-1} which are assigned to α-helices, β-turn and β-sheets, respectively. Changes in the tertiary structure are reflected in the Amide II region, 1400-1580 cm^{-1} [2]. On the other hand, the characteristic peaks of fibrinogen are placed at 1230, 1530 and 1630 cm^{-1} [3]. By comparing the spectra in Figure 9.1 with those of pure proteins and with the spectra without proteins, it can be concluded that both proteins are perfectly integrated into the hydrogel matrix and that fibrinogen maintains its structure, while tertiary structure of BSA changes from the native form to a less compact one, probably because of interactions with gelatin and alginate chains.

The incorporation, in addition to the distribution, of the different components within the hydrogel matrix was further confirmed by high resolution confocal Raman microscopy. Figure 9.2 shows the optical micrographs where the combined maps of the individual components were identified using their specific bands: 966 cm^{-1} for hydroxyapatite, 2934 cm^{-1} for fibrinogen and BSA and 812 cm^{-1} and 1454 cm^{-1} for alginate and gelatin respectively (these peaks were chosen because both components shared the 2941 cm^{-1} peak, hindering the proper identification). As shown in Figure 9.2, the main components of the hydrogel, gelatin and alginate, are well distributed forming a coherent and homogeneous matrix, as it had been predicted by FTIR measurements. All images indicate the stability and preservation of the two initial components. Interestingly, no interference was observed, and as a result the shape of the scaffold was clearly resolved. The introduction of hydroxyapatite nanoparticles shows the profile that can be seen in the Figure 9.2a. The distribution of nanoparticles is not homogeneous, as can be seen, two well-differentiated sizes coexist one with and average size of 4 µm and the other with a size of 1.5 µm. The size of the hydroxyapatite nanoparticles we synthetized is of 75 nm long. So, the origin of both clusters in Figure 9.2 is the self-assembly of the nanoparticles. On the other hand, aggregates tend to form in gelatin-rich regions due to the electrostatic interactions with the positive residues of gelatin, as had already confirmed FTIR analysis. Figures 9.2a and 9.2c, show the patterns of the samples after the incorporation of fibrinogen and BSA, respectively. The images show a homogeneous distribution of both proteins throughout the scaffold. This is an important topic because to fulfill biological functions, proteins incorporated into scaffolds should maintain native conformation. Previous studies have demonstrated that fibrinogen aggregations in gelatin hydrogels are dependent on protein concentration. At high fibrinogen concentrations, the protein is forming the pore walls of the scaffolds in an aggregated state and denatured conformation, which results in a rough surface. On the contrary, at low concentrations the pore wall surface of the hydrogels appeared to be smooth and homogeneous because the reaction feed aggregation of fibrinogen was negligible [4]. Because of the low concentration of fibrinogen used in this study, obtained results confirm that the protein is not in an aggregation state. With regard to the BSA, the pattern is similar to that of fibrinogen, previous studies found that due to the hydrophilic character and the flexibility of the molecule, it interacts positively with the scaffold favoring its incorporation into it [5]. It is important to note that the incorporation of both proteins modifies the distribution of alginate, making it much more homogeneous, suggesting that further optimization of scaffold has taken place. It is obvious that this reorganization has to do with interactions with the proteins. Interestingly, the similar morphology we observed in the hydrogel with both proteins disappears when we incorporate hydroxyapatite nanoparticles into the systems. As can be observed in Figure 9.2d, the presence of hydroxyapatite

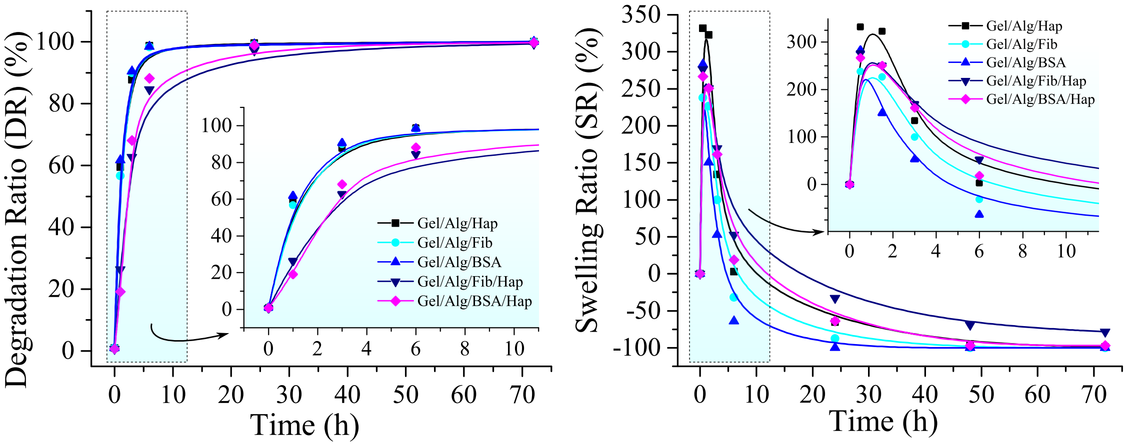

Figure 9.3: a) Degradation over time of the hydrogels. b) Close-up of the first 10 hours of degradation. a) Swelling behavior over time. b) Close-up of the first 10 hours of swelling.

the fibrinogen hydrogel results in a distinct pattern with islands of higher alginate intensity, while fibrinogen and hydroxyapatite maintain the morphology they had in the original samples (Figures 9.2a and 9.2b). The pattern of the sample with BSA (Figure 9.2e) is completely different, in this case the alginate is distributed much more homogeneously, just as the hydroxyapatite does. In this case, the integration of the BSA into the scaffold, gives it the flexibility and adaptability necessary for the incorporation of hydroxyapatite nanoparticles in a homogeneous way.

9.3.2 Swelling and degradation behavior

In order to study the degradation of the hydrogels over time, samples were synthesized, weighed and placed in PBS at room temperature. After the immersion, they were dried with blotting paper and weighed periodically to study their mass evolution.

Results from Figure 9.3 show that the degradation of the films occurs in a very short period of time, having a degradation over 80 % in the first 5 hours and over 90 % within a day, for all the five samples. This mentioned degradation is a consequence of the dilution of the protein in the media, and as the protein concentration in these gels is relatively low, their degradation occurs fast. One way to delay the release is to promote the interaction of the protein ligands to form supramolecular aggregates. As can be seen in graphs, samples containing both HA nanoparticles and proteins had an effective impact in slowing down the process. This synergistic effect is due to the formation of new bonds between the nanoparticles and the proteins which results in a decrease of the mesh size of the crosslinked network. Furthermore, as the length of the pores become smaller, the protein release is also delayed because of lower rates of diffusion.

Simultaneously, the ability to swell is also an important property of hydrogels when placed within a thermodynamically compatible solvent. To evaluate this feature, dried oven samples were weighed and then put in contact to a 37 °C PBS solution. For both cases, results demonstrated that highly cross-linked scaffolds show a facilitated entrapment of water in their framework (Figure 9.3b), due to a narrow pore distribution which captures and holds water through capillary action. One more time, the swelling behavior of hydrogels with the incorporation of hydroxyapatite and protein are superior through time. It is well known that nanoparticles contribute to the increase of water uptake because of its water adsorbing properties. However, in function of the results, it is proven that this effect is enhanced by the presence of proteins. This fact always may play an essential role in the steady mass loss over time found in the nanoceramic-loaded samples, turning them into better potential materials to use in guided bone regeneration.

9.3.3 Viscoelastic properties

Flow curve tests were performed for the five samples: giving the relationship between the sear rates, the shear stress and the viscosity of the samples. Analyzing the graph of the viscosity against the shear stress at 25 °C (Figure 9.4), it can be concluded, that the different concentration of HA nanoparticles has a noticeable impact in the viscosity values. The graphs show a rapid viscosity descent which finally stabilize into a plateau area. Moreover, in the five systems, the results demonstrate that the shear thinning takes place at relatively low shear rates.

The fall of the viscosity values as the applied stress is becoming greater, is mainly caused by the rupture of active alginate joints within the sample structure. These active joints are formed by fragmented alginate junctions, which can re-associate among them to create larger and stronger active junctions. As the concentration in nanoparticles arises, the properties and behavior of these junctions is notably modified. The presence of Hydroxyapatite nanoparticles enhances the possibilities, causing the formation of new additional active joints, giving the network a higher strength and therefore higher values of viscosity as can observed in Plots 9.4c, 9.4f and 9.4g. The effect of BSA on the matrix produces a slight improvement in strength compared to that produced by fibrinogen. This effect is preserved when hydroxyapatite nanoparticles are added. This effect is due to the greater flexibility of BSA, which guarantees the optimization of interactions, both with the original matrix and with nanoparticles.

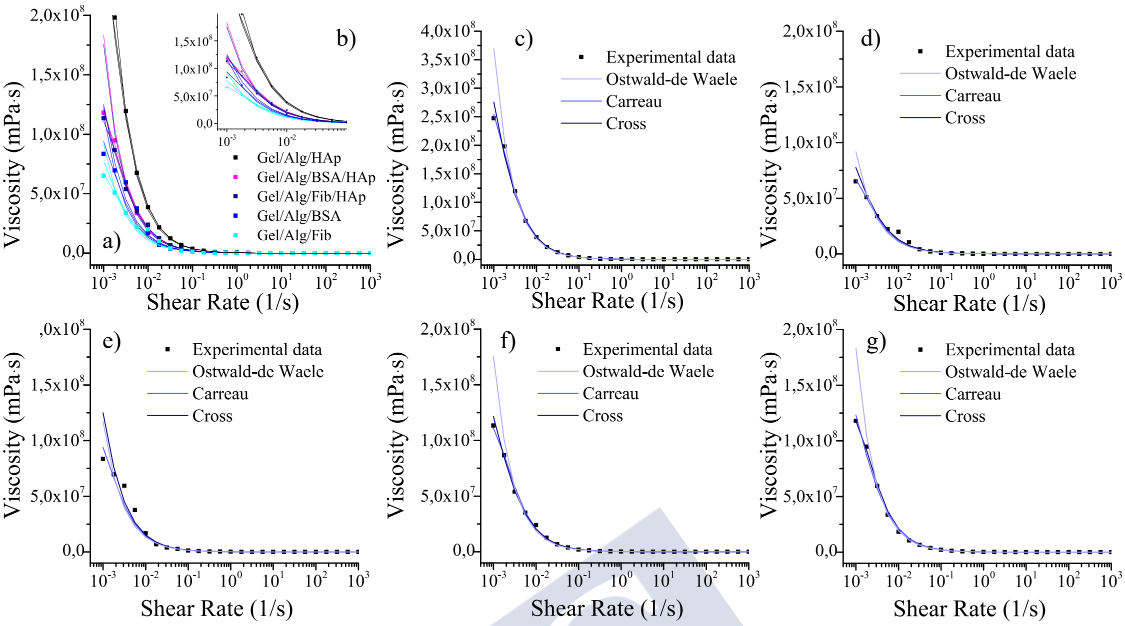

Figure 9.4: Fitting results. a) Experimental and obtained data for the 5 studied samples. b) Close up. c) Gel/Alg/HAp. d) Gel/Alg/Fib. e) Gel/Alg/BSA. f) Gel/Alg/Fib/HAp. g) Gel/Alg/BSA/HAp.

The models described in Chapter 2 were fitted to the experimental data by means of multiple non-linear regressions. The obtained parameters are listed in Table 9.1. The correlation coefficient (r^2) of the estimated viscosities show that the Carreau model best fits the experimental data for all samples, followed by the Cross model. On the other hand, Ostwald de Waele model also fits the experimental data but results are not as good. In the Carreau's model, the power law index, n, characterizes the fluid behavior and values of $0 < n < 1$, correspond to a shear thinning behavior. As could be expected, all the samples exhibit shear thinning behavior. It is clear that the addition of hydroxyapatite clearly increases this index, as well as BSA containing samples results in higher values than those with fibrinogen. This increase reflects the transit to a more complex internal structure (for $\mathrm{n} > 1$ the behavior becomes shear thickening).

Analyzing the results of the Frequency sweep measurements, a relationship between the viscoelastic properties of the films and the frequency ca be found. At the working temperature, 25 °C the films present a gel-like behavior as the storage modulus is greater than the loss modulus [6]. This condition is the same for all the samples throughout the frequency domain studied. It can also be concluded that loss and storage moduli are dependent of the frequency, fact that has already been investigated in previous works [7]. Plots of Figure 9.5 are analogous to the results achieved measuring soft glassy materials with a gel structure [8]. Again, as expected,

Table 9.1: Flow Curve modeling

		Samples				
		G/A/Fib	**G/A/BSA**	**G/A/Fib/HA**	**G/A/BSA/HA**	**G/A/HA**
Ostwald de Waele	K	148.31	170.09	207.17	212.11	351.63
	n	0.0692	0.0542	0.0240	0.0213	0.0068
	r^2	0.88	0.87	0.80	0.81	0.85
Carreau	η_0	8.44 x 10^7	1,29 x 10^8	1.32 x 10^8	1.41 x 10^8	3.25 x 10^8
	η_∞	57.688	83,806	91.906	95.432	98.690
	λ	784.61	968,68	641.72	666.37	787.3
	n	0.4753	0,4830	0.4960	0.4969	0.5096
	r^2	0.98	0,95	0.99	0.99	0.99
Cross	η_0	2.00 x 10^8	2.14 x 10^8	2.78 x 10^8	2.68 x 10^8	7.87 x 10^8
	η_∞	69.151	85.956	96.405	92.515	99.621
	K_1	1606.6	6396.6	1294.2	1176.9	1837,0
	d	0.9631	0.9727	0.9951	0.9978	1.0188
	r^2	0.96	0.94	0.99	0.99	0.98

the modulus of each of the three samples presents firm nanoparticle concentration dependence. Both the loss and the storage modulus are higher in the samples were the HA has more presence. This evidence was previously reported in different studies [9, 10]. Furthermore, as it has been previously demonstrated [11, 12], the Ca atoms present on the HA interact with the oxygen sites of alginate. The CaOH active site of HA surface form bonds with the COO^- group of alginates. On the other hand, the ${HPO_4}^{-2}$ groups do not interact with the biopolymer, in particular the phosphate-hydroxyl active group [13]. Still, and gathering the information, it can be assured the alginate is successfully grafted on the hydroxyapatite surface, making the structure of the films ordered at the nanoscale range. This reinforces the hypothesis that the rheological behaviour of the material corresponds to a soft glass material, as it has been previously inferred from the dependence of the moduli with the frequency. The particle bonding to the polymer network has an immediate effect on the toughness, but it is not the unique factor, as it has been proved the content of nanorods is crucial as well to the microstructures and the strength of the films [14]. One more time both proteins follows the same pattern we have found previously.

Thixotropy is a time dependent, non-Newtonian characteristic of some fluids, where the apparent viscosity decreases when a constant shearing is applied; and it rises or falls when the shear rate is changed in step. In the same way, when the shear rate is changed circularly, it causes the appearance of hysteresis loops, which is associated with the energy loss [15]. The hysteresis area is a useful tool for the estimation of the degree of thixotropy [16]. Figure 9.6 shows the results for the 3-ITT tests at 25 °C. Once again, the behaviour is analogous for the five different samples: in the first interval, viscosity values remain constant and in the third step the material shows a reasonable thixotropic recovery, around 80 %. It is commonly

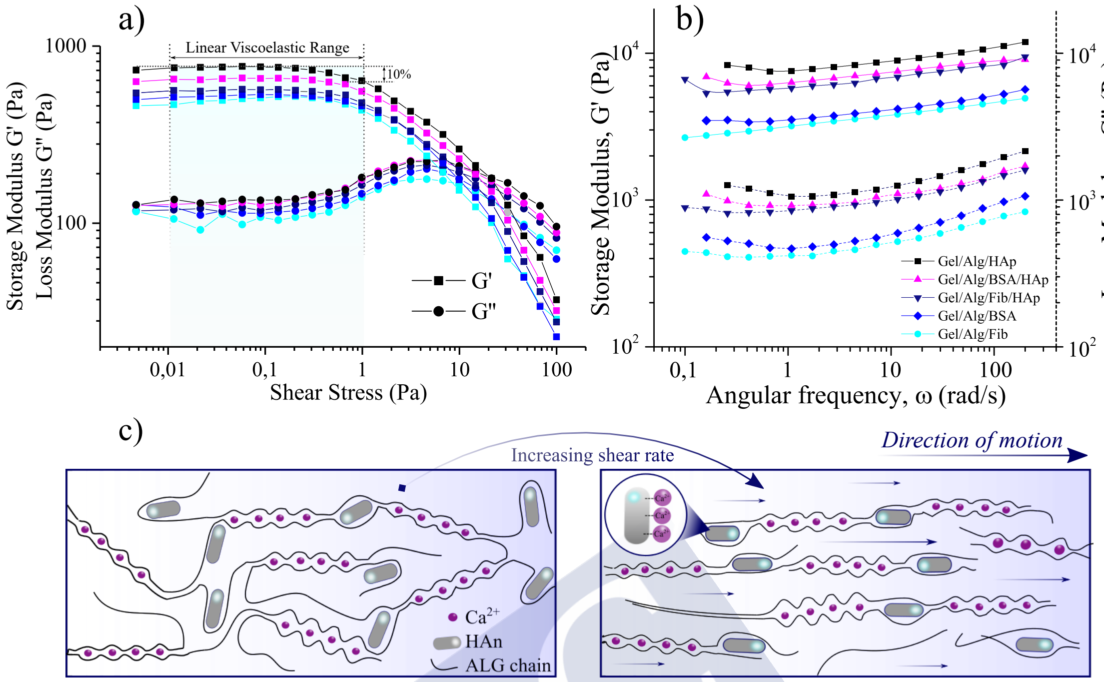

Figure 9.5: a) Linear viscoelastic range. b) Oscillatory frequency sweep. c) Scheme representing the alignment of HA within the hydrogel along the streamline when shear rate increases. The ALG-Ca^{2+} and ALG-HA interactions are also represented.

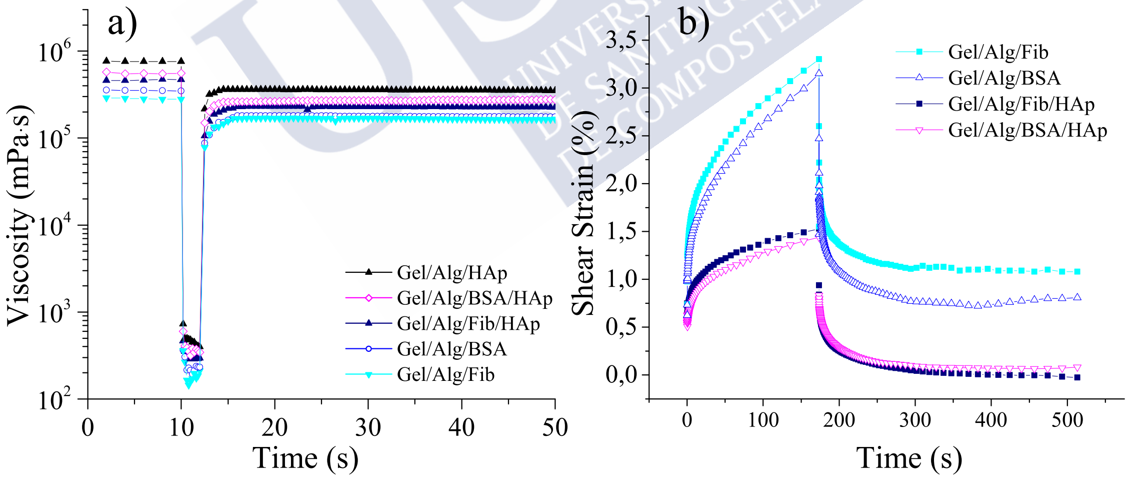

Figure 9.6: a) Three interval thixotropy (3-ITT) test. b) Creep-recovery curves of the four studied samples.

believed that the internal structure changes with the formation of aggregates with different crosslinking degree. When the shear rate is high enough, the network is destroyed, making the entanglements turn into monomers [17], on the other hand, when the applied shear is stopped, the structure progressively rebuilds. That means, in this case, that the rate of disentanglement and the re-entanglement is slightly different, and consequently the subtle thixotropic behaviour comes out.

Table 9.2: Values of the Burger model parameters. Results from the fits by Eq. (2.20)

	G_0 x 10^{-3} (Pa)	**η_0 x 10^{-4} (Pa · s)**	**G_1 x 10^{-3} (Pa)**	**η_1 x 10^{-4} (Pa · s)**	**r^2**
Gel/Alg/BSA	5.62 ± 0.21	53.95 ± 2.22	6.52 ± 0.34	3.32 ± 0.49	0.986
Gel/Alg/Fib	4.64 ± 0.19	56.99 ± 2.81	5.97 ± 0.35	2.86 ± 0.47	0.980
Gel/Alg/BSA/HAp	9.29 ± 0.11	165.94 ± 5.32	12.21 ± 0.29	12.45 ± 6.95	0.997
Gel/Alg/Fib/HAp	7.75 ± 0.10	169.31 ± 8.17	12.01 ±0.40	10.51 ± 8.27	0.992

Results obtained from the creep tests are shown in Figure 9.6b. Usually, creep curves follow a typical behaviour that can be divided in sections. In the load phase, immediately after the start of the test, the deformation is purely elastic, giving a jump-like response which corresponds to the spring S_1 (see Figure 2.2) and represents the instantaneous compliance. After that, a delayed viscoelastic response can be observed, corresponding to the dashpot D_2 and the spring S_2 together and represents the viscoelastic compliance. The values of compliance $J = \gamma/\sigma$, as a function of time are depicted in Figures 9.7a and 9.7b. The time interval for all the tests is from 0 to 173 s. The corresponding recovery, which will be below analysed, is represented for the interval $173 \leq \mathrm{t} \leq 513$ s. For the creep tests, sample Gel/Alg/HAp was not included, as the major objective of this analysis was to compare the different behaviour of the gels in function of the protein added (Fib or BSA) and, at the same time, to study the influence of the nanoparticles in their response.

Burger model (2.20) was used to fit $J = f(t)$ in the interval $0 \leq \mathrm{t} \leq 173$ s. obtaining values of $r^2 \geq 0.98$ in all cases. Calculated G_0, G_1, η_0 and η_1 parameters with each respective error and the correlation coefficients are shown in Table 9.2.

As it can be seen in Table 9.2, G_0 is lower for the gels with no presence of hydroxyapatite. Added to that, values of η_0, G_1 and η_1 are from two to three times lower to that found for the HA-loaded samples. This fact explains why the deformation seen in Figure 9.6b is greater for samples Alg/Gel/BSA and Alg/Gel/Fib. This is in well accordance with the previously demonstrated hypothesis that the inclusion of nanorods reinforces the structure of the gels, contributing to strengthen them. Apart from that, differences found for the samples with BSA or Fib continue to corroborate previous results, suggesting that the addition of BSA exhibits a better rheological behaviour.

The increase in the elastic moduli (G_0 and G_1) and the viscosity represented by the Maxwell dashpot can be attributed to the alignment of the nanorods to the direction of the movement on applying constant shear stress to the systems. Such movement, and the consequential redistribution of the gel network, requires and additional work, which causes an increment in the opposition to deformation.

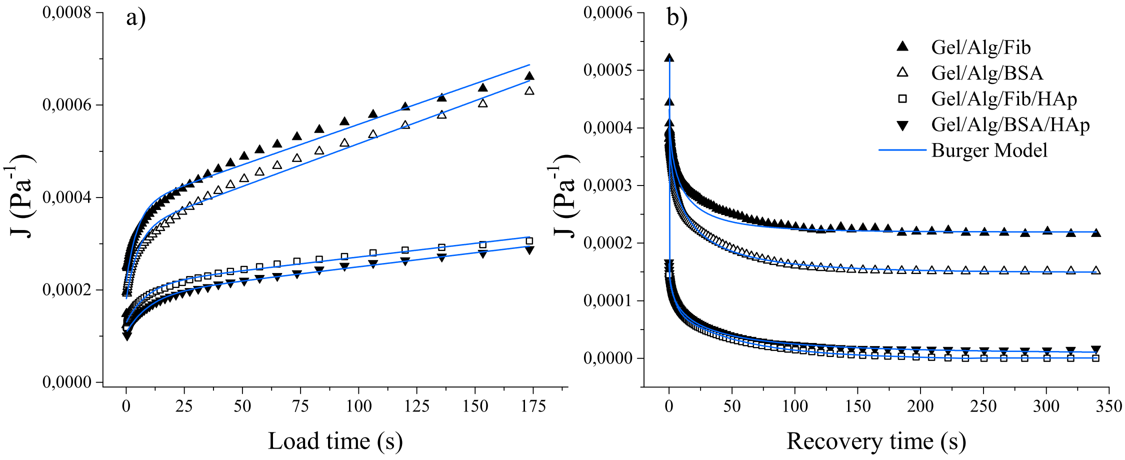

Figure 9.7: a) Fitted curves for the creep phase. b) Fitted curves for the recovery phase.

Table 9.3: Compliance of the Maxwell dashpot, Kevin-Voigt element and parameters obtained from the fitting by Eq. (2.21)

	J_∞ **x** 10^5 **(Pa**$^{-1}$**)**	J_{KV} **x** 10^5 **(Pa**$^{-1}$**)**	α **(s**$^{-1}$**)**	β	**r**^{2}
Gel/Alg/BSA	14.88 ± 0.13	25.08± 0.34	0.21 ± 0.01	0.56 ± 0.01	0.997
Gel/Alg/Fib	21.92 ± 0.37	22.69 ± 1.35	0.31 ± 0.05	0.54 ± 0.05	0.953
Gel/Alg/BSA/HAp	0.79 ± 0.08	14.63 ± 0.16	0.25 ± 0.01	0.48 ± 0.01	0.999
Gel/Alg/Fib/HAp	0.87 ± 0.03	13.88 ± 0.49	0.16 ± 0.02	0.59 ± 0.03	0.989

This higher resistance capacity can help to produce stability, which is an essential factor to the field of soft tissue engineering applications [18].

When the stress is stopped, $\sigma = 0$, the system is in a state of maximum deformation, which is represented with J_{MAX}. After that, the compliance values are recorded periodically in order to see the recover ability of the gels. Figure 9.7a reports how materials react in the interval from 173 s until the end of the experiment. To better understand and make a proper analysis, data was fitted to the Equation (2.20) obtaining J_∞ and J_{KV}, the compliance values of the Maxwell dashpot and of the Kelvin – Voight elements, respectively. One more time, results proved to be sufficiently precise as r^2 is close to 1. Those values, alongside J_∞ and J_{KV} are presented in Table 9.3.

As explained, J_{MAX} values correspond to the compliance obtained at t = 173 s, therefore, and using Equation (2.22), the compliance values corresponding to the Maxwell spring, J_{SM} can be calculated (Table 9.4):

Once these parameters are known, the contribution of the Kelvin-Voight elements and the Maxwell elements to the total deformation of the systems, as well as the percentage of recovery of the gels, can be calculated through Equations (2.23) and (2.24). Results are shown in Table 9.5:

Table 9.4: Maximum compliance and compliance of the Maxwell spring.

	J_{MAX} **x 10^5 (Pa^{-1})**	J_{SM} **x 10^5 (Pa^{-1})**
Gel/Alg/BSA	56.965 ± 0.01	17.006 ± 0.51
Gel/Alg/Fib	66.094 ± 0.01	21.490 ± 1.71
Gel/Alg/BSA/HAp	28.726 ± 0.01	13.309 ± 0.23
Gel/Alg/Fib/HAp	30.624 ± 0.01	15.875 ± 0.61

Table 9.5: Percentage contribution of the Burger elements to the total recovery of the systems.

	J_{SM} (%)	J_{KV} (%)	J_{∞} (%)	R_G (%)
Gel/Alg/BSA	29.85	44.03	26.12	73.88
Gel/Alg/Fib	32.51	34.32	33.16	66.84
Gel/Alg/BSA/HAp	46.33	50.92	2.75	97.25
Gel/Alg/Fib/HAp	51.84	45.33	2.83	97.16

In gels with presence of HA, the contribution of the Maxwell spring to the total deformation is heavier. Same occurs with the J_{kv} values, meaning that the total recoverable compliance is increased for this samples, which may be attributed to the increasing compactness of the structures due to the crosslinking bonds between HA and alginate. On the contrary, the greatest contribution to the Maxwell dashpot, is found on the samples Alg/Gel/BSA and Alg/Gel/fib, coincident with the previously described fact that those are the samples with a more liquid-like behaviour.

Finally, the aforementioned increased strength of the loaded gels is again demonstrated through the values of the recovery percentage in which they reach a notable high ratio of about 97 %, clear indicator that their structure, even though is more complex, is much more homogeneous and with a heavier complete response.

Bibliography

[1] B. Sarker, D. Papageorgiou, R. Silva, T. Zehnder, F. Gul-E-Noor, M. Bertmer, J. Kaschta, K. Chrissafis, R. Detsch, and A. Boccaccini, "Fabrication of alginate-gelatin crosslinked hydrogel microcapsules and evaluation of the microstructure and physico-chemical properties," *Journal of Materials Chemistry*, vol. 2, 12 2013.

[2] G. Navarra, C. Peres, M. Contardi, P. Picone, P. San Biagio, M. Carlo, D. Giacomazza, and V. Militello, "Heat- and ph-induced bsa conformational changes, hydrogel formation and application as 3d cell scaffold:," *Archives of Biochemistry and Biophysics*, vol. 606, 07 2016.

[3] S. Cavalu, V. Simon, F. Banica, and C. Deleanu, "Fibrinogen adsorption onto bioglass alumino-silicates," *ROMANIAN J. BIOPHYSICS*, vol. 17, pp. 237–245, 01 2007.

[4] M. B. Dainiak, I. U. Allan, I. N. Savina, L. Cornelio, E. S. James, S. L. James, S. V. Mikhalovsky, H. Jungvid, and I. Y. Galaev, "Gelatin–fibrinogen cryogel dermal matrices for wound repair: preparation, optimisation and in vitro study," *Biomaterials*, vol. 31, no. 1, pp. 67–76, 2010.

[5] M. Moura, F. Aouada, S. Fávaro, E. Radovanovic, A. Rubira, and E. Muniz, "Release of bsa from porous matrices constituted of alginate–ca^{2+} and pnipaam-interpenetrated networks," *Materials Science and Engineering: C*, vol. 29, pp. 2319–2325, 10 2009.

[6] K. Nishinari, "Rheological and dsc study of sol-gel transition in aqueous dispersions of industrially important polymers and colloids," *Colloid and Polymer Science*, vol. 275, no. 12, p. 1093, 1997.

[7] A. S. Sarvestani and E. Jabbari, "Modeling and experimental investigation of rheological properties of injectable poly (lactide ethylene oxide fumarate) / hydroxyapatite nanocomposites," *Biomacromolecules*, vol. 7, no. 5, pp. 1573–1580, 2006.

[8] B. S. Chae, Y. S. Lee, and M. S. Jhon, "The scaling behavior of a highly aggregated colloidal suspension microstructure and its change in shear flow," *Colloid and Polymer Science*, vol. 282, no. 3, pp. 236–242, 2004.

[9] R. Rial, J. F. A. Soltero, P. V. Verdes, Z. Liu, and J. M. Ruso, "Mechanical properties of composite hydrogels for tissue engineering," *Current Topics in Medicinal Chemistry*, vol. 18, no. 14, pp. 1214–1223, 2018.

[10] S. Chynoweth and Y. Michopoulos, "Generic properties of rheological flow curves," *Journal of Non-Newtonian Fluid Mechanics*, vol. 69, no. 1, pp. 1–14, 1997.

[11] M. Rajkumar, M. N, and R. Venkatachalam, *Development of nanocomposites based on hydroxyapatite/sodium alginate: Synthesis and characterisation*, vol. 62. 2011.

[12] P. Parhi, A. Ramanan, and A. Ray, *Preparation and characterization of alginate and hydroxyapatite-based biocomposite*, vol. 102. 2006.

[13] Y. Guesmi, H. Agougui, R. Lafi, M. Jabli, and H. Amor, *Synthesis of Hydroxyapatite-Sodium alginate via a co-precipitation technique for efficient adsorption of Methylene Blue dye*, vol. 249. Journal of Molecular Liquids, 2017.

[14] Q. Wang, R. Hou, Y. Cheng, and J. Fu, "Super-tough double-network hydrogels reinforced by covalently compositing with silica-nanoparticles," *Soft Matter*, vol. 8, no. 22, pp. 6048–6056, 2012.

[15] P. Achayuthakan and M. Suphantharika, “Pasting and rheological properties of waxy corn starch as affected by guar gum and xanthan gum,” *Carbohydrate Polymers*, vol. 71, no. 1, pp. 9–17, 2008.

[16] J. Ma, Y. Lin, X. Chen, B. Zhao, and J. Zhang, “Flow behavior, thixotropy and dynamical viscoelasticity of sodium alginate aqueous solutions,” *Food Hydrocolloids*, vol. 38, pp. 119–128, 2014.

[17] S. Zhu, X. Yu, S. Xiong, R. Liu, Z. Gu, J. You, T. Yin, and Y. Hu, “Insights into the rheological behaviors evolution of alginate dialdehyde crosslinked collagen solutions evaluated by numerical models,” *Materials Science and Engineering: C*, vol. 78, pp. 727–737, 2017.

[18] S. Kumar and R. Nussinov, “Experiment-guided thermodynamic simulations on reversible two-state proteins: implications for protein thermostability,” *Biophysical chemistry*, vol. 111, no. 3, pp. 235–246, 2004.

10

Microfluidic-based synthesis of hydrogel microspheres

Contents

10.1 Overview **169**
10.2 Experimental procedure **170**
  10.2.1 Monosized sodium alginate microdroplets 170
  10.2.2 Ca-Alg microparticles and Chi-covered microspheres . . 170
  10.2.3 Adsorption, kinetic and desorption. 171
10.3 Results and discussion **172**
  10.3.1 Flow simulations of the microdroplet generation 172
  10.3.2 Formation of sodium alginate microdroplets 174
  10.3.3 Gelation of Ca-Alg and Chi covered microparticles . . . 176
  10.3.4 Adsorption of Prop and Clox onto HA nanoparticles . . 177
  10.3.5 Desorption/release profiles 178

10.1 Overview

This chapter presents an innovative method for the synthesis of crosslinked alginate hydrogel microspheres for doped-hydroxyapatite encapsulation and controlled drug delivery. Combining external gelation (collecting bath) and internal (caused by the bonding formed between Ca^{2+} present on the HA surface and the oxygen sites of COO^{--} groups of ALG), it is possible to obtain Ca-ALG microparticles and core-shell ALG-CHI microspheres with homogeneous sizes and morphologies and load them with doped HA. The effect of the water-to-oil volume ratio, and the differences in the collecting bath, morphology and dispersion of hydrogel microparticles were investigated. Propranolol hydrochloride (Prop) and Cloxacillin sodium salt monohydrate (Clox) were used as the drug models. The adsorption kinetics for each drug onto bioactive HA has been studied and discussed using Avrami's parameters and the posterior desorption profiles have been analysed through the Korsmeyer-Peppas model.

10.2 Experimental procedure

10.2.1 Monosized sodium alginate microdroplets

To prepare the disperse phase, a known amount of sodium alginate was dissolved in triple distilled water for 3 h at 37 °C and 250 rpm., until obtaining a homogeneous and viscous solution with a 2 wt.% concentration. This solution was pumped into the system through the first inlet. (Figure 10.1b, inlet A) Next, previously loaded HA nanoparticles were introduced in the microchip through the following middle inlet (Figure 10.1b, inlet B) in such a way that the particles were wrapped up by the alginate solution, obtaining spherical microdroplets with drug-loaded nanoparticles in their centre (Figure 10.1b, point P_1).

The continuous phase was inserted through the C and D side inlets and consisted of a solution of sunflower seed oil with 2 wt.% Span 80 pre-dissolved. The use of this surfactant regulates the interfacial surface tension of the oil/water system, helping to obtain less fragile droplets and avoiding coalescence.

The inputs were attached to two syringe pumps (KDS 101 Legacy Syringe Pump) configured in such a way that allowed to maintain a precise and controlled flow in each inlet. After any modification in the flow rate of the oil or water phases, the system was stabilised for a minimum of 5 minutes in order to assure stationary state and to avoid instabilities or inhomogeneous flows, before removing droplets for gelation or imaging.

10.2.2 Ca-alginate microparticles and chitosan-covered microspheres

In a typical experiment, doped HA–ALG droplets were formed inside the main channel of the microfluidic chip. These microdroplets were transferred trough a silicone tubing to the respective gelation baths. The end of this collecting tubing was maintained at the surface of the bath to avoid deformation on the dripping process. The collecting baths contained 20 mL of a 20 % (w/v) $CaCl_2$ water solution

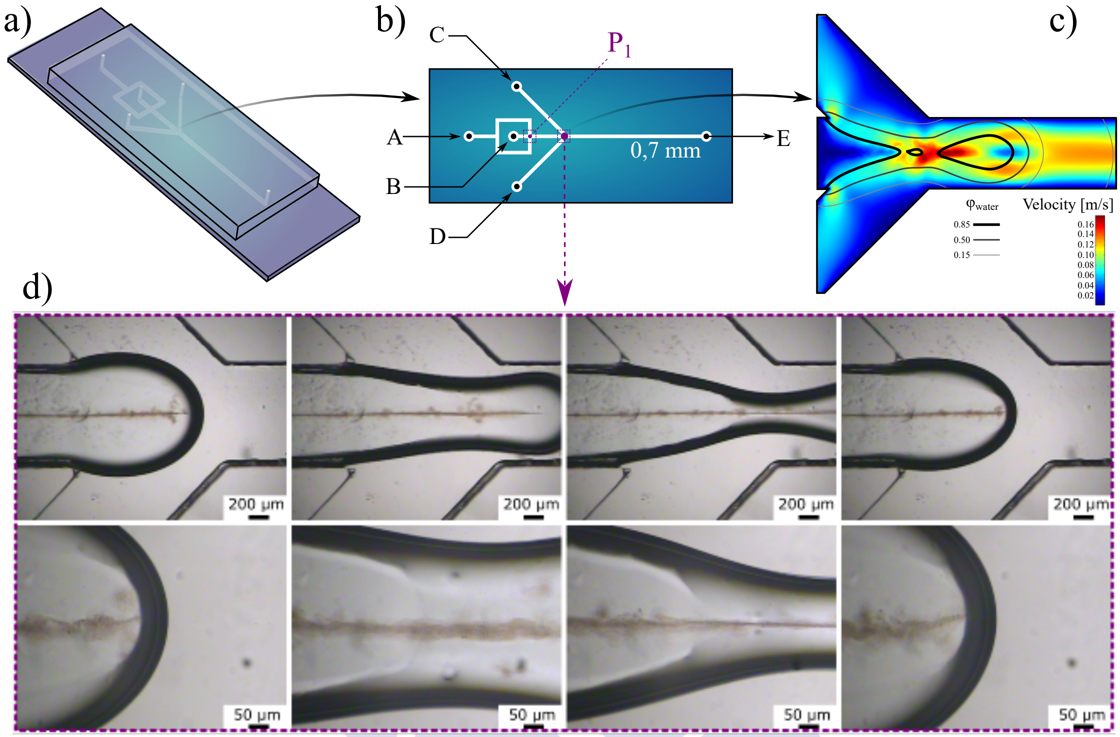

Figure 10.1: a) Tridimensional representation of the microfluidic device. b) Schematic representation. Geometry, inlets, outlets and significant points. c) Computational simulations results. d) Optical images. The continuous formation of the droplets as well as the nanoparticle flow can be tracked in this point.

(to obtain calcium alginate microdroplets) or 20 mL of a 20 % (w/v) $CaCl_2$ and 0,1 % (w/v) Chitosan in a 1 % (v/v) acetic acid solution (to obtain chitosan-covered calcium alginate microspheres). A period of 24 h was allowed for complete gelation before the synthesized microgel particles were further characterized.

10.2.3 Adsorption, kinetic and desorption.

The drug loading for both the active ingredients, Propranolol and Cloxacillin, was carried out by incubation of the HA nanoparticles in solutions of the drugs for 7 days. Specifically, known amounts of Prop and Clox were weighed and dissolved in 20 mL of water to obtain initial concentrations (C_0) of 0.05 mM and 0.1 mM, respectively. Next, 3.5 mg of the nanorods were added to the solutions and left at room temperature. At each time point, samples were centrifuged at 5000 rpm for 5 minutes and a small aliquot (3 mL) of the supernatant was collected. The concentrations of drug in the supernatant, c_t, were then determined by UV-Vis spectroscopy (Cary 100 Bio UV-vis spectrophotometer) by measuring absorbance at λ_{max}, 290 nm for Prop [1] and 344 nm for Clox [2]. Standard curves in the concentrations range for each one of the active ingredient were previously performed. Then, the adsorption kinetics were evaluated using Avrami's model.

Similarly, for the desorption studies, samples of loaded HA nanorods, ALG microparticles and CHI-ALG microspheres were left in the same amount of media at room temperature and UV-vis measurements of the supernatants were measured for each time point for 60 days and finally the results were fitted by Korsmeyer-Peppas model.

The adsorption quality of the drugs was determined by the following expression:

$$Q_t = \frac{(c_0 - c_t) \cdot V}{m} \tag{10.1}$$

where Q_t is the amount of drug adsorbed on HA nanoparticles (mmol g^{-1}), c_o and c_t are the initial and residual concentrations of the drugs in the supernatant at time t (mM), respectively; V is the volume of the drug solutions (L), and m is the mass of HA added (g).

10.2.3.1 Loading and release efficacy

The adsorbed and released percentages for both drugs were obtained as follows:

$$L_{AI}\% = \frac{[AI]_i - [AI]_f}{[AI]_i} x\ 100 \tag{10.2}$$

$$R_{AI}\% = \frac{[AI]_i}{[AI]_a} x\ 100 \tag{10.3}$$

$$[AI]_a = [AI]_i - [AI]_f \tag{10.4}$$

Being, [AI]$_a$ and [AI]$_l$ the adsorbed and released concentration of active ingredient (Prop or Clox), L$_{AI}$% and R$_{AI}$% the percentage of the active ingredient, adsorbed onto the hydroxyapatite nanorods and released, respectively, and [AI]$_i$, [AI]$_f$ the initial and final supernatant concentration of active ingredient where nanorods of HA are incubated.

10.3 Results and discussion

10.3.1 Flow simulations of the microdroplet generation

In this work, in order to anticipate and predict the behaviour of the two immiscible phases, COMSOL Multiphysics® (5.2 version) [3] was used to model the droplet formation and studying the dependence on the physical properties and the rates of

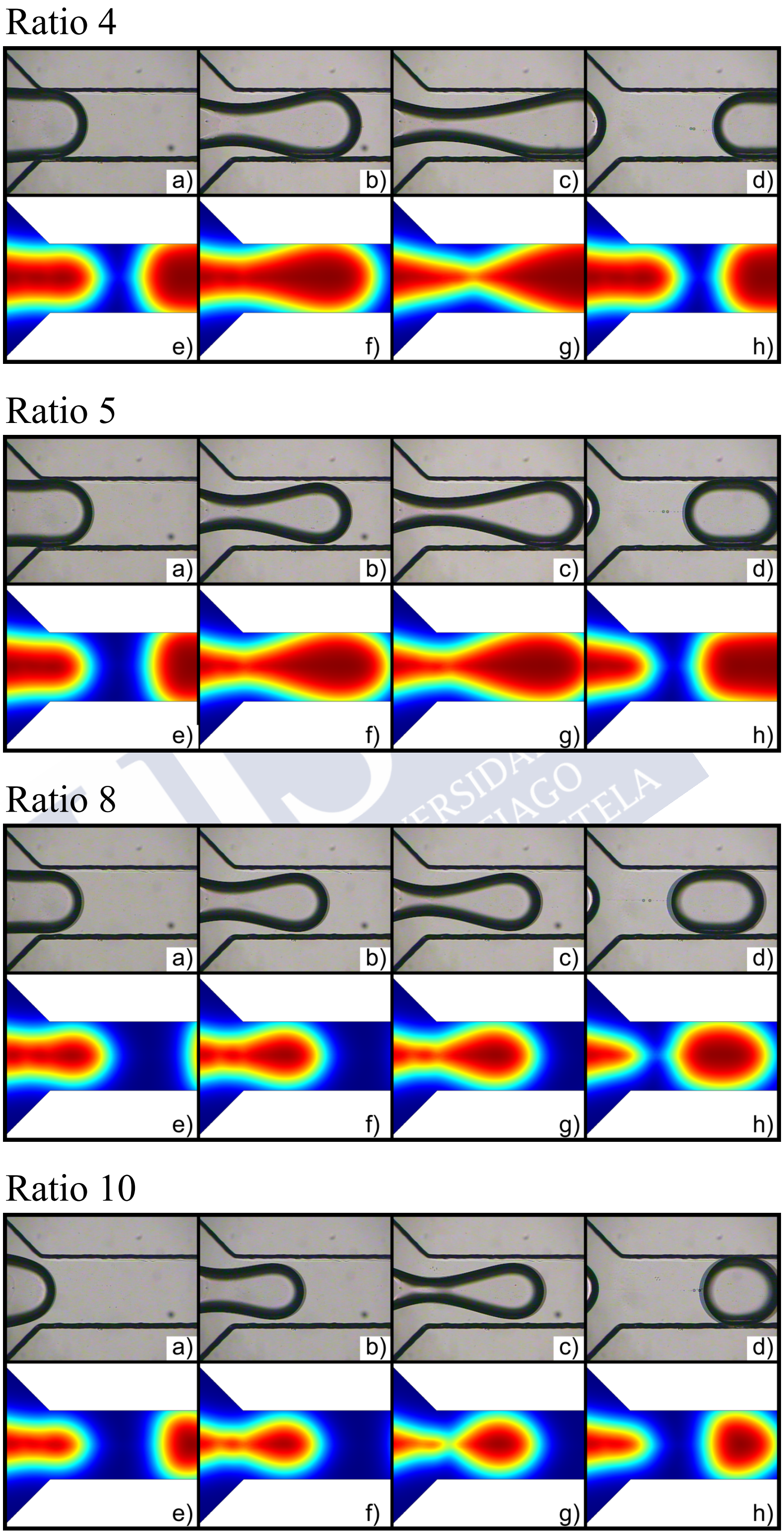

Figure 10.2: Droplet generation inside the microchannels depending on the Oil/Water phase flow rate. Optical images of the experimental assays from a) to d), and their respective counterparts using COMSOL Multiphysics simulation software from e) to h).

the respective flows. This method involves the modelling with finite elements. A more complete description of this well-known and tested procedure can be found on Chapter 1. In particular, in this study, the two-dimensional geometry was built respecting the real scale of the microfluidic chip as well as the angles of the channels in the intersection point. The corresponding values for density and viscosity of water and vegetable oil were used as provided in the database of the software, while the chosen surface tension was pre-set as corn oil/water. Even though it is true that the vegetable oil used in the laboratory assays was from sunflower seed origin, this configuration provides a more than adequate approximation.

Calculations were ran introducing fixed values for the normal velocity of the flow inlets, and the domain elements defined by the mesh were solved through Finite Element Method. As the study is time-dependent, the software required a time range, which in this particular case was from 0 to 3 seconds, and a time step, 0.02 seconds, to assure convergence.

In Figure 10.2, the volume fraction of the two phases are represented, being the blue colour the corresponding to $\varphi_{oil} = 1$, red corresponding to pure water phase and light green to the interphase or $\varphi_{oil} = \varphi_{water} = 0.5$.

The results of the simulations show a clear relation between velocity, size and rate of droplet formation. As the continuous phase flow increases, the viscous shear-stress augments, overcoming interfacial tension and “breaking” the water droplets with higher frequency, obtaining smaller droplets with a larger distance between them. At smaller Oil/Water ratios, Rayleigh-Plateau instabilities start to appear and the water phase develops undulations. If this ratio descends to a limit, water phase reaches a stable parallel regime flow, known as jetting, and the droplet formation is not achieved, which is in good agreement with theory [4, 5].

10.3.2 Formation of sodium alginate microdroplets

The microdroplet formation in a T or Y-junction is a common topic of research in the recent years and has been already discussed in detail [6, 7]. From those studies it is known that diverse factors as the geometry of the chip, dispersed solution viscosity or flow rates, as discussed in the previous section, affect the size and shape of the droplets.

In this case, as the chip design was fixed, the concentration of sodium alginate solution was maintained constant at 2 wt. %, and the composition of the oil phase was the same in all experiments, the flow rate was the main factor to manipulate. Figure 10.3 shows a diagram of the relationship between sizes and flows with real optical images of the droplets.

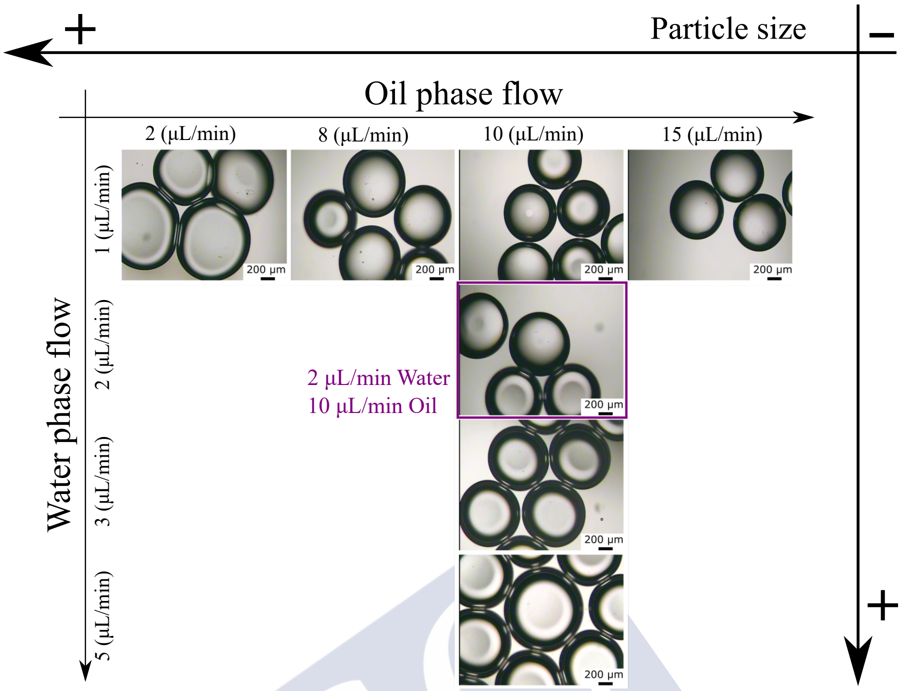

Figure 10.3: Scheme illustrating the dependence between the water-oil flow ratio and the droplet size and distribution.

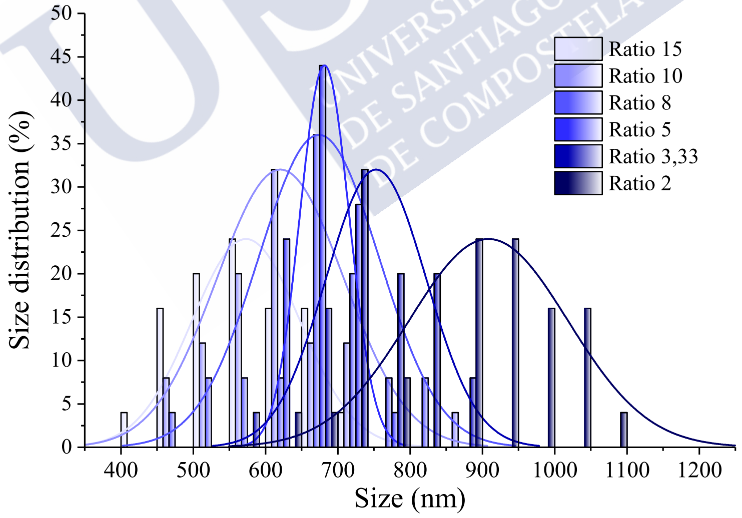

Figure 10.4: Droplet size distribution at different Oil/Water ratios.

Table 10.1: Size distribution. Mean and standard deviation. A minimum amount of 40 droplets were measured for each condition.

Oil/Water Ratio	Mean Size (nm)	Standard Deviation
2	908.47	110.21
3.33	753.03	69.43
5	681.69	34.23
8	673.86	83.44
10	620.63	80.02
15	573.09	74.83

As expected, mean size of the droplets increase inversely to the Oil/Water ratio and the values seem consistent with the dimensions of the chip channels and orifice, being in the range of 700 nm. It is interesting to note that, due to the aforementioned fluctuations and instabilities in the channel flows when the ratio is too low or high, the homogeneity of the sizes decreases.

10.3.3 Gelation of calcium alginate microparticles and chitosan covered microspheres

In the recent years, various methods for obtaining diverse polymeric alginate microparticles using microfluidic techniques have been developed. Fundamentally, the crosslinking reaction of alginate follows the equation:

$$2\ \mathrm{Na-alginate} + \mathrm{CaCl_2} \rightarrow \mathrm{Ca-alginate} + 2\ \mathrm{NaCl}$$

Commonly, this hydrogel particles are generated by external [8–10] or internal gelation [11–13]. With internal gelation, the crosslinking starts, virtually, at the same time than the formation of the droplets [14, 15]. This method is better to maintain a more evenly distributed and more homogeneous size and shape, resulting in particles with spherical structure. On the other hand, internal gelation is slower, as it depends on the diffusion of Ca^{2+} ions from their centre to the surface [16], and what is more, the final particles tend to have a weak stiffness as the crosslinking is usually incomplete. Furthermore, the internal gelation method is way more sensitive, with a high degree of dependence on the initial concentrations and control of the process, since the particle solidification inside the microchip will provoke undesired fluctuations on the flow or clogging in microchannels. For its part, external gelation is typically achieved collecting the alginate droplets, that are originated inside the microchip, in a gelation bath with a moderate-to-high concentration of calcium ions, leading to a crosslinking reaction of Ca^{2+} and the carboxyl groups of alginate. As the droplets get in contact with the bath, Ca^{2+} ions start to diffuse through the droplets until obtaining fully crosslinked hydrogel microparticles. Due to the relatively high speed with which the crosslinking takes place, added to the gravitational and interfacial forces when they drip into the bath [17], the sphericity of the resulting particles is way more difficult to achieve, commonly obtaining pear-like or droplet-shaped morphologies with a wide size distribution [18]. Added to that, the quick gelation of the surface prevents the Ca^{2+} ions from diffusing to the inner core, and, in this case, is the centre of the particles which is not completely solidified [19]. In the more recent years, the interest in this topic of authors like Wang et al [20], has led to new processes combining both internal and external gelation, solving partially the mentioned problems.

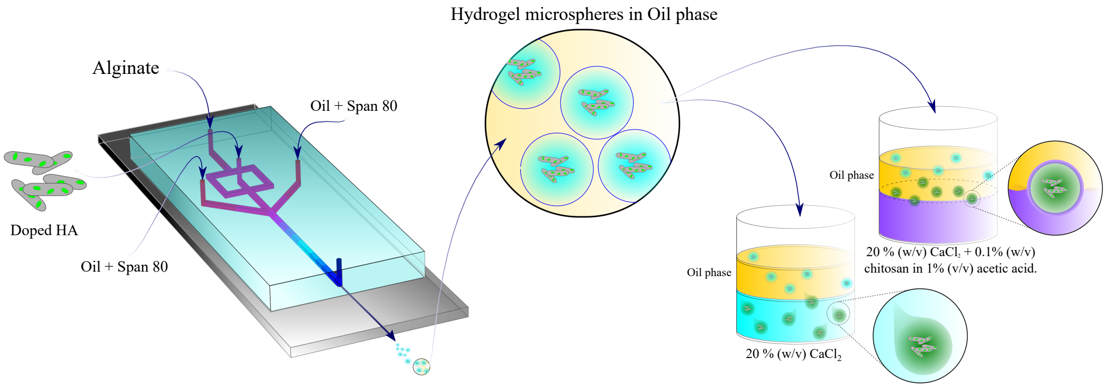

Figure 10.5: Schematic representation of the microfluidic system. Spherical droplets are formed before the collection in the gelation baths. The gravitational and interfacial forces when the droplets drip into the first bath results in teardrop-shaped Ca-Alg microparticles. In the second case, the addition of Chi and the acidic environment produce spherical core-shell ALG-CHI microgels.

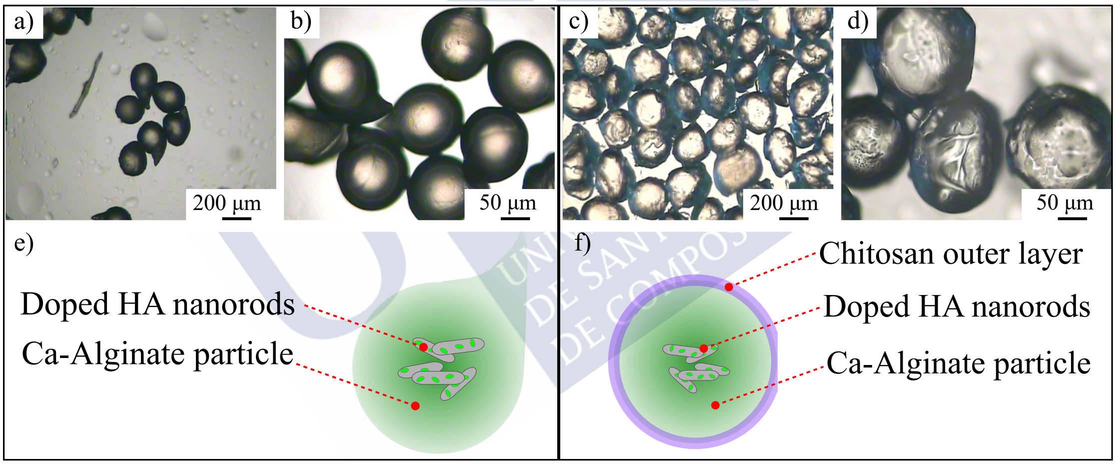

Figure 10.6: a-b) Optical images of the crosslinked Ca-ALG microparticles. The teardrop shape can be clearly identified. c-d) Chitosan-covered microparticles. In this case, samples exhibit an spherical or spheroidal shape. All images were taken after crosslinking in the external gelation bath, and then filtered and dried with blotting paper. e-f) Schemes representing the two different microparticle shape and composition.

10.3.4 Adsorption of Prop and Clox onto HA nanoparticles

To analyze the adsorption process, results were fitted to the Avrami's equation:

$$\boldsymbol{q_t = q_e \left(1 - \; e^{-[K_{av} \bullet t]^n}\right)} \tag{10.5}$$

The relationship between time and adsorbed concentrations of Prop and Clox is depicted in Figure 10.7 With a first quick glance at the curves it can already be noticed that both drugs follow a similar behaviour, reaching the adsorption

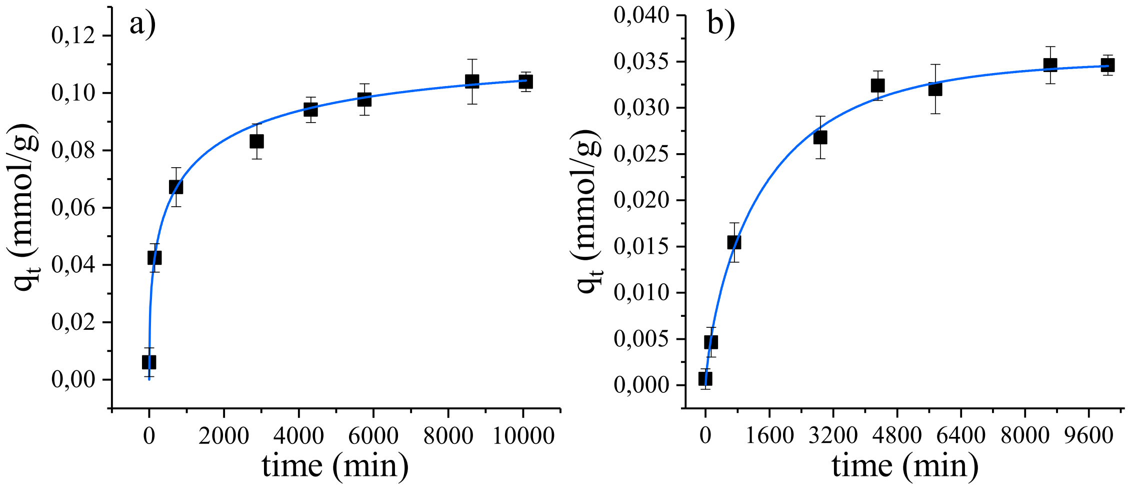

Figure 10.7: Kinetic adsorption studies for a) Prop and b) Clox. Avrami's model at 37 °C.

Table 10.2: Kinetic adsorption parameters of Prop and Clox onto HA, obtained using Avrami equation at 37 °C

	q_e (mmol/g)	***K_{av} (min^{-1})***	***n***	***R^2***
Prop	0,1134 ± 0,014	$1{,}03 \cdot 10^{-3} \pm 7{,}53 \cdot 10^{-4}$	0,395 ± 0,097	0,995
Clox	0,0351 ± 0,0011	$6{,}37 \cdot 10^{-3} \pm 1{,}03 \cdot 10^{-4}$	0,759 ± 0,076	0,998

equilibrium at around 2000 min. The results of the fittings for the order of the kinetic process (n) and its constant (K_{sv}) are shown in Table 10.2.

Data show a satisfactory fit with correlation coefficients close to 1. As observed, n values for both drugs are low (0.2–0.8) suggesting that distribution of drug to the support is homogenous and adsorption does not occur with constant growth rate. At the same time, the values obtained for the K_{sv} indicate that the adsorption, while relatively low in both cases, is notably higher in the case of Prop, probably due to the better affinity of this drug to the negatively charged surface of the hydroxyapatite nanorods.

10.3.5 Desorption/release profiles

For analyzing the desorption data, the model chosen was the Korsmayer - Peppas [21]:

$$Q = \frac{M_t}{M_\infty} = kt^n \tag{10.6}$$

Where M_t, is defined as the mass of drug released at time t, and M_∞, is the mass of drug released. Thus, M_t/M_∞ represents the fractional solute release by desorption at time t. k is a constant incorporating characteristics of drug and

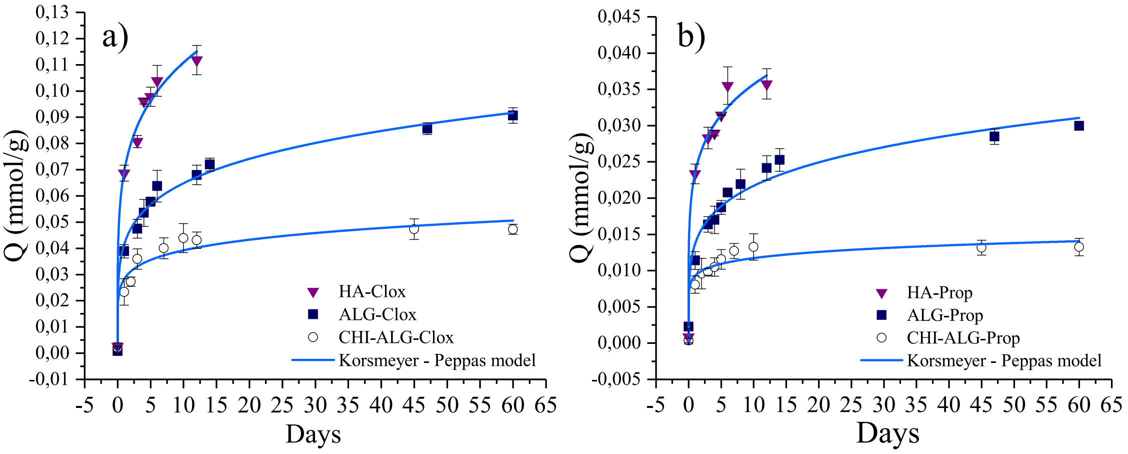

Figure 10.8: Desorption studies a) Propranolol and b) Cloaxacillin. All data fit to Korsmeyer-Peppas model.

Table 10.3: Desorption studies for Prop. Parameters of Korsmeyer – Peppas model for the three different samples.

	K (s^{-1})	n	R^2
HA-Prop	$2.97 \cdot 10^{-3} \pm 1.16 \cdot 10^{-3}$	0.382 ± 0.030	0.985
ALG-Prop	$1.41 \cdot 10^{-3} \pm 0.39 \cdot 10^{-3}$	0.200 ± 0.020	0.962
CHI-ALG-Prop	$2.94 \cdot 10^{-3} \pm 0.86 \cdot 10^{-3}$	0.101 ± 0.021	0.944

the macromolecular network system, and n is the diffusional exponent, which is indicative of the transport mechanism. All parameters are shown in Tables 10.3 and 10.4.

Peppas et al. have demonstrated that the morphology of the structure of release has a notable impact in the desorption process [21, 22]. In the present case, as the desorption occurs from nanorods, n values will depend on the relation between length and diameter. Apart from that, it should not be forgotten the fact that the homogeneity of the nanorods in aqueous solution can be variable due to their instability and tendency to agglomerate. Furthermore, and based on their works, the first steps of the release are predominantly directed by the smaller particles, while the bigger ones have a more notable impact in the rest of the process. Having

Table 10.4: Desorption studies for Clox. Parameters of Korsmeyer – Peppas model for the three different samples.

	K (s^{-1})	n	R^2
HA-Clox	$6.84 \cdot 10^{-3} \pm 2.34 \cdot 10^{-3}$	0.304 ± 0.026	0.989
ALG-Clox	$4.61 \cdot 10^{-3} \pm 0.75 \cdot 10^{-3}$	0.193 ± 0.011	0.990
CHI-ALG-Clox	$5.65 \cdot 10^{-3} \pm 2.06 \cdot 10^{-3}$	0.142 ± 0.026	0.942

Table 10.5: Cumulative in vitro release of Propranolol and Cloxacillin from HA nanoparticles, ALG micropartiles and CHI-ALG microspheres.

	Cumulative Release
HA-Prop	100 %
ALG-Prop	86.60 %
CHI-ALG-Prop	38.31 %
HA-Clox	100 %
ALG-Clox	87.27 %
CHI-ALG-Clox	45.46 %

this into account it is safe to assure that the behaviour of the HA in water influence the whole desorption activity, which is probably why the diffusional exponent do not reach the values of $n = 0.451$ for Fickian release from cylinders that Peppas and coworkers reported. It is interesting to note that for both drugs, n is in the same range, suggesting that the transport mechanism is similar in the two cases. When the particles are wrapped in the hydrogel matrix, the stability in water of crosslinked alginate and chitosan prevents the drugs from be released to the media. As Table 10.5 shows, within the time range studied, 60 days, Chi-covered spheres have a cumulative release of 38.31 % and 45.46 % for Prop and Clox, respectively; while values for Alginate tear-shaped particles are substantially higher reaching 87.27 %.

To fully comprehend and analyze the mechanisms of the desorption process of these more complex systems, further studies are on their way, but the early qualitative results serve for comparative purposes and allow to probe that drug delivery ratios can be partially manipulated depending on the structures designed and the applications purposed. Both the tunability and the complexity of the resultant materials put them as a very promising solution for different medical processes in the field of interventional therapy or regenerative medicine.

Bibliography

[1] J. M. Marques Junior, A. L. H. Muller, E. L. Foletto, A. B. da Costa, C. A. Bizzi, and E. Irineu Muller, “Determination of propranolol hydrochloride in pharmaceutical preparations using near infrared spectrometry with fiber optic probe and multivariate calibration methods,” *Journal of Analytical Methods in Chemistry*, vol. 2015, p. 795102, 2015.

[2] J. Malakar, A. Nayak, and D. Pal, “Development of cloxacillin loaded multiple-unit alginate-based floating system by emulsion-gelation method,” *International journal of biological macromolecules*, vol. 50, pp. 138–47, 2012.

[3] C. Multiphysics, “Introduction to comsol multiphysics®,” *COMSOL Multiphysics, Burlington, MA, accessed Feb*, vol. 9, p. 2018, 1998.

[4] C. N. Baroud, F. Gallaire, and R. Dangla, “Dynamics of microfluidic droplets,” *Lab on a Chip*, vol. 10, no. 16, pp. 2032–2045, 2010.

[5] A. S. Utada, A. Fernandez-Nieves, H. A. Stone, and D. A. Weitz, “Dripping to jetting transitions in coflowing liquid streams,” *Physical Review Letters*, vol. 99, no. 9, p. 094502, 2007. PRL.

[6] I.-L. Ngo, T.-D. Dang, C. Byon, and S. W. Joo, “A numerical study on the dynamics of droplet formation in a microfluidic double t-junction,” *Biomicrofluidics*, vol. 9, no. 2, p. 024107, 2015.

[7] F. Y. Ushikubo, F. S. Birribilli, D. R. B. Oliveira, and R. L. Cunha, “Y- and t-junction microfluidic devices: effect of fluids and interface properties and operating conditions,” *Microfluidics and Nanofluidics*, vol. 17, no. 4, pp. 711–720, 2014.

[8] C.-H. Yeh, Q. Zhao, S.-J. Lee, and Y.-C. Lin, “Using a t-junction microfluidic chip for monodisperse calcium alginate microparticles and encapsulation of nanoparticles,” *Sensors and Actuators A: Physical*, vol. 151, no. 2, pp. 231–236, 2009.

[9] Y. S. Lin, C. H. Yang, Y. Y. Hsu, and C. L. Hsieh, “Microfluidic synthesis of tail-shaped alginate microparticles using slow sedimentation,” *Electrophoresis*, vol. 34, no. 3, pp. 425–31, 2013.

[10] T. D. Dang and S. W. Joo, “Preparation of tadpole-shaped calcium alginate microparticles with sphericity control,” *Colloids and Surfaces B: Biointerfaces*, vol. 102, pp. 766–771, 2013.

[11] W. H. T. Tan and S. Takeuchi, “Monodisperse alginate hydrogel microbeads for cell encapsulation,” *Advanced Materials*, vol. 19, pp. 2696–2701, 2007.

[12] K. Liu, H.-J. Ding, J. Liu, Y. Chen, and X.-Z. Zhao, “Shape-controlled production of biodegradable calcium alginate gel microparticles using a novel microfluidic device,” *Langmuir*, vol. 22, no. 22, pp. 9453–9457, 2006.

[13] S. Ching, N. Bansal, and B. Bhandari, “Alginate gel particles–a review of production techniques and physical properties,” *Critical reviews in food science and nutrition*, vol. 57, 2015.

[14] V. Workman, S. Dunnett, P. Kille, and D. Palmer, “On-chip alginate microencapsulation of functional cells,” *Macromolecular Rapid Communications*, vol. 29, p. 165, 2008.

[15] E. Amici, G. Tetradis-Meris, C. P. de Torres, and F. Jousse, “Alginate gelation in microfluidic channels,” *Food Hydrocolloids*, vol. 22, no. 1, pp. 97–104, 2008.

[16] E. Tumarkin and E. Kumacheva, “Microfluidic generation of microgels from synthetic and natural polymers,” *Chemical Society Reviews*, vol. 38, no. 8, pp. 2161–2168, 2009.

[17] L. Capretto, S. Mazzitelli, C. Balestra, A. Tosi, and C. Nastruzzi, “Effect of the gelation process on the production of alginate microbeads by microfluidic chip technology,” *Lab on a Chip*, vol. 8, no. 4, pp. 617–621, 2008.

[18] L. Mazutis, R. Vasiliauskas, and D. A. Weitz, “Microfluidic production of alginate hydrogel particles for antibody encapsulation and release,” *Macromol Biosci*, vol. 15, no. 12, pp. 1641–6, 2015.

[19] T. Braschler, A. Valero, L. Colella, K. Pataky, J. Brugger, and P. Renaud, “Link between alginate reaction front propagation and general reaction diffusion theory,” *Analytical Chemistry*, vol. 83, no. 6, pp. 2234–2242, 2011.

[20] Q. Wang, S. Liu, H. Wang, J. Zhu, and Y. Yang, “Alginate droplets pre-crosslinked in microchannels to prepare monodispersed spherical microgels,” *Colloids and Surfaces A: Physicochemical and Engineering Aspects*, vol. 482, pp. 371–377, 2015.

[21] P. L. Ritger and N. A. Peppas, “A simple equation for description of solute release i. fickian and non-fickian release from non-swellable devices in the form of slabs, spheres, cylinders or discs,” *Journal of Controlled Release*, vol. 5, no. 1, pp. 23–36, 1987.

[22] N. A. Peppas, “A model of dissolution-controlled solute release from porous drug delivery polymeric systems,” *J Biomed Mater Res*, vol. 17, no. 6, pp. 1079–87, 1983.

11

Final conclusions

In the present work, different nanostructured systems and complex hybrid materials with potential applications in biomedical areas have been developed. Its study, analysis and characterization have led to establish a series of deductions and conclusions. Concerning what is referenced to in Chapter 3 about protein aggregations and interactions, a combination of theoretical and experimental approaches was used to deepen and better understand their evolution, behaviour and binding mechanisms. Analyzing the *in silico* together with the empirical reults, the following outcomes should be highlighted:

- About the evolution and structure of bovine serum albumin with the addition of surfactancts, molecular dynamic simulations revealed that this protein, when no ligands are present, exhibits an expanded form that allows the formation of dimers. SAXS results, in combination with SRCD, demonstrated that the system in solution is composed by partially unfolded monomers (75 %) and respective dimer (25 %) with no changes in secondary structure. With the addition of the ligands, the most important characteristics of the structural and numerical pathway were obtained from ITC analysis, showing that both surfactants interact with the monomer and the dimer at molar ratios below 30:1. After reaching saturation, the ligands form small aggregates distributed throughout all the BSA surface. SAXS and MD studies gave support to infer that the number of ligands that form the mentioned aggregates is similar for both surfactants but their structures suffer some changes: stretched with very similar shape and almost overlapped in the case of SFPO and a wider distribution with good superposition for SDS. SRCD data confirmed that apart from the aggregation process, BSA also suffers alterations in its secondary structure from α-helix to β-sheet.

- Regarding the binding properties and structural effects that betablockers (acebutolol and propranolol) have on fibrinogen, results from ITC and zeta potential demonstrated that the interactions were relatively weak for both cases, being a little more pronounced in the case of propranolol. Concomitantly, SAXS data also gave some insight on the fact that acebutolol is not able to cause neither conformational changes nor aggregation on fibrinogen, in total agreement with computational results. Nevertheless, SAXS data pointed out that propranolol does have a significant impact on the fibrinogen's structure. These results may be notably important to understand the first steps of the coagulation processes where the binding of thombin at E-domain and subsequently fibrinogen polymerization are essential aspects.

- For its part, the experimental data from ITC confirmed the results from Gibbs free energy of binding and the interactions involved in the binding process of fibrinogen with BTS. Likewise, it was demonstrated that all the BTS-binding poses can directly affect the normal modes of flexibility by decreasing the collectivity degree in the fibrinogen binding-site (residues of E-region). UV-vis and fluorescence measurements supported the latter results. These outcomes were also confirmed by SAXS, technique that not only corroborated the presence of conformational changes in fibrinogen, but also demonstrated that they are dependent on drug concentration. These results open new horizons on understanding the influence of conformational binding modes in protein-ligand interactions, which is of paramount importance in rational drugs-design.

- Also, the experimental results of fibrinogen when in contact with β-lactam antibiotics, excellently corroborated the computational predictions from: binding energies, target-residues and stoichiometry. Furthermore, the huge impact the penicillin molecular structure has in the binding process was confirmed by quantitative calorimetric data on ITC. For its part DSC enabled to also quantify energetically the role played by the elasticity of fibrinogen. Finally, the obtained results are the paramount importance during the "*de novo rational drug-design*" of new derivatives of β-lactam antibiotics to avoid potential fibrinolytic side-effects, increase the target selectivity/specificity with optimal benefit/risk rates beyond the β-lactam antibiotic drug resistance phenomena, and favor the implementation of rigorous criteria for a more personalized antibiotic therapy.

Focusing on the inorganic precursor, Chapter 4, the structural morphology of the synthetized hydroxyapatite nanorods was proved to be relatively homogeneus and uniform with a desultory network pattern composed by highly agglomerated nanoparticles, similar in size. The resulting distributions were found to be not isotropic, but bimodal. On the other hand and based on previous studies proposing effective routes for the synthesis and control of HA nanoparticles with different morphologies, it has been theoretically proposed and experimentally successfully developed a noble system for the nanoparticle synthesis using a microfluidic system. With proper design and appropriate conditions, this device is capable of engineering nanoparticles of different size, by just varying the flow rates. These results can also shine light upon the potential of microfluidics devices as a tool for the automation of high quality nanoparticle synthesis due to the high-performance capacity, flexibility and low cost properties. Further studies are under way to functionalize the surface of the nanoparticles with proteins and growth factors and determine the implications of concentration and flow effects in the structural formation and future applications in bone repair.

In this line, a multiple experimental approach was used in Chapter 5 to understand and characterize the adsorption of bovine serum albumin onto hydroxyapatite nanoparticles. Microcalorimetric analysis revealed that the binding between BSA and HA nanoparticles is exothermic and gradually decreases with increasing HA concentration. The best model fitting experimental values suggested that all the protein is adsorbed in the same way onto the nanoparticle surface, also corroborated by zeta potential, by non–covalent bonds. Following the Förster resonance energy transfer (FRET), it can be inferred that the quenching is static and the mechanism involves complex formation. The kinetic studies also revealed that the interaction between the protein and the inorganic compound is quite slow, keeping over time as the maximum value is obtained after 24 hours of interaction. Furthermore, CD spectral results confirmed that the excellent adaptation of the BSA on the nanoparticle surface is rooted in the flexibility of its 3D structure.

With the combination of an inorganic precursor and an adequate protein, a unique composite design can be created in order to obtain a biomaterial interface that mimics the properties of natural bone by coupling ceramic layers with soft matter ones. As explained throughout the document, the elongated shape, compared to spherical formulations, of the HA nanorods results in an increase of its surface area. This peculiarity enhances the electrostatic interactions with polycations and enables the LbL build up. This type of materials obtained by the LbL technique are suitable for coating implantable devices as they are osteoconductive and support cell adhesion, spreading and viability, opening a whole new range of possibilities to create a biocompatible interfaces.

Taking into account these considerations, multiple complex and hybrid structures with biomedical purposes can be designed. In this regard, a two-sided membrane reproducing the structure and function of the periosteum was created. Alginate and diverse concentrations of nanohydroxyapatite have been combined to develop bilayer membranes with a different chemical composition, roughness and porosity on each side. An efficient interaction between the HA nanorods and ALG chains was demonstrated to occur. With higher HA concentrations, the length and ramifications of the polymer networks increased and, in turn, decreased the amount of water in the structure. This condition resulted into an increase in the viscosity and, consequentially, on the strength of the fresh hydrogel, while the plasticity was reduced. The membrane was constituted by a highly porous fibrous side and a mineral-rich side with higher roughness, confirming its bilayer functionality. A favourable cellular response was observed for all the membranes tested, specifically growing osteoblasts on the mineral-rich side and fibroblasts on the fibrous side. Furthermore, membranes with the highest amount of HA notably induced osteoblast differentiation. The physico-chemical properties of the bilayer membranes can be easily tuned, therefore providing versatility to meet the complex requirements of bone tissue engineering.

Similarly, mechanically robust scaffolds were also created, Chapter 8. These complex biomaterials present a highly interconnected fiber mesh structure, due to the optimal distribution of HA nano-rods within the gelatin-TA network. Samples showed a definite degree of roughness in the pore wall surface, a quality that is essential to attain a suitable host tissue acceptance. In addition, the homogeneous distribution of HA among TA and protein chains results in a higher GE renaturation level in comparison with uncross-linked GE leading to an improved strength scaffolding. Highly cross-linked scaffold facilitated the entrapment of water in its framework and this fact leads to believe that they would have promising water retention properties to prevent the loss of body fluid and nutrients. Finally, degradation properties in different biological conditions, and also their capacity to induce, under physiological fluids, a biogenic hydroxyapatite coating, were corroborated.

In order to analyze the rheological behaviour of this kind of hydrogel scaffolds, five mechanically robust composite gels with the combination of Gelatin, Alginate, Fibrinogen, Bovine Serum Albumin and Hydroxyapatite were created. All of them exhibiting a highly interconnected mesh structure, confirmed by FT-IR. Confocal Raman microscopy revealed that both BSA and Fib are incorporated into the scaffolds while maintaining its native conformation. While fibrinogen gels maintain initial distributions, the presence of BSA homogenizes much better all components. This fact is attributed to the greater flexibility of the BSA that allows more degrees of freedom to the scaffold to minimize the energy of the hydrogel formation. Besides, Gel/Alg/BSA/HAp hydrogel exhibited better degradation and swelling properties through time because of the better distribution of HA which contribute to the increase of water uptake because of its water adsorbing properties. Rheological analysis reveals that the behaviour of the materials corresponds to a soft glass material. Creep analysis demonstrated that the inclusion of nanorods reinforces the structure of the gels, contributing to strengthen them and corroborated that the addition of BSA exhibits a better rheological behaviour. Finally, it has been also demonstrated that the morphological and mechanical properties of the hydrogels can be easily tuned by including several components, therefore providing better performances to soft tissue engineering applications.


USC
UNIVERSIDADE
DE SANTIAGO
DE COMPOSTELA

USC
UNIVERSIDADE
DE SANTIAGO
DE COMPOSTELA

CAMPUS VIDA
CAMPUS DE EXCELENCIA INTERNACIONAL

The present dissertation focuses on the different properties of self-aggregation processes of mixed molecular systems with the aim of designing and optimizing complex structures that promote the triggering of sequences leading to the deposition, nucleation and growth of hydroxyapatite crystals with the proper geometry and orientation. New strategies and novel synthetic routes were effectively developed, resulting in economically viable materials that mimic the structure and composition of the extracellular matrix, making them eligible and suitable for numerous applications in tissue regeneration and biomedical engineering.